ATMOSPHERIC SULFUR COMPOUNDS IN THE TROPOSPHERE AND STRATOSPHERE MEASURED WITH AN ATOMIC EMISSION DETECTOR

Dissertation

zur Erlangung des Grades

"Doktor *rerum naturalium* (Dr. rer. nat.)"

"Doktor der Naturwissenschaften"

im Promotionsfach Chemie

am Fachbereich Chemie, Pharmazie und Geowissenschaften

der Johannes Gutenberg-Universität in Mainz

Einar Karu

geboren in Tallinn

Max Planck Graduate Center

mit der Johannes Gutenberg-Universität Mainz

angefertigt am Max-Planck-Institut für Chemie

Paul Crutzen Graduate School

Mainz, April 2019

Tag der mündlichen Prüfung: 14.06.2019

To my family and friends

The Cosmos is all that is or ever was or ever will be.

Carl Sagan

ABSTRACT

Carbonyl sulfide (OCS) plays a crucial role in the Earth's sulfur budget. Globally OCS is the predominant reduced sulfur species in the Earth's atmosphere with typical tropospheric mixing ratios of around 500 ppt. During volcanically quiescent periods OCS controls the atmospheric sulfur budget within the troposphere and stratosphere, and the upward transport governs the background stratospheric aerosol loading due to its long atmospheric lifetime. The stratospheric sulfate aerosol layer (Junge layer) affects the global radiative balance, as sulfate aerosol particles scatter a fraction of incoming solar energy back to space. Sulfate particles can also act as cloud condensation nuclei (CCN) and ice nuclei (IN), thus further increasing the albedo of the Earth. Furthermore, OCS also acts as a climate forcing gas, absorbing longwave outgoing infrared radiation.

Research into OCS has a long history, but nevertheless the atmospheric OCS budget remains unbalanced. Therefore, improving knowledge of OCS sources, and sink processes is essential for improving current models and thereby for accurate future climate forecasts.

Throughout this PhD work a novel analytical system was developed to measure volatile organic compounds (VOCs), with primary focus on organosulfur species. The system consists of a gas phase cryogenic pre-concentration system (Entech), gas chromatographic (GC) separation and 3rd generation atomic emission detection (AEDIII), hence termed Entech-GC-AEDIII. The setup and performance of this newly established system is demonstrated. The Entech-GC-AEDIII enables various VOC measurement, including organosulfur species, non-methane hydrocarbons (NMHC), halogenated compounds, volatile nitrogen compounds, monoterpenes etc. This is the first instrument report of a gas phase air sample analysis method with an AED instrument.

Whole air samples (WAS) were collected globally from the upper troposphere / lowermost stratosphere (UT/LMS) region onboard a Lufthansa Airbus A340-600 IAGOS-CARIBIC passenger aircraft into flasks by a fully automated system. The post-flight flask analyses were conducted between December 2015 and December 2018 by the automated Entech-GC-AEDIII system in a laboratory. From the OCS measurements a global OCS lifetime of 2.1 ± 1.3 years, and a significantly longer stratospheric lifetime of 47 ± 16 years were determined. Furthermore, a flux of 118 ± 39 Gg (S) yr^{-1} of OCS from the troposphere into the stratosphere was estimated, and the stratospheric sink estimate yielded 44 – 90 Gg (S) yr^{-1} of OCS. The 43% smaller sink serves as a 51 Gg (S) yr^{-1} estimate of the OCS fraction which is transported back from the stratosphere to the troposphere.

The global 3D ECHAM5 / MESSy Atmospheric Chemistry (EMAC) model was used to run the numerical calculations and sampled at the CARIBIC flight paths. A comparison between CARIBIC observations and EMAC model simulations led to a conclusion that the EMAC model substantially overestimates OCS MRs in the upper atmosphere.

A first of its kind measurement campaign with the new Entech-GC-AEDIII detector was conducted in a Finnish boreal forest at the Hyytiälä measurement station in September 2016. The boreal forests comprise 33% of the Earth's forest cover, making it the second largest biome in the world. Therefore, it is an essential component of the atmospheric biosphere – geosphere interface. The OCS measurements demonstrated the boreal forest as a strong vegetative sink for OCS, which could be one of the reasons for the discrepancy between the EMAC model and CARIBIC observations in the tropopause region. Furthermore, the nighttime uptake of OCS was analyzed, concluding the light independence of OCS fixing carbonic anhydrase (CA) enzyme.

ZUSAMMENFASSUNG

Carbonylsulfid (OCS) spielt eine entscheidende Rolle im Schwefelhaushalt der Erde. OCS ist die am meisten vorkommende reduzierte Schwefelverbindung in der Erdatmosphäre mit einem Anteil von circa 500 pptv. In Epochen mit geringerer vulkanischer Aktivität wird der atmosphärische Schwefelhaushalt in der Stratos- und Troposphäre durch OCS dominiert und aufgrund seiner langen atmosphärischen Lebensdauer hat OCS einen großen Anteil an der stratosphärischen Aerosol Bildung. Die stratosphärische Sulfat-Aerosolschicht (Junge-Schicht) beeinflusst die globale Strahlungsbilanz, da Sulfat-Aerosolpartikel einen kleinen Teil der einfallenden Sonnenenergie in den Weltraum streuen und auch als Wolkenkondensationskeime (CCN) und Eisnukleationskerne (IN) wirken können, wodurch sie weiter die Albedo der Erde erhöhen. Darüber hinaus fungiert OCS auch als Klima Gas, das die von der Erde zurückgestrahlte langwellige Infrarotstrahlung absorbiert.

Die Erforschung von OCS hat eine lange Geschichte, dennoch ist der atmosphärische OCS-Kreislauf noch nicht aufgeklärt. Daher ist die Erforschung der Prozesse von OCS, speziell Quellen und Senken, und das atmosphärische Budget für aktuelle Modellverbesserungen und genaue künftige Klimavorhersagen unerlässlich.

In dieser Doktorarbeit wurde ein neuartiges Analysesystem entwickelt, um flüchtige organische Verbindungen (VOCs) zu messen, wobei der Schwerpunkt auf Organoschwefelverbindungen lag. Das System besteht aus einem kryogenen Gasphasen-Vorkonzentrationssystem (Entech), einer gaschromatographischen Trennung (GC) und einem Atomemissionsspektrometer der dritten Generation (AEDIII), der im Folgenden Entech-GC-AEDIII genannt wird. Aufbau und Leistung dieses neu etablierten Systems werden erklärt und demonstriert. Der Entech-GC-AEDIII ermöglicht die Messung verschiedener VOCs, einschließlich Organoschwefelspezies, Nicht-Methan-Kohlenwasserstoffe (NMHC), halogenierte Verbindungen, flüchtige Stickstoffverbindungen, Monoterpene usw. Dies ist der erste Instrumentenbericht einer Gasphasen-Probenanalyse mit einem AED-Instrument.

Luftproben (WAS) wurden an Bord eines Lufthansa Airbus A340-600 IAGOS-CARIBIC-Passagierflugzeugs mit einem einer vollständig automatisierten Kollektor gesammelt. Die Proben umspannen ein weltweites Netz und wurden in der oberen Troposphäre / der untersten Stratosphäre (UT/LMS) gesammelt. Die Probenanalysen nach dem Flug wurden zwischen Dezember 2015 und Dezember 2018 vom automatisierten Entech-GC-AEDIII-System in einem Labor durchgeführt. Aus den OCS-Messungen wurden eine globale OCS-Lebensdauer von 2,1 ± 1,3 Jahren und eine signifikant längere Lebensdauer in der Stratosphäre von 47 ± 16 Jahren ermittelt. Darüber hinaus wurde ein Fluss von 118 ± 39 Gg (S) yr^{-1} von OCS aus der Troposphäre in die Stratosphäre abgeschätzt, und die Schätzung der Stratosphärensenke ergab 44 - 90 Gg (S) yr^{-1}. Nach Abschätzung der OCS-Fraktion, baut die stratosphärische Senke ca. 51 Gg (S) yr^{-1} ab, die von der Stratosphäre in die Troposphäre zurücktransportiert wird.

Das globale 3D-Modell ECHAM5 / MESSy Atmospheric Chemistry (EMAC) wurde für numerische Berechnungen verwendet und simuliert die Konzentrationen auf den CARIBIC-Flugstrecken. Ein Vergleich zwischen CARIBIC-Beobachtungen und EMAC-Modellsimulationen zeigt, dass das EMAC-Modell in der oberen Atmosphäre die OCS MRs wesentlich überschätzt.

Eine weitere Messkampagne mit dem neuen Entech-GC-AEDIII-Detektor wurde im September 2016 in einem finnischen Borealwald an der Hyytiälä-Messstation durchgeführt. Die Borealwälder machen 33% der Waldfläche der Erde aus und sind damit das zweitgrößte Biom an Land. Die Wälder sind daher eine wichtige Schnittstelle für die atmosphärischen Bio-Geo-Emissionen. Die OCS-Messungen zeigen den Borealwald als starke vegetative Senke für OCS, was einer der Gründe für die Diskrepanz zwischen dem EMAC-Modell und den CARIBIC-Messungen in der Tropopause sein könnte. Darüber hinaus wurde die nächtliche Aufnahme von OCS untersucht, und somit die Lichtunabhängigkeit der OCS-Fixierung durch das Carboanhydrase (CA) gezeigt.

CONTENTS

1 INTRODUCTION

1.1 Earth's atmosphere

The word of atmosphere originates from Ancient Greek, meaning *atmos* – vapour and *sphaira* – sphere, is a set of layers of gases surrounding a planet (or other material body) that is held in place by the gravity of that planet (or body). The mixture of gases retained in the Earth's atmosphere is commonly known as air. The Earth's atmosphere is normally divided into 5 layers, starting from the Earth's surface: troposphere (0 – 16 km), stratosphere (16 – 50 km), mesosphere (50 – 85 km), thermosphere (85 – 600 km) and exosphere (600 – 10 000 km) (Zell, 2013), and first 3 are depicted in *Figure 1.1*. The 4 primary layers closest to the surface protect our planet by absorbing harmful radiation and maintain temperatures required for life. The Earth's atmosphere has a mass of 5.148×10^{18} kg (Trenberth and Smith, 2005) of which about ¾ lays in the first 11 km from the surface (in the troposphere) and 99.9% in the first 50 km (Jacob, 1999). The mass of whole the Earth's atmosphere is by around a factor of million lighter compared to the mass of the Earth (5.972×10^{24} kg) (Williams, 2017).

In the troposphere air cools with altitude with an average wet lapse rate of -6.5°C km^{-1} and reaches minima around -60°C at the tropopause region. The troposphere is generally well mixed. In the stratosphere temperature increases with rising altitude. The stratospheric ozone layer absorbs harmful ultraviolet (UV) radiation originating from the Sun. As the UV radiation is absorbed, it heats the affected air parcel.

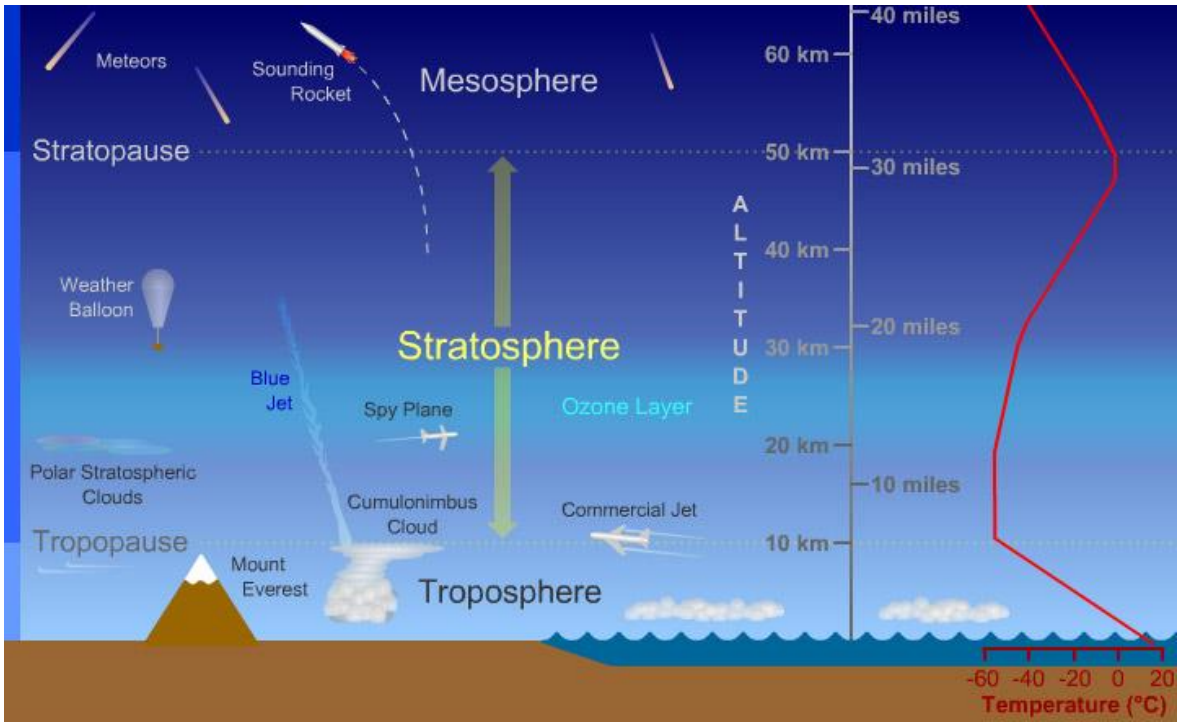

Figure 1.1 The first 3 main atmosphere layers closest to the Earth's surface. The air pressure and density decrease with rising altitude, the temperature decreases in troposphere and mesosphere but increases in stratosphere. Figure adopted from Russell 2011.

1.1.1 Atmospheric composition

1.1.1.1 Gas phase

The dominant gas constituents of dry air are: nitrogen (N_2, 78.08 vol%), oxygen (O_2, 20.95 vol%), argon (Ar, 0.93%), carbon dioxide (CO_2, 408 ppmv), neon (Ne, 18.18 ppmv), helium (He, 5.24 ppmv), methane (CH_4, 1 850 ppbv), krypton (Kr, 1 140 ppbv) and hydrogen (H_2, 550 ppbv). The minor components include other noble gases, various oxides, non-methane hydrocarbons (NMHCs), volatile organic compounds (VOCs), oxygenated VOCs (OVOCs), intermediate-volatility organic compounds (IVOCs), semi-volatile organic compounds (SVOCs), halogenated compounds and other trace gases. There are both natural and anthropogenic sources of these gases. The major relative composition of air remains relatively constant in the troposphere. The molar mass of dry air is 28.96 g mol^{-1}.

Water vapor (H_2O) content varies a lot temporally and locally, roughly in the range of 10 ppmv to 5 vol%. Water vapor normally decreases with altitude in the atmosphere, whereas most of H_2O is located in the troposphere on average around 1 vol% at sea level. Water vapor is about 0.25% by mass over the entire atmosphere. Water vapor content dilutes the other gases in the gas mixture, reducing the total density of the air. Air containing liquid or ice droplets might be denser than dry air.

Especially the trace gases impact the climate radiative forcing and can adversely harm the life quality of organisms, including human health via air pollution.

1.1.1.2 Particulate phase

Water vapor as well as other trace gases can saturate to form liquid or solid droplets in the air when the temperature is decreased or pressure is increased forming particulate matter (PM), i.e. aerosol particles. They are microscopic solid or liquid particulate matter suspended in the atmosphere, in combination called aerosols. They include inorganic, organic and biological (bioaerosol) particles. Aerosols can serve as cloud condensation nuclei (CCN) and ice nuclei (IN), which provide growth bodies for cloud droplet and ice crystal formation. The principal trace gas responsible for atmospheric PM nucleation is thought to be sulfuric acid (H_2SO_4), mainly derived from the further oxidation of sulfur dioxide (SO_2) (Kirkby *et al.*, 2011). It has been measured that peak daytime MR is around 0.04 – 1.2 pptv (Kerminen *et al.*, 2010). Organosulfur species like carbonyl sulfide (OCS), dimethyl sulfide (DMS) and carbon disulfide (CS_2) further oxidize into SO_2 in the atmosphere (discussed in more detail in *Section 1.3*), thus indirectly play an important role on PM formation.

Inorganic PM includes primary emissions of mineral dust (often mineral oxides from the Earth's crust), sea salt consisting mainly of sodium chloride (NaCl), considered as the first and second largest contributors by mass to the global aerosol budget. In addition, sporadic volcanic ash contributes to the inorganic PM. Secondary inorganic aerosols (SIA) originate from volatile inorganic compound (i.e. SO_2, NO_2 and NH_3) further chemical processing in the atmosphere to form particles (containing SO_4^{2-}, NO_3^- and NH_4^+ ions). SIA plays an important role for regional haze formation.

Organic aerosol constitutes of the emissions from both natural (vegetation and micro-organisms) and anthropogenic (combustion of fossil and biofuels, industry exhaust and biomass burning). Organic PM is subcategorized into primary organic aerosol (POA) and secondary organic aerosol (SOA). POA is considered as organic compounds emitted in the particulate phase or condensed into the particulate matter without undergoing chemical reactions. SOA on the other hand, originates from VOC gas phase oxidation or nucleation in the atmosphere, where the products are of sufficiently low vapor pressure to form particles (gas-to-particle partitioning). Examples of organic PM are: black carbon (BC), elemental carbon (EC), brown carbon (BrC), various condensed VOC. Organic aerosols make up around ½ of the total fine particulate matter (0.49 – 0.95 μm) mass at continental mid-latitudes (Saxena and Hildemann, 1996) and up to around 95% in tropical forest area

(Andreae and Crutzen, 1997). POA contributes about 35 Tg (C) yr^{-1} to the total carbon budget, where the major contribution (around 70%) comes from biomass burning (Bond *et al.*, 2004). Globally, most of SOA originates from biogenic sources, but especially at northern mid-latitudes could play equally important role (Lin *et al.*, 2012). In addition, it has been recently suggested that SOA formation from BVOCs might be significantly increased by anthropogenic pollution as: elevated levels of nitrogen oxides ($NO_x = NO + NO_2$) enhance BVOC atmospheric oxidation; high anthropogenic POA levels facilitate faster VOC, OVOC, IVOC and SVOC transformation into particle phase (Hoyle *et al.*, 2011). Up to now still large uncertainties are associated with SOA formation, global budget estimates range from 20 – 380 Tg yr^{-1} (Hallquist *et al.*, 2009; Spracklen *et al.*, 2011).

Bioaerosols are material of biological background suspended in the atmosphere in the form of pollens, fungal spores, bacteria, viruses and any fragments from plant or animal origin (Jones and Harrison, 2004). It has been suggested that from the total airborne PM by volume in remote continental areas 28% fraction is made up by bioaerosols. The proportion for populated continental and remote maritime locations are 22% and 10%, respectively (Matthias-Maser *et al.*, 2000). Bioaerosols can range from around less than 0.25 – 58 µm, where normally the viruses are the smaller and pollen the larger PM. Bioaerosols can also significantly contribute to the formation of cloud droplets and ice crystals by serving as a CCN and IN (Sun and Ariya, 2006). Furthermore, bioaerosol can have a major negative effect on the public health in the form of allergens, pathogenic bacteria, fungi, viruses and bacterial endotoxins (Douwes *et al.*, 2003).

Most aerosol particles are primarily scatterers (PM > 0.1 µm), which scatter most of their incident solar radiation in the forward the Earth's surface direction and less back to the space (cooling effect). Particulate matter can also lead to formation of tropospheric ozone, which is also a greenhouse gas (warming effect). Combustion products like BC and BrC are primarily absorbers and thus heat the atmosphere. In total, aerosols have a net cooling effect on the the Earth with a net estimate from anthropogenic aerosol fraction since 1750 of -0.27 W m^{-2} (-0.77 – 0.23 W m^{-2}). In addition, further cooling by cloud adjustments due to anthropogenic aerosol contribution by -0.55 W m^{-2} (-1.33 – -0.05 W m^{-2}) since 1750 (Stocker *et al.*, 2013).

As for the gas phase atmosphere constituents also particulate matter has both natural and anthropogenic sources. They also affect the climate's radiative balance, change the precipitation patterns and negatively influence health and well-being of organisms. Especially harmful are particulate matter with diameter less than 10 µm (PM_{10}) and 2.5 µm

($PM_{2.5}$) as they can effectively enter the blood stream as they penetrate deeply into the respiratory tract and lungs, causing cardiovascular, respiratory diseases, DNA mutations and premature deaths. Furthermore, aerosols and especially cloud adjustments still contribute the largest uncertainty to the Earth's changing energy budget estimates and interpretations through radiative forcing (Stocker *et al.*, 2013).

1.1.2 Tropopause determination

The tropopause layer is situated between troposphere and stratosphere and located lower in winter and higher in summer. At the poles it lays the lowest, at around 6 – 9 km (~ 300 hPa) and at the highest in the tropics, at around 16 – 18 km (~ 100 hPa). There are many possibilities how to define the tropopause. In this thesis I consider dynamical, thermal and chemical tropopause.

Dynamical tropopause is often described with a potential vorticity (PV). Often a PV > 1.5 to 5 potential vorticity units (PVU) is defined for tropopause in the extratropics (1 PVU = 1.0×10^{-6} km^2 kg^{-1} s^{-1}). The steeper the PV gradients are on the isentropes the stronger the transport barrier of the dynamical tropopause is (Kunz *et al.*, 2011).

Thermal tropopause is the most commonly used definition of a tropopause, it is defined with a lapse rate. When the temperature decrease with altitude is less than 2°C km^{-1} and remains below this value for a depth of at least 2 km then the air parcel is situated in thermal tropopause as defined by the World Meteorological Organization (WMO). Nevertheless, the tropopause height is not always unambiguous with this definition: the transition from tropospheric to stratospheric lapse rates can occur over a depth of several kilometers rather than occurring rapidly at a well-defined height (Bethan, Vaughan and Reid, 1996).

The chemical tropopause can be inferred from the rapid increase of ozone (O_3) MR in the tropopause – stratosphere region. The troposphere has much higher MR of carbon monoxide (CO) and water content (H_2O), thus the steep gradients of O_3, CO and H_2O between the troposphere and tropopause can be used for chemical tropopause determination (Zahn and Brenninkmeijer, 2003). It has been reported that chemical tropopause best agrees with dynamical tropopause with threshold PV > 2 PVU (Zahn, Brenninkmeijer and van Velthoven, 2004).

1.2 Current and future climate concerns

Our atmosphere is thin but we are all living within it. It is of a vital importance to limit the anthropogenic emissions to the atmosphere and to understand the processes taking place within it, in order to better protect our environment during the new epoch of the Anthropocene (Crutzen, 2006b). At the time of writing, our Earth remains as the only habitable place for life as we know it. Observational data helps to advance the mechanistic understating of the processes taking place in the atmosphere, which in turn help to further develop the global 3D chemistry models for even more accurate future climate forecasting. This is of an utmost importance during the period of rapid human caused climate change in order to select the best mitigation and adaptation polices required.

1.2.1 Human-induced climate change

Fossil fuel burning and cement manufacturing released on average 30.4 Pg yr^{-1} of CO_2 (8.3 Pg C yr^{-1}) into the atmosphere in between 2002 – 2011, with uncertainty taking into account ranging from 27.8 – 33.0 Pg yr^{-1} of CO_2 (7.6 – 9.0 Pg C yr^{-1}), a mean growth rate of 3.2% yr^{-1} (Stocker *et al.*, 2013). Furthermore, they estimated that between 1750 and 2011 humankind released 1374 Pg of CO_2 (375 Pg C) into the atmosphere, which causes anthropogenic global warming.

The industrial revolution, which took place roughly between 1750 – 1850 is often taken as the start of human-induced climate change. Mankind has already caused a global average warming of about 1°C (0.8°C – 1.2°C range with uncertainties) over the period of 1880 (since the records begin) to 2017 and is currently forecasted to warm with a rate of 0.2°C per decade (0.1°C – 0.3°C per decade range with uncertainties with high confidence) as reported in the recent IPCC Special Report: Global Warming of 1.5ºC (Masson-Delmotte *et al.*, 2018). Radiative forcing has caused warming greater than the global average in many regions, and it is estimated that 20 – 40% of the global human population (global world population was 7.7 billion at the time of writing (Worldometers, 2019)) live in region which have already experienced warming more than 1.5ºC above pre-industrial times in at least one season (Masson-Delmotte *et al.*, 2018). The amount of glaciers that have already melted and the amount of ice and snow that have diminished are vast and caused sea level rises. Already today, we are experiencing climate refugees from oceanic island countries and the rate is rapidly increasing. It is probable that human-induced climate change has caused more deadly extreme weather events. It is likely that the frequency of hot heat waves has increased since

1950s, very likely that cold temperature extremes have decreased, likely that the number of heavy precipitation events in a number of regions has increased and likely that extreme sea levels have increased (IPCC, 2014). Furthermore, biodiversity is diminishing with ever growing unprecedented rate. The current extinction rates are about 1 000 times faster than the natural background rates of extinction and future rates are likely to be 10 000 times higher (De Vos *et al.*, 2015). Thus, it is extremely important to try to stick to the 1.5ºC Paris Agreement which was signed in 2015, but it will be extremely difficult.

1.2.2 Climate geoengineering via stratospheric sulfur injections

Climate geoengineering is a deliberate act of trying to change (to cool) the Earth's climate by humankind to ameliorate some of the effects of anthropogenic climate change, which was discussed above in *Section 1.2.1* (Keith, 2000). Clearly, the first and preferable choice is to significantly reduce greenhouse gas emissions, but some authors say that current energy system transformation to green energy and reduction is too slowly to avoid the high risks of the dangerous climate change (Stocker *et al.*, 2013). Thus, it might be important to investigate different geoengineering strategies to help to partly mitigate the planetary warming, to treat the symptoms over the causes. It is vital to study these potential ideas as thoroughly and to great extent as possible before planning to alter the natural Earth systems. That said, during the Anthropocene mankind needs to be ready for everything.

One of such geoengineering idea is to intentionally produce stratospheric aerosols which reflects some of the incoming solar energy back to space and increases the planetary albedo. This idea dates back to early as 1974 when Budyko and later Crutzen speculated the deliberate injection of sulfur into the stratosphere for the Earth's albedo enhancement (Будыко(Budyko), 1974; Budyko, 1977; National Academy of Sciences, 1992). More recent studies have suggested that the amount of the stratospheric aerosol injections required to cool the Earth's climate back to the pre-industrial levels is equal to about the scale of Mount Pinatubo volcanic eruption (in June 1991) aerosol injection every second year (Wigley, 2006). Mount Pinatubo injected around 10 Tg of sulfur into the tropical stratosphere, initially as SO_2 gas (Bluth *et al.*, 1992), which cooled the Earth's surface globally on average by 0.5°C in the year after the eruption (Lacis and Mishchenko, 1995). Paul Crutzen suggested stratospheric sulfur injections as an emergency measure in 2006 to prevent the climate system from going out of control. The artificial enhancing of the Earth's albedo is by far not the best solution, but as stated before mankind should be ready for the currently occurring rapid changes. Artificially adding sunlight reflecting particulate matter into the stratosphere

by means of sulfur is one possibility and should be studied to even greater extent (Crutzen, 2006a).

The sulfur injection for particle formation can be established by burning diatomic sulfur (S_2) or hydrogen sulfide (H_2S) gas in the stratosphere. For example, this can be established by carrying S_2 or H_2S gas into the stratosphere by balloons and firing them with artillery guns to produce SO_2, which will further process into H_2SO_4 and sub-micrometer sulfate particles by chemical and micro-physical processes in the stratosphere. For enhanced aerosol particle residence time in the stratosphere and to minimize the necessary amount, the reactants might be released near the tropical upward draft of the stratospheric circulation system and so distributed over time. Sulfate particles have a climate cooling effect also in the troposphere (Stocker *et al.*, 2013), but their residence time is only about a week compared to 1 – 2 years in the stratosphere, thus requiring only few percent of the sulfur load. (Crutzen, 2006a)

To transport sulfur into the tropical stratosphere from ships or tropical island sites would be a messy operation. An alternative option could be to release sulfur containing gas from the ground level. A potential candidate is OCS due to its long atmospheric lifetime and is also naturally the main source of the stratospheric sulfate particles in the Junge layer during volcanically low activity periods (Crutzen, 1976). Currently, around ¾ of emitted OCS is taken up by plants, how it would impact the long-term ecological stability is to a great extent unknown. It has been estimated that only around 5% of emitted OCS reaches into the stratosphere to locally produce SO_2 and sulfate aerosol (Chin and Davis, 1993). Thus, releasing OCS at the Earth's surface is not recommended and transport via balloons could be a better idea. Still, it could be possible to manufacture a specific gas that would only undergo photochemical reactions in the stratosphere to produce sulfate particles. Essentially, the gas should be non-toxic, non-reactive with atmospheric oxidants like OH, NO_3 and O_3, insoluble in water, should have a lifetime around 10 years and should not contribute to the climate warming in significant manner. This criteria disqualifies for example sulfur hexafluoride (SF_6) gas. (Crutzen, 2006a) Nevertheless again, the real long-term environmental and ecological safety are extremely difficult to test and mankind needs to be extremely careful when trying to change natural systems even further.

1.2.3 Outdoor air pollution

Air pollution has been broadly underestimated as a health hazard. It has been found that air pollution can significantly shorten life expectancy and lower life-quality. It has been found

that $PM_{2.5}$ and tropospheric ozone are the main pollutants causing premature deaths (Lelieveld *et al.*, 2015). Fine particulate matter penetrates deeply into the respiratory tract and lungs where it can enter the blood stream and can cause respiratory infections, cardiovascular diseases like hypertension and heart attacks, chronic obstructive pulmonary disease, strokes and lung cancer. In addition, the irritant ozone trace gas contributes to respiratory health effects. The World Health Organization (WHO) has listed climate change and air pollution in the top 10 global health threats. Air pollution is considered as the greatest environmental risk to health (WHO, 2019). The WHO has reported that 90% of people breath polluted air every day and that air pollution is killing 7 million people globally every year (WHO, 2018). This global mortality rate due to air pollution has been recently increased up to 8.8 million people per year, in Europe alone nearly 800 thousand. They reported that on average air pollution shortens the lifespan of European people by 2 years (Jos Lelieveld *et al.*, 2019). Polluted air claims at least as many lives as smoking (WHO estimates smoking kills around 7.2 million people yearly), whereas smoking could be a free will, but living in polluted air is not. It is found that children aged younger as 5 are most affected by the air pollution (Lelieveld, Haines and Pozzer, 2018). A recent study suggest that around 65% of premature deaths cause by air pollution originate from fossil fuel generated emissions. Thus, phasing out the use of fossil fuels and shifting over to renewable energies could prevent the death of more than 3 million people annually. The PM content in the atmosphere, which reflects some of the solar radiation back to space and affects the cloud cover with a net cooling effect, would quickly decline, which could lead to a further short-term 0.5ºC climate warming. This PM pollution removal caused warming could be simultaneously offset via the reduction of the GHGs methane, ozone and hydrofluorocarbons (CFCs) (J. Lelieveld *et al.*, 2019).

Anthropogenic emissions, including fossil fuel burning, shipping and biomass burning emit 106.4 Tg yr^{-1} of SO_2 (53.2 Tg S yr^{-1}) into the atmosphere (Smith *et al.*, 2011). During the Great Smog of London which lasted over 5 days in December 1952 caused at least 4 000 acute deaths and further 12 000 deaths during the next 2 months were associated with the smog event (Bell and Davis, 2001; Davis, 2002). The smog event emissions originated mainly from burning high sulfur content coal, which released a great amount of SO_2 into the air. Furthermore, sulfur emissions can cause ecological damage, for instance through SO_2 wet precipitation, causing acid rain. Therefore, outdoor sulfur pollution also plays a substantial role on human health and environmental damage.

1.2.4 Indoor air pollution

Nowadays, an average European and American spends on average about 85 – 90% of their time indoors (Klepeis *et al.*, 2001; European Comission, 2003). It has been reported that an average indoor air can be 2 to 5 times more polluted compared to outdoors (Wallace, 1987; European Comission, 2003). It has been measured that more than 300 VOCs were more concentrated indoors compared to outdoors, where the abundance of at least 50 of them was a full order of magnitude higher (Liu *et al.*, 2017). Indoor pollutants include toxic VOCs (i.e. benzene, formaldehyde, various aromatic and chlorinated solvents, phthalate esters and brominated flame-retardants), polycyclic aromatic hydrocarbons (PAHs), tobacco smoke, asbestos, radon and non-ionic surfactants (Weschler, 2009). It has been reported that the main emissions originate from the building itself (new building materials are often releasing chemical species with unknown toxicity) and the contents in it, mainly through degassing. Short-time high emissions have been associated with human activities, like cooking and cleaning (Liu *et al.*, 2017). For particulate matter, in developed countries most important emissions originate from cooking, fireplaces, toasters, gas stoves and candles. In megacities ventilating often brings in PM in higher concentration. For developing countries, indoor open fireplaces for cooking and heating are causing the biggest health concerns and problems, associated with significantly shorter life expectancy. Often sulfur rich fuel (e.g. coal) is used which produces significant SO_2 emissions. Furthermore, human emissions, which include both gas and particulate phase further influence the indoor air. In the wide population 77% of people are unaware that indoor air can be more polluted compared to outdoors (YouGov, 2018). Thus, indoor air quality also plays a major role on human health and life quality and is one of the current hot topics of science.

1.3 Organosulfur compounds

Organosulfur compounds like carbonyl sulfide (OCS, also often abbreviated as COS), dimethyl sulfide (DMS) and carbon disulfide (CS_2) play a crucial role in the Earth's sulfur budget. Globally OCS is the predominant reduced sulfur species in the Earth's atmosphere.

It is found that during volcanically quiescent periods to great extent OCS controls the atmospheric sulfur budget and the upward transport controls the stratospheric background aerosol loading, with estimate of 70% contribution from OCS to the sulfate layer (Brühl *et al.*, 2012). OCS enters atmosphere via direct, e.g. ocean, wetland, anoxic soil, volcanic and anthropogenic emissions, and also indirectly via e.g. CS_2, DMS oxidation. Both, direct and

indirect anthropogenic emissions significantly contribute to the OCS budget. The anthropogenic CS_2 emissions (especially from rayon production) further oxidize to OCS (Chin and Davis, 1995) and contribute about double as much compared to direct anthropogenic OCS emissions (Campbell *et al.*, 2015). The total anthropogenic contribution is estimated to be over ⅓ of the OCS emission budget (Watts, 2000). A model study estimates 74% of total sulfur mass coming from OCS in the troposphere and 70% in the stratosphere (Sheng *et al.*, 2015).

The schematics of the most important sulfur species, transport and processes therein involved in the atmospheric sulfur cycle are seen in *Figure 1.2*. Due to the long lifetime of OCS it does not necessarily require a deep convection to be transported to the tropopause region (Kremser *et al.*, 2016). More reactive organosulfur species, like dimethyl disulfide (DMDS, mean atmospheric lifetime around 1.5 hours, Lenschow et al. 1999), methanethiol i.e. methyl mercaptan (CH_3SH, average lifetime about 3 hours, Graedel 1977), DMS (mean lifetime around 1 day, Lenschow et al. 1999), CS_2 (average lifetime about 5 days, (Lelieveld *et al.*, 1997) and ethanethiol (CH_3CH_2SH, mean lifetime about 25 days, Graedel 1977) would typically require strong emissions, e.g. biomass burning event, to occur together with deep convective meteorological conditions to reach the upper troposphere and lower stratosphere (UTLS) region directly (Marandino *et al.*, 2013). Often the more reactive sulfur species are further oxidized in the atmosphere and converted to OCS, which acts as a vector compound to input sulfur to stratosphere (Burkholder *et al.*, 2015). OCS is further oxidized to SO_2 and H_2SO_4 and thereafter converted into aerosol, described in detail in *Section 1.4.2* and *1.4.6*. The IAGOS-CARIBIC aircraft in cooperation with Lufthansa is flying near the tropopause region, which makes it especially interesting to study the fluxes from the troposphere into the stratosphere, and *vice versa*. The OCS flux into the stratosphere is particularly interesting as it is one of the main precursors for the stratospheric sulfate aerosol during volcanically quiescent periods.

The IAGOS-CARIBIC (In-service Aircraft for a Global Observing System – Civil Aircraft for the Regular Investigation of the Atmosphere Based on an Instrument Container) (discussed in detail in *Chapter 3*) measurements of organosulfur species are very valuable as they provide a firsthand global OCS distribution measurement data, develop more insight into better understanding the sulfur flux from the troposphere into stratosphere, a basis dataset for global 3-dimensional (3D) atmospheric chemistry model and help to better constrain the unbalanced tropospheric sulfur budget (see *Section 1.5*).

1.4 Atmospheric sulfur chemistry

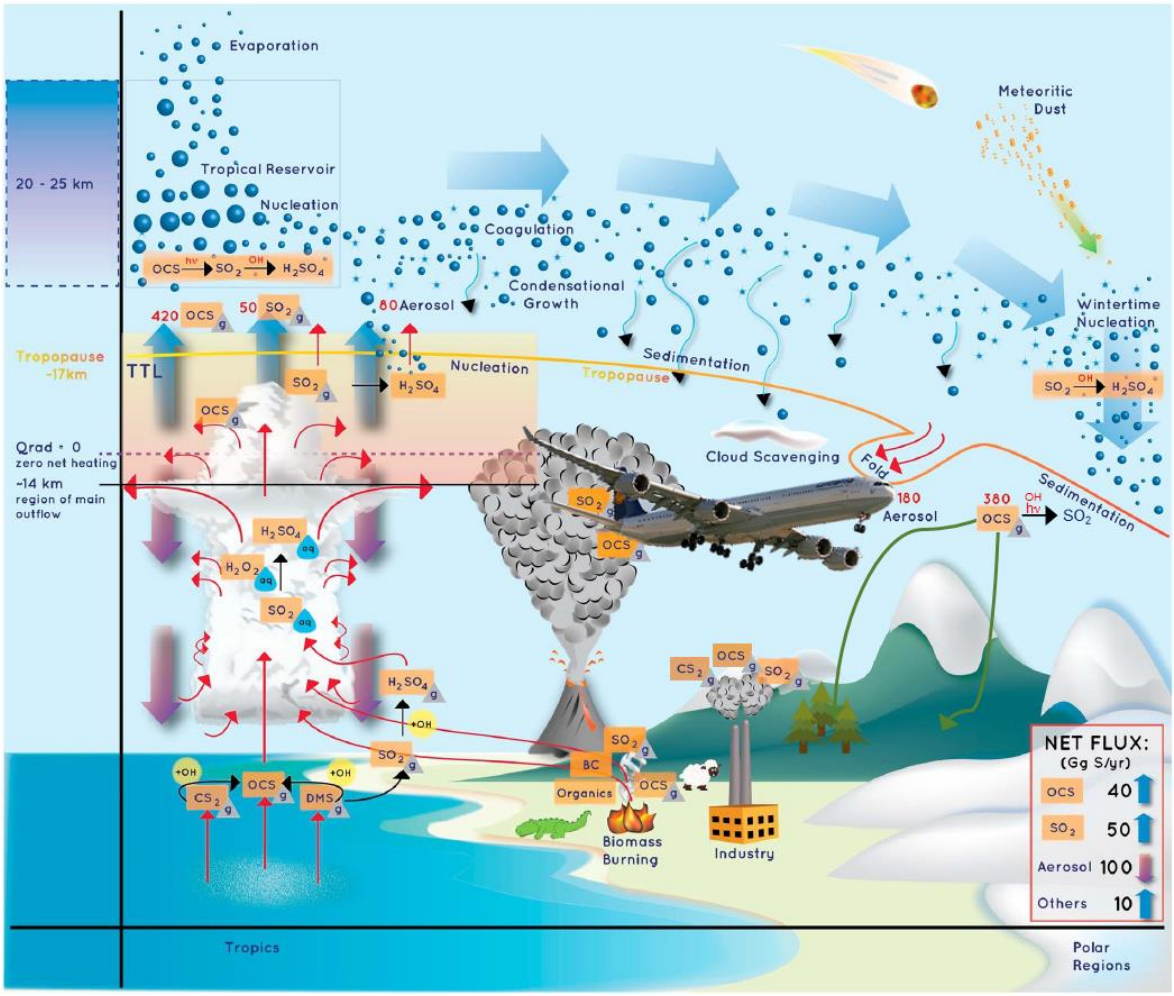

Figure 1.2 Graphical representation of the most important sulfur cycle distribution and reactions in the atmosphere. The thick blue arrows show the large-scale Brewer-Dobson atmospheric circulation, and the small red arrows indicate the transport processes. The black arrows show chemical conversions between the sulfur species. The thin blue arrows indicate the sedimentation processes of sulfate aerosol from the stratosphere to the troposphere. The small green arrows represent the OCS uptake via vegetation and oxic soil sinks. The red numbers indicate the net fluxes of OCS, SO_2 and sulfate aerosol in Gg (S) yr^{-1}, based on a model simulation by Sheng *et al*. 2015. The net estimate of sulfur compounds through the tropopause by Sheng *et al*. 2015 is depicted in the bottom right grey box, where the "others" could be mainly ascribed to DMS and H_2S. The Lufthansa Airbus A340-600 airplane indicates the typical sampling of CARIBIC in the UT/LMS region. Figure modified and adopted from Kremser *et al*. 2016.

1.4.1 Physical data of carbonyl sulfide

OCS has a boiling point of -50.2°C at 760 mm Hg (Lide, 2016), vapor pressure 9 412 mm Hg at 25°C (Daubert and Danner, 1989) and Henry constant 2.0×10^{-4} mol m^{-3} Pa^{-1} (Sander, 2015), thus classified as volatile organic compound (VOC). OCS solubility in water is 1.22 g L^{-1} at 25°C where it is effectively hydrolyzed to H_2S and CO_2 and the rate is dependent on temperature and pH (Elliott, Lu and Rowland, 1989).

1.4.2 Atmospheric reactions of sulfur compounds

Most gas phase organosulfur species react rapidly with the OH radical. Therefore, for many sulfur compounds the chemical lifetimes are short, in the rage of few days or less. This is much shorter compared to the typical air transport time from surface to the stratosphere (Kremser *et al.*, 2016). In contrast, the tropospheric lifetime of OCS is estimated between 1.5 – 3 years (Montzka *et al.*, 2007; Suntharalingam *et al.*, 2008), long enough for successful transport from troposphere to stratosphere, where it plays a crucial role on the stratospheric aerosol layer (Junge layer) formation (Crutzen, 1976). This more recent OCS lifetime estimation by *Montzka et al*. in 2007 is 2.5 times shorter than the earlier 5.7 year estimation by *Ulshöfer and Andreae* in 1997, mainly due to an upward revision of surface sink by factor of ≥ 2. Most sulfur species reactions are either much faster or much slower compared to the typical transport times to the stratosphere, thus uncertainties associated with the reaction kinetic rates are not critical for being able to model stratospheric sulfate (Kremser *et al.*, 2016). In contrast, for understanding the sulfur budget and closing the sulfur cycle accurately, accurate knowledge of atmospheric processes and kinetics are required to be understood. The Junge layer was first described in 1961 with maximum concentration in the middle atmosphere around 15 – 23 km (Junge and Manson, 1961).

In the stratosphere OCS is further converted to SO_2 and H_2SO_4, ~ 80% via photolysis (hν), ~ 17% via the reaction with singlet oxygen radical ($O(^1D)$) and ~ 3% via the reaction with hydroxyl radical (OH), *Equations 1.1 – 1.3* (Sheng *et al.*, 2015). The photodissociation and kinetic rate parameters Sheng *et al*. used in their 2015 modelling study originate from Sander *et al*. 2011. As photolysis of OCS occurs effectively only in the UV regime (at 388, 285 and 209 nm), the photolysis rate increases with altitude (Chin and Davis, 1995). The Envisat Michelson Interferometer for Passive Atmospheric Sounding (MIPAS) satellite retrieval analysis show the maximum concentration of SO_2 at around 25 km altitude, where the production is described by OCS photodissociation (Höpfner *et al.*, 2013).

Further, sulfur dioxide readily undergoes reaction with OH and conversion to SO_3 mainly in the stratosphere. With addition of water, H_2SO_4 is produced, with sum reactions indicated in *Equation 1.4*. An overview of gas and aqueous phase sulfur species reactions in the troposphere and stratosphere are summarized in *Figure 1.3*.

$$\begin{aligned} OCS &\xrightarrow{h\nu} S + CO \\ S + O_2 &\rightarrow SO_2 \end{aligned} \qquad (1.1)$$

$$OCS + O(^1D) \rightarrow SO + CO$$
$$SO + OH \rightarrow SO_2 + H \quad (1.2)$$

$$OCS + OH \rightarrow SO + CO + H$$
$$SO + OH \rightarrow SO_2 + H \quad (1.3)$$

$$SO_2 + OH \rightarrow HSO_3$$
$$HSO_3 + O_2 \rightarrow SO_3 + H_2O$$
$$SO_3 + H_2O \rightarrow H_2SO_4 \quad (1.4)$$

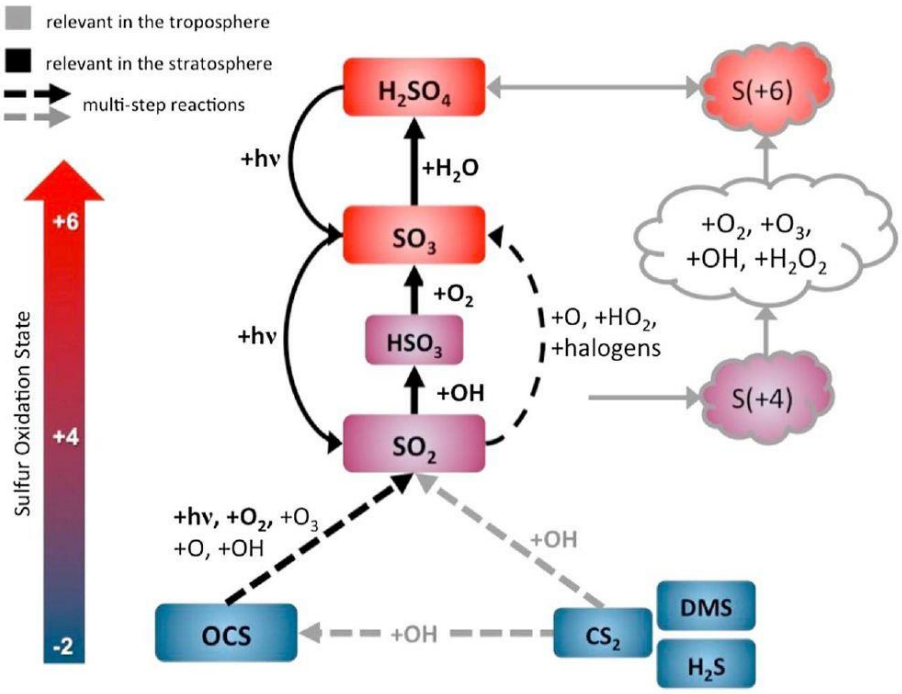

Figure 1.3 Schematics of most important atmospheric sulfur compounds and reactions in gas (middle section) and in aqueous phase (right section). Predominant reactions are indicated in bold. Black arrows show mainly stratospheric reactions, while grey arrows indicate reactions mostly taking place in the troposphere. Dashed lines show conversions with multistep reactions, which are omitted here for clarity. Color of the species shows the oxidation state of sulfur in the compound. The oxidation state of sulfur species is gradually increasing on the way from the troposphere till middle stratosphere. SO_2 can dissolve in rain, fog and cloud droplets, also in moist aerosol particles, where S(+4) denotes sum of $[SO_2 \cdot H_2O]$ + $[HSO_3^-]$ + $[SO_3^{2-}]$ and can be oxidized by various oxidants to S(+6) combining the sum of $[H_2SO_4 \cdot H_2O]$ + $[HSO_4^-]$ + $[SO_4^{2-}]$. Figure from Kremser *et al.* 2016.

Effectively, all gaseous organosulfur species that are emitted into the atmosphere from surface sources and are not taken up by ground level sinks will be eventually converted to H_2SO_4, which readily condenses to aerosol particles in the presence of water vapor. This sulfate aerosol is in turn washed out in the troposphere by wet and dry deposition. In addition to these sulfur atmospheric processes, biochemical reactions also play an important role in sulfur bio-geo cycle. Living organisms often use sulfur as an energy source or oxidizing agent in their metabolic processes. Sulfur also plays a role as a structural component in cells. Plant sulfur biochemical cycle significantly influence the atmospheric sulfur budget. The sulfur cycle biological control can lead to complex feedback mechanisms in the epoch of the Anthropocene as the ecosystems are changing due to human activity (Kremser *et al.*, 2016).

If only considering the photochemical sinks of OCS, the tropospheric lifetime has been estimated around 36 years (Chin and Davis, 1995). This lifetime is 16 times longer than the total tropospheric lifetime (Montzka *et al.*, 2007), advocating the bio-geo sinks on the surface play a dominant role on OCS uptake, mainly via vegetative and oxic soil uptake routes. In contrast, the stratospheric lifetime of OCS is much longer, estimated as 64 ± 21 years by Atmospheric Chemistry Experiment (ACE) satellite Fourier transform spectrometer study during the years 2004-2006 (Barkley *et al.*, 2008) and 68 ± 20 years at polar latitudes and 58 ± 14 years at tropical latitudes by balloon-borne spectrometer observational study during 2011-2012 (Krysztofiak *et al.*, 2015). Both studies use the tracer-tracer species correlation method presented by *Plumb and Ko* in 1992 and further discussed in *Section 3.3*. The results they present are in agreement, but perhaps for different reasons, as *Krysztofiak et al.* report and use an average OCS stratospheric MR of 550 ± 40 pptv from their measurements for the lifetime calculation, which seems unreasonably high for the stratospheric region. Within this an estimate the OCS stratospheric lifetime from CARIBIC samples is made.

1.4.3 Carbonyl sulfide and sulfate aerosol effects on climate

On the Earth's climate perspective, OCS backscatters far infrared (longwave) radiation emitted by the Earth’s surface, trapping the energy in the lower atmosphere and leading to global warming, the so called greenhouse effect (Turco *et al.*, 1980). On the other hand, stratospheric sulfate aerosol absorbs incoming near-infrared solar energy and backscatters shortwave radiation to space, leading to a cooling effect (Baldwin *et al.*, 1976).

It has been computed that the direct radiative forcing efficiency by 1 kg of OCS is 724 times higher that of 1 kg CO_2. Considering 30% anthropogenic fraction of OCS in the atmosphere, based on 350 year history derived from ice core data (Montzka *et al.*, 2004), this corresponds to total anthropogenic radiative forcing of 0.003 Wm^{-2} by OCS. In addition, stratospheric aerosol produced from OCS oxidation, as shown in *Figure 1.3*, contributes to an overall negative direct solar forcing (cooling) of -0.007 Wm^{-2} for the anthropogenic fraction. Nevertheless, the cooling effect is > 2 times larger than the warming effect, the both effects approximately cancel as the lifetime of OCS is twice that of stratospheric aerosol (Brühl *et al.*, 2012). Furthermore, sulfate aerosol particles, both in the troposphere and in the stratosphere, can act as cloud condensation nuclei (CCN) and ice nuclei (IN) for enhanced cloud formation (Andreae and Crutzen, 1997). In general this leads to a higher albedo and less energy from the Sun will reach the surface of the Earth, leading to an overall net cooling effect.

Sulfate aerosol also plays a role in heterogeneous ozone chemistry in the stratosphere, contributing to the ozone hole formation (Ravishankara *et al.*, 1993; Solomon *et al.*, 1996).

1.4.4 Main sources of sulfur into the stratosphere

The stratospheric aerosol mainly consists of sulfate droplets combined with water, meteoritic dust or other particulate matter, and on their combinations. The most abundant transport pathways of sulfur to the stratosphere are via carbonyl sulfide convection, volcanic eruptions, tropical convection, Asian monsoon and deep convective transport.

1.4.5 Path of sulfur dioxide to sulfate aerosol

The conversion of SO_2 to H_2SO_4 is dominated by the OH radical in the free troposphere and lower stratosphere. The rate constant is well known (Burkholder *et al.*, 2015). Thus, the SO_2 conversion rates can be relatively well constrained in climate models as long as the OH abundance is sufficiently well known. Typical atmospheric SO_2 lifetimes range from days to weeks and the longer lifetime estimate of several weeks are prevailing in the dry low stratosphere, where the OH concentrations are typically low (Rex *et al.*, 2014). In terms of stratospheric sulfur budget, changes in the OH MRs within the tropical tropopause layer (TTL) are especially important as they can change the SO_2 flux efficiency to the stratosphere. The uncertainties associated with the spatial and temporal variability of OH concentrations in the troposphere and stratosphere remain large and are of a hot topic until now (Voulgarakis

et al., 2013; Li *et al.*, 2018). In the boundary layer the lifetime of SO_2 can be even shorter under polluted conditions, for instance 58 ± 20 h in winter and only 19 ± 7 h in summer in the east of USA (Lee *et al.*, 2011). This limits the anthropogenic fraction of SO_2 being transported to the free troposphere or higher. Additionally, uptake by cloud droplets leads to much faster conversion to H_2SO_4 via the aqueous phase chemistry compared to the gas phase reactions (Kremser *et al.*, 2016).

Within volcanic plumes, aerosol loadings and concentrations of gaseous organosulfur compounds increases substantially, which leads to a very specific chemistry (von Glasow, 2010). It has been shown that the loss rates within a plume vary from a few minutes to several weeks, depending on the meteorological, atmospheric and plume conditions. The SO_2 turnover into sulfate aerosol can be especially fast inside convective eruption columns, which can lead to sulfate directly entering the stratosphere (Oppenheimer, Francis and Stix, 1998).

In the stratosphere, > 35 km above the surface H_2SO_4 photolysis into SO_2 and 2OH molecules (at 234 nm) takes place (Burkholder *et al.*, 2015; Kremser *et al.*, 2016).

1.4.6 Microphysical sulfate aerosol properties

There are 5 major processes which govern sulfate aerosol lifecycle: nucleation, coagulation, condensation, evaporation and sedimentation. The total sulfate aerosol number concentration, size distribution, lifetime and composition depend on the 5 microphysical processes (Seinfeld and Pandis, 2016).

1.4.6.1 Nucleation

The vapor partial pressure of H_2SO_4 is normally supersaturated in the stratosphere, thus the gaseous sulfuric acid readily condenses. The condensation together with water vapor is the preferential pathway as regularly there is enough water vapor present (Curtius *et al.*, 2005). The new sulfate particles are commonly forming through binary homogeneous nucleation (Vehkamäki *et al.*, 2002). Nucleation of new aerosol particles occur normally over short time periods and at high number concentration (Deshler, 2008).

1.4.6.2 Coagulation and condensation

The new freshly formed particles can further grow in size via coagulation and condensation. Through coagulation the various aerosol particles in different size and composition, collide to combine into a single bigger particle. Thus, coagulation efficiency is dependent on the

aerosol number concentration. The condensational growth of particles primarily takes place via organics, H_2SO_4 and H_2O further condensing on the aerosol particle. The condensational growth is limited by sulfuric acid concentration and uptake efficiency and thermodynamic properties. Coagulation regularly also occurs over a short time period like nucleation (Deshler, 2008), while condensational growth can occur throughout the whole lifetime of an aerosol particle. Further growth of larger aerosol particles is substantially slower due to their lower random motion (Seinfeld and Pandis, 2016).

1.4.6.3 Evaporation and sedimentation

Evaporation of sulfate aerosol repartitions sulfur between particulate and gaseous phase. Sedimentation in the stratosphere irreversibly transports sulfur downwards, eventually leads to a loss into the troposphere. Thus, the spatially distinct aerosol layer in the stratosphere, i.e. the Junge layer, is partially governed by evaporation and sedimentation. Aerosol particles near the tropopause region can be conveyed to the troposphere via several methods, significantly by gravitational growth (sedimentation). Sedimentation is especially vital loss mechanism for volcanic stratospheric aerosol flux into the troposphere, expressly after a major volcanic eruption like Mount Pinatubo, Philippines in 1991 (Kremser *et al.*, 2016).

1.5 Tropospheric OCS budget

An overview of the tropospheric OCS budget, based on a review of many publications reflects the current knowledge about atmospheric sulfur cycle, is seen in *Figure 1.4*. The sources and sinks of OCS have large uncertainties, however it is often determined that the budget is not balanced. As the concentration of OCS in the atmosphere does not show a large trend (Montzka *et al.*, 2007), and discussed further in *Section 3.7*, the budget should be more or less balanced.

According to the current knowledge, oceans are the single largest sources of OCS, via direct emissions and also via DMS and CS_2 following further oxidation in the atmosphere (Launois *et al.*, 2015). The second largest source contributors are the anthropogenic emissions, again through the combination of direct OCS emissions and CS_2 and DMS further processing in the atmosphere (Campbell *et al.*, 2015). Biomass burning also serves as a significant OCS source (Montzka *et al.*, 2007).

In turn, to the best available understanding the single largest sink of OCS is the vegetative uptake (Sandoval-Soto *et al.*, 2005; Montzka *et al.*, 2007). The vegetative uptake accounts

for around 60 – 70% of the total OCS removal from the atmosphere according to the most recent estimates. The second largest sink is oxic soil (20 – 30%), where the sink strength depends on the soil moisture, temperature and soil CO_2 concentration (Kettle *et al.*, 2002; Van Diest and Kesselmeier, 2008; Berry *et al.*, 2013; Bunk *et al.*, 2017). From the three largest atmospheric sinks the dominant one is the OCS molecule oxidation by the OH radical, followed by photochemical photolysis and $O(^1D)$ oxidation. The total atmospheric sink is substantially smaller (accounting for less than 10% from the total OCS removal processes) compared to the vegetation and oxic soil sink.

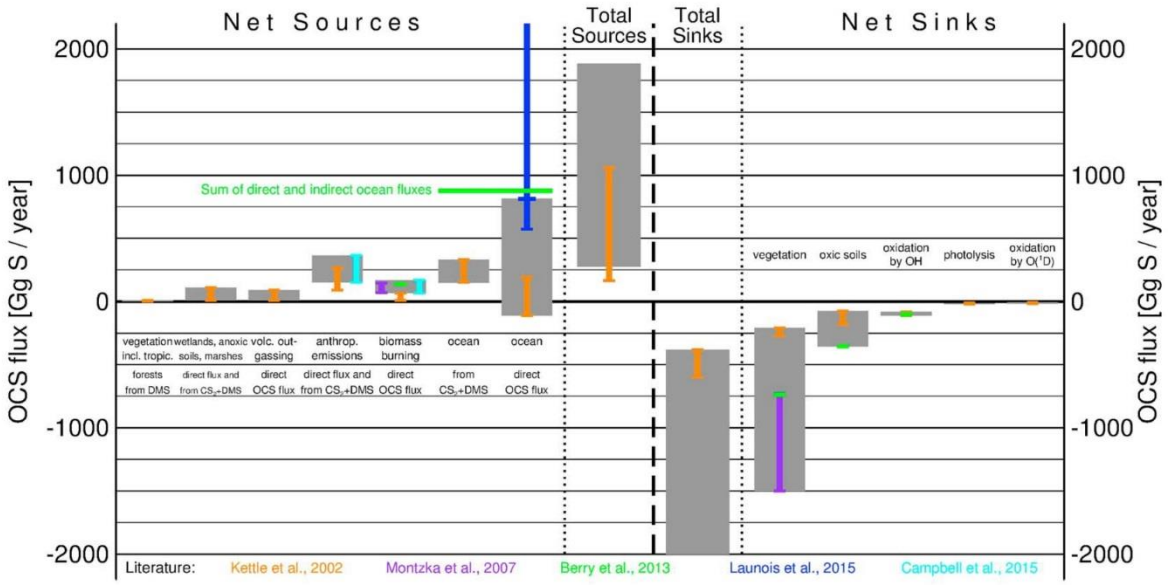

Figure 1.4 Literature review of tropospheric OCS budget. Left side represent the net sources and right side the net sinks of OCS. The gray rectangles show the current literature spread of the distinct OCS source / sink flux estimate. The error bars show the literature combined uncertainties. Adopted from Kremser et al. 2016.

1.6 Past OCS atmospheric MRs

Ice core analysis helps to reconstruct the past climate atmospheric composition. The ice core analyses collected from several Arctic and Antarctic sites show that generally atmospheric OCS remained in the 330 – 350 pptv range over hundreds of years (1650 – 1850) before the industrial revolution (Montzka *et al.*, 2004; Aydin *et al.*, 2008, 2014), shown in *Figure 1.5*. The pre-industrial background level of OCS was substantially lower (about ⅓) than the current global average 480 – 490 pptv (discussed in more detail in *Section 3.7*). The more recent firn air measurements also show that OCS MRs were increasing throughout most of the 20th century. The reported results indicate OCS MR increase from 350 – 400 pptv at the

beginning of the 20th century to a peak around 550 pptv at the late 20th century and then falling slightly below 500 pptv mark at the beginning of the 21st century (Sturges *et al.*, 2001; Montzka *et al.*, 2004). The past measurements of the OCS MRs in the high latitudes of the southern hemisphere indicated that the MRs have decreased by 60 – 90 pptv (10 – 16%) since the 1980s. The historical levels are closely related to anthropogenic sulfur emissions.

As it seems that anthropogenic emissions are strongly influencing the global OCS levels, however the anthropogenic emissions account only for around 20% of the natural emissions according to the most recent OCS budgets (Berry *et al.*, 2013; Campbell *et al.*, 2015). The increase seen in the OCS MRs during the 20th century could be explained only with 0.3 – 0.6% fraction of the total anthropogenic sulfur emission as OCS (including direct OCS emissions and further atmospheric processing of other sulfur species to OCS) (Montzka *et al.*, 2004). In addition, it is possible that also changes in the terrestrial vegetative plant uptake sink strengths of OCS further contributed to the atmospheric trends seen during the 20th century (Campbell *et al.*, 2015).

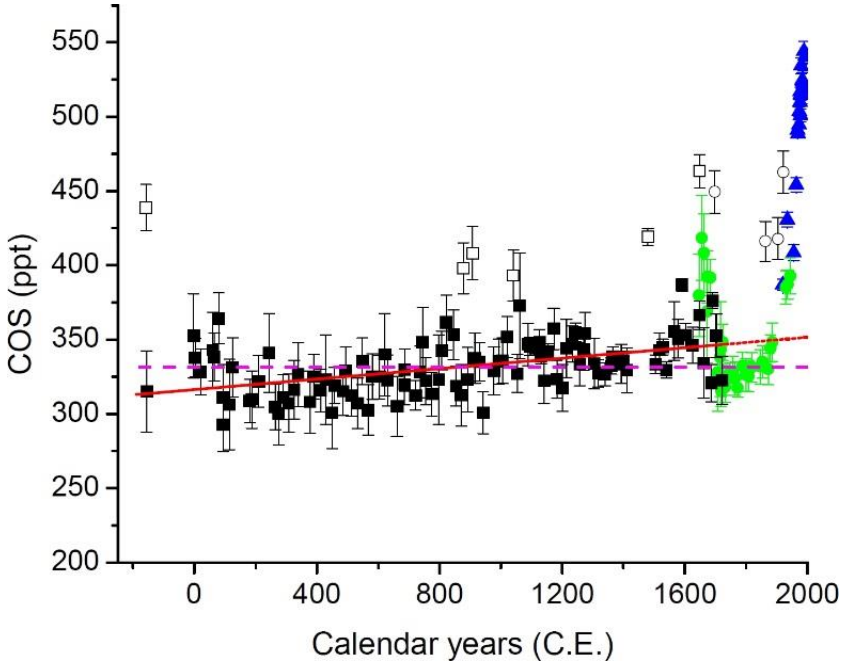

Figure 1.5 Past atmospheric OCS MR determined from air trapped in ice cores drilled near South Pole, East Antarctica (SPRESSO), represented with black squares. The ice cores originate from 135 – 291 m depth, relating to 278 – 2155 years before year 2000. Overlaid are also data from Siple Dome C (Antarctica) ice cores (green circles) and South Pole firn air (blue triangles) (Montzka *et al.*, 2004)**. The open squares and circles denote the outliers. The error bars represent 1σ uncertainties. The red line signifies the linear trend in the SPRESSO sample data excluding the outliers and extending to the year 2000 with dashed red line with linear extrapolation. The purple dashed line is the mean of the SPRESSO sample data excluding the outliers. Figure adopted from Aydin *et al.* 2008.**

It has been shown that on timescales longer than a few thousand years, ice core measurements from different Antarctic ice core drilling locations demonstrate systematic

differences related to the thermal history of the ice cores. The OCS levels in the ice cores from warmer locations are increasingly more depleted with ice core depth (thus also with age) relative to the measurements from the colder locations. This suggests temperature dependent OCS hydrolysis loss in the ice core air bubbles. This loss kinetics have been parameterized and measurements have been corrected for this feature using model based temperature histories specific to each location (Aydin *et al.*, 2014).

The ice core sample measurement from the West Antarctic Ice Sheet (WAIS) go 54 300 years back from present. The samples indicate that atmospheric OCS levels were at its minima, around 160 – 210 pptv, at the beginning of the Holocene, as shown in *Figure 1.6*. During the last glacial minima (LGM) the atmospheric OCS MR was around 250 – 300 pptv, about 80 – 100 pptv higher compared to the last glacial / interglacial transition minima. This decline was to a high probability due to an increase in the gross primary productivity of terrestrial vegetation. In addition, a possible contributor could also be a decreased ocean source. In the late Holocene, OCS levels were above 300 pptv. These large changes indicate that large changes took place in the OCS biogeochemical cycle during the Holocene (Aydin *et al.*, 2016).

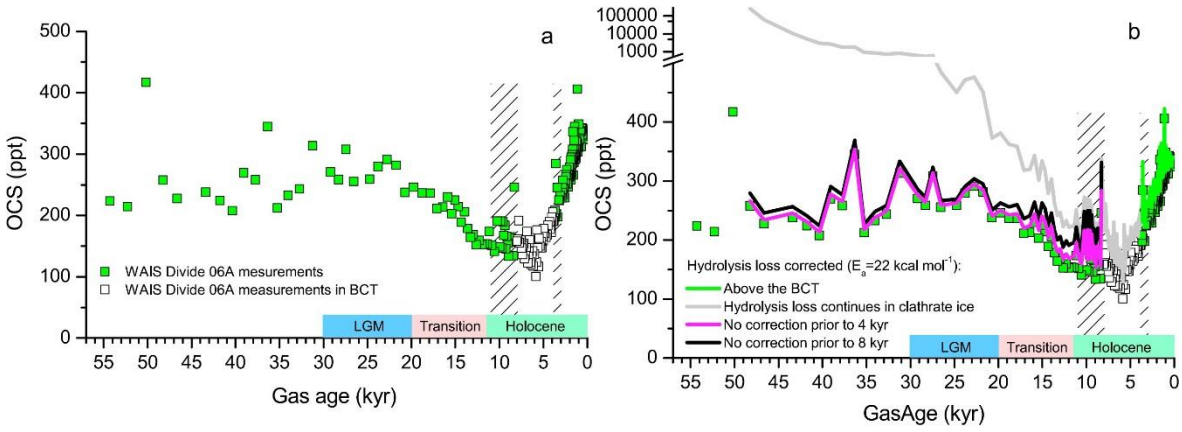

Figure 1.6 Historical OCS MR data derived from ice core measurements drilled deep at West Antarctic Ice Sheet (WAIS). (a) The white squares represent the samples where air was extracted from the bubble-clathrate transition (BCT). The dashed areas denote the full range of samples that may have been influenced by the clathrate (bubble free ice) formation. The approximate timings of the Holocene, last transition and last glacial maximum (LGM) are indicated on the x-axis. The transition from the LGM conditions to the Holocene, which involved large-scale deglaciation, occurred between 20 and 11.5 kyr from the present. (b) The OCS analysis is corrected for hydrolysis loss under three different scenarios: magenta line – no hydrolysis loss prior to 4 kyr; black line – no hydrolysis correction prior to 8 kyr due to clathrates; and gray line – scenario test assuming OCS hydrolysis loss continues through clathrate ice. All corrections were applied with a hydrolysis activation energy of 22 kcal mol^{-1}. On graph (b) on the y-axis the OCS MR after 500 pptv is on a logarithmic scale. Figure adopted from Aydin *et al.* 2016.

1.7 OCS as gross primary productivity tracer

Carbonyl sulfide has been investigated as a tracer for gross primary productivity (GPP) as the uptake of OCS and CO_2 are closely related (Whelan *et al.*, 2018). An OCS molecule enters a leaf through a stomata (small pores on the surface of plant leaves) and diffuses into mesophyll cells the same way as CO_2, shown in *Figure 1.7*. In the chloroplast, the enzyme called carbonic anhydrase (CA) catalyzes the hydrolysis process of OCS and produces H_2S and CO_2 (Protoschill-Krebs, Wilhelm and Kesselmeier, 1996; Stimler *et al.*, 2010). The enzymatically catalyzed hydrolysis is strongly favorable in one direction, thus OCS is irreversibly taken up by the plant and re-emission is strongly unlikely. In contrast, CO_2 is re-emitted during respiration. Assuming that the other sources and sinks are negligible, the tropospheric drawdown of OCS above an ecosystem reflects the uptake of OCS by plants. As the pathways of OCS and CO_2 from the ambient air to the mesophyll cells are to a large extent the same, the correlation between OCS and CO_2 at the leaf level could be used to estimate the GPP (Campbell *et al.*, 2008; Asaf *et al.*, 2013). The GPP could be estimated as shown with *Equation 1.5*, where F_{OCS} is the ecosystem flux of OCS, LRU is the leaf scale relative uptake ratio, $[CO_2]$ and [OCS] are the atmospheric MRs of CO_2 and OCS, respectively. The LRU is the ratio of the OCS to CO_2 deposition velocity (uptake), which is a function of the plant type, water and light conditions. The deposition velocities are calculated as the ratio of the leaf scale flux over the MR of the OCS or CO_2 (Whelan *et al.*, 2018).

$$GPP = F_{OCS} \times \frac{1}{LRU} \times \frac{[CO_2]}{[OCS]} \tag{1.5}$$

In reality, there are also other sinks and sources for OCS. Thus, a comprehensive and accurate characterization of all the OCS sources and sinks are required to use OCS as a tracer for photosynthesis tracer. Recently, it was found that the CA enzyme is light independent and stomatal conductance can continue at nighttime (Kooijmans *et al.*, 2017). Thus the vegetative nocturnal OCS uptake further complicates the use of OCS as a tracer for photosynthesis. With further multi-regional and seasonal OCS uptake and emission studies and characterization could lead to an accurate OCS flux parameterization to use it as a GPP tracer.

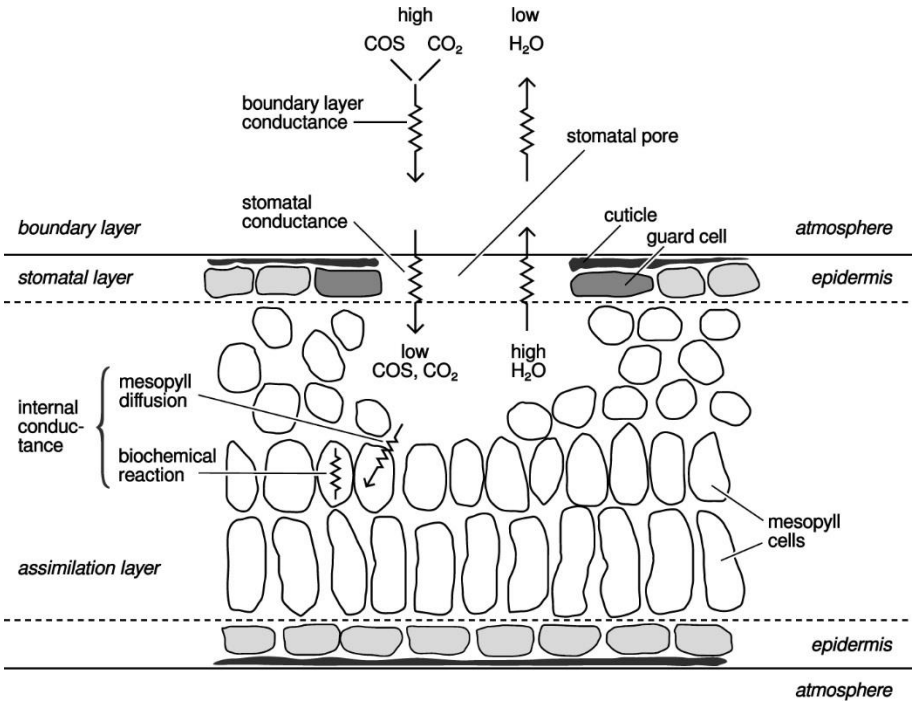

Figure 1.7 Schematic view of a leaf cross section showing the stomatal pathways of OCS uptake, water transpiration and CO_2 uptake and transpiration. Figure adopted from Moene and van Dam 2014 as in Kooijmans 2018.

2 EXPERIMENTAL DESCRIPTION OF ENTECH-GC-AEDIII

2.1 Intro

For the quantitative assessment of organosulfur compounds in troposphere and stratosphere a new analytical system was developed and characterized throughout this thesis work. In order to reliably study their atmospheric abundance, transport dynamics, and chemical fate depends on precise high quality measurement data and accurate calibration. During the work thorough efforts were undertaken to optimize the performance and detection limits for sulfur containing species. In addition to the targeted sulfur containing species, other VOCs like NMHCs, halogenated trace gases and monoterpenes were measured by the same system within the C3 – C14 range. These species also play an important role in tropospheric ozone production, stratospheric ozone depletion and climate forcing, and they can be useful in interpreting the sulfur species.

The system described here is based on a third generation atomic emission detector (AEDIII, Joint Analytical Systems GmbH, Germany). This new detector was coupled with a cryogenic pre-concentration system (CryoTrap) and a gas chromatograph (GC) for measuring volatile organic compounds (VOCs) in the gas phase. The whole system consists of three stages: a cryogenic liquid nitrogen pre-concentration system (Entech 7200, Entech Instruments Inc., USA); followed by a gas chromatographic separation of analyte compounds (Agilent 7890B GC, Agilent Technologies Inc., USA); and leading to an atmospheric pressure helium plasma based AEDIII for analyte detection. Ultra-high purity (purity of 99.9999%) helium (Westfalen AG, Germany) flowing through a heated catalyst for further purification (VICI HP2 Helium Purifier, Valco Instruments Co., USA) is used throughout the system as the carrier gas. These are the first attempts to measure gas phase atmospheric samples with the AED instrument. A schematic summary of the instrumental setup is shown in *Figure 2.1*.

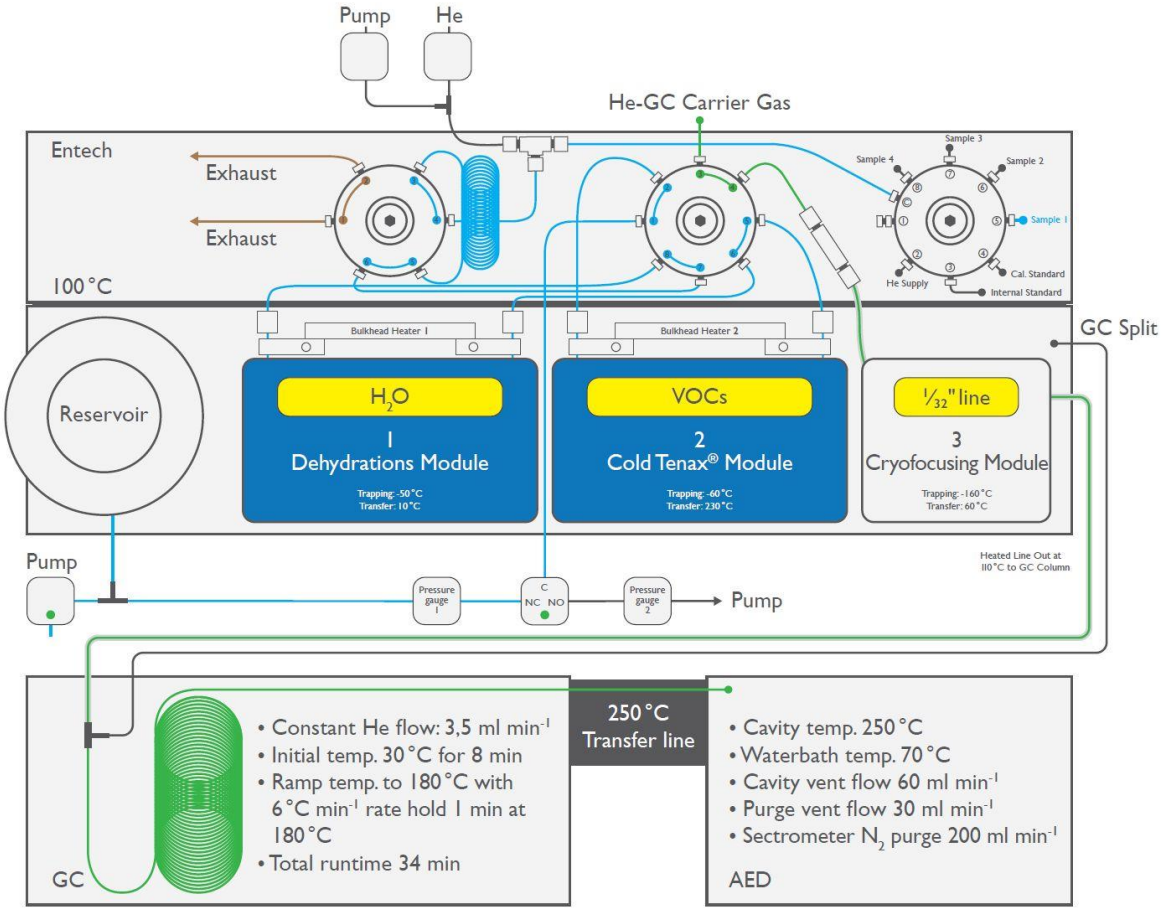

Figure 2.1 A schematic summary of the instrumental setup of Entech-GC-AEDIII.

2.2 Cryogenic pre-concentration (Entech)

2.2.1 Analyte trapping principle

Cryogenic pre-concentration on adsorptive material is a widely used practice in trace gas analysis for boosting the detection limits of analytical instruments. The adsorptive material, e.g. glass beads, HayeSep D, Tenax® or similar is contained in a packed form within a tube forms an adsorbent trap. Different adsorptive materials and their properties are discussed in (Woolfenden, 2010a, 2010b). Sampling an air sample through the adsorbent trap will retain certain analytes of interest via physical interactions with the adsorbent material mostly on their surface, whereas the most abundant and volatile constituents of air, like N_2, O_2 and Ar will not be retained.

The adsorption properties can be further enhanced with trapping under reduced temperatures, which moves the steady state equilibrium towards adsorption. Cooling the adsorbent, i.e. cryofocusing under ambient temperatures increases the analyte breakthrough

volume and especially increases the trapping efficiency of highly volatile compounds. There are three main cooling techniques used: liquefied cryogen that evaporates and removes heat in the process, like liquid nitrogen; compression-evaporation based closed refrigerant systems, like regular compressor fridges; pure electrical cooling systems, like Peltier elements and Stirling coolers.

After successfully trapping a required amount of sample, the packed trap needs to be reheated under a carrier gas flow to remobilize the analytes prior to the prefocusing step. This heating will shift the steady state equilibrium of the adsorbent material towards desorption, termed thermosorption. The prefocusing trap can be a stainless steel line with a small diameter (circa 1/32″ or 0.79 mm outer diameter) or even a loop of capillary column (circa 0.25 – 0.80 mm) either with or without stationary phase. It is normally cooled by the same means as the main trap. The main trap usually allows collection of large volumes rapidly, after which the concentrated sample is transferred to a prefocusing trap with a smaller volume. An injection from prefocusing trap to a GC column allows a sharp, split free and non-tailing chromatographic peaks. For some analytical setups a prefocusing step might not be necessary.

The process of adsorption and desorption both need to be reproducible and quantitative between samples and calibration standards for accurate and precise results. Active cooling below ambient temperatures enables the use of less strong adsorbent materials which would be required for higher temperature analyte trapping which in turn would lead to higher thermosorption temperatures which could cause thermal decomposition of more sensitive molecules of interest. Lower desorption temperatures also prolong the lifetime of the adsorbent material.

2.2.2 Entech pre-concentration method development and parameters

First, the sample is introduced to the pre-concentration unit via an 8 position multi position valve, consisting of helium supply gas, 4 sample introduction lines, an internal standard, a calibration standard and a blind port. The 4 sample introduction lines are each 2.0 m long (Restek Corp., Silcosteel, outer diameter 1/16″ (1.59 mm), inner diameter 0.040″ (1.02 mm), volume 1.62 mL), which can be connected to sample canisters or calibration cylinder bottles. The sample is drawn onto the two enrichment traps by means of an evacuated volumetric reservoir, where the sample introduction volume is accurately controlled measuring the

pressure. All the Entech internal flow path surfaces are coated with Silonite-D coating to provide highly inert surfaces.

The Entech internal flow path is flushed with sample gas before each pre-concentration of a sample. After which the sample air is pulled through the first dehydration module, where H_2O is selectively removed on an empty Silonite-D coated stainless steel trap (outer diameter 1/8″ (3.18 mm), 31 cm long) held at -50°C. After collecting requested volume of sample, the trap is flushed with 75.0 mL of Helium to remove any remaining air. Then the module 1 is heated to 10°C and forward purged with 50.0 mL Helium flow to the main Tenax® packed and Silonite-D coated VOC enrichment trap (module 2, outer diameter 1/8″ (1.02 mm), 31 cm long) held at -60°C, which is in series with the module 1 trap. Module 2 temperature was held at -60°C during the module 1 to module 2 transfer as this helps to eliminate most of the co-trapped CO_2 from the dehydration step when the main VOC trap is kept at -100°C. This is necessary for highly volatile compound trapping. The forward helium purge helps to successfully transfer heavy, polar and Semivolatile Organic Compounds (SVOCs) onto the main module 2 VOC trap, which depends again on the inertness of Silonite-D coatings. Last pre-concentration step is precooling the cryofocusing trap (module 3, ~ 4 cm long part of Silonite-D coated 1/32″ (0.79 mm) transfer line) to -180°C and kept at -160°C while module 2 is back flushing at 230°C for 2.5 min, which will refocus the volatiles onto a much smaller dead volume for splitless injection. Finally, the module 3 1/32″ (0.79 mm) transfer line is rapidly heated to 60°C for 2 min inside covering 1/8″ (3.18 mm) perfluoroalkoxy alkane (PFA) tube with hot air supplied through the rotary plate which is kept at 100°C. This ensures rapid and split-less injection of analyte molecules to GC column through a heated transfer line at 110°C.

The pre-concentration unit is equipped with two bulkhead heaters in between the heated rotary plate and the traps for better water management. Bulkhead heater 1, which is connected to module 1 trap is kept at 10°C during the sample pre-concentration step and heated to 60°C during the sample transfer from module 1 to module 2 trap. At the same time, bulkhead heater 2 is kept at 30°C during the sample pre-concentration and module 1 to 2 transfer, heated to 70°C during module 2 to 3 transfer. Such a temperature management and the flow path inertness due to the Silonite-D coating allows for final sample injection to have water contents as low as 0.2 – 0.3 µl for 1.4 L ambient air sample.

During the 10-15 min bakeout step after the injection the modules 1 and 2 are heated to 150°C and 210°C respectively, whereas the bulkhead heaters are kept at 150°C. This step ensures elimination of all the rest of the water in the system and preconditions it for the next

sample pre-concentration. All the pre-concentration temperatures are summarized in *Table 2.1*.

Table 2.1 Entech 7200 pre-concentration method temperatures of the 3 traps.

	Trap temp. (°C)	M1 Preheat (°C)	M1 -> M2 (°C)	M3 Precool (°C)	M2 Preheat (°C)	M2 -> M3 (°C)	Inject (°C)	Bakeout (°C)
Mod 1 Trap	-50	10	10					150
Mod 1 Bulkhead	10		60					150
Mod 2 trap	-100		-60		-60	230		210
Mod 2 Bulkhead	30				70			150
Mod 3 trap				-180		-160	60	

Liquid nitrogen is supplied from a large 120 L cryogenic liquid nitrogen dewar (Cryo Anlagenbau GmbH). The dewar is maintained at 2.3 bar overpressure and is fitted with a safety overpressure valve. All cryogen transferlines are insulated. With one filling about 40 samples can be preconcentrated. The lab temperature is maintained and monitored at around 21°C for lowering the losses from the liquid nitrogen dewars and speeding up the GC oven cooling times.

2.2.3 Entech sensor calibration

The internal Entech temperature thermocouples, pressure gauges and rotary multi-port valves were recalibrated during the instrument development phase of this thesis work. Each of the three enrichment modules has a separate thermocouple to monitor the respective module temperatures and to control them. The two bulkhead heaters of module 1 and 2 are connected to heat the trap connection lines in between the rotary plate gas flow system to the trapping modules. The bulkhead heaters help to maintain the temperatures required for effective transfer of analytes, and if required makes it also possible to condense out any remaining water which is carried on after module 1 dehydration step. Condensing out the remaining water is possible by using a lower temperature for the bulkhead heater 1 relative to the module 1 and rotary plate temperatures. Furthermore, there are two thermocouples for rotary plate temperature measurement used for controlling the rotary plate heaters. Also, the transferline between Entech and GC is heated and controlled via the thermocouple temperature measurement, which was also recalibrated.

The temperature thermocouple calibration was done by setting new zero and gain values for each thermocouple using two physical constants, ice slurry and liquid nitrogen. A 500 mL beaker full of ice and filled to ¾ level with water was used to achieve 0°C readings via tuning the respective thermocouple zero values. Liquid nitrogen in a small dewar was used as a second physical constant to adjust the respective gain values for receiving desirable -196°C readings. For double checking the effectiveness of calibration for higher temperatures the thermocouples were immersed into boiling water to monitor how close the value will be to 100°C, see summary *Table 2.2* for details. The maximum false reading for uncalibrated thermocouple was 12°C for ice water instead of 0°C; 118°C for boiling water instead of 100°C; and -178°C for liquid nitrogen instead of -196°C. The calibrated thermocouples measured the three physical constants within accuracy better than ± 2°C. Accurate temperature measurements are essential for achieving desired analyte trapping efficiencies, quenching water from the sample stream and scrubbing out CO_2 and other major air constituents, like N_2, O_2 and Ar gases.

Pressure gauges were also recalibrated by adjusting their zero and gain values. Local lab ambient pressure and pump vacuum pressure were used as two calibration points. First, the zero was set with evacuating the capped system with the pump low to 1.08 psi (75 mbar), which is the lowest pressure achievable with that vacuum pump (pressure was measured with a Greisinger GDH-12 NL baro- and vacuum-meter, GHM Messtechnik GmbH, Germany). Pressure gauge gains were adjusted with an open inlet to the lab ambient pressure, 14.75 psi (1017 mbar). The sample trapping volume is calculated from the pressure difference as the exact volume of the reservoir is known. Calibration values can be seen in *Table 2.3*. Accurate pressure gauge readings are required for the accurate sample collection volume calculations, thus for the accurate concentration determination.

For rotary valve calibration, the Entech 7200 built-in software procedure was used to align the valves. This automated procedure changes the voltage of each rotary valve in turn by finding the correct voltage for each port stall, flow and off positions. The rotary valve recalibration data can be found in *Table 2.4*.

Table 2.2 Entech 7200 thermocouples recalibration data.

a) Thermocouple readouts before recalibration

Sensor	**Gain**	**Zero**	**Ice (°C)**	**Boiling (°C)**	**Lq. N_2 (°C)**
Module 1	1151	81	10	116	-187
Module 2	1150	80	5	110	-190
Module 3	1100	80	5	106	-178

M1 Bulkhead	1150	80	11	116	-185
M2 Bulkhead	1150	80	4	110	-191
Front Rotary	1150	80	2	108	-198
Back Rotary	1150	80	10	115	-189
GC XferLine	1150	80	12	118	-182

b) Thermocouple readouts after recalibration

Sensor	**Gain**	**Zero**	**Ice (°C)**	**Boiling (°C)**	**Lq. N_2 (°C)**
Module 1	1103	173	0	102	-196
Module 2	1127	131	0	101	-196
Module 3	1122	127	0	102	-196
M1 Bulkhead	1099	183	0	100	-196
M2 Bulkhead	1126	129	0	102	-196
Front Rotary	1120	107	0	102	-196
Back Rotary	1096	174	0	99	-196
GC XferLine	1095	199	0	100	-196

Table 2.3 Entech 7200 pressure gauges recalibration data.

Sensor	**Gain**	**Zero**	**Lab pressure**	**Vacuum pressure**
System pressure	1140	252	14.76 psi (1017 mbar)	1.12 psi (77 mbar)
Reservoir pressure	1131	242	14.74 psi (1016 mbar)	1.22 psi (84 mbar)

Table 2.4 Entech 7200 rotary valves recalibration voltages.

Position	**Voltage (V)**
Trap Upper Stall	2.06
Trap Upper Flow	1.92
Trap Upper Off	1.90
Trap Lower Off	1.53
Trap Lower Flow	1.51
Trap Lower Stall	1.34
Loop Upper Stall	2.00
Loop Upper Flow	1.86
Loop Upper Off	1.84
Loop Lower Off	1.28
Loop Lower Flow	1.26
Loop Lower Stall	1.10

Position	**Voltage (V)**
Trap Target M1M2	2.02
Trap Target Off	1.68
Trap Target M2M3	1.38

Position	**Voltage (V)**
Loop Target Inline	1.96
Loop Target Off	1.58
Loop Target Flush	1.14

2.3 Analyte separation (GC)

An Agilent 7890B gas chromatograph (GC) was used for the compound separation. The GC was fitted with Supelco SPB®-624 capillary column (L × I.D. 60 m × 250 μm, d_f 1.40 μm), which is an intermediate polar, proprietary phase bonded fused silica GC column. The matrix active group belongs to the USP G43 nomenclature. The 624 columns are often the choice for volatile non-halogenated, halogenated, and aromatic compounds analysis. Helium was used as the column carrier gas, controlled over the GC electronic pneumatic control (EPC) valve 3. First helium flowed from the GC EPC valve 3 in a 1/16″ (1.59 mm) stainless steel line to the Entech rotary valve number 2, where after the pre-concentration procedure the helium flow with the analytes was guided back to the GC oven through a heated (110°C) Silonite-D coated 1/32″ (0.79 mm) transferline. Then, in the GC oven a Swagelok T-split union guided the flow to the analytical column for compound separation and the other end of the capillary column was led to the AED cavity through a heated transferline (250°C) for the speciated detection. The complete coupled system flow paths are illustrated in *Figure 2.1*.

2.3.1 GC oven program

Three main GC oven programs were used throughout this thesis work, which are summarized in *Table 2.5* below. Equilibration time of the oven temperature was set to 1 min. Within all the three main methods, a constant flow mode at 3.5 mL min^{-1} was used. This constant flow relates to He supply overpressure of 36.52 psi (2.52 bar) at -20°C, 44.25 psi (3.05 bar) at 30°C and to 66.66 psi (4.06 bar) at 180°C, accordingly. No post run option was used. Throughout the method development the GC was also equipped with an active liquid nitrogen oven cooling valve, which allows the oven to be cooled down to -80°C for the separation of the low-boiling compounds.

2.3.2 Regular GC maintenance

A regular maintenance of the GC flow paths, including Entech pre-concentration side and AED detection part, were carried out throughout this thesis work for making sure the system was leak tight. Primarily an electronic leak detector (Agilent model G3388B, Agilent Technologies Inc., USA) was used, which compares the thermal conductivity of ambient air and the flow gas. In addition, as the end of a GC column goes thorough the heated transfer

line directly into the AED helium plasma cavity, it is sometimes required to cut off a small part of the column due to the aging of the column part closest to the plasma.

Table 2.5 Three main GC oven programs used throughout the thesis work.

Method 1 – "CARIBIC-2018"

Rate (°C min^{-1})	Temperature (°C)	Hold time (min)
	30	8
6	180	1
Total runtime: 34.0 min		

Pressure (psi)	Average velocity (cm sec^{-1})	Holdup time (min)
44.25	44.02	2.27

Method 2 – "AQABA-2017"

Rate (°C min^{-1})	Temperature (°C)	Hold time (min)
	-20	5
6	180	1
Total runtime: 39.3 min		

Pressure (psi)	Average velocity (cm sec^{-1})	Holdup time (min)
36.52	41.75	2.40

Method 3 – "IBAIRN-2016"

Rate (°C min^{-1})	Temperature (°C)	Hold time (min)
	35	5
6	180	5
Total runtime: 34.2 min		

Pressure (psi)	Average velocity (cm sec^{-1})	Holdup time (min)
45.02	44.23	2.26

2.4 Analyte detection – atomic emission detector (AED)

2.4.1 AED background

A qualitative atomic spectrometry analyzing alkali and earth-alkali metals over a Bunsen burner flame was already established in 1860 and provides the basis to the other atomic spectrometry techniques (Kirchhoff and Bunsen, 1860). Atomic spectrometric analysis gives the opportunity to gain high sensitivity accurate elemental composition data of a sample. By combining the analyte separation with a Gas Chromatograph (GC) compound specific data is obtainable. The first Atomic Emission Detector with a plasma as an excitation source coupled with GC was introduced in 1965 (Mccormack, Tong and Cooke, 1965). They were the first to recognize the possibility of combining microwave induced plasma excitation detector with GC separation for forming a powerful analytical tool. The first AEDs using microwave induced plasmas were operated at reduced pressures (Risby, Talmi and Uden, 1983), atmospheric pressure version was developed in 1977 (Beenaker, 1977). The first commercial AED based on a microwave induced plasma and photodiode array detector coupled to a GC was released by Hewlett Packard in 1990 (Quimby and Sullivan, 1990).

2.4.2 AED principle

The AED relies on the fundamental atomic emission spectroscopy (AES) principles. The detector measures characteristic wavelength energy emitted by atoms in the atmospheric pressure helium plasma cavity to quantify the amount of atoms present in the incoming sample gas flow. Combining this data with GC analyte separation, the amount of the substance can be determined.

The helium carrier gas (3.5 mL min^{-1}) is led to the AED cavity through the capillary column that is in the heated transfer line (250°C). The helium plasma discharge cavity is also kept at constant 250°C temperature. The carrier gas then mixes with the helium gas flow that maintains the plasma and is joined by hydrogen and oxygen reagent gases from the gas module. The gas mixture flows through the glass discharge tube where the gases get ionized into the plasma state by microwave energy. In the high-energy plasma the eluted compounds from GC are broken down into free radicals, ions and atoms. As they return from their excited state to ground state configuration, light radiation is emitted in their element specific characteristic bandwidths. This light radiation travels through a lens into the spectrometer. All the gases are vented into an exhaust.

The light radiation that enters through a fused silica lens passes through a narrow slit and is reflected onto a reflective holographic grating by a fixed mirror. The lens prevents the mixture of cavity gases from entering the spectrometer unit. A constant helium purge flow in front of the lens keeps it clean and contamination free. The grating disperses the light into discrete vertical bandwidths and disperses it along a plane-concave polychromatic grating. Thereafter, the grating reflects and focuses the measured wavelengths (161 – 211 nm) in a horizontal plane onto two back-thinned Charge-Coupled Devices (CCDs). Due to a physical hardware gap between the two CCDs, there is a 7 nm gap in the wavelength spectra between 183 – 190 nm range. The CCDs directly measure diode intensities which are transmitted to the AED III Instrument Control Software through a USB cable. The AEDIII Instrument Control Software calibrates the received light intensity from the CCD diodes into wavelengths intensity data according to a calibration table. This wavelength calibration is called element installation in the software, and takes place automatically before every sample measurement. The spectral resolution of the spectrometer is 0.01 nm in the provided range. The AED III Instrument Control Software layout and an idle state spectrum is shown in *Figure 2.2*.

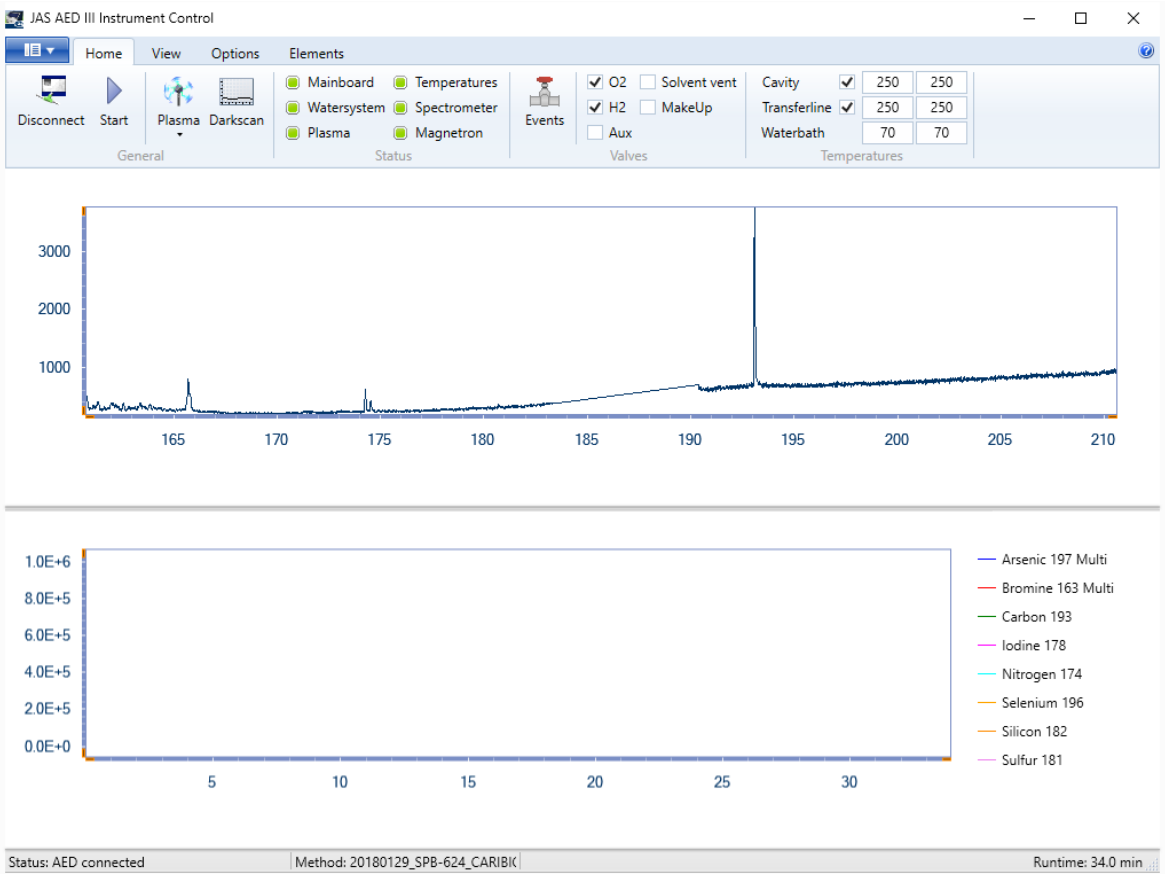

Figure 2.2 AED III Instrument Control Software idle state layout.

2.4.3 AED spectrometer purge

It is important to keep the spectrometer oxygen and water moisture free, as both cause a loss in the sensitivity due to their light absorption in the UV range *Figure 2.3*. Therefore, the spectrometer is constantly purged with ultra-high purity nitrogen gas (purity 99.9999%, Westfalen AG, Germany) combined with a trap (Agilent Big Universal Trap, Agilent Technologies, USA) at 200 mL min^{-1}. If the nitrogen flow is stopped for some reason, e.g. the nitrogen supply bottle runs empty, the AEDIII is equipped with spectrometer quick purge mode, which can be activated with a click of a physical button on the instrument. This quick purge mode allows for a much quicker spectrometer purge with a nitrogen flow of around 2 L min^{-1}. This mode permits a good spectrometer purge after around 30 min for a completely unpurged spectrometer.

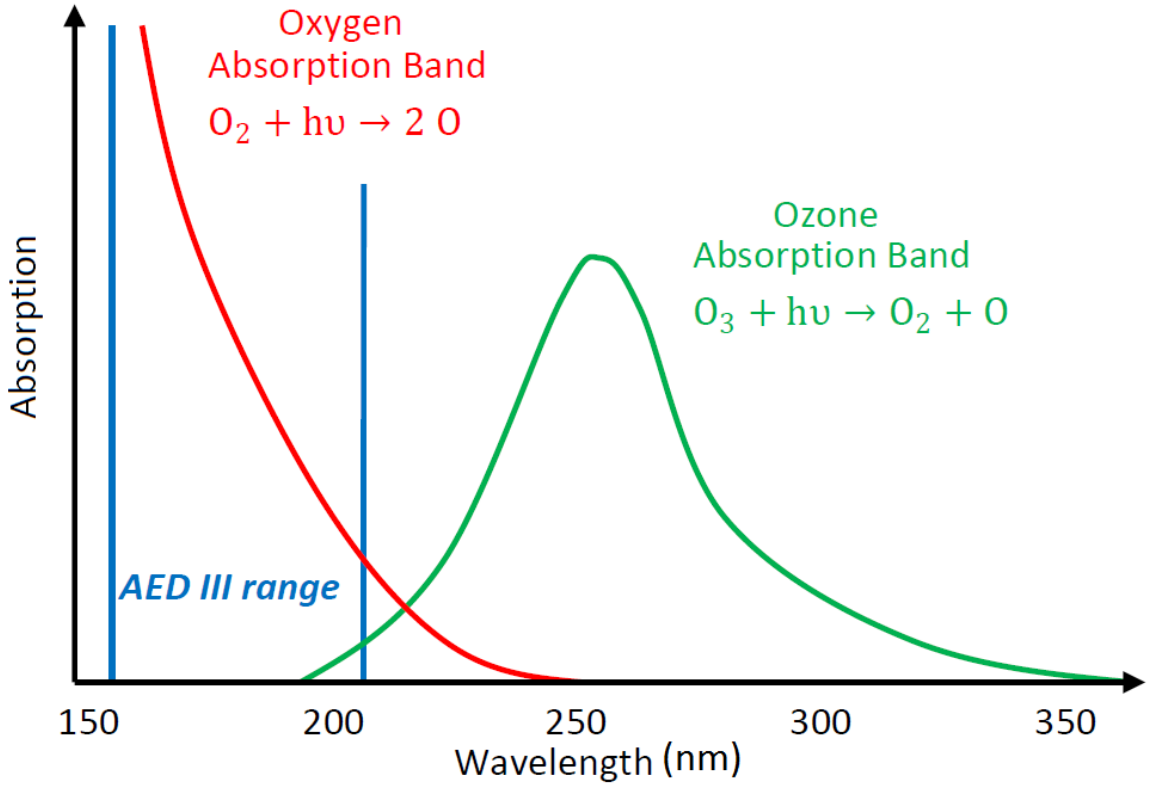

Figure 2.3 AEDIII spectrometer light absorption in the UV range. Adopted from *Joint Analytical Systems GmbH 2017a*.

2.4.4 AED reagent gases

The AED uses extra ultra-high purity H_2 (purity > 99.99999% by a Parker Balston Hydrogen Generator, model H2-300, Parker Hannifin Corporation USA) and ultra-high purity O_2 (purity 99.9999%, Westfalen AG, Germany) as reagent gases in the cavity, which are vented off thereafter. Hydrogen enhances reduction reactions of sample analytes and matrix, and

further reduces the discharge tube wall effects. Oxygen helps to provide CO bands for carbon elemental line detection, reduces the formation of elemental black carbon in the cavity, and increases the combustion rate of sample analytes and matrix. The reagent gases are provided through GC EPC ports. During an active GC run, slightly lower supply pressures of H_2 and O_2 are used compared to the GC idle mode. Lower reagent gas flows dilute the analytes slightly less, allowing for higher sensitivities. Higher reagent flows at the end of a GC run and at the idle state help to recondition the helium plasma discharge tube for a next sample injection. The reagent gas supply pressures are indicated in *Table 2.6*.

Table 2.6 AEDIII reagent gas supply pressures.

Reagent	Pressure GC run state	Pressure GC idle state
Hydrogen (EPC2)	12 psi (0.83 bar)	15 psi (1.03 bar)
Oxygen (EPC1)	15 psi (1.03 bar)	20 psi (1.38 bar)

2.4.5 Most sensitive AED elemental lines

While the AEDIII Instrument Control Software is able to record the whole raw spectra between 161 – 211 nm, up to 8 element channels can be chosen to be automatically exported to Chemstation software as specific elemental emission line integrals for further data processing. Each measurable element in this range has its own optimum reagent gas configuration mode, called recipe. The H_2, O_2 reagent gases and high He makeup flow valves can be either opened or closed, and all the underlying combinations of the three valves are possible. For the purpose of this thesis work, a combination of the 8 most anticipated and sensitive elemental lines were determined with the H_2 and O_2 reagents turned on and the high He makeup flow turned off mode. This combination allows for highest sulfur and carbon sensitivities. The most sensitive elemental spectral lines are summarized in *Table 2.7*.

Table 2.7 AEDIII most sensitive elemental spectral lines.

Element (Symbol)	Most sensitive spectral line (nm)
Bromine (Br)	163
Nitrogen (N)	174
Iodine (I)	178
Sulfur (S)	181

Silicon (Si)	182 (199)
Carbon (C)	193
Mercury (Hg)	194
Selenium (Se)	196
Arsenic (As)	197

2.4.6 AEDIII spectrometer calibration emission lines

Before the measurement of every sample, an automatic spectrometer emission wavelength calibration takes place. For that purpose, first the vent valve opens for few seconds and then follows a H_2 reagent gas valve opening. The relative background elemental emission line peak locations and the distance between them are used to realign the spectrometer. The two combined CCDs consists of total of 4096 diodes, providing 0.01 nm spectral resolution. An example calibration spectra of reagent valves in the off position overlaid with reagent H_2 reagent valve being opened for the realignment purpose are shown in *Figure 2.4*.

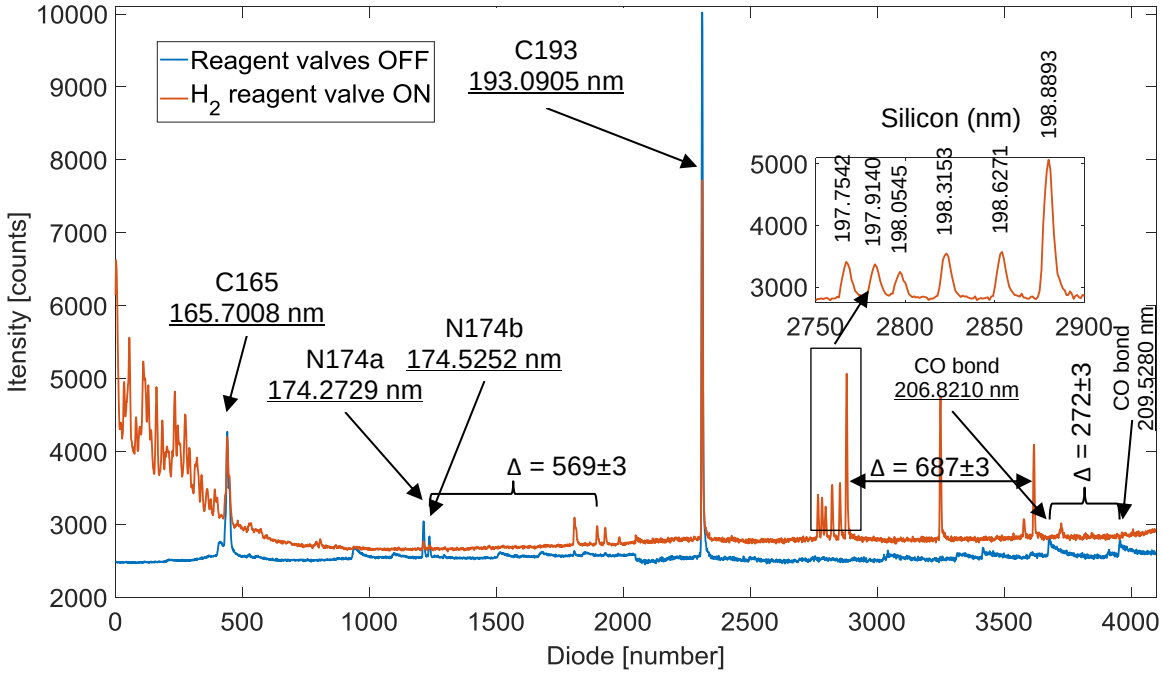

Figure 2.4 AEDIII spectrometer wavelength calibration graph. The 2 combined CCDs make up total of 4096 diodes. The background elemental emission line peak wavelengths are annotated on the graph.

2.4.7 Example AEDIII chromatogram

The AEDIII is simultaneously measuring wavelength spectra from 161 – 211 nm, but in the Agilent GC software Chemstation it is only possible to simultaneously record the emission lines of up to 8 different elements. This limitation of 8 elements comes from the GC Chemstation software. In the raw spectra (if chosen to be saved) all the wavelengths in the range are stored with 0.01 nm resolution. A typical AEDIII raw spectra file (*sample.aed3*) takes about 0.11 GB min^{-1} storage, i.e. 3.67 GB for every 34 min long chromatogram. An example calibration standard chromatogram can be seen in *Figure 2.5*, where 5 different elements (bromine, carbon, iodine, sulfur and nitrogen), which are contained in the 84 component Apel-Riemer-2015 calibration gas standard (gravimetric VOC gas standard at ~ 50 ppbv MR, Apel-Riemer Environmental Inc., USA. See *Table 6.1* in *Appendix*) are overlaid on a normalized counts y-axis plot. *Figure 2.6* shows a 3D representation of a section of the same AEDIII calibration standard raw data chromatogram. Each component of the calibration standard has a MR of ~ 50 ppbv in ultra-high purity nitrogen, see *Table 6.1* in *Appendix* for reference. The calibration gas is diluted with synthetic air in a system with a catalyst at 500°C for removing any NMHC contaminants in the synthetic air, and diluted with two mass flow controllers (MFCs) directly before the pre-concentration of the sample in Entech. For the calibration standard shown in *Figure 2.5* & *Figure* 2.6, flows of 5 mL min^{-1} calibration standard in 1 L min^{-1} synthetic air were used to achieve the MR of ~ 250 pptv of each component. Some example compounds are annotated in *Figure 2.5*. It can be seen that every elemental line has a different sensitivity and that the detector has an equimolar response. Compounds that have other elements than carbon in them will have a peak in the overlying elemental line of interest. By knowing how many atoms of different elements are in the compound of interest, a compound independent calibration (CIC) is possible. From the detector point of view, the CIC is possible to a high degree of accuracy, but the limiting factor is the potentially different pre-concentration efficiencies in the Entech traps and the carry-through potential for the different compounds. Normally, CIC works well if it is used for compounds belonging to similar compound class and having similar number of atoms. Box plot of Apel-Riemer-2015 gas calibration standard component AEDIII carbon emission line (193 nm) response factors can be seen in *Figure 2.7*, and will be further discussed in *Section 2.4.8.1*.

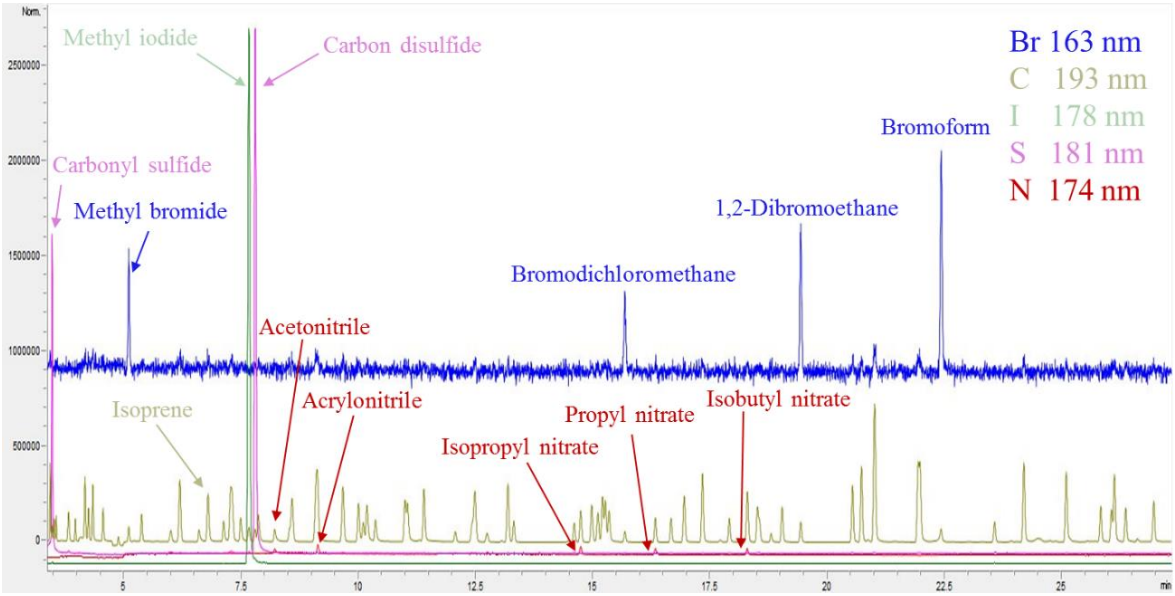

Figure 2.5 Example AEDIII normalized multi-element overlay chromatogram of ~250 pptv 84 component Apel-Riemer-2015 gas calibration standard.

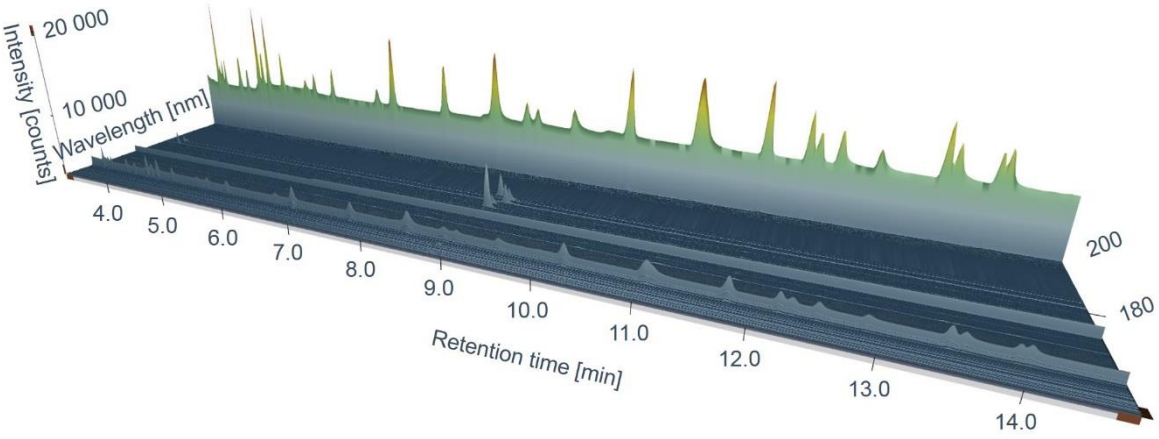

Figure 2.6 3D representation of AEDIII multi-element raw data chromatogram section of ~250 pptv 84 component Apel-Riemer-2015 calibration gas standard.

2.4.8 AEDIII analytical performance

The AEDIII system was always recalibrated before the measurement of the air samples, mainly with Apel-Riemer-2015, NPL-2015, NPL-2017 and NOAA-2017 gas calibration standards as appropriate. From the calibration standard measurements, the linearities (R-squared), limits of detection (LODs) and response factors (RFs) per atom were determined for all quantifiable compounds in the standard. Normally 1.4 L of air was preconcentrated with the Entech system during each sample and calibration standard measurement. With NPL standards (30 component ozone precursor NMHC NPL Primary Reference Standard, National Physical Laboratory, UK. See *Table 6.2* in *Appendix)* normally 40 – 250 mL of the ~ 4 ppbv standard was trapped and correlated with the other 1.4 L samples. With the Apel-

Riemer-2015 gas calibration standard the certified 50 ppbv volume mixing ratios were diluted with zero-air prior to the 1.4 L sample trapping. Dilution zero-air (synthetic air passed through Pt catalyst at 500°C to oxidize HC contaminants and through Supelcarb HC trap to remove impurities) flow was normally fixed at 1 L min^{-1} with one MFC, and a range of different Apel-Riemer-2015 flows were used with another MFC in the range of 1 – 20 mL min^{-1}, providing MRs of around 50 – 1000 pptv which are relevant for ambient air measurements.

LODs were calculated from the average height of the lowest calibration levels and the average height of the noise signals corresponding to the same chromatogram for each separable and measurable compound of the calibration standards. For the noise height, suitable retention time windows were chosen and the background noise data points were fitted with a second order polynomial, and the standard deviations to the fit were calculated. Noise was defined as three times the standard deviation of the background height fit. These noise values were used to determine the LOD MRs from the lowest calibration level points. Three times signal-to-noise ratio (by peak height) was defined for LODs, representing the 99.7% confidence interval. The LOD calculation is represented by *Equation 2.1*.

$$LOD = 3 \times \frac{\overline{Noise} \times MR}{Peak\ height} \tag{2.1}$$

The per carbon atom RFs were calculated separately for each species using the underlying area under curve (AUC, peak area), corresponding MRs and number of carbon atoms present. RFs were calculated separately for all compounds and their individual calibration MR levels, and thereafter all the individual RFs over the whole calibration range were averaged to a single RF per compound. The formula used for the calculation is summarized with *Equation 2.2*. This per compound method was used for a higher accuracy if the analyte of interest existed in the calibration gas standards. Without the specific compound of interest in the calibration gas the MR was estimated from the elemental response factor.

$$\overline{RF} = \frac{\overline{AUC}}{\overline{MR} \times Number\ of\ carbon\ atoms} \tag{2.2}$$

2.4.8.1 Entech-GC-AEDIII system carbon emission line performance

The Entech-GC-AEDIII system carbon emission line (193 nm) LODs derived from Apel-Riemer-2015 calibration standard measurements are listed in *Table 2.8*. The determined RTs and standard certified compound MRs can be found in *Table 6.1* in *Appendix*. The

determined LODs range from 0.8 – 9.7 pptv, for propene and trichloroethylene, respectively. The average and median LODs of the whole Entech-GC-AEDIII measurement method of the Apel-Riemer-2015 gas standard are 3.2 and 2.7 pptv, respectively. The compound specific LODs depend on the Entech pre-concentration efficiency, compound transmission efficiency through the gas transferlines, GC separation and carry through efficiency and AED helium plasma atomization and excitation efficiency. Throughout the instrument development best efforts were taken to use suitable transferline and Swagelok gas union materials, like silcosteel, stainless steel, PFA, Teflon for minimizing analyte flow path losses, i.e. through wall losses etc. Furthermore, high quality stainless steel pressure regulators were used for calibration standard gas bottles with non analyte degassing O-rings.

The coefficients of determination (R^2 values) were calculated for determining the whole system compound specific response linearities. The R^2 values for Apeal-Riemer-2015 calibration standard, determined for the range of about 50 – 1000 pptv are stated in *Table 2.8* and the individual calibration curves can be seen in *Figure 6.1* in *Appendix*. The average R^2 value was calculated to be 0.99060 and median 0.99468, from which it can be stated that the system performs linearly in the range of ambient trace gas measurements.

The Entech-GC-AEDIII system carbon emission line (193 nm) RFs per carbon atom derived from Apel-Riemer-2015 calibration standard measurements are also listed in *Table 2.8*. Each compound's RF is the average of 18 independent data points in the whole 50 – 1000 pptv calibration range. The RFs for these compounds lie between 343 – 745 counts C^{-1} $pptv^{-1}$, which correspond to benzyl chloride and chlorodifluoromethane (HCFC-22) respectively. The average and median RFs per carbon atom were calculated to be 587 and 610 counts C^{-1} $pptv^{-1}$. The per carbon atom RF relative standard deviation (RSD) derived from the Apel-Riemer-2015 constituents which are listed in *Table 2.8* to be 19.1%, which include NMHCs, sulfides, chlorinated, fluorinated and brominated halocarbons, nitrates and other VOCs. All the component RFs are depicted with a boxplot in *Figure 2.7*. It can be seen that the RF standard deviation is large for instance for methanol and nitrates, which could most likely be explained due to their viscosity and adhesion to surfaces within the analytical system as a whole. As discussed before in the LOD section, the RFs depend on the whole Entech-GC-AEDIII system, and the efficiency depends on each individual component for the whole method. Even if the AEDIII detector is completely equimolar, the final sensitivities and RFs also depend on the pre-concentration. The performance of the whole system equimolarity can be assessed with the RF RSD value of 19.1%. Within 1σ (68.3%) confidence interval compound independent calibration (CIC) can be used for compounds not present in the

calibration gas, as far as the retention time (RT) and the number of carbon atoms in that compound is known, for estimating the MR with 19.1% error. 2σ (95.4%) and 3σ (99.7%) confidence intervals rise the CIC MR estimation error to 38.2% and 57.3%, respectively.

Table 2.8 Entech-GC-AEDIII system limits of detection (LODs) on 3σ level, R^2 linearity and response factors (RFs) per carbon atom values derived from Apel-Riemer-2015 gas calibration standard measurements. 1.4 L of diluted gas standard was preconcentrated.

Compound	LOD (pptv)	R-squared	No. of C atoms	RF per C atom (counts C^{-1} $pptv^{-1}$)
Carbonyl sulfide	6.1	0.99832	1	637
Dichlorodifluoromethane (R-12)	2.7	0.99189	1	589
Chlorodifluoromethane (HCFC-22)	2.4	0.99589	1	745
Chloromethane	2.9	0.99581	1	661
Methanol	3.7	0.92247	1	529
Methyl bromide	5.1	0.99429	1	553
Trichlorofluoromethane	5.6	0.99431	1	652
Methyl iodide	6.7	0.99668	1	552
Carbon disulfide	5.4	0.99015	1	696
Chloroform	5.7	0.99474	1	652
Tetrachloromethane	7.0	0.99447	1	637
Bromoform	5.8	0.99384	1	737
Vinyl chloride	2.0	0.99492	2	549
Acetaldehyde	1.8	0.99402	2	636
Chloroethane	2.6	0.99469	2	550
Acetonitrile	4.8	0.96653	2	523
1,1-Dichloroethane	3.9	0.97800	2	430
1,2-Dichloroethane	3.3	0.99494	2	563
Trichloroethylene	9.7	0.95093	2	457
1,1,2-Trichloroethane	3.3	0.99287	2	715
1,2-Dibromoethane	3.4	0.99489	2	638
1,1,2,2-Tetrachloroethane	3.2	0.99468	2	654
Propene	0.8	0.99478	3	620
2-Propanol	1.7	0.99457	3	698
Isopropyl nitrate	2.2	0.99886	3	742
Propyl nitrate	9.6	0.99813	3	439
cis-1,3-Dichloropropene	2.8	0.99452	3	512
Isobutene	0.9	0.99532	4	666
1,3-Butadiene	1.0	0.99492	4	580
Methacrolein	1.5	0.99458	4	728
Butanol	2.5	0.99537	4	384
Isobutyl nitrate	2.0	0.99878	4	800
Pentane	1.1	0.98933	5	595
Isoprene	1.2	0.99494	5	628
Hexane	1.0	0.99496	6	643
Benzene	0.9	0.99451	6	676
4-Methyl-2-pentanone (MIBK)	1.9	0.99513	6	566
2-Hexanone	2.7	0.99284	6	357

Hexanal	6.1	0.98819	6	386
Chlorobenzene	1.4	0.99540	6	573
1,3-Dichlorobenzene	2.8	0.98789	6	399
Benzyl chloride	4.7	0.97921	6	343
1,2-Dichlorobenzene	2.6	0.99017	6	412
Toluene	0.9	0.99502	7	643
Ethylbenzene	0.9	0.99536	8	610
1,3,5-Trimethylbenzene	0.9	0.99470	9	665
1,2,4-Trimethylbenzene	1.1	0.99135	9	584

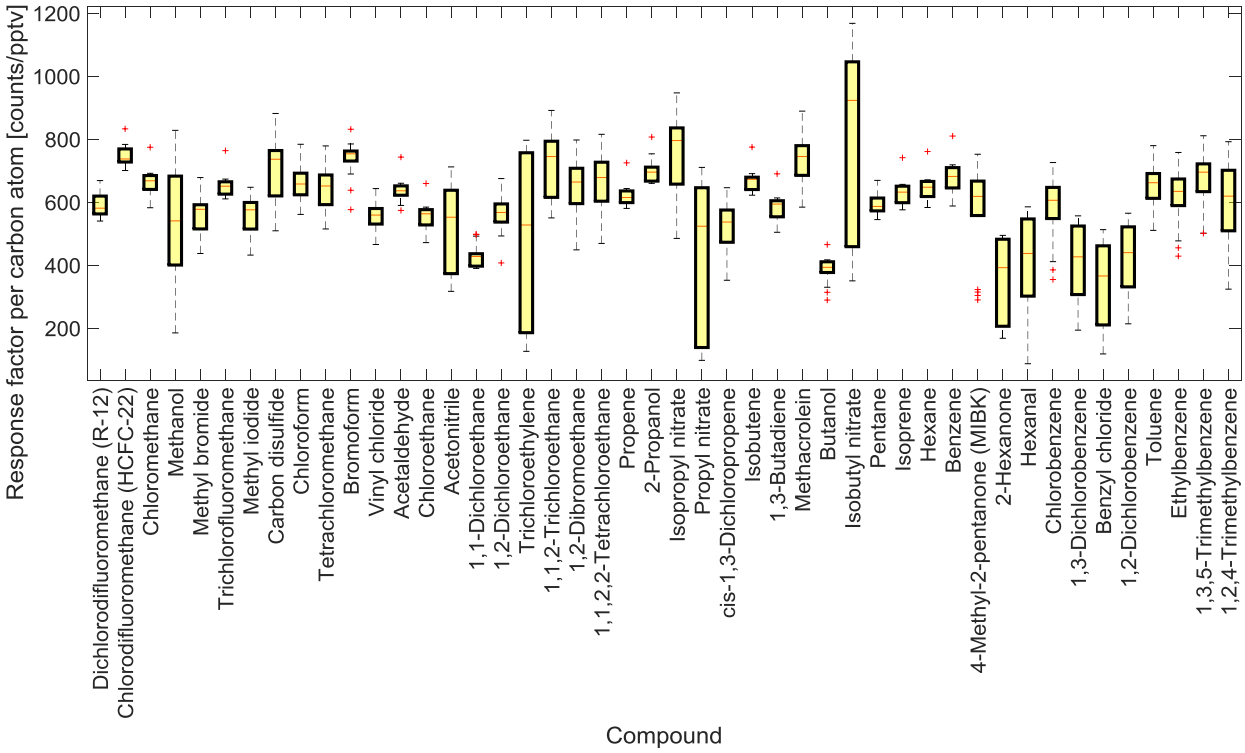

Figure 2.7 Boxplot of Entech-GC-AEDIII Apel-Riemer-2015 gas calibration standard compound carbon emission line (193 nm) response factors in a growing order of carbon atoms. Central red lines indicate the medians, top and bottom edges of the box represent the 75th and 25th percentiles respectively, the whiskers extend to the highest and lowest data points not considered as outliers, and the individual red '+' signs indicate the outliers.

The same type of analysis was undertaken also for National Physical Laboratory (NPL-2017) 30 component NMHC ozone precursor primary standard. The determined RTs on the Entech-GC-AEDIII system and certified MRs can be found in *Table 6.2* in *Appendix*. The carbon emission line (193 nm) calculated LODs, R^2 values and RFs per carbon atoms are listed in *Table 2.9*, and all the individual calibration curves seen in *Figure 6.2* in *Appendix*.

The LODs range from 0.5 – 1.1 pptv (3σ) with average and median value of 0.7 and 0.8 pptv, respectively allowing for low pptv level trace gas measurements. The average linearity coefficient of determination being 0.98567 and median 0.99173, providing proof for good

calibration linearity. The RFs per carbon atom range from 581 – 913 counts C^{-1} $pptv^{-1}$, corresponding to 1,2,4-trimethylbenzene and toluene, respectively. Average RF for these NMHCs being 684 counts C^{-1} $pptv^{-1}$ and median 660 counts C^{-1} $pptv^{-1}$. The RF RSD determined with this calibration gas standard compounds was calculated to be 12.9%, 25.8% and 38.7%, within 1σ (68.3%), 2σ (95.4%) and 3σ (99.7%) confidence intervals, respectively. The RFs are statistically presented with a boxplot in *Figure 2.8*. A trend in the RFs groups with the same number of carbon atoms can be seen. This indicates that compound independent calibration could be successfully used within similar compound groups with 12.9 – 38.7% uncertainty. Similar effect is known from FID instruments, where different per carbon response factors have been observed within different groups of similar molecules, for example like in (Baker, Slemr and Brenninkmeijer, 2010). The uncertainty error is estimated to be smaller for the NPL-2017 compounds compared to the Apel-Riemer-2015 compounds, as the former consists only of hydrocarbons, whereas more various VOC groups are included in the Apel-Rimer-2015 standard as discussed earlier.

Table 2.9 Entech-GC-AEDIII system limits of detection (LODs) on 3σ level, R^2 linearity and response factors (RFs) per carbon atom values derived from NPL-2017 primary NMHC gas calibration standard measurements.

Compound	LOD (pptv)	R-squared	No. of C atoms	RF per C atom (counts C^{-1} $pptv^{-1}$)
Propene & Propane	0.8	0.99444	3	627
Isobutane	0.8	0.99164	4	659
1,3-Butadiene	0.8	0.99432	4	594
trans-2-Butene	0.8	0.99083	4	598
cis-2-Butene	1.0	0.99129	4	585
Isopentane	1.1	0.99598	5	593
1-Pentene	0.9	0.99263	5	654
n-Pentane	0.9	0.99263	5	660
trans-2-Pentene	0.9	0.99026	5	633
Isoprene	1.0	0.99181	5	628
2-Methylpentane	0.9	0.97498	6	684
n-Hexane	0.8	0.96687	6	701
Benzene	0.7	0.96992	6	695
n-Heptane	0.6	0.99386	7	775
Toluene	0.5	0.99127	7	913
2,2,4-Trimethylpentane	0.6	0.99205	8	824
n-Octane	0.5	0.98977	8	796
Ethylbenzene	0.5	0.92709	8	743
o-Xylene	0.5	0.99552	8	748
1,3,5-Trimethylbenzene	0.5	0.96353	9	736
1,2,4-Trimethylbenzene	0.6	0.99727	9	581
1,2,3-Trimethylbenzene	0.6	0.99681	9	619

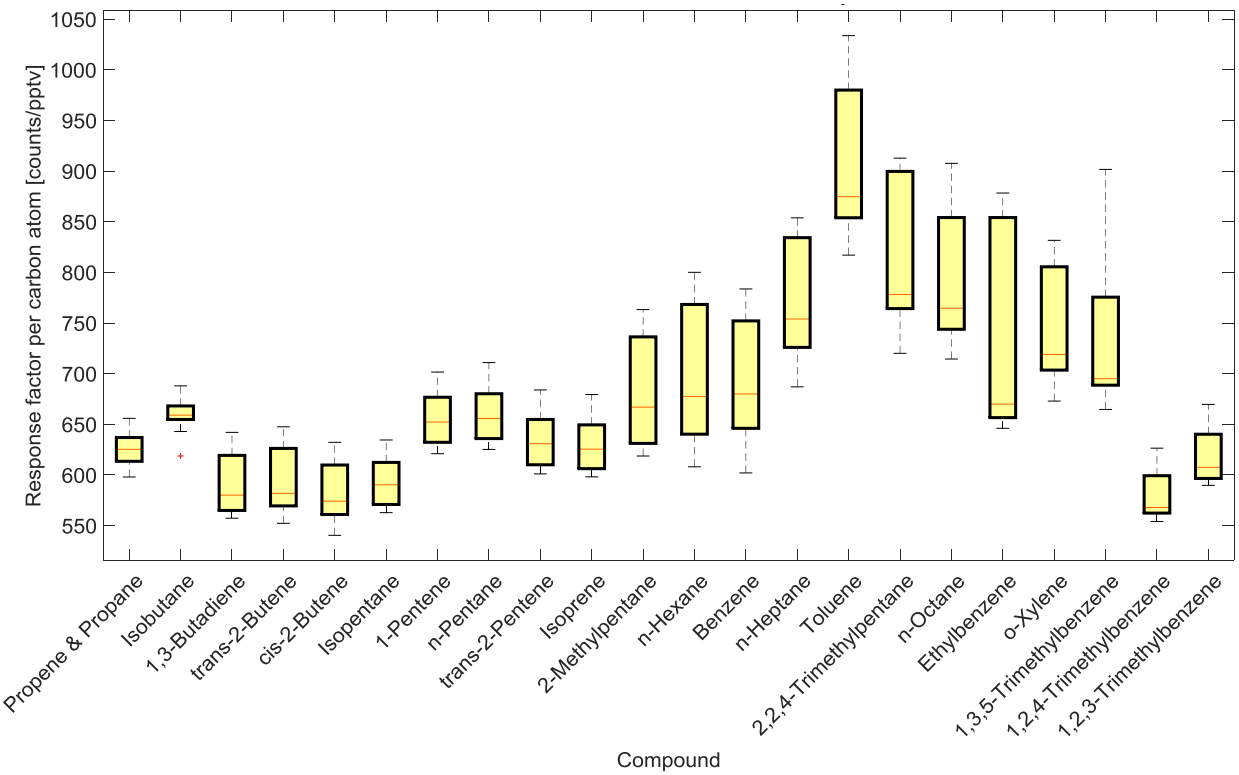

Figure 2.8 Boxplot of Entech-GC-AEDIII NPL-2017 NMHC primary gas calibration standard compound carbon emission line (193 nm) response factors ordered in a growing number of carbon atoms. Central red lines indicate the medians, top and bottom edges of the box represent the 75th and 25th percentiles respectively, the whiskers extend to the highest and lowest data points not considered as outliers, and the individual red '+' signs indicate the outliers.

2.4.8.2 Entech-GC-AEDIII system iodine, sulfur, bromine and nitrogen emission line performances

Apel-Riemer-2015 gas phase calibration standard (see *Table 6.1* in Appendix) was used to evaluate the performance of other available and relevant atomic emission lines for atmospheric chemistry. *Equations 2.1* and *2.2*, discussed in *Section 2.4.8*, were used to determine the LODs and RFs, respectively and are listed in *Table 2.10*. The element specific calibration curves are shown in *Figure 2.9* and *Figure 2.10*. The most sensitive AEDIII emission line was determined to be iodine at 178 nm wavelength with 0.7 pptv LOD (3σ level) for methyl iodide, and having RF of 1635 counts I^{-1} $pptv^{-1}$. The LOD of methyl iodide on iodine emission line was 9.6 times more sensitive compared to carbon emission line. The second most sensitive emission line was determined to be sulfur at 181 nm. Carbonyl sulfide (OCS) and carbon disulfide (CS_2) had LODs of 1.9 and 1.8 pptv (3σ level), respectively. OCS had RF of 342 counts S^{-1} $pptv^{-1}$, and CS_2 had RF of 476 counts S^{-1} $pptv^{-1}$. The sulfur emission line at 181 nm was determined to be on average 3.1 times more sensitive compared to the carbon 193 nm emission line, calculated from OCS and CS_2 LOD values. Low

detection limits of organosulfur compounds made this instrument especially interesting for this thesis work. Bromodichloromethane, 1,2-dibromoethane and bromoform at bromine emission line at 163 nm had significantly higher LODs of 115.7, 61.9 and 64.2 pptv (3σ level), respectively compared to iodine, sulfur and carbon emission lines. The RFs for the three bromine compounds in the same stated order were calculated to be 9.9, 9.0 and 8.3 counts Br^{-1} $pptv^{-1}$, which are significantly less sensitive compared to iodine, sulfur and carbon emission lines. The bromine emission line had low noise, but also the compound peak heights and areas were low. From the evaluated emission lines, nitrogen at 174 nm proved to be least sensitive element for AEDIII detector. Nitrogen containing compounds varied significantly with their LODs, nevertheless they all consisted of a single nitrogen atom. Acetonitrile had lowest sensitivity in the nitrogen emission line group with LOD 265.1 pptv (3σ level), see *Table 2.10*. Isobutyl nitrate had highest sensitivity with LOD at 57.1 pptv (3σ level), which is 4.6 times more sensitive than acetonitrile on the nitrogen 174 nm emission line. The per nitrogen atom RFs ranged from 19.8 – 35.8 counts N^{-1} $pptv^{-1}$, with RSD (1σ level) at 20.8%, average at 27.6 counts N^{-1} $pptv^{-1}$ and median at 28.2 counts N^{-1} $pptv^{-1}$. Acetonitrile's detection limit was 55.2 times better on carbon 193 nm emission line, whereas isobutyl nitrate's LOD was 28.6 times higher. Overlay carbon and nitrogen emission line calibration curve comparison of the 5 organonitrogen species present in the calibration gas are shown in *Figure 2.10*. On average the peak areas were 68 times higher for C-193 nm vs N-174 nm emission lines, determined from the same chromatograms.

Table 2.10 Entech-GC-AEDIII system limits of detection (LODs) on 3σ level, R^2 linearity and response factors (RFs) per iodine, sulfur, bromine and nitrogen atom values derived from Apel-Riemer-2015 gas calibration standard measurements. 1.4 L of diluted gas standard was preconcentrated.

Compound	LOD (pptv)	R-squared	Element	RF per atom (counts $pptv^{-1}$)
Methyl iodide (iodine)	0.7	0.99668	I	1635
Carbonyl sulfide (sulfur)	1.9	0.99964	S	342
Carbon disulfide (sulfur)	1.8	0.99966	S	476
Bromodichloromethane (bromine)	115.7	0.98930	Br	9.9
1,2-Dibromoethane (bromine)	61.9	0.99226	Br	9.0
Bromoform (bromine)	64.2	0.99082	Br	8.3
Acetonitrile (nitrogen)	265.1	0.98281	N	19.8
Acrylonitrile (nitrogen)	139.4	0.99657	N	28.2
Isopropyl nitrate (nitrogen)	64.6	0.98954	N	35.8
Propyl nitrate (nitrogen)	82.0	0.99180	N	25.8
Isobutyl nitrate (nitrogen)	57.1	0.99060	N	28.2

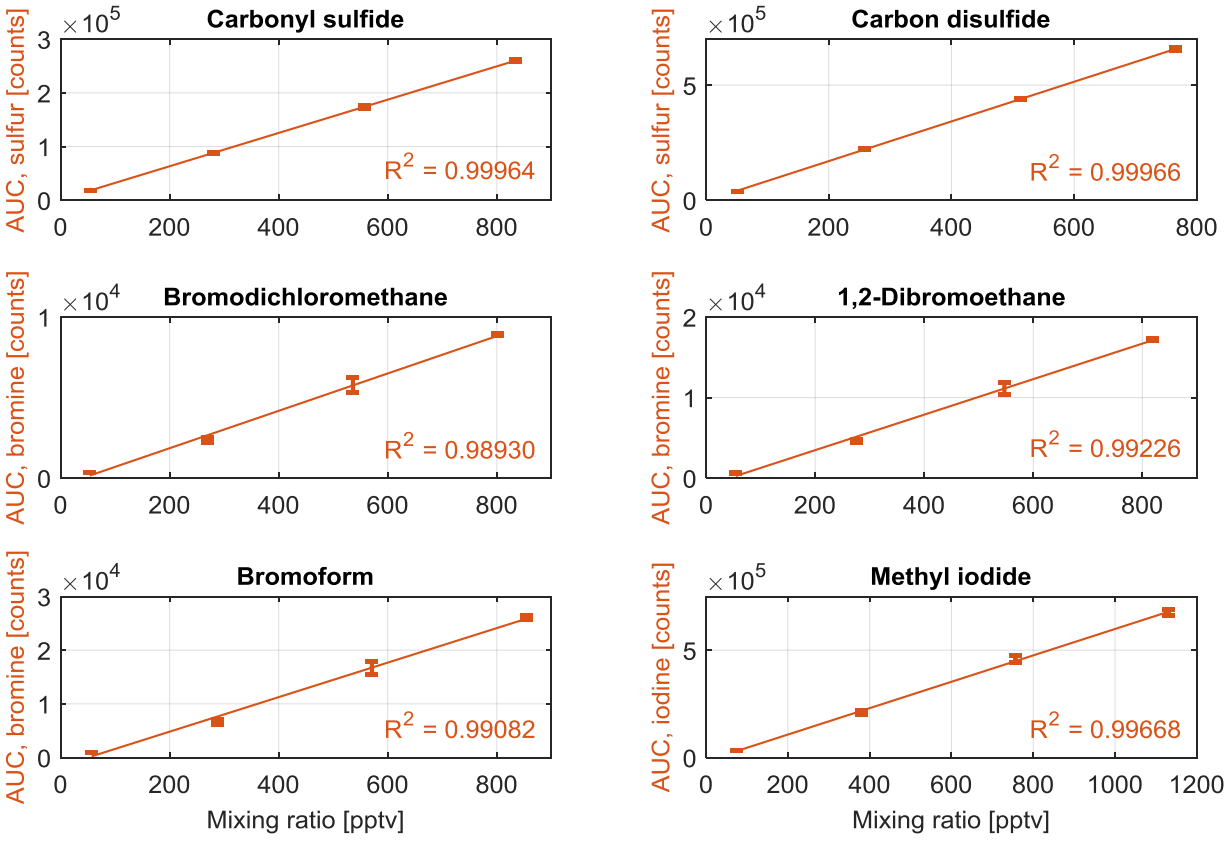

Figure 2.9 Entech-GC-AEDIII system sulfur (181 nm), bromine (163 nm) and iodine (178 nm) emission line calibration curves determined with Apel-Riemer-2015 gas standard. 1 – 15 mL min^{-1} standard gas was diluted with 1 L min^{-1} zero-air prior to 1.4 L sample pre-concentration.

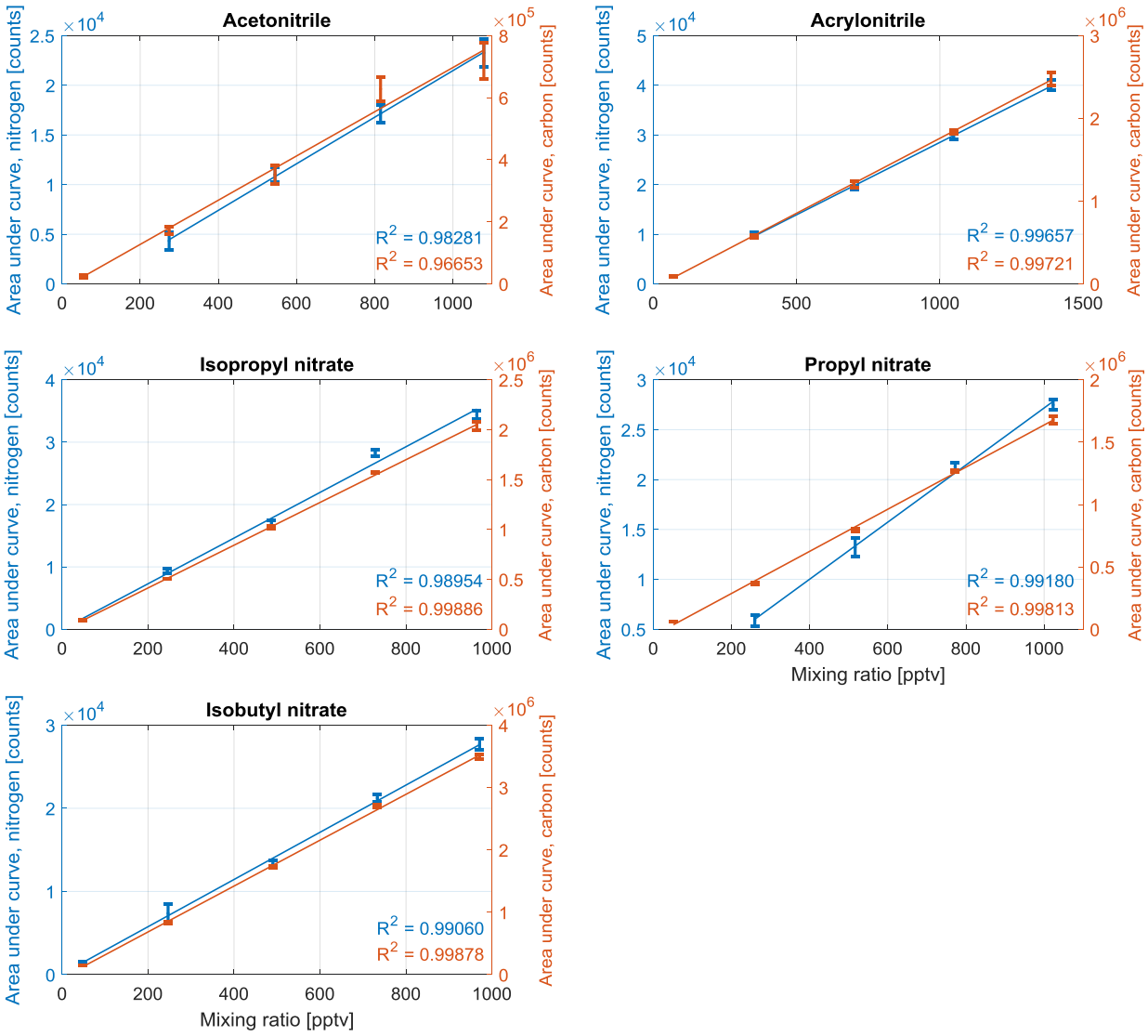

Figure 2.10 Entech-GC-AEDIII system overlay of nitrogen (174 nm) and carbon (193 nm) emission line calibration curves determined with the Apel-Riemer-2015 gas standard. 1 – 20 mL min^{-1} standard gas was diluted with 1 L min^{-1} zero-air prior to 1.4 L sample pre-concentration.

2.4.8.3 AEDIII performance comparison with JAS stated values

The determined LODs were used to calculate minimum detectable limits (MDLs) in pg s^{-1} of the AEDIII instrument for direct comparison with the instrument producing company JAS stated values. *Equation 2.3*, summarizes how MDLs were calculated from LODs. LOD, limit of detection in volume mixing ratio (pptv); V, gas volume which was preconcentrated (L); P, pressure in the lab (atm); $M_{\Sigma atom}$, molar mass sum of all atoms of interest (g mol^{-1}); R, ideal gas constant (0.08206 L atm mol^{-1} K^{-1}); T, lab temperature (K) and Peak Width, chromatographic peak width of compound of interest (s).

$$MDL = \frac{LOD \times V \times P \times M_{\sum atoms}}{R \times T \times Peak\ Width} \quad (2.3)$$

$$MDL\ (benzyl\ chloride) = \frac{4.7 \times 1.4 \times 1 \times (7 \times 12.01)}{0.08206 \times 295.15 \times 8.20} = 2.8\ pg\ s^{-1} \quad (2.4)$$

Example LOD to MDL calculation is shown with *Equation 2.4*, where benzyl chloride's (C_7H_7Cl) LOD of 4.7 pptv was calculated to MDL of 2.8 pg s^{-1} on the carbon 193 nm emission line. The comparison of JAS stated MDLs with this work MDLs are shown in *Table 2.11*. For this thesis work measured MDL for sulfur at 181 nm was averaged from carbonyl sulfide and carbon disulfide detection limits, and nitrogen at 174 nm MDL was averaged from acetonitrile, acrylonitrile, isopropyl nitrate, propyl nitrate and isobutyl nitrate detection limits. For sulfur, carbon and nitrogen the JAS stated MDLs are 4.5, 6.2 and 4.1 times more sensitive compared with the findings of thesis work. It is very difficult to directly compare the MDL values, as they do not state which methods were used for the calculations nor which compounds were used for their calculation. For example, 3σ confidence interval levels were used in this study.

Table 2.11 AEDIII minimum detectable limits (MDLs) stated by the instrument producing company Joint Analytical Systems (JAS) compared to MDLs resulting from this thesis work. JAS MDLs from *Joint Analytical Systems GmbH 2017*.

Element (Symbol)	Wavelength (nm)	JAS stated MDL (pg s^{-1})	Measured MDL, 3σ (pg s^{-1})
Sulfur (S)	181	≤ 0.2	0.9
Carbon (C)	193	≤ 0.5	3.1
Nitrogen (N)	174	≤ 3.0	12.4

2.4.9 Drawback of AED – breaking of discharge tubes

The helium plasma is sustained in a small quartz glass tube (47 mm long, 1 mm inner diameter) with brown polymer coating (27 mm long) in the middle part of the outside surface. The discharge tube is fitted in the cavity of the AED. The cavity is water-cooled, the cooling water is maintained at 70°C. A very important shortcoming of the AED instrument is the very short lifetime of the discharge tube. The median lifetime of the discharge tube is around 5 to 30 days, depending a lot on the number and concentration of the samples measured, and successfulness of the replacement of the discharge tube, as it is very fragile and can be easily damaged during the replacement procedure. When a discharge tube breaks, it will flood the whole cavity, part of the gas drawer and the fly ash filter with the cooling water. Furthermore, with every discharge tube replacement the sensitivity and response factors of the analytes change, which means the system needs to be recalibrated

every time after the tube replacement procedure. This is especially undesirable during a measurement series of one group of samples, as you would like to measure all the samples with same conditions. Unfortunately, discharge tube breaking occurs often also during the sample measurement, for example during the monthly measurement of CARIBIC flight campaign wholeair samples (see *Chapter 3*). Only recently, the manufacturer of AED instrument, Joint Analytical Systems GmbH, introduced a new feature in the firmware of their device so that the water pump switches off once discharge tube breaking is detected. Unfortunately, this features does not always work as it should. Also, false positive discharge tube breaking detections occur, which ruins the measurement of a sample, causing the loss of sample and data. Due to the discharge tube replacement service procedure and recalibration efforts, the sample measurement will slow down significantly and affects the measurement quality. Another drawback is the difficulty and time consumption of the replacement of the discharge tube. It takes around one hour of experienced person to change the discharge tube together with drying and cleaning the cavity. As the discharge tube is very fragile, it can easily happen that the tube gets damaged during the installation, and that can significantly reduce its lifetime. It is not unusual that the tube breaks again only within one day after the installation of a new discharge tube, which is very frustrating. Sometimes it takes several discharge tubes during the replacement procedure to successfully ignite the plasma again, as it is very difficult to find the exact torque to tighten the gas union nut to make the cavity leak tight. If the gas union nut is too loose, cooling water will leak to the cavity, and tightening the nut too tightly can crack the fragile quartz tube. The exact strength slightly varies every time due to the alignment of the corresponding ferrule and O-ring. This fact also brings up the running cost of an AED instrument, as one replacement discharge tube kit costs 51 EUR. This discharge tube breaking is a very important disadvantage of the AED detector, as it significantly brings down the uptime, reliability and reproducibility of the measurements.

3 IAGOS-CARIBIC

3.1 Description of IAGOS-CARIBIC project

The whole air canister samples were collected by the IAGOS-CARIBIC flying observatory (In-service Aircraft for a Global Observing System – Civil Aircraft for the Regular Investigation of the Atmosphere Based on an Instrument Container; www.caribic-atmospheric.com) on board a Lufthansa Airbus A340-600 aircraft, see *Figure 3.1*, with global long distance flight routes, see *Figure 3.2*. IAGOS-CARIBIC is forward-thinking and cost-efficient scientific collaboration project between 13 international institutes and 6 high tech companies to examine, analyze and monitor important chemical and physical processes in the Earth's atmosphere. Airplane measurements based on a civil aircraft are significantly cheaper compared to specialized aircraft for airborne measurements, e.g. compared to DLR High Altitude and Long Range Research Aircraft (HALO) or NASA Earth Resources 2 (ER-2). The cost for the CARIBIC container airfreight cargo fee for 4 flight sequences is ~ 21 500 EUR, which is only ~ 512 EUR per flight hour. Additional costs including pre checks, container transport, consumables, repairs, aircraft checks, depreciation etc., which brings the average cost per flight hour to ~ 684 EUR. This is still significantly cheaper than other research airplane-based projects. For example, flight hour of DLR HALO aircraft costs ~ 10 000 EUR, which makes CARIBIC nearly 20 times cheaper.

CARIBIC project is special as it is based on a Lufthansa civil aircraft, and the measurements are conducted during regular passenger flights along air traffic corridors. This mode of flying restricts the aircraft to certain routes, meaning it is not possible to divert the aircraft to explore an interesting atmospheric feature or phenomenon. However, it does mean the instruments have a global coverage and fly regularly over multiple seasons. The instrument airfreight container weighing approximately 1.6 t is fixed in the aircraft’s cargo bay prior to the flights. The Airbus A340-600 aircraft is specially modified for the CARIBIC project and has a permanently installed inlet pylon under the fuselage, pointing to the direction of travel (air flow ~ 250 m s^{-1}). There is a separate inlet for measuring VOCs and aerosol particles, furthermore there is a camera for post-monitoring i.e. cloud intersection. All the instruments in the CARIBIC container are fully automated after the installation of the airfreight container into the aircraft cargo bay. The container automation is controlled by one master computer

which gives commands to the instrument dependent slave computers and microcontroller systems to control and start the measurements and sample collection. The instrument container is fitted with various safety measures, e.g. smoke detectors and temperature sensors. The pilots also have a manual kill switch to cut off the power to the complete CARIBIC container. Since the beginning of CARIBIC-2 in December 2004 until August 2018 428 flights have been carried out with the flying observatory, totaling up to flight distance of 3,514,038 km, which is nearly 9 times the mean distance to the Moon and total flight duration is 3,994 hours, equaling ~ 166 days of permanent flying. The average flight altitude of 10 900 m above the sea level (10 – 12 km range) of CARIBIC flights allow to study the processes in the lowermost stratosphere and upper troposphere (LMS/UT).

The second generation flying observatory (CARIBIC-2) flew on board the Airbus A340-600 from December 2004 until March 2016. There was a loading accident with the CARIBIC-2 airfreight instrument container in March 2016. This event halted the CARIBIC project, and thus the sample feed required for the analysis work for this PhD thesis until December 2017 when the newly built container with all the instruments in it was finally certified again for complete airworthiness. The refurbished CARIBIC atmospheric flying observatory container made its first successful flights in December 2017 between Munich and Seoul, and between Munich and Cape Town. That sums up to 21 months unplanned break of CARIBIC samples which required significant revision of the project planning of this PhD work.

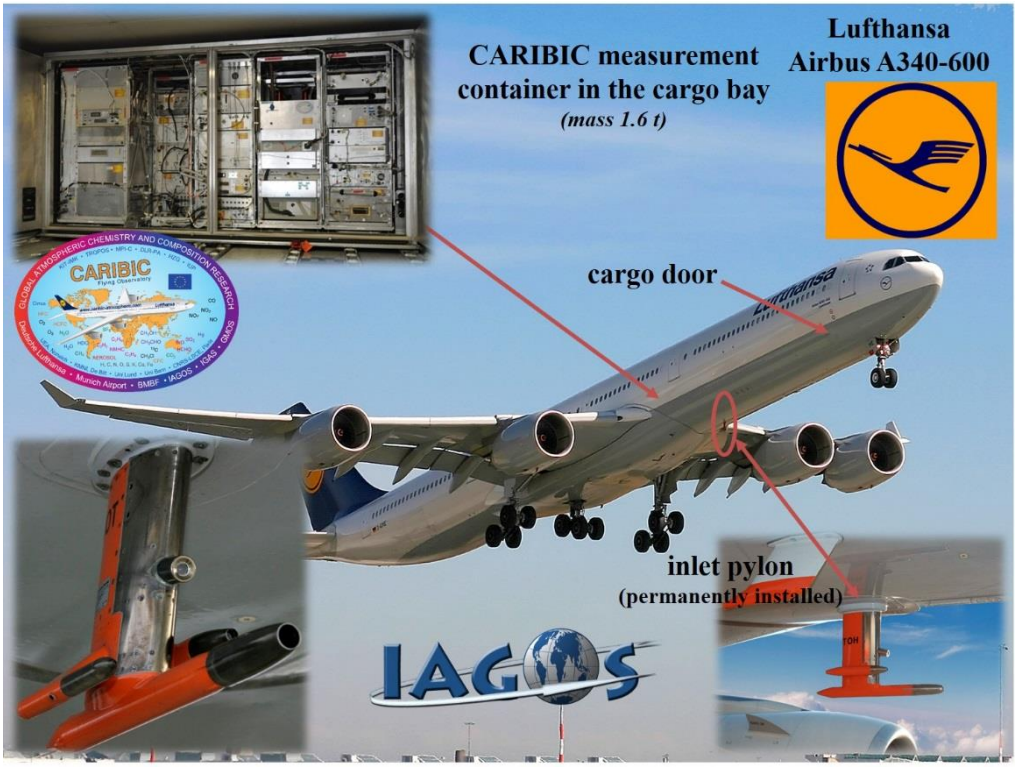

Figure 3.1 CARIBIC measurement container onboard Lufthansa Airbus A340-600.

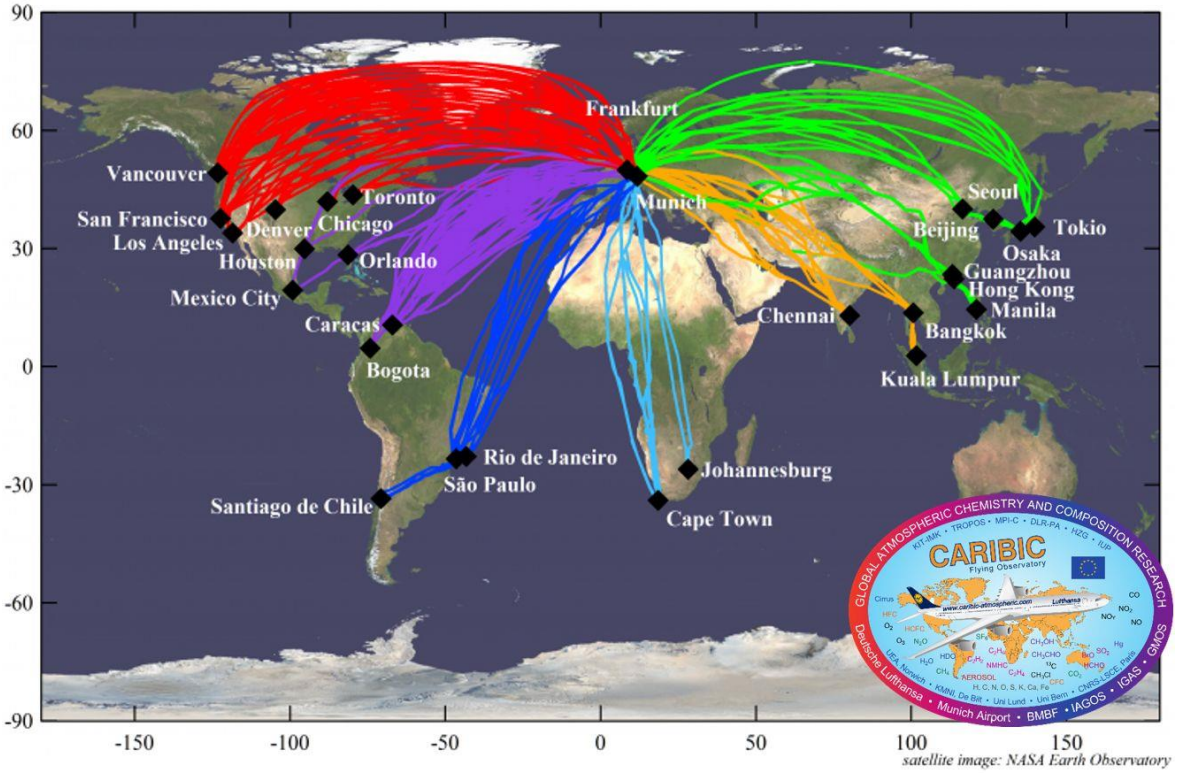

Figure 3.2 Global flight paths of CARIBIC-2 Lufthansa Airbus A340-600 aircraft. Home airport Frankfurt (Main), Germany until April 2014. After aircraft D-Check flights resumed in August 2014 with home base at Munich, Germany.

3.1.1 Typical CARIBIC flight schedule

One CARIBIC flight normally consists of 4 flight sequences. This means the instrument container is installed in the cargo bay and stays there for 4 flight sequences, e.g. from CARIBIC Lufthansa Airbus A340-600 home base at Munich, Germany to Los Angeles, USA and back, and directly after that from Munich to Tokyo, Japan and back. After the completion of the fourth flight the container is unloaded from the aircraft and transported to the Karlsruhe Institute of Technology (KIT). From there some individual instruments are transported from the KIT to other institutes. This includes the TRACs and HIRES whole air samplers which are transported back to MPIC in Mainz for the laboratory measurements. Nominally, 12 CARIBIC flights (48 flight sequences) take place during a year, 1 flight per month. In reality, the number is slightly smaller due to unexpected problems and difficulties. Flight booking for the CARIBIC Lufthansa A340-600 becomes more difficult and destinations less flexible as Lufthansa is gradually retiring all of its A340-600 fleet. CARIBIC flights are expected to stop with this aircraft in mid-2020, as one of the last aircraft replacements. After this the new generation of CARIBIC-3 container will be fitted to the

new more efficient Lufthansa Airbus A350-900 long haul aircraft primarily made of reinforced carbon fiber polymer.

Typically, during a monthly CARIBIC flight the first half of the HIRES whole air sampler (45 stainless steel samples) is filled during the first flight sequence, and during the second flight leg first TRAC (14 glass containers) is filled. With the third flight sequence the second half of HIRES is being filled (43 stainless steel samples), and with the fourth flight leg the second TRAC (14 glass containers). The sampling frequency is equally divided between each flight sequence distance and available number of samples.

On arrival at the MPIC GC laboratory, the two TRACs are first measured by the Entech-GC-AEDIII instrument developed during this PhD work. The NMHC and GHG system first measure the HIRES samples, followed by the Entech-GC-AEDIII as the latter instrument can deal with lower pressures in the sample containers.

As there are 6 replicates of TRAC samplers (always two loaded in the CARIBIC container), and the glass container volume is larger at 2.74 L (pressurized to ~ 4 bar absolute), there is enough sample air leftover to have a chance to rotate the TRACs samplers to collaboration partner laboratories. After the AEDIII, NMHC and GHG instrument measurements at the MPIC the TRACs are sent to UEA or MPI-BGC Jena for parallel halocarbon or GHG measurements, respectively.

3.1.2 Current CARIBIC instrumentations

With the newest IAGOS-CARIBIC-2 container rebuilding and payload modification there are currently 19 instruments integrated into the container, and around 100 trace species are being measured.

Ozone MRs measurements are based on two ozone sensors: OSCAR (Ozone Sensor CARIBIC), based on a dry chemiluminescence technique with 10 Hz resolution, and OMCAL (Ozone Monitor Calibrator) which is a modified UV absorption ozone analyzer used to calibrate OSCAR (Güsten *et al.*, 2003). Water vapor and water / ice content of clouds are analyzed by two H_2O analyzers with 10 s resolution, consisting of a two-channel Photoacoustic laser Spectrometer (PAS) and a chilled-mirror Prost-Point Hygrometer (FPH, CR2) (Zahn *et al.*, 2014). New IAGOS – CARIBIC PTR-MS with improved ion funnel guide for improved sensitivities, being able to measure acetone, acetonitrile, methanol, benzene, formaldehyde etc. (Brito, 2011). ISOWAT – compact tunable diode-laser absorption spectrometer for measuring water isotope ratios, $^{18}O/^{16}O$ and D/H (Dyroff, Fütterer and

Zahn, 2010). For post-flight lab analysis of NMHCs, GHGs, halocarbons, nitrogen / sulfur compounds and other VOCs 2 TRACs (Triggered Retrospective Air Collectors) consisting of 14 glass flasks each (Brenninkmeijer *et al.*, 2007) and 1 HIRES (High Resolution Sampler) consisting of 88 stainless steel flasks (Umezawa *et al.*, 2014) are integrated into the measurement container. These are automatically filled with air samples at the flight altitude. The TRAC and HIRES samples are analyzed for GHGs (Schuck *et al.*, 2009), NMHCs (Baker, Slemr and Brenninkmeijer, 2010), halocarbons (O'Sullivan, 2008; Leedham Elvidge *et al.*, 2015), nitrogen compounds (Sauvage, C. PhD thesis) and for sulfur compounds (this PhD work). The sample collection and analysis procedure of TRACs and HIRES will be further discussed in *Section 3.1.2.1* and *3.1.2.2*, as are of great relevance for the measurements and analysis presented here. CO is measured by a fast-response UV resonance fluorescence instrument (Model AL 5002, Aero-Laser, Germany). The CARIBIC CO instrument has a precision of 1 – 2 ppbv at a time frequency of 1 s (Scharffe *et al.*, 2012). Single Particle Soot Photometer (SP2, Droplet Measurement Technologies, Inc., USA) uses intracavity laser-induced particle incandescence to measure black carbon (BC, soot) mass in individual aerosol particles (Ditas *et al.*, 2018). Wideband Integrated Bioaerosol Spectrometer (WIBS, Droplet Measurement Technologies, Inc., USA) is used to measure fluorescent bioaerosol particles in the UT/LMS region. WIBS uses the single-particle elastic scattering strength at 535 nm to calculate the optical size of the particles (Yu *et al.*, 2016). CARIBIC AMS (Aerosol Mass Spectrometer) to measure chemical composition of nonrefractory particles in the 50 – 700 nm size range with few seconds time resolution. CARIBIC AMS is currently in final development stage (already integrated to the CARIBIC container), after optimizations particulate organics, SO_4, NO_3, NH_4, and Cl will be identified and quantified. CARIBIC OPSS (Optical Particle Size Spectrometer) based on a modified KS93 particle sensor (Rion Co. Ltd., Japan) measures the accumulation mode particle number size in the range of 130 – 1110 nm diameter (Hermann *et al.*, 2016). Combination of three Condensation Particle Counters in parallel (CPCs, TSI Inc. Model 7610, USA) modified for low-pressure conditions and aviation requirements are operated for the particle number concentrations with lower threshold diameters at 4 nm, 12 nm and 18 nm, for each CPC (Hermann and Wiedensohler, 2001). The NO and NO_y measurements are performed using a two-channel cooled chemiluminescence detector (Model SR 79501, Eco Physics, Switzerland) with ~ 1 s integration time. NO_2 can be measured in combination with a photolytic converter (Stratmann *et al.*, 2016). The new CARIBIC DOAS (Differential Optical Absorption Spectroscopy) consisting of 3 temperature stabilized (± 0.05°C) spectrometers which are connected to the CARIBIC inlet pylon via quartz fiber bundle. New

CARIBIC DOAS measures in the 297 – 452 nm wavelength range with 0.6 nm spectral resolution, and MRs of NO_2, SO_2, BrO, HCHO, HONO, O_3, O_4, IO and glyoxal are measured. DOAS instrument takes a full spectrum every 8 s but for noise reduction 10 spectra are co-added, resulting in a temporal resolution of ~ 80 s. With the aircraft speed of ~ 250 m s^{-1}, it corresponds to ~ 20 km spatial resolution (Walter *et al.*, 2012). IAGOS-CORE Aerosol Package (Package 2, option c, P2c) is designed to measure the aerosol number concentration of the total and the non-volatile particles via CPC measurements, and the aerosol size distribution is measured by an Optical Particle Counter (OPC) in the diameter range of 0.25 – 3 µm. The time resolution for the IAGOS-CORE P2c is 4 s (spatial resolution ~ 1 km) with precision of ± 10 and ± 5 particles cm^{-3}, respectively for each instrument (Bundke *et al.*, 2015). CARIBIC GHG instrument is based on Cavity Ring-Down Spectroscopy (CRDS) commercial instrument (Picarro Model G2301-m, USA) and was repacked to new rack to fit into the CARIBIC container. The CARIBIC GHG instrument will measure CO_2 and CH_4 with approximately 0.13 ppmv and 1.3 ppbv uncertainty determined from lab studies (Filges *et al.*, 2015). The Picarro instrument was newly integrated to the CARIBIC set-up, and final adjustments and optimizations are being currently made. CARIBIC 16-channel aerosol sampler collects aerosol filters with an impaction technique. The flow rate for sampling is 10.4 L min^{-1}. Each channel consists of two sample types, which are used for post-flight quantitative lab measurements employing Particle-Induced X-ray Emission (PIXE) and single particle analysis with Electron Microscopy (EM). LODs with PIXE instrument after 1.5 h sampling are 2.0, 0.14 and 0.02 ng m^{-3} for sulfur, potassium and nickel, respectively (Nguyen, Gudmundsson and Martinsson, 2006). Meteorological support for CARIBIC project is computed by KNMI utilizing the European Centre for Medium-Range Weather Forecasts (ECMWF) model. 5-day and 8-day backward trajectories are calculated. Furthermore, potential vorticity (PV), static and dynamic tropopause height and pressure, potential temperature, wind speed and direction, relative humidity and cloud cover are calculated by ECMWF model (van Velthoven, 2018). The new CAvity Ring-Down Instrument for the detection of Nitrogen Oxides (CARDINO) is based on CRDS and will measure NO_2, NO_3, N_2O_5 and O_3 MRs simultaneously. The CARDINO measurements are based on 4 specialized optical cavities (~ 44.1 cm, expected path length ~ 176 km). Two cavities are operated at NO_2 maximum absorption wavelength (405 nm) and two other at NO_3 maximum absorption wavelength (662 nm). The inlet to one of the 662 nm cavity is heated to thermally decompose N_2O_5 completely, thus the sum of NO_3 is measured. N_2O_5 MR is directly determined from the difference to an unheated NO_3 channel. One of the NO_2 cavity channel is continuously

flushed with NO to measure O_3 MR via quantitative conversion to NO_2. CARDINO has data acquiring time resolution of 1 s for the nitrogen oxides and 1 min for O_3 measurements. The lab based test yielded preliminary LODs of 25 pptv for NO_2, 0.8 pptv for NO_3, 1.0 pptv for N_2O_5 and 5 pptv for O_3 (Goulette *et al.*, 2016). *Table 3.1* summarizes the employed instruments, institutes and the PIs.

Table 3.1 Current instruments integrated into the CARIBC flying observatory container with the abbreviations of the institutes and principal investigators. Data from underlined instruments were used for analysis in this chapter of the thesis.

Institute		Instruments (19)	PI
KIT		O_3, H_2O, new PTR-MS, ISOWAT	Zahn / Bönisch
	Lelieveld	2 TRACs, HIRES, CO	Williams
MPIC	Pöschl	SP2, WIBS	Cheng / Su
	Bormann	Aerosol Mass Spectrometer	Schneider
TROPOS		OPSS, CPCs	Hermann
DLR		NO, NO_2, NO_y	Ziereis
IUP		DOAS	Friess
FZJ		IAGOS-CORE Package-2c	Petzold / Bundke
MPI-BGC		Picarro (CO_2, CH_4)	Gerbig
Lund		Aerosol filter sampler	Martinsson
UEA		Halocarbons, VOCs in TRACs	Oram
KNMI		Meteorological support	v. Velthoven
Uni Cork		CRDS (NO_3, N_2O_5, NO_2, O_3)	Ruth
NOAA			Brown

3.1.2.1 WAS sampling with TRACs and HIRES system

Collecting air samples is a classical but powerful method for performing more complex post-flight lab analysis, especially for species which are difficult to measure in-situ. These species are, for example, hydrocarbons, especially the shorter chained alkanes / alkenes (C2 – C4) and their derivatives, halocarbons, nitrates, organosulfur compounds and isotope composition measurements. Limitations of air sampling include low sample time (spatial) resolution and the analytes must be sufficiently stable in the canisters.

The whole air samples (WAS) are collected with two Triggered Retrospective Air Collectors (TRACs). Each TRAC consists of 14 specially manufactured glass vessels by Louwers Hapert Ltd., Netherlands (2.74 L, 45 cm length, 10 cm outer diameter, 5 mm wall thickness) from borosilicate glass (Schott AG, Germany) and rated for an absolute pressure of 7 bar. Glass vessels are more difficult to construct and handle due to their fragileness, but have a significant advantage thanks to their inertness towards analytes. TRACs have an inlet and

an outlet port, and two multiposition (16-position) Valco valves (VICI Valco Instruments Co. Inc., Switzerland) are used to switch between each canister's inlet and outlet. The vessels are covered with a protective polymer liner and housed inside a metal structure within a rack of 14. The inlet and outlet ports are connected with sample vessels via stainless steel tubing through the VICI multiposition (MuPo) valves leading into the vessels with cemented (Araldite 2020, Vantico AG, Switzerland) line endings. Prior to sampling the air in the TRAC canisters is replaced ~ 10 times by continuously flushing with air from the aircraft trace gas inlet pylon. After flushing ~ 9.5 – 11 L STP (vessels nominally at 4 bar) of sample is collected to each glass canister within short time (~ 1 min, giving ~ 15 km spatial resolution), which often allows to resolve synoptic scale features, like tropopause folds, boundary layer detection, rapid convective uplift from lower altitudes and biomass burning plumes. The sampling takes place at equally distanced preprogrammed regular intervals, and is initiated by outside pressure of 600 mbar trigger. The sampling end cutoff pressure is set to 700 mbar as a contamination safety for the case where not all the preprogrammed regular sampling intervals do not equal the flight distance. In total there are 6 TRAC replicates for enabling sample rotation between international collaboration labs, whereas always two TRACs must be integrated to the CARIBIC container for container integrity and completeness. Each TRAC unit weighs ~ 69 kg and is fitted into 62 × 36 × 60 cm (length × height × depth) aluminum case. The TRAC and HIRES sampling is fully automated by V25 microcontroller system (Brenninkmeijer *et al.*, 2007; Baker, Slemr and Brenninkmeijer, 2010).

Since 2010 WAS are also collected with High Resolution Sampler (HIRES), which consists of 88 stainless steel canisters (1.0 L), which significantly increased the sampling resolution and data coverage along the flight tracks. The construction principle is the same as for TRACs, but instead of a separate inlet and outlet port it has a single connection port. Thus, flushing takes place via pressurizing the canisters and then releasing the pressurized air again. HIRES is fitted with 6 16-position MuPo valves for trapping the 88 samples, while the last MuPo has 3 blind positions instead of 1 as the all other HIRES MuPo valves. The size of the HIRES is 54×36×59 cm (length×height×depth) and is also fitted in an aluminum case. Integrating the HIRES into CARIBIC container together with 2 TRACs increased the number of WAS nominally from monthly 28 samples to 116 samples. TRAC and HIRES samplers are depicted in *Figure 3.3*.

Ozone is quenched in the sampling stage in the two metal bellow pumps (Model PWSC 28823-7, Senior Aerospace Inc., USA) which are typically at 50°C temperature. The first

pump has the two bellows in parallel as a first stage, and the second pump has the bellows in series as the second and the third stage to pressurize the air from outside at 200 – 250 hPa pressure to nominally about 4 bar absolute pressure into the flasks (Brenninkmeijer *et al.*, 2007).

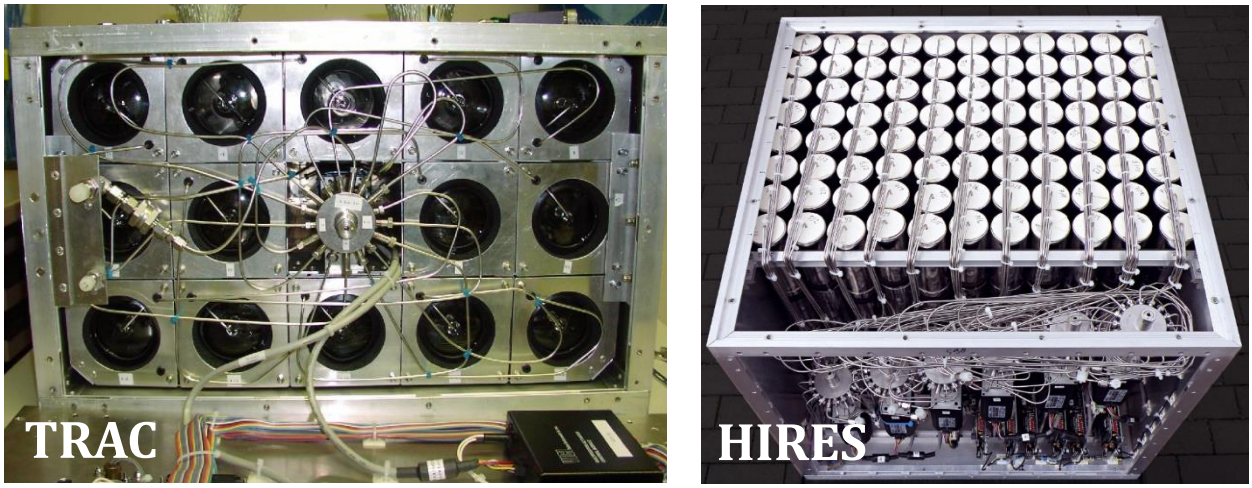

Figure 3.3 Photos showing inside TRAC (14 glass flasks) and HIRES (88 stainless steel flasks) CARIBIC WAS samplers.

3.1.2.2 Post-flight CARIBIC TRAC and HIRES WAS analysis

GHGs in the TRACs and HIRES are measured at the MPIC by gas chromatography, involving direct injection of the air sample from the flasks onto the GC column without any previous pre-concentration. Gas chromatograph (Hewlett-Packard Model 6890, USA) equipped with two detectors. First detector is Flame Ionization Detector (FID) for measuring CH_4 and CO_2 MRs, second detector is mini Electron Capture Detector (mECD) for measuring N_2O and SF_6. It is automated to measure the calibration gases and the CARIBIC samples in a sequence. Duration on a measurement cycle is 12 min. The GC oven is shared with separate columns for FID and mECD detectors. Sample air is collected on 10 ml and 15 ml loops for FID and mECD channel, respectively. The FID channel is fitted with a packed Porapak Q column (3 m length, 100/120 mesh). Methane is detected directly by FID, but after 3.9 min GC runtime a valve is switched which guides the sample air through a methanizer where CO_2 is converted to CH_4 with H_2 over nickel catalyst, and then a methane peak from CO_2 is detected again. For the mECD channel two columns are required for the separation of N_2O and SF_6. A Porapak Q (1.8 m, 80/100 mesh) packed column and a HayeSep Q (1.8 m, 80/100 mesh) column are employed in series. Each CARIBIC sample is measured 4 times with consecutive injections. After the analysis, the 4 data points for each compound's MR are averaged and standard deviation is used for precision calculations. The typical precisions obtained on the GHG system for 0.17% for CH_4, 0.08% for CO_2, 0.15%

for N_2O and 1.5% for SF_6. The analysis of 2 TRACs (28 samples) takes ~ 48 h, within this timeframe small changes in lab pressure and temperature can occur, which can affect the sensitivity of the detectors. Between every sample 3 working standard (pressurized ambient air) samples are analyzed and the detector drifts can be corrected thereafter. Before every CARIBIC flight sample analysis, the GHG system is calibrated with 6 different NOAA ESRL ambient air calibration standards, which are certified for CH_4 (adjusted CMDL83 scale), CO_2 (WMO-X2007 scale), N_2O (NOAA 2006 scale) and SF_6 (NOAA 2006 scale) MRs (Schuck *et al.*, 2009).

Non-methane hydrocarbons (NMHCs) from C_2 – C_8 compounds (e.g. from ethane to xylenes) are measure on a separate GC-FID system. It is also based on a HP 6890 GC-FID (Hewlett-Packard, USA) coupled with an in-house built pre-concentration system based on liquid nitrogen as trapping cryogen. Furthermore, also the GC oven is cooled to -10°C temperature at the beginning of each chromatographic run for good C_2 (ethyne, ethane and ethane) separation. The pre-concentration unit is fully automated by V25 microcontroller system, which also controls the TRAC and HIRES sample position. The pre-concentration system consists of a magnesium perchlorate ($Mg(ClO_4)_2$) drying tube to remove water from the samples, stainless steel cryotrap loop (1/8″ (3.2mm), 15 cm long) filled with Carbopack BHT adsorbent (mesh 60/80) held above liquid nitrogen dewar, maintained at -131°C with coiled heating wire. The last phase is a cryofocusing loop based on a looped empty (without stationary phase) capillary column (175 cm long), and 30 cm part of the looped column is submerged into liquid nitrogen. Trapping temperature of -131°C is sufficiently cold to trap the NMHCs of interest, whereas the major constituents of air, like N_2, O_2, Ar and minor constituent CH_4 are almost completely removed during the trapping process. After mobilizing and equilibrating the sample from the main trapping loop to the cryofocusing loop, the cryofocusing loop is lifted from the immersed liquid nitrogen to the ambient lab temperature, which initiates the injection onto GC column and starts the GC temperature and pressure program. During the 20 min CARIBIC sample trapping process, 1.0 L air is trapped (at flow of 50 ml min^{-1}). Due to a large sample volume requirement, only one sample measurement is conducted from each canister. The separation of the compounds takes place in the GC oven on a long 150 m Supelco Petrocol DH 150 (0.25 mm inner diameter, 1.00 µm film thickness, Sigma-Aldrich Inc., USA) capillary column. The pre-concentration and GC carrier gas is extra ultra-high purity H_2 (purity > 99.99999%, Parker Balston Hydrogen Generator model H2-300, Parker Hannifin Corporation, USA). The total sample pre-concentration time with all the separate stages, back flushing and bake out included is 60

min, also the GC run duration is 58 min, whereas next sample will be already preconcentrated in parallel with the GC run to shorten the total analysis time. For calibrating the CARIBIC NMHC GC-FID system, at the beginning of each TRAC and HIRES MuPo valve (at the beginning of each 14 samples for TRACs and at the beginning of each 15 samples for HIRES) analysis sequence a zero-air blank, ambient air working standard and a 30 component ozone precursor NMHC NPL Primary Reference Standard (National Physical Laboratory, UK. See *Table 6.2* in *Appendix*) sample is measured before the CARIBIC WAS samples. The 8 NPL standard sample response factors are averaged for each compound of interest and used for calculating CARIBIC WAS MRs. The working standard is used to monitor the stability and drift of the system (Baker, Slemr and Brenninkmeijer, 2010).

The measurement principle with Entech-GC-AEDIII as explained in detail in *Chapter 2* is applied to measure CARIBIC TRAC and HIRES whole air samples. At the beginning of each measurement sequence, 2.0 m long sample line (Silcosteel, outer diameter 1/16″ (1.59 mm), inner diameter 0.040″ (1.02 mm), volume 1.62 mL, Restek Corporation, USA) is connected to a TRAC or HIRES sampler port, and a leak check is conducted via evacuating the connected sample line to ~ 3.0 psi (0.21 bar) with the Entech pump system. After the pressure stabilization in the line, a leak check is carried out for 3 min. If the pressure reading is less than ± 0.5 psi (0.03 bar) different, which is in the precision range of the pressure gauge, the line is considered leak tight. After the leak check the Entech traps M1 and M2 are baked out at 150 ºC and 220 ºC, respectively for 20 min. The measurement sequence starts with calibration standard measurements, the first sample of each calibration standard is used for pre-purging the standard lines and are excluded in the MR calculations. Three independent gas phase calibration standards are used for calibrating the system: an 84 component Apel-Riemer-2015, 30 component NMHC ozone precursor NPL-2017, which were described earlier and also a NOAA Earth System Research Laboratory 2017 ambient air primary standard is used (National Oceanic and Atmospheric Administration, Earth System Research Laboratory, Global Monitoring Division, USA). NOAA-2017 standard is compressed into aluminum gas cylinder with Aculife internal coating for extra inertness (Scott Specialty Gases, USA. Now Air Liquide America Specialty Gases, USA). NOAA-2017 standard was filled at Niwot Ridge, Colorado, USA in April 2017 and is certified for VOCs listed in *Table 3.2*. During CARIBIC measurements, 1,400 mL WAS and calibration standards are preconcentrated in order to have exactly the same conditions and to thereby minimize the uncertainty. The only exception is NPL-2017 standard where 50 mL of undiluted calibration standard is preconcentrated. In each measurement sequence, first a

zero-air blank (same zero-air as described above for NMHC GC-FID) is measured, followed by diluted Apel-Riemer-2015 calibration standard (5 mL min^{-1} of calibration gas in 1 L min^{-1} zero-air, giving ~ 250 pptv MR), followed by 50 mL NPL-2017 primary standard (giving related MR of ~ 280 pptv for 1,400 mL samples), followed by NOAA-2017 primary ambient air calibration standard. After standard measurements, CARIBIC WAS measurements take place with NPL-2017 and NOAA-2017 standards in between each 5 CARIBIC samples. The high number of standard measurement improves the precision of the analysis and allows the calculation of the measurement standard deviations for the uncertainty determination. Furthermore, instrumental drift is analyzed and corrected if necessary. The MRs of the analytes are calculated using the individual RFs determined from averaged calibration standard measurements. Furthermore, the complete AEDIII raw spectra in the measurable 161 – 211 nm wavelength range is recorded during all CARIBIC measurements and stored on the CARIBIC data archive server. Despite the large file size of each sample (3.7 GB), summing up to 686 GB hard disk space for each full CARIBIC container flight (4 flight sequences), this data provides an opportunity to analyze other elemental emission lines after the measurement if a compound of interest is being found at a later point in the future.

Table 3.2 NOAA ESRL year 2017 ambient air primary gas reference standard. Gas cylinder serial number CC470932.

Compound	MR [pptv]	Uncertainty [pptv]	NOAA scale year
OCS	534.9	1.6	2004
CH_3Cl	614.6	1.9	2003
CH_3Br	7.2	0.1	2003
HCFC-141b	25.6	0.1	1994
HCFC-142b	22.8	0.1	1994
HFC-134a	97.8	0.2	1995
HCFC-22	247	0.4	2006

3.2 Carbonyl sulfide CARIBIC measurements

During the Entech-GC-AEDIII measurements the lab temperature and pressure were logged. In total, data for 708 AEDIII OCS samples from HIRES and TRACs were obtained in the time frame from December 2015 until December 2018. A map overview of these carbonyl sulfide MR is shown in *Figure 3.4* and *Figure* 3.5. Total of 1,183 UEA OCS samples from October 2006 until December 2015, MRs range from 6.5 – 772 pptv are available. For the

data analysis and overview plots within this thesis the UEA data was filtered. All UEA OCS data points > 550 pptv and < 300 pptv were considered as outliers. With this filter applied the total number of 1,090 UEA OCS samples were included in the analysis, which are depicted in *Figure 3.6* and *Figure* 3.7.

3.2.1 Effect of water in sample canisters

Most of the samples are collected during cruising flight altitude of 8.5 to 12.5 km. The sampling of the trace gas samples into canisters takes place perpendicular to the flight direction from the specially built permanently installed inlet pylon, which itself is parallel to the flight direction. The forward facing inlet orifice of the pylon is 16 mm in diameter and the outlet rear orifice is 12 mm in diameter (Schuck *et al.*, 2009). The saturation pressure of water in the lab at 21°C is 24.9 mbar, assuming around 4 bar pressure in the canisters, even high water vapor content of 5000 ppmv is still under the saturation point (~ 80%, vapor pressure 20 mbar). The average CARIBIC 2 water vapor integral for TRAC and HIRES samples until flight 528 is 247 ppmv (4.0% relative humidity), the corresponding median being 135 ppmv (2.2% relative humidity) (Wexler, 1976; Buck, 1981). As the water is effectively removed in Entech's first water removing module, only around 0.2 – 0.3 µl in total is injected into the GC column. Therefore, from Entech-GC-AEDIII measurements the dry mixing ratios are directly determined.

Table 3.3 CARIBIC instrument container flights where OCS data was obtained with AED instrument. Letter G corresponds to samples from TRAC glass flask sampler, SS to samples from HIRES stainless steel container WAS sampler.

Date [UTC]	Flight no.	From	To	No. of OCS samples
01/12/2015	526	Cape Town	Munich	14 G
02/12/2015	527	Munich	São Paulo	4 SS
02/12/2015	528	São Paulo	Munich	14 G
13/01/2016	530	Cape Town	Munich	14 G
14-15/01/2016	532	São Paulo	Munich	14 G
14-15/02/2016	533	Munich	Cape Town	23 SS
15/02/2016	534	Cape Town	Munich	14 G
16-17/02/2016	536	São Paulo	Munich	14 G
14/03/2016	CARIBIC container accident at Munich Airport, 21 months break			

11-12/12/2017	537	Munich	Seoul	38 SS
12/12/2017	538	Seoul	Munich	14 G
12-13/12/2017	539	Munich	Cape Town	39 SS
13/12/2017	540	Cape Town	Munich	14 G
25/01/2018	542	Munich	Cape Town	14 G
26/01/2018	543	Cape Town	Munich	42 SS
22/03/2018	544	Munich	Denver	39 SS
22/03/2018	545	Denver	Munich	14 G
15/05/2018	546	Munich	Mexico City	32 SS
16/05/2018	547	Mexico City	Munich	14 G
17/05/2018	548	Munich	Tokyo	42 SS
18/05/2018	549	Tokyo	Munich	14 G
29/07/2018	550	Munich	Tokyo	45 SS
30/07/2018	551	Tokyo	Munich	14 G
30/07/2018	552	Munich	Shanghai	41 SS
31/07/2018	553	Shanghai	Munich	14 G
08/10/2018	554	Munich	Shanghai	44 SS
09/10/2018	555	Shanghai	Munich	14 G
10/10/2018	556	Munich	San Francisco	1 SS
11/10/2018	557	San Francisco	Munich	14 G
04/12/2018	558	Munich	Shanghai	44 SS
05/12/2018	559	Shanghai	Munich	14 G
06/12/2018	560	Munich	Los Angeles	41 SS
07/12/2018	561	Los Angeles	Munich	13 G

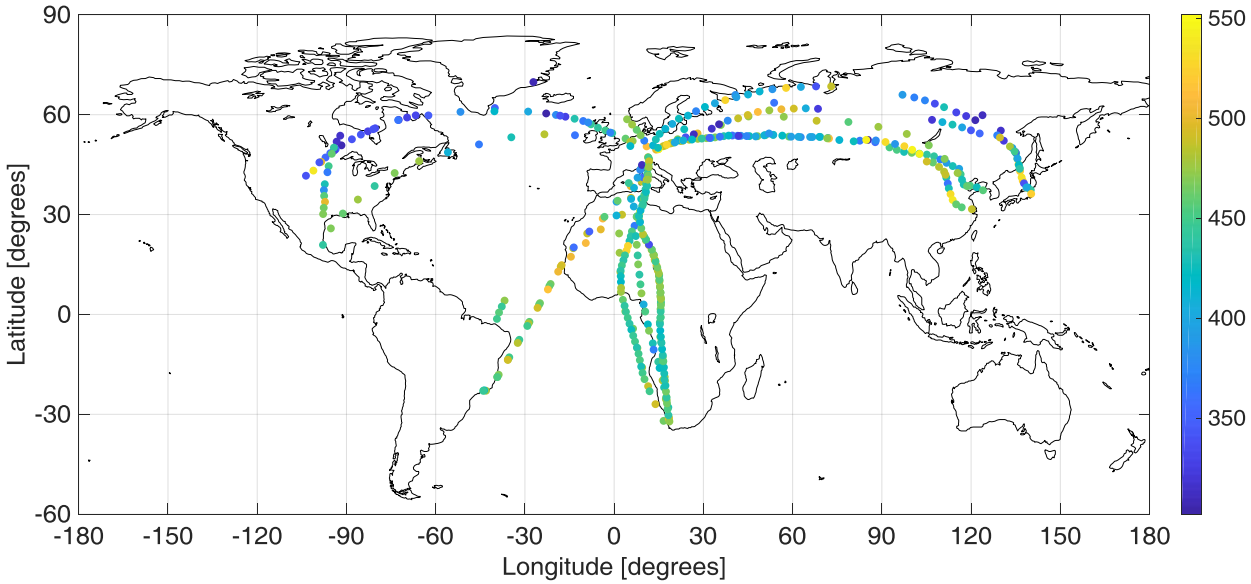

Figure 3.4 Global overview of CARIBIC MPIC Entech-GC-AEDIII OCS measurement data. Color coded circles represent OCS MRs [pptv].

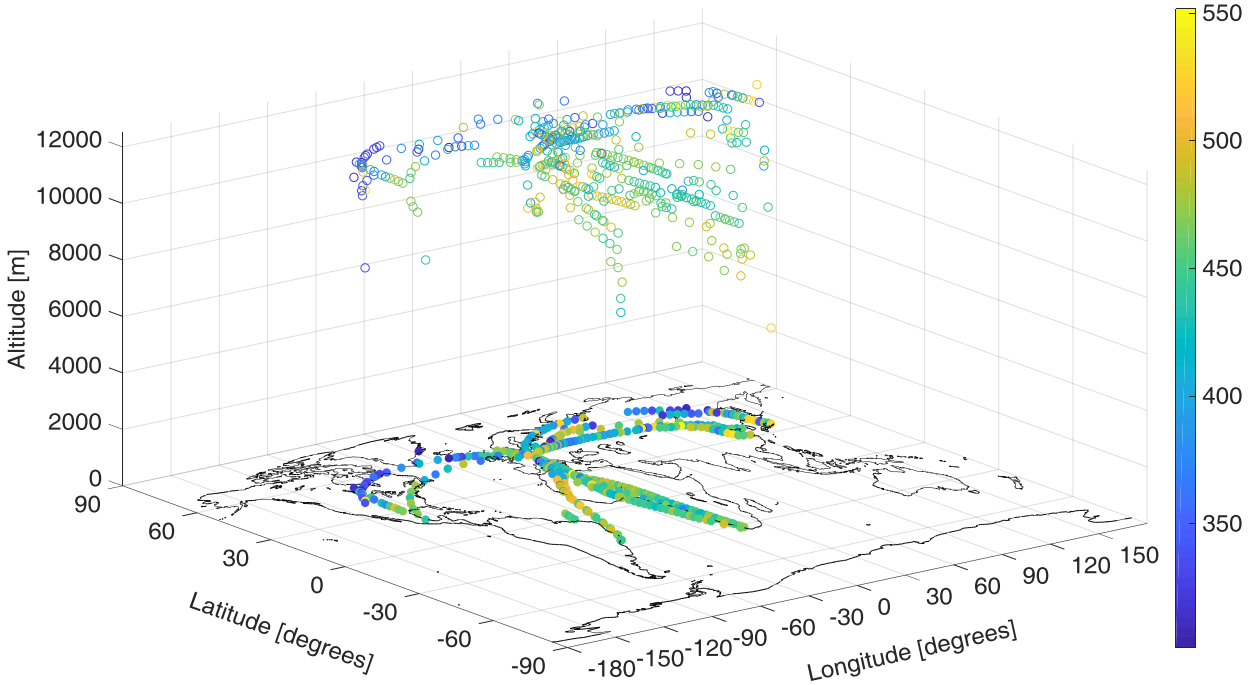

Figure 3.5 3D representation of global CARIBIC MPIC Entech-GC-AEDIII OCS measurement data. Z-axis denotes the flight altitude where the sample was collected. Color coded circles represent OCS MRs [pptv]. The *Figure 6.3* in *Appendix* represents the same graph with pressure for z-axis.

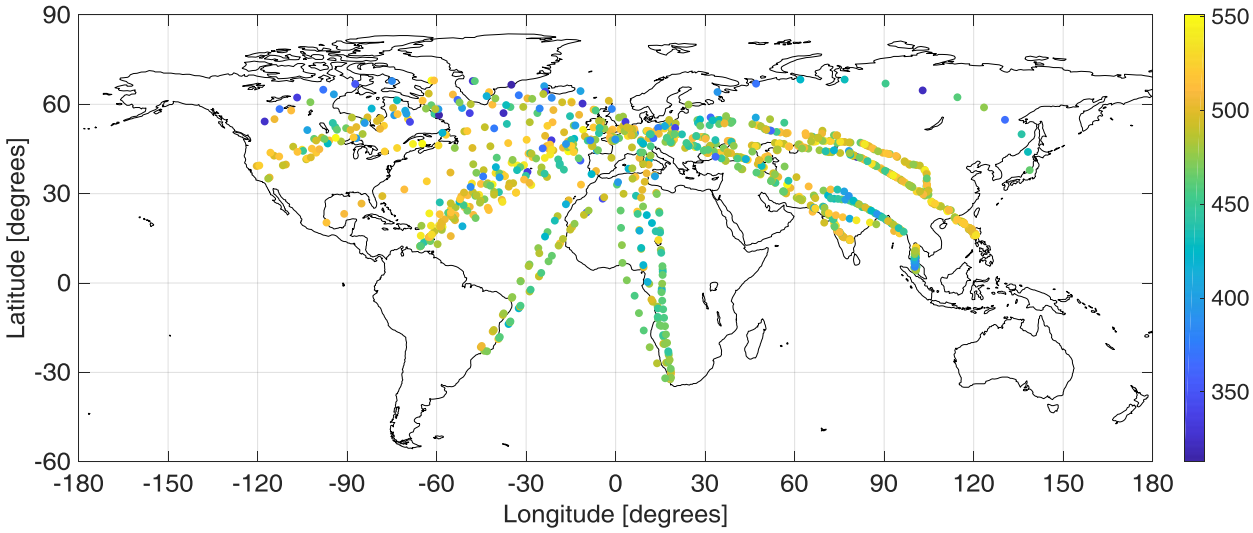

Figure 3.6 CARIBIC global flight paths. Color coded circles represent OCS MRs [pptv] collected with TRAC samplers and analyzed by UEA from October 2006 until December 2015.

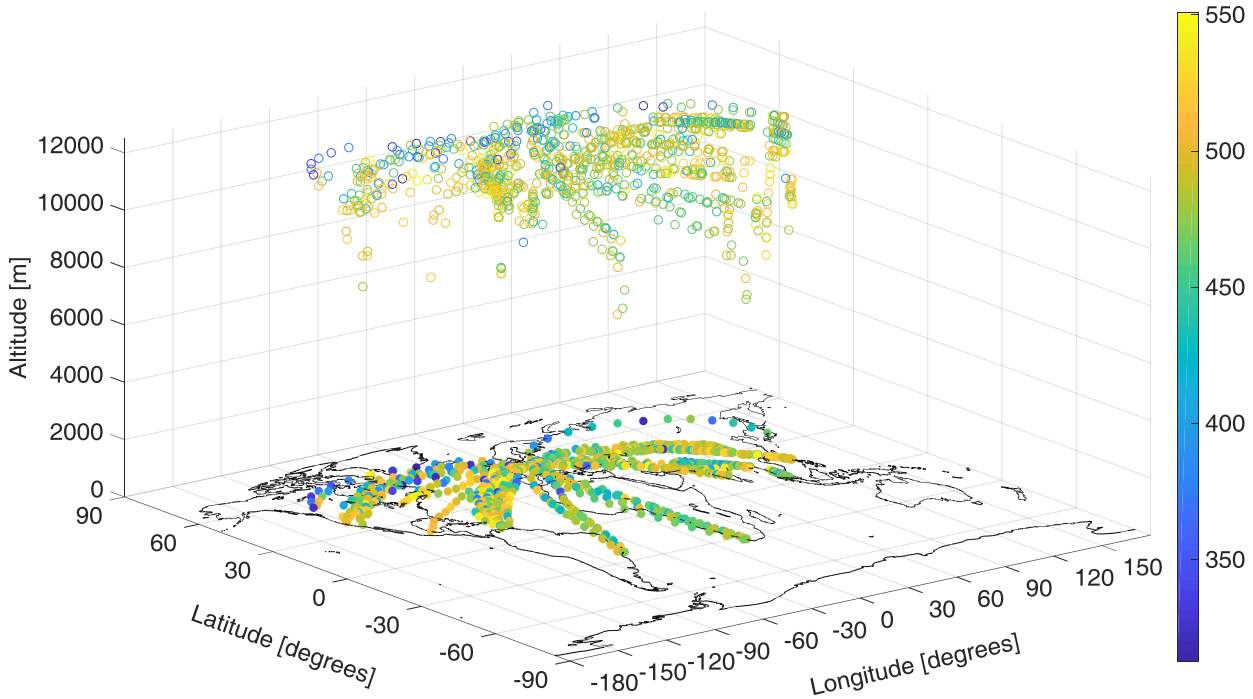

Figure 3.7 3D graph of OCS MRs [pptv] collected with TRAC samplers on board CARIBIC aircraft and analyzed by UEA. The *Figure 6.4* in *Appendix* embodies the same graphs with pressure for z-axis.

3.3 OCS flux estimation to the stratosphere

An important aspect of the OCS budget is the flux from the troposphere to the stratosphere. The CARIBIC dataset, often collected near to the tropopause region is well suited to constrain this flux. Murphy and Fahey in 1994 used observed correlations of N_2O and NO_y/O_3 to calculate the globally averaged net downward transport of reactive nitrogen (NO_y) and ozone from stratosphere to troposphere through the tropopause. The linearity of observed tracers with N_2O in the lowermost stratosphere allows calculation of the downward or upward flux of a long-lived tracer. The photochemistry of nitrous oxide in the stratosphere is well studied, the destruction rate of N_2O in the stratosphere is relatively well known and as there are no significant sinks in the troposphere, therefore the destruction rate of N_2O in the stratosphere equals the total emission rate (Murphy and Fahey, 1994). A negative slope represents a downward flux from the stratosphere to troposphere, and positive slope represents upward flux. The great advantage of this approach is that a detailed knowledge of the UT – LMS exchange processes is not required in order to estimate the net global annual flux. The theoretical concept was derived by Plumb and Ko in 1992 who reasoned that pairs of long-lived atmospheric species consistently display simple linear relationships in the LMS, so that the measured mixing ratios of one species can be used to predict the other. The requirement here is a sufficiently long enough lifetime of the tracers. They argued that species whose local lifetimes are longer than quasi-horizontal transport time scales (~ 1 year) are in climatological slope equilibrium. Furthermore, for species whose atmospheric lifetimes are determined by removal in the stratosphere, their linear relationship slope in the LMS can be related to their ratio of atmospheric lifetimes (Plumb and Ko, 1992).

3.3.1 OCS flux estimation to the stratosphere, method based on CARIBIC observational data

Therefore, it could be postulated that simultaneous CARIBIC observations of OCS and N_2O and the linear correlation between these tracers would allow estimation of the carbonyl sulfide global upward flux from the troposphere to stratosphere. Therefore, the same approach which was applied by (Murphy and Fahey, 1994) on NO_y and O_3 was also applied on OCS data for the stratospheric flux and lifetime calculations.

The derivation of the theoretical equation by (Plumb and Ko, 1992; Murphy and Fahey, 1994) shows that observed OCS vs N_2O correlation slope (m) can be used to derive the OCS flux (ϕ_{OCS}) through the relationship described with *Equation 3.1*, where S_{N2O} is the annual

global average stratospheric sink of N_2O. M_S and M_{N2} are the molar masses of sulfur and two nitrogen atoms, respectively.

$$\phi_{OCS} = m \times S_{N2O} \times \frac{M_S}{M_{N2}} \quad (3.1)$$

Since the slope between OCS and N_2O is positive, *Figure 3.11*, the flux goes in the same direction as N_2O, i.e. from the troposphere to stratosphere. The convention here is that S_{N2O} is negative, thus also ϕ_{OCS} will be negative. According to mass balance conservation theorem it can be said that if two long-lived tracers are observed to have tight correlation, then they should be linearly related. Curvature in a tightly correlated scatter plot could indicate species accumulation in the atmosphere or chemical processing by one or both species.

The slope (m) in *Equation 3.1* is the net number of OCS molecules flowing to stratosphere per N_2O molecule with unit pptv ppb^{-1}. The unit used here for S_{N2O} flux is in Tg (N) yr^{-1}. The total stratospheric sink of OCS (ϕ_{OCS}) is Gg (S) yr^{-1} (note that the factor of 1,000 difference for Tg (N) yr^{-1} to Gg (S) yr^{-1} rises from the slope m unit pptv $ppbv^{-1}$).

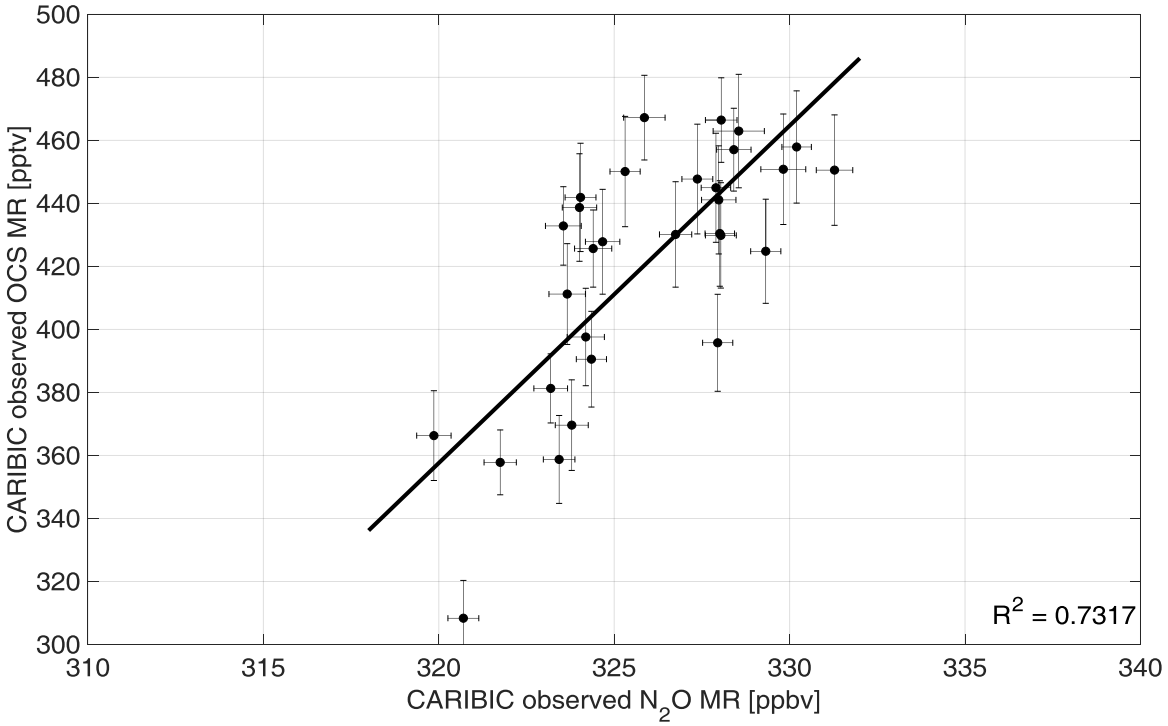

Figure 3.8 Example plot of an orthogonal fit of N_2O vs OCS with 1σ uncertainty error bars from flight 537 (December 2017).

3.3.2 Orthogonal correlation between N_2O and OCS

For a tracer-tracer correlation in atmospheric sciences an orthogonal fit (total least squares) should be used as both trace species have an uncertainty associated to their measurement value (Cantrell, 2008). Thus, also for the slope calculation between N_2O and OCS trace species an orthogonal correlation was used to take into account both species uncertainty values. The regular square fit produces unsuitable slope and intercept results as it assumes uncertainty free x-axis.

3.3.3 Total yearly N_2O emissions / destruction rate

Current combined global average MR of N_2O on the ground level is 331 ppbv (July 2018, on NOAA 2006A scale) from combined (13 global measurement stations) background nitrous oxide data from the NOAA/ESRL Global Monitoring Division measurement programs. NOAA/ESRL has measured a steady state increase in N_2O concentrations since 1977. The global average nitrous oxide MR growth rate per year from 2000 – 2017 was 0.84 ppbv yr^{-1}, and for more recent 2012 – 2017 years the corresponding growth rate was 0.95 ppbv yr^{-1}, which is ~ 14% larger than the previous timespan (data from NOAA/ESRL HATS group). The data is represented by *Figure 3.9* (NOAA/ESRL HATS 2018).

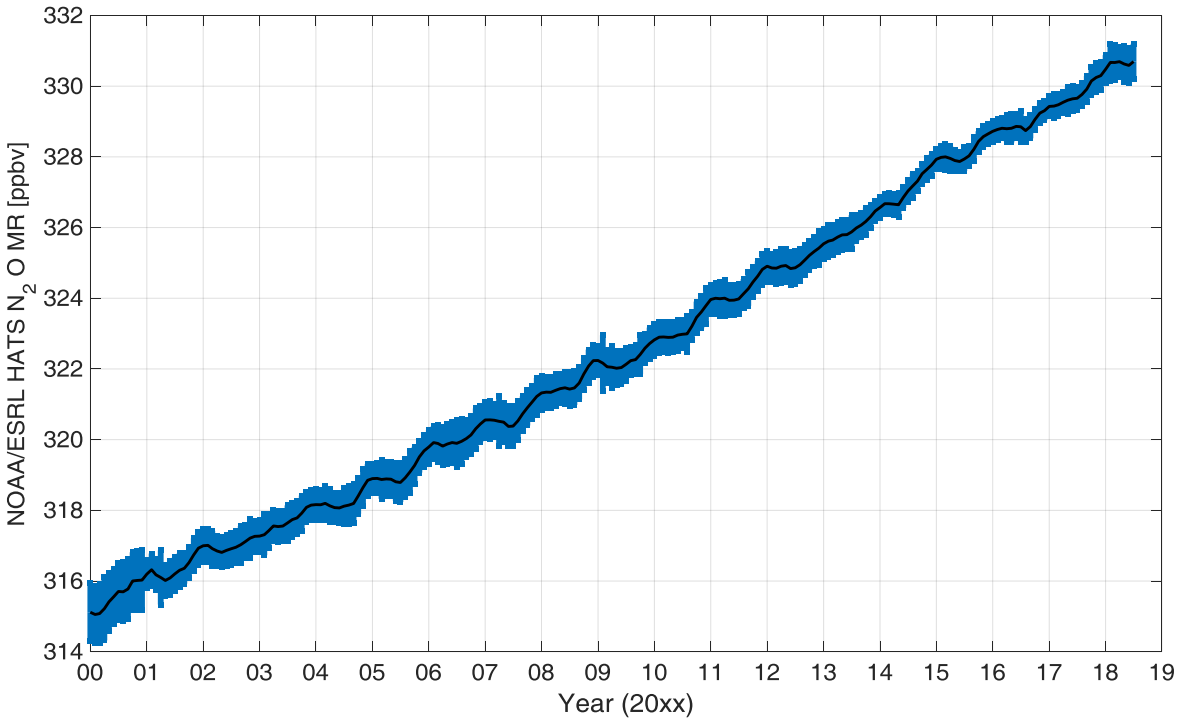

Figure 3.9 National Oceanic and Atmospheric Administration Earth System Research Laboratory (NOAA/ESRL) Combined Global Halocarbons & other Atmospheric Trace Species Group (HATS) global monitoring station (13 stations) monthly average N_2O MRs showing steady increase year by year. Error bars (blue shadow) show 1σ uncertainties. Courtesy of NOAA *Elkins et al.*, August 2018.

The nitrous oxide emissions can be derived from the global N_2O sink strength, which is the burden and lifetime plus the rate of increase in the burden, as no significant vertical gradient can be seen in the troposphere (Houghton *et al.*, 2001). Also, the relationship can be used *vice versa*. The main sink is in the stratosphere, where the main destruction of N_2O takes place, mostly by reaction with $O(^1D)$ radical above 25 km height (Ko, Sze and Weisenstein, 1991). The yearly accumulation of N_2O in the atmosphere (~ 0.3% yr^{-1}) is not significant enough to interfere with the tracer flux estimation into or out of stratosphere (Murphy and Fahey, 1994). Several different studies have estimated the nitrous oxide stratospheric destruction rate, which are shown in *Table 3.4*. For the OCS flux estimation into the stratosphere, calculation using *Equation 3.1*, average N_2O flux of 16 Tg (N) yr^{-1} is assumed.

Table 3.4 N_2O destruction rate estimation in the stratosphere from several studies.

N_2O destruction rate [Tg (N) yr^{-1}]	**Uncertainty [Tg (N) yr^{-1}]**	**Study**
15.7	± 1.1	(Prather, Holmes and Hsu, 2012)
18.8	–	(Syakila and Kroeze, 2011)
15.4	+ 1.7 / - 1.3	(Huang *et al.*, 2008)
17.3	± 1.4	(Hirsch *et al.*, 2006)
13.5	–	(Murphy and Fahey, 1994)

3.3.4 Filter for stratospheric air

CARIBIC data was filtered with two independent criteria to find data points which represent lowermost stratosphere. Firstly, via potential vorticity (PV), secondly via modelled geopotential height relative to thermal tropopause (H_{tp}) according to ECMWF model.

3.3.4.1 Potential vorticity as LMS sample filter

In order to make the OCS flux estimate it is necessary to delineate tropospheric and stratospheric samples. One means of making this distinction is to filter the samples according to potential vorticity. Potential vorticity can be described via *Equation 3.2*:

$$PV = -g\,(\zeta_\theta + f)\frac{\partial\theta}{\partial p} \qquad (3.2)$$

where, PV – potential vorticity [10^{-6} m^{-2} s^{-1} kg^{-1} K]; g – gravitational acceleration; ζ_θ – relative isentropic vorticity; f – Coriolis parameter; θ – potential temperature. In troposphere the values of PV are typically low. The PV usually increases rapidly when going from the troposphere to the stratosphere due to the change in static stability. It has been demonstrated that PV of 2 potential vorticity unit (PVU) value (2×10^{-6} m^{-2} s^{-1} kg^{-1} K) has been successfully used in the literature to separate stratospheric air from tropospheric air, also referred as the dynamical tropopause (Appenzeller and Davies, 1992). Thus, also within this thesis PV > 2 was applied as one criterion to find stratospheric air samples from CARIBIC data set.

3.3.4.2 Thermal tropopause height as LMS sample filter

As a separate criterion for the tropopause the potential temperature (or static stability) was used to determine the tropopause height by thermodynamical means. Geopotential height relative to the tropopause for CARIBIC data was determined for CARIBIC data set, and a filter of H_{tp} > 0 km was applied separately. The H_{tp} is the product of the European Centre for Medium-Range Weather Forecasts (ECMWF) model, and that data at CARIBIC pathways was obtained from Peter van Velthoven at the Dutch KNMI institute. The analysis results with both filtering criteria are discussed later in this thesis, *Section 3.3.5*. The advantage of using PV for filtering stratospheric air is the ability to understand the tropopause in both, dynamic and thermodynamic terms. For example, sudden lowering (abrupt folding) of the dynamical tropopause is often named an upper PV anomaly (positive PV anomaly), meaning stratospheric air parcels penetrates into the troposphere, which causes higher PV values compared to the surroundings. In contrast, at the lower levels of the troposphere often strong baroclinic zones occur, regarded as low level PV anomalies (negative PV anomaly).

Carbonyl sulfide data measured by the newly developed Entech-GC-AEDIII system was separated for tropospheric and lowermost stratospheric air by the H_{tp} parameter in *Figure 3.10*. Theil-Sen estimator was used to calculate the trend slopes for both regions. Theil-Sen estimator is a non-parametric method for fitting a regression line to data points in the plane via median of the slopes of all lines through pairs of points (Akritas, Murphy and LaValley, 1995). This approach helps to give a lower rank to outliers. Within the troposphere, with the data available from current CARIBIC routes the OCS MRs seem to be relatively stable

within the distribution rage, with Theil-Sen slope of 0.667. For stratospheric air a decreasing trend is seen. The deeper in stratosphere was the measurement, the lower the OCS MR was observed, with clear Theil-Sen estimator slope of -42.2.

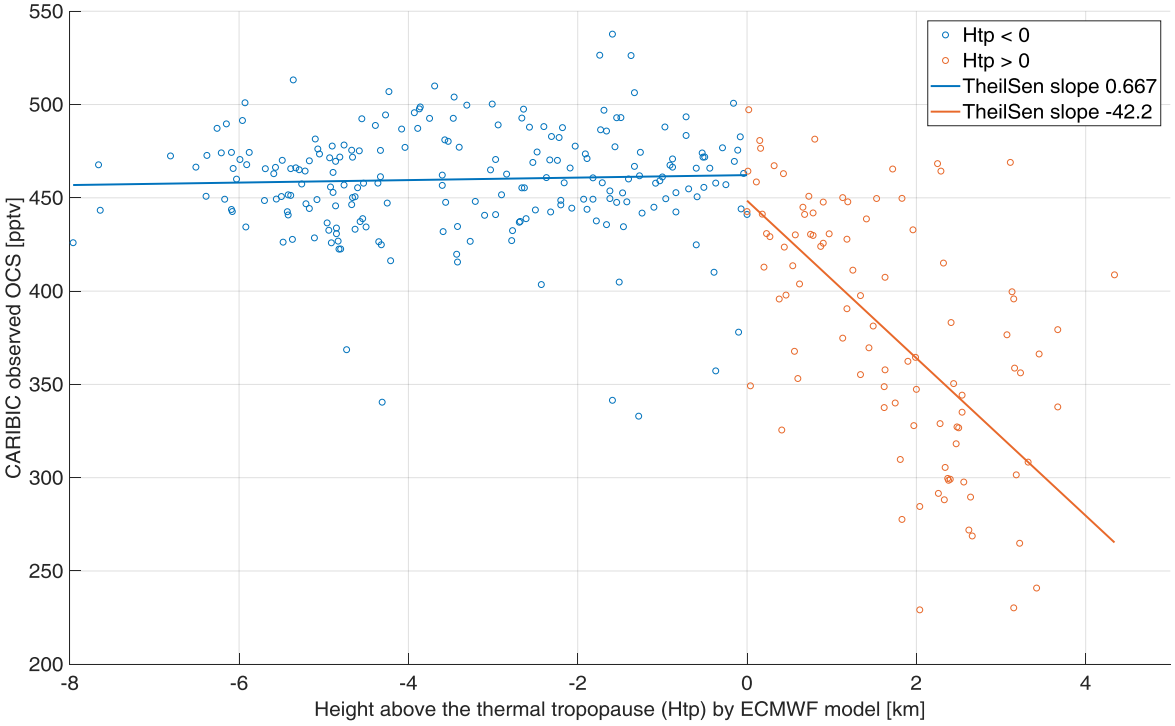

Figure 3.10 Tropospheric (blue) and stratospheric (orange) air separation to show OCS trends with Theil-Sen linear estimators.

3.3.5 OCS flux estimation results to the stratosphere based on CARIBIC observations

With the method described in *Section 3.3.1* and filters applied for the stratospheric air described in *Sections 3.3.4.1* and *3.3.4.2* the yearly OCS flux from the troposphere to the stratosphere was calculated. With the filter PV > 2 PVU, 6 flights with at least 3 data points matched the criteria. The correlation significance was ≥ 95% for 4 of the flights (N = 40) with the PV criteria. For the correlation significance the Zweiseitiger Test was used, where the significance is dependent on the degrees of freedom (Sachs, 1999). The degrees of freedom is equal to number of data points minus 2 (f = n – 2). A corresponding correlation coefficient for the specific number of data points was obtained from the Zweiseitiger Test lookup table (Sachs, 1999) and compared to each flight's N_2O vs OCS orthogonal fit correlation coefficient to only use the flights with correlation significance ≥ 95%. The average slope determined was 6.44 ± 2.13, which corresponds to a flux of 118 ± 39 Gg (S) yr^{-1} of OCS to the stratosphere.

The same analysis was conducted with the H_{tp} > 0 km filter, which limits to 4 flights with ≥ 3 data points matching the criteria. For 3 of these flights the correlation significance was ≥ 95% (N = 33). The average slope calculated was 6.42 ± 1.33, which corresponds to a very similar flux of 117 ± 24 Gg (S) yr^{-1} of OCS to the stratosphere, whereas the 1σ uncertainty is 38% lower.

The latest CARIBIC N_2O observational dataset is available until flight 540 (13/12/2017), which means the N_2O vs OCS correlations are not available for year 2018 flights (542 – 561), whereas 510 OCS data points were collected in 2018, and thus cannot be used for this correlation for flux determination.

The same OCS flux into stratosphere calculations were done with UEA November 2014 until December 2015 measurement data from the TRAC collectors, which were shipped to University of East Anglia, UK. With the filter PV > 2 PVU criteria and correlation significance ≥ 95%, 5 flights were determined (N = 42). The mean slope of 6.02 ± 2.53 was calculated, which corresponds to a flux of 110 ± 46 Gg (S) yr^{-1} of OCS to the stratosphere. For the UEA OCS data with the Htp > 0 km LMS filter, 4 flights (N = 32) with N_2O vs OCS correlation with correlation significance ≥ 95% were determined. The average slope of these flights was calculated to be 6.06 ± 3.13, thus a flux of 111 ± 57 Gg (S) yr^{-1} of OCS to the stratosphere. The flux results agree between the MPIC and UEA measurements within the uncertainty limits, whereas higher uncertainty was associated with the UEA flux calculations.

The average Entech-GC-AEDIII OCS flux estimate of 118 ± 32 Gg (S) yr^{-1} (221 ± 60 Gg OCS yr^{-1}) based on CARIBIC observational measurements and theoretical N_2O correlation was obtained. The upper range of the estimate is in agreement with the EMAC model (combined with aerosol module GMXe (Pringle *et al.*, 2010) and chemistry module MECCA (Sander *et al.*, 2010)) flux result of 150 Gg (S) yr^{-1} (Brühl *et al.*, 2012). A more recent modelling study by an alternative coupled aerosol-chemistry-climate model SOCOL-AER coupled to the European Centre / Hamburg 5 (ECHAM5) global circulation model by ETH Zurich group estimated 40.7 Gg (S) yr^{-1} OCS flux from troposphere to stratosphere (Sheng *et al.*, 2015). The estimate by *Sheng et al*. is substantially lower, thus the CARIBIC OCS measurements seem to support the result by *Brühl et al*. EMAC-MECCA-GMXe model. The two model discrepancy might rise from an underestimated transport of primary aerosol and / or SO_2 from the troposphere to the stratosphere. Another argument would be a missing surface emission of short-lived sulfur species like DMS, H_2S and CS_2 (Sheng *et al.*, 2015).

Brühl et al. estimated 35 Gg (S) yr^{-1} of OCS which is transported to the stratosphere is converted into aerosol, i.e. 23% (Brühl *et al.*, 2012). Adapting this conversion rate to CARIBIC flux estimation, 27.5 ± 4.3 Gg (S) yr^{-1} of OCS is converted to aerosol.

3.4 Tropospheric lifetime of carbonyl sulfide

From the variability in CARIBIC trace species measurements the average global lifetime of carbonyl sulfide was calculated. The inverse relationship between trace gas variability in the atmosphere to their lifetime *Equation 3.3* was first discussed by *Junge* in *1974* and later examined by various observations (Jobson *et al.*, 1998; Williams *et al.*, 2001). Where σ_{lnX} is the standard deviation of the natural logarithm of a trace species, τ is the corresponding lifetime of the trace gas, A and b are fitting parameters.

$$\sigma_{lnX} = A\tau^{-b} \tag{3.3}$$

Standard deviation correlation relationship between 6 species: propane (C_3H_8), ethane (C_2H_6), carbon monoxide (CO), methyl chloride (CH_3Cl), methane (CH_4) and nitrous oxide (N_2O) from the corresponding carbonyl sulfide (OCS) CARIBIC dataset were used for the relationship graph is seen in *Figure 3.11*. Their corresponding atmospheric lifetimes derived from hydroxyl radical (OH) reactivity from the WMO report as 0.03, 0.15, 0.17, 1.5, 12 years (Montzka *et al.*, 2011), respectively and 116 years for N_2O (Prather *et al.*, 2015). The vertical axis of the figure represents the natural logarithm of the standard deviation of a measured compound's MR. For each compound the data point represents the average derived from all analyzed CARIBIC flights, grouped per flight leg. The y-axis error bars show a 1σ standard deviation derived from per flight MR average. Only the flights where the R^2 correlation between the 6 species was > 0.5 were used for the OCS lifetime calculation. The x-axis OCS error bar shows the 1σ uncertainty in the calculation.

The average tropospheric OCS lifetime derived from the CARIBIC dataset was calculated to be 2.1 ± 1.3 years with this method. This value is in agreement with paper by Montzka *et al*. in 2007, where they estimate OCS atmospheric lifetime in the range of 1.5 – 3.0 years. Therefore, the analysis in this thesis work further supports the upward revision of the surface sinks, and thus a shorter tropospheric lifetime as suggested by (Sandoval-Soto *et al.*, 2005; Montzka *et al.*, 2007).

As the vegetative sink is much larger and the atmospheric burden of OCS has not changed substantially during the last 10 years, this suggests a shortfall in OCS sources of up to

substantial 800 Gg (S) yr^{-1} (Watts, 2000; Kettle *et al.*, 2002; Montzka *et al.*, 2007). Here I would suggest two major sources to consider:

- Anthropogenic emissions from industrial Asian regions (directly via OCS, and indirectly via DMS and CS_2 further conversion to OCS in the atmosphere). The rayon production in China has increased significantly during the last decade (Campbell *et al.*, 2015). Furthermore, Asian monsoon anticyclone, which develops yearly around June and September above Asia, is a significant pathway which pumps heavily polluted surface air to the free and upper atmosphere and can also directly inject pollution into the stratosphere (Randel *et al.*, 2010).
- Conversion efficiencies of other shorter lived organosulfur species (DMS, CS_2 etc.) into OCS are still associated with high uncertainties. For example, the conversion efficiency of DMS to OCS has been estimated to be 0.7 ± 0.2% (S), and found to be dependent on NO_x concentration in an OH initiated oxidation lab study (Barnes, Becker and Patroescu, 1994). This is still associated with significant uncertainty as the conversion efficiencies have not been measured under ambient conditions. In terms of CS_2, conversion efficiency of 0.81, based on PhD thesis lab experiments (Chin and Davis, 1993) has been reported and is often used in modelling studies. Thus, new studies of atmospheric processing of DMS and CS_2 are required. In addition, the DMS and CS_2 global emission magnitudes and inventories are poorly constrained.

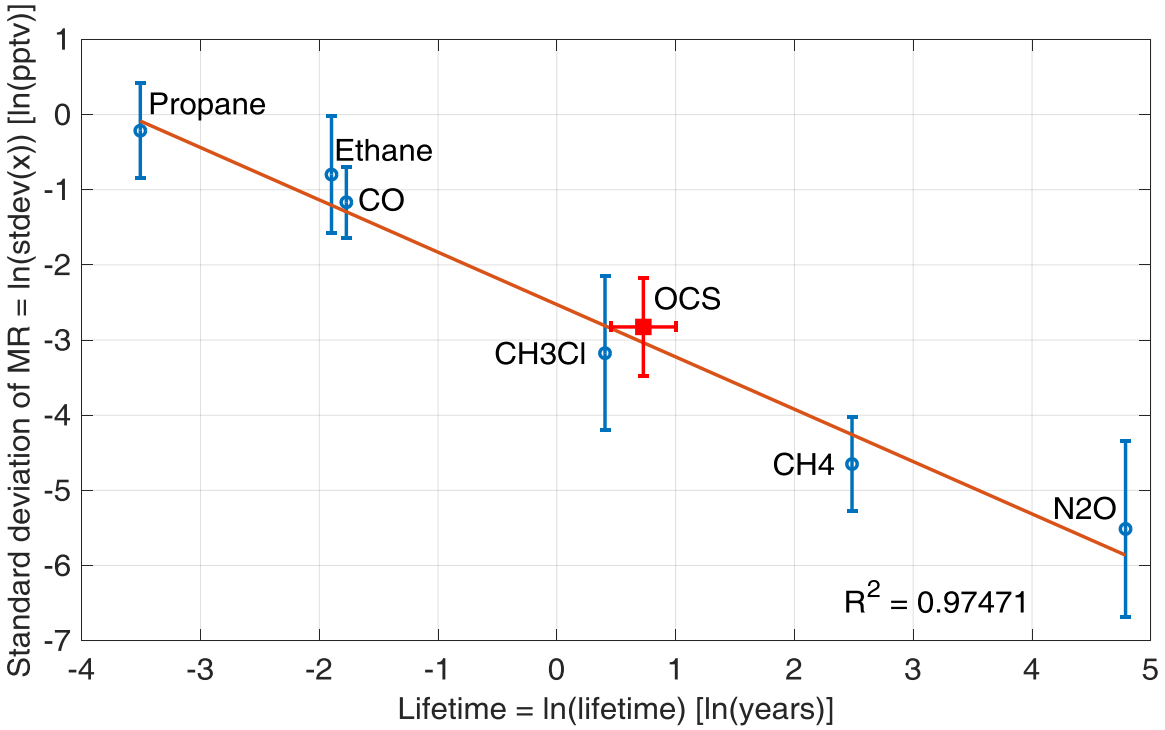

Figure 3.11 Standard deviation correlation of CARIBIC MR dataset (natural logarithm taken) of 6 atmospheric trace gas species with various atmospheric lifetimes for determining the corresponding global atmospheric lifetime of carbonyl sulfide. Data obtained from 5 CARIBIC measurement instruments. Red square with red error bars indicates the average modelled atmospheric lifetime of OCS derived from this linear regression model.

3.5 Stratospheric lifetime of carbonyl sulfide

Similar approach as used for the stratospheric OCS flux calculations (discussed in *Section 3.3.1*), was also applied for the average stratospheric OCS lifetime calculations. The tracer-tracer correlation for estimating the atmospheric lifetime of a compound, is possible when simultaneous MR measurements of two long-lived species is carried out and the atmospheric lifetime of one is known (Plumb and Ko, 1992). The AED measured OCS MRs and GHG system measured N_2O MRs from the CARIBIC HIRES and TRAC samplers were used to estimate the stratospheric lifetime of OCS as stated with *Equation 3.4*.

$$\tau_{OCS} = \frac{\overline{MR_{OCS}}}{\overline{MR_{N2O}}} \times m \times \tau_{N2O} \qquad (3.4)$$

Two separate filters, potential vorticity > 2 PVU and thermal tropopause height > 0 km, were used to sort out tropopause and stratosphere region samples as described in *Section 3.3.4.1* and *3.3.4.2*, respectively. Samples were sorted per CARIBIC flight leg basis. Orthogonal fit, which takes into account both x and y-axis uncertainty, between OCS and N_2O was used to

determine the per flight slopes (*m*) with significant correlations, as described in *Section 3.3.2*. The mean atmospheric lifetime of 116 ± 9 years (τ_{N2O}) by (Prather *et al.*, 2015) was used.

With the PV > 2 PVU lowermost stratosphere filter, an average OCS MR of 0.415 ± 0.032 ppbv (MR_{OCS}), and a mean N_2O MR of 324.0 ± 0.2 ppbv (MR_{N2O}) was determined. A mean slope of 265.0 ± 82.3 (*m*) was calculated. With applying *Equation 3.4*, an average stratospheric OCS lifetime (τ_{OCS}) of 39 ± 15 years was determined, where the uncertainty assembles the geometric mean of the 1σ of the slopes determined lifetime and the N_2O atmospheric lifetime.

The same approach was also used with the thermal tropopause, H_{tp} > 0 km filter. An average OCS MR of 0.416 ± 0.035 ppbv, and a mean N_2O MR of 323.7 ± 0.2 ppbv was calculated. An average slope of 367.6 ± 107.2 was computed, which refers to a mean stratospheric OCS lifetime of 55 ± 18 years.

Significant difference of the estimated OCS stratospheric lifetime is observed between PV and H_{tp} filter methods, where the latter estimates 41% longer lifetime. In this case, the modelled thermal tropopause height, H_{tp} > 0 km, based on the ECMWF metrological analysis, limits to 43 samples and PV > 2 PVU leads to 65 samples. Thus, the more samples collected in this region in the future will lead to a better estimate. The mean of these two estimates with a weighted average uncertainty leads to an average stratospheric OCS lifetime of 47 ± 16 years. This lifetime is somewhat shorter than reported by ACE satellite and balloon-borne study by *Barkley et al*. in 2008 and *Krysztofiak et al*. in 2015, respectively (see in detail in *Section 1.4.2*), but still in agreement within the uncertainty range.

3.6 Stratospheric sink of carbonyl sulfide

A shorter stratospheric lifetime of OCS will lead to a larger stratospheric sink of OCS. Stratospheric sink (*S*) of a species equals its atmospheric burden (*B*) divided by the compound's stratospheric lifetime (τ), as presented with *Equation 3.5*.

$$S = \frac{B}{\tau} \tag{3.5}$$

Assuming a total atmospheric mass of 5.148×10^{21} g (Trenberth and Smith, 2005), and a global yearly median (2001-2017) surface OCS MR of 490.8 ± 1.5 pptv (*Table 3.5*), yields a total OCS atmospheric mass of 5.241×10^{12} g (via converting OCS volume mixing ratio to a mass mixing ratio with the dry air molar mass of 28.96 g mol^{-1}). Using the CARIBIC OCS stratospheric lifetime, leads to an OCS stratospheric sink estimate of 83 – 169 Gg yr^{-1}

(44 – 90 Gg (S) yr^{-1}). As the tropospheric transport of OCS is considered as the only major source of OCS to the stratosphere and the OCS MR do not show a substantial trend, thus the stratospheric OCS sink should balance the net OCS flux from the troposphere. This stratospheric sink is 43% smaller compared to the tropospheric influx as estimated in *Section 3.3.5*, but still within the uncertainty range. The 43% smaller OCS stratospheric sink compared to the one-way influx from the troposphere estimate hints to around 54 Gg yr^{-1} (29 Gg (S) yr^{-1}) back-flux of OCS from the stratosphere back to the troposphere without being converted to sulfate aerosol. A large backward flux was also discussed by Thomason and Peter in 2006 and by Kremser *et al*. in 2016.

3.7 Global ground level observed OCS seasonality and trend

Global annual mean ground level OCS MR of 481.0 ± 1.9 pptv was determined from January 2001 until December 2017 from 15 measurement station NOAA/ESRL / GMD HATS flask analysis data (Montzka and Elkins, 2018). The corresponding northern hemisphere (NH) and southern hemisphere (SH) global annual mean OCS MRs for stated period were 475.9 ± 1.8 pptv and 496.6 ± 2.1 pptv, respectively (see *Table 3.5* for more statistics). The corresponding OCS annual mean values for the same data set from February 2000 to February 2005 were 484 ± 2 pptv globally, 476 ± 4 pptv for NH and 491 ± 2 pptv for SH as published by (Montzka *et al.*, 2007).

The newest available OCS MR time series (~ January 2000 – August 2018) for all individual 14 measurement station by NOAA/ESRL/GMD HATS GC-MSD flask analysis is depicted with *Figure 3.12*. Data by (Montzka and Elkins, 2018). In the NH a minimum OCS MR of 286.6 ± 1.8 pptv and maximum of 573.5 ± 1.8 pptv was measured with a standard deviation of 45.9 ± 1.5 pptv throughout all the combined data set from 10 measurement stations.

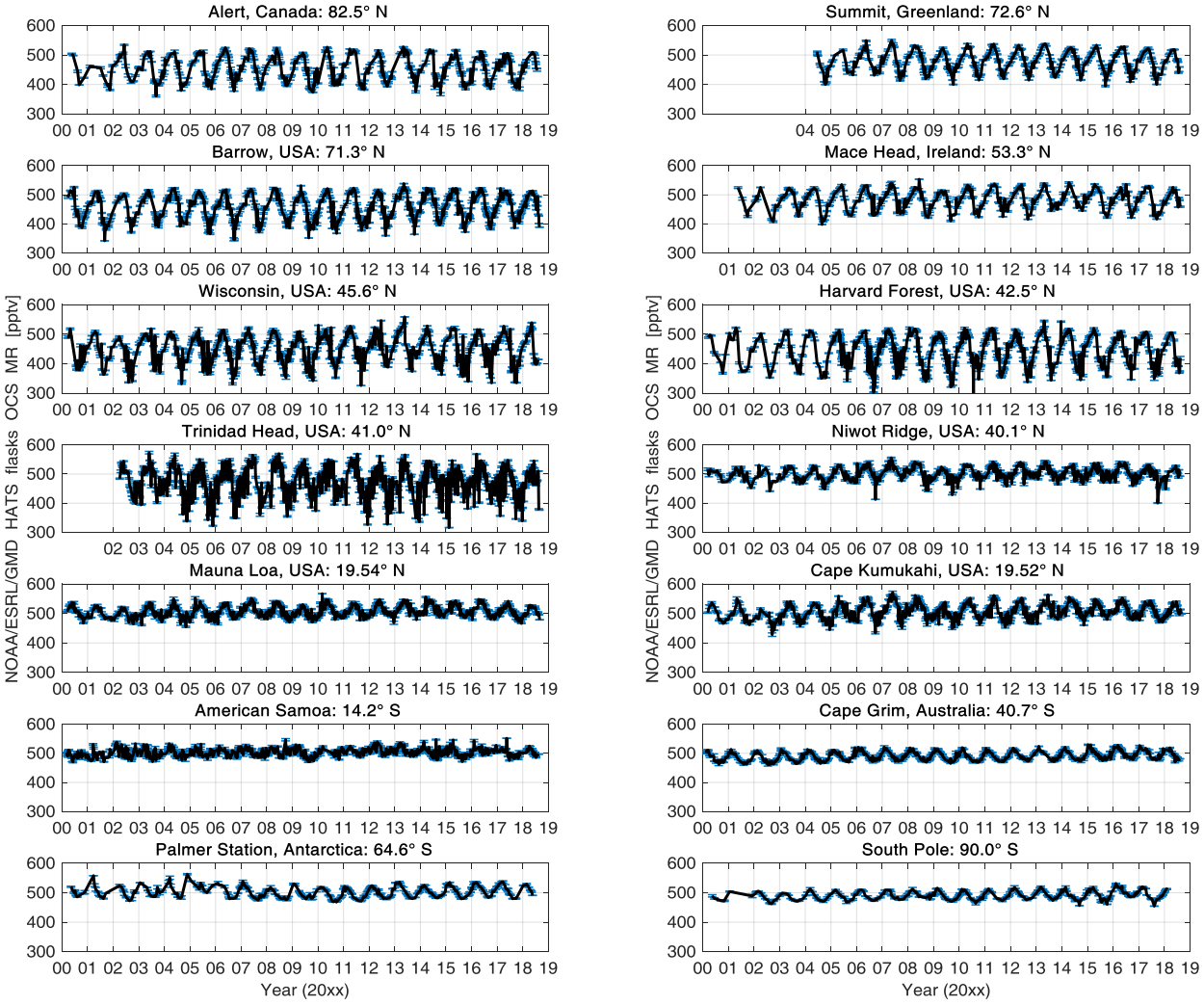

Figure 3.12 Global background (14 stations) carbonyl sulfide MR time series from flask measurements provided by the Global Monitoring Division of the National Oceanic and Atmospheric Administration's Earth System Research Laboratory (NOAA/ESRL/GMD) Halocarbons & other Atmospheric Trace Species Group (HATS) as a result of analysis on gas chromatography with mass spectrometry instrumentation. Error bars show 1σ uncertainties. Years from ~ 2000 – Aug 2018, total number of samples N = 7806. Courtesy of NOAA *Montzka* and *Elkins*, September 2018.

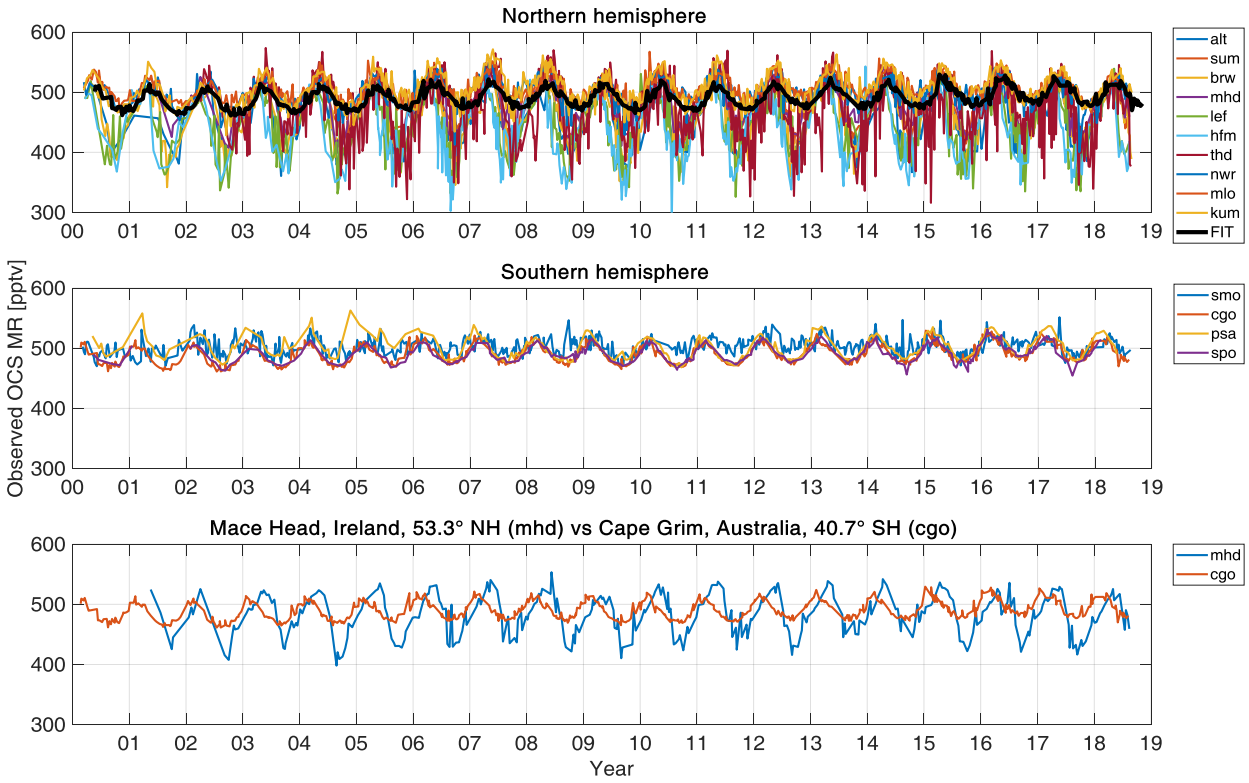

Figure 3.13 Northern and southern hemisphere OCS measurement time series overlay and separation with subplots. Measurement station codes in the legend are described as in *Table 3.5*. Bottommost subplot represents a comparison of Mace Head, Ireland (mhd) station in the NH with Cape Grim, Australia (cgo) station in the SH. Black line labelled FIT on the uppermost NH subplot is cgo SH station time series, pushed 3 solar months (91.31 days) forward in time on x-axis. Measurement station Data obtained from NOAA/ESRL / GMD HATS (Montzka and Elkins, 2018)**.**

All the 10 overlaid ground based OCS MR measurement station time series in the northern hemisphere show the same seasonality (uppermost subplot in *Figure 3.13*), also the 4 overlaid OCS MR measurement station time series in the southern hemisphere show the same seasonality (middle subplot in *Figure 3.13*), whereas NH and SH seem to show little coherence at first look (example on bottommost subplot in *Figure 3.13*). SH OCS MR seems to show 3 solar months (91.31 days) delay in OCS seasonality compared to NH. Black line labelled FIT on the uppermost NH subplot in *Figure 3.13* is Cape Grim, Australia (cgo) measurement time series data, but shifted forward by +91.31 days. Like this the OCS seasonalities between NH and SH appear to fit relatively well. 3 months difference in SH and NH seasonality are indicative for different OCS sources and / or sinks. Terrestrial uptake, mainly active vegetation dominates the OCS seasonality throughout the NH, whereas oceanic emissions dominate OCS seasonality in the SH (Kettle *et al.*, 2002).

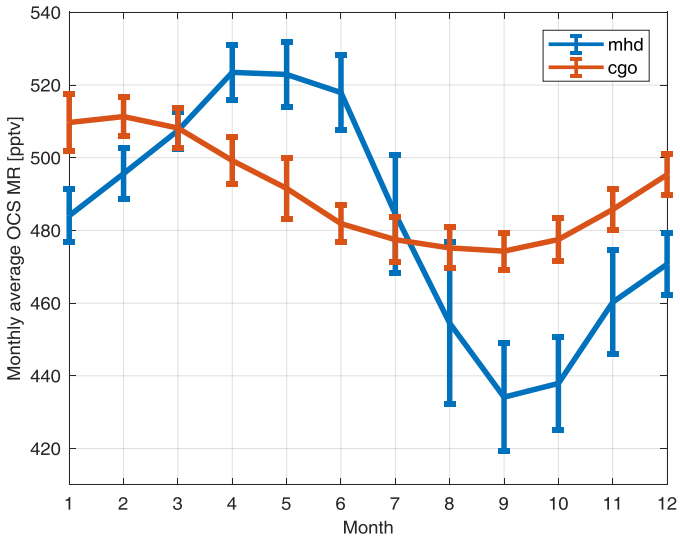

Figure 3.14 Monthly average OCS MR to represent the yearly cycle in the northern hemisphere (Mace Head, Ireland (mhd) station data from 2001-2018) and in the southern hemisphere (Cape Grim, Australia (cgo) station data from 2000-2018). Error bars represent 1σ uncertainties. Measurement station data obtained from NOAA/ESRL/GMD HATS (Montzka and Elkins, 2018)**.**

The seasonality of carbonyl sulfide is much more prevalent in the northern hemisphere (Mace Head, Ireland station) where the MR monthly average reaches its maxima, 523 ± 8 pptv, in April after the winter months where the OCS uptake has been the lowest. The NH monthly average minima of OCS, 434 ± 15 pptv, occurs in September during the end of gross primary production season, where the cumulative uptake sums to the greatest quantity. In the southern hemisphere (Cape Grim, Australia station) monthly average maxima, 511 ± 5 pptv, is seen in February and minima, 474 ± 5 pptv, nevertheless different hemisphere but also in September. The monthly average OCS MR amplitude of the NH maxima and minima is 89 pptv, which is significantly (2.4 times) higher than the amplitude in the southern hemisphere, which is 37 pptv. The monthly average seasonality is depicted in *Figure 3.14*.

Table 3.5 Global (14 stations) background OCS MRs overview from flask data provided by the NOAA/ESRL/GMD HATS working group by GC-MSD analysis. Averaged for years from ~ 2001 – 2017 for valid seasonality, total number of samples N = 7330. Courtesy of NOAA *Montzka* and *Elkins*, September 2018.

Station	Latitude	Elevation (m above sea level)	Yearly average MR ± σ [pptv]	Growth rate per year [pptv yr^{-1}]
Alert, Canada (alt)	82.5° N	210	451.8 ± 2.2	- 0.70
Summit, Greenland (sum)	72.6° N	3200	475.0 ± 1.5	- 1.32
Barrow, USA (brw)	71.3° N	8	456.7 ± 1.8	0.79
Mace Head, Ireland (mhd)	53.3° N	42	483.3 ± 1.8	0.35
Wisconsin, USA (lef)	45.6° N	868 (inlet 396 m above ground)	447.8 ± 1.7	0.76

Harvard Forest, USA (hfm)	42.5° N	340 (inlet 29 m above ground)	442.5 ± 1.7	0.00
Trinidad Head, USA (thd)	41.0° N	120	471.7 ± 1.6	- 1.10
Niwot Ridge, USA (nwr)	40.1° N	3475	500.8 ± 2.1	0.39
Mauna Loa, USA (mlo)	19.54° N	3397	507.2 ± 1.8	0.82
Cape Kumukahi, USA (kum)	19.52° N	3	507.0 ± 1.8	0.94
American Samoa (smo)	14.2° S	77	503.1 ± 2.2	0.41
Cape Grim, Australia (cgo)	40.7° S	164 (inlet 70 m above ground)	489.8 ± 2.0	0.97
Palmer Station, Antarctica (psa)	64.6° S	10	501.5 ± 2.3	- 0.06
South Pole (spo)	90.0° S	2837	491.8 ± 1.6	0.80

	Average MR ± σ [pptv]	**Median MR ± σ [pptv]**	**Average growth rate per year [pptv yr^{-1}]**	**Median growth rate per year [pptv yr^{-1}]**
Global yearly mean	481.0 ± 1.9	490.8 ± 1.5	0.22	0.40
Northern hemisphere yearly mean	475.9 ± 1.8	487.0 ± 1.4	0.09	0.37
Sothern hemisphere yearly mean	496.6 ± 2.1	495.9 ± 1.7	0.53	0.61

3.8 USA west coast vs east coast OCS MR comparison

NOAA ESRL measurement site Trinidad Head and Harvard Forest are located at very similar latitudes: at 41.0° N and 42.5° N, respectively. Trinidad Head is located at the west coast (124.1° W) of the USA directly at the North Pacific Ocean, whereas Harvard Forest is at the east coast (72.2° W), 110 km away from North Atlantic Ocean. The monthly average time series are shown in *Figure 3.15*, for Trinidad Head station from year ~ 2002 – ~ 2019, and for Harvard forest from year ~ 2000 – ~ 2019. The MRs from the west coast measurement station (thd) show a tendency towards higher MR. Yearly average MR for the west coast measurement station is 29.2 ± 1.6 pptv higher compared to the west coast. Furthermore, the seasonality of the two sites show a different pattern. There seems to be

around 2 months delay for the seasonal maxima and minima for the west coast site in contrast to the east coast site.

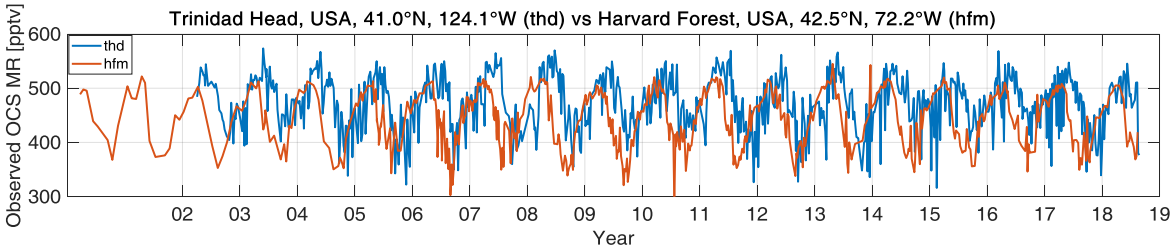

Figure 3.15 NOAA ESRL OCS MRs obtained from the HATS program from the US west coast (Trinidad Head) overlaid with the east coast (Harvard Forest) measurement station samples.

Most likely there are several factors influencing the difference in MRs observed at the west coast compared to the east coast. The prevalent westerly winds advect OCS over the Pacific Ocean, where marine OCS production may occur towards to the west coast of the USA. Thereafter, the air masses continue over continental North America where OCS can be uptaken by vegetation. The uptake depends on the vegetation type and time of year. One plausible explanation for the delay in the seasonality could be the slow warm up of the ocean, which leads to a delay in the oceanic OCS maximum production rate. Under oceanic OCS production is meant direct OCS emissions from the ocean and also the fast conversion of DMS and CS_2 into OCS in the atmosphere, primarily by the OH radical pathway.

3.9 EMAC sulfur chemistry model

3.9.1 EMAC model description

The global 3D ECHAM5 / MESSy Atmospheric Chemistry (EMAC) model was used to run the numerical calculations. ECHAM5 is the 5th generation atmospheric general circulation model developed at the Max Planck Institute for Meteorology (Roeckner *et al.*, 2003). The Modular Earth Submodel System version 2 (MESSy2), which describes atmospheric chemistry and meteorological processes in a modular structure is coupled to the ECHAM5 general circulation model (Jöckel *et al.*, 2010). Recently developed Mainz Organics Mechanism (MOM) was used to advance VOC chemistry in the EMAC general circulation model. The MOM as mass-conserving model calculates significantly higher OH reactivity from VOC oxidation compared to previous models. The scheme accounts for around 630 compounds and 1,630 reactions. In the MOM hydroxyl radicals have twice as large secondary sources compared to primary sources, mainly due to free troposphere OH recycling (Lelieveld *et al.*, 2016). This update to the OH radicals in the model significantly

also affects the sulfur chemistry. The model simulations were conducted at the Max Planck Computing and Data Facility (MPCDF) in Garching, Germany, at the cross-institutional supercomputer facility of the Max Planck Society.

3.9.2 Carbonyl sulfide MRs with the EMAC model

Ground based OCS observational measurement data by NOAA/ESRL/GMD group from the HATS analysis program were used to prescribe the Mainz EMAC model with the ground level MR, see *Section 3.7* for more detail. 2D surface plot representing global zonal monthly average OCS MRs ranging from 405 to 535 pptv during years 2000 – 2016, is seen in *Figure 3.16*. The lowest OCS MRs were measured in northern hemisphere boreal forests, during the end of growing season in autumn. At that time of year, the cumulative vegetative OCS uptake has been the strongest for couple of months. The highest MRs were observed in spring around 20° north after the northern hemisphere winter.

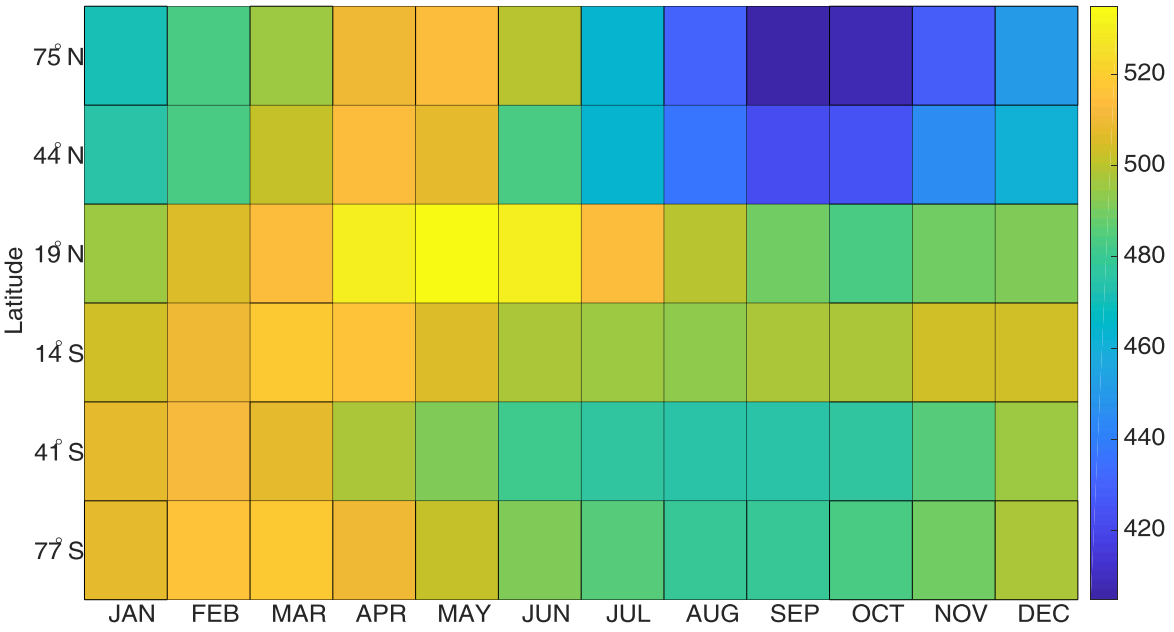

Figure 3.16 Global zonal monthly average OCS MRs [pptv] prescribed to the EMAC model surface condition (z = 1,000 hPa) from year 2000 to 2016. The RSD is in the range of 1-3%, to see the specific corresponding RSD graph see *Figure 6.5* in *Appendix*.

The monthly average Mainz EMAC model simulation output was studied at a mean CARIBIC flight pressure (225 hPa) level. The lowest average per month OCS MR at 225 hPa calculated was 476 pptv and highest 516 pptv. The average monthly difference between the ground level and CARIBIC flight level OCS MRs are depicted in *Figure 3.17*. The biggest discrepancies can be seen between 40° – 80° N (the Earth's second largest biome – Taiga region) in the end of summer till autumn. Up to 74 pptv higher OCS MR was

calculated at flight level compared ground level. It could be reasoned with strong vegetational uptake in boreal forest, which leads to depleted lower air masses, as also seen in boreal forest in Finland, see *Chapter 4* for details. On average in January – February around 80° S and April – May around 80° N, 30 pptv (up to 36 pptv) lower MR were calculated at typical commercial jet flight altitude compared to the ground level. The most likely removal pathways in the atmosphere are the reaction with OH radicals, O^3P and photolysis. Also the meteorological conditions play a substantial role in the mixing of the atmosphere.

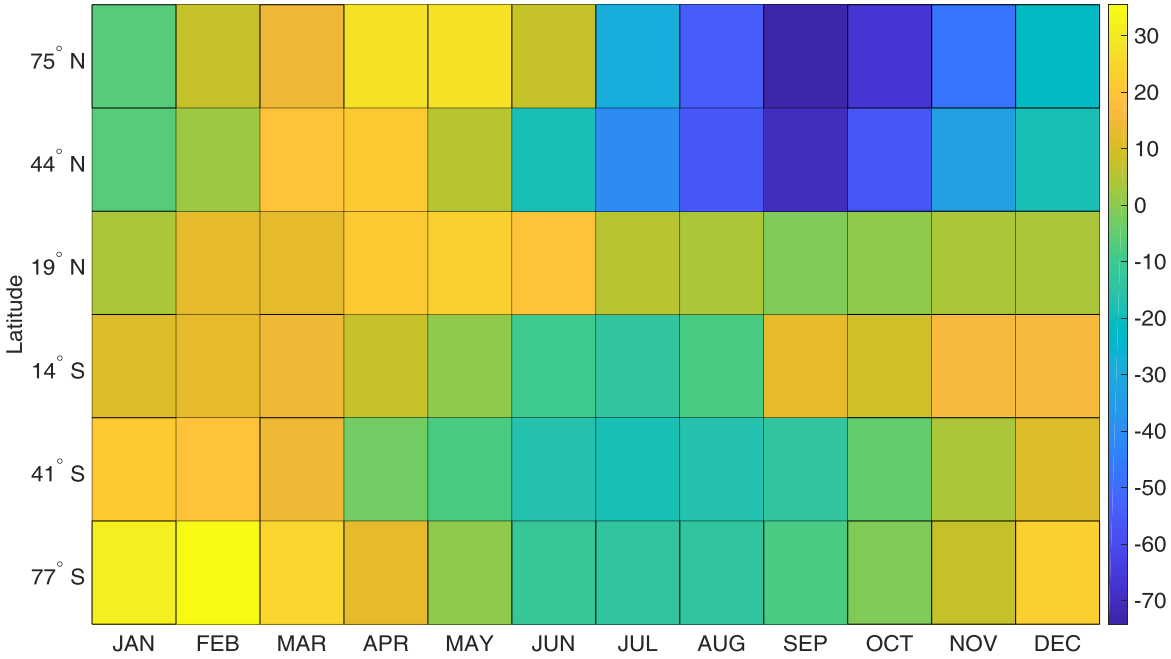

Figure 3.17 Carbonyl sulfide MR difference between measured ground level (z = 1,000 hPa) and modelled EMAC sampled at an average CARIBIC flight pressure (z = 225 hPa). Color scale represents the OCS MR difference in pptv, the blue colors indicate higher MRs at higher atmosphere compared to the ground level and yellow lower.

3.9.3 CARIBIC OCS observation comparison with EMAC OCS model results

The EMAC MOM model run was sampled at the CARIBIC flight paths from May 2005 until February 2016. The ground level OCS climatology used is shown in *Figure 3.18*. More details about the model OCS surface conditions can be found in (Brühl *et al.*, 2012).

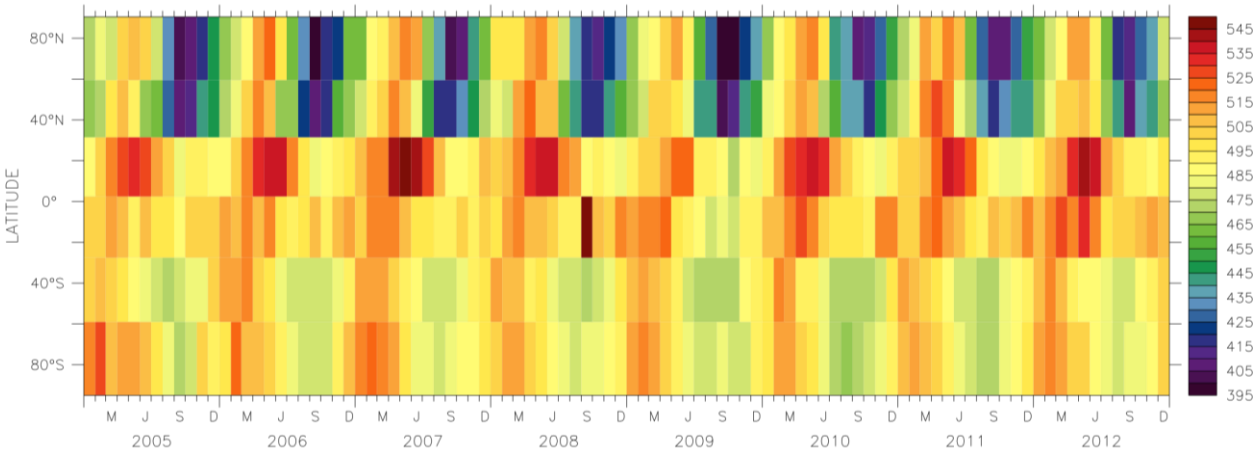

Figure 3.18 Zonal average OCS MRs [pptv] prescribed to the EMAC MOM model surface condition (1,000 hPa) from year 2005 to 2013.

For the years 2009, 2012 and 2013 both, EMAC model simulation and CARIBIC observation results exist for carbonyl sulfide. The CARIBIC observational data and model result comparison are seen in *Figure 3.19* to see how well the model resolves OCS MR in the atmosphere. The comparison was carried out at 4 vertical levels, at pressure, CH_4, N_2O and O_3 coordinate. This approach was used as a direct comparison at the pressure coordinate is often not the best method because the EMAC model does not readily reproduce the sudden convective folds in the atmosphere. Best correlation was obtained with EMAC at O_3 coordinate, where the correlation coefficient was 0.7056. The correlation at N_2O coordinate was 0.5582, which makes also that correlation 99.9% significant according to the Zweiseitiger Test, which takes the number of data points into account for the confidence level. The poorest correlation was obtained at the EMAC CH_4 coordinate with correlation coefficient 0.0873.

Nevertheless, EMAC MOM model simulations substantially overestimate OCS MRs at lower MRs (which often corresponds to LMS) compared to the CARIBIC observations by UEA. At higher OCS MRs (troposphere region) EMAC model compares better to the CARIBIC observations, but this times often underestimates the MRs compared to observations. The discrepancies between the observations and model could possibly arise from oversimplified sulfur chemistry in the EMAC model.

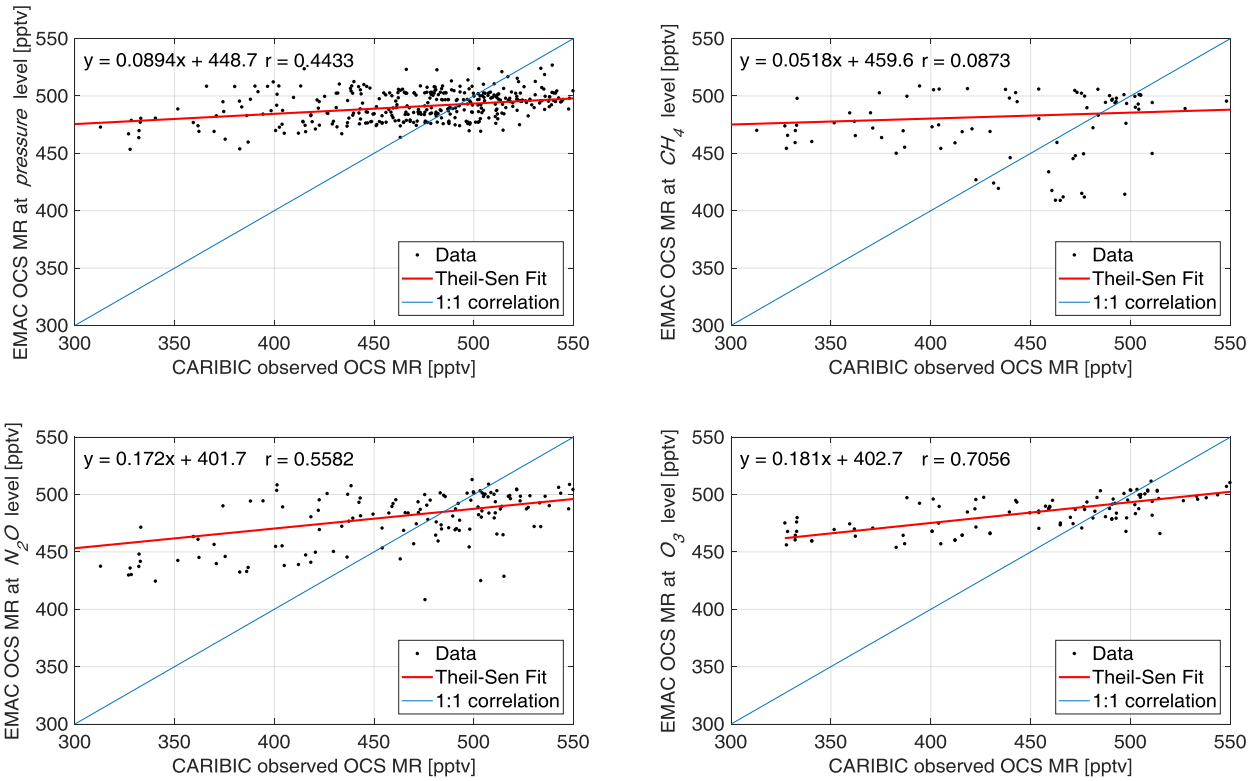

Figure 3.19 CARIBIC OCS observation and EMAC MOM model OCS MR comparison. Red lines are the Theil-Sen fits and blue lines show the 1:1 correlation. Model results are plotted at 3 different vertical coordinates: at pressure, CH_4 and N_2O. Last graph represents N_2O comparison between the observational and model data.

3.9.4 GHG EMAC model performance at CARIBIC sampled flight tracks

The general performance of the EMAC MOM model results for 2009 – 2016 was checked against CARIBIC observations. The EMAC model was sampled at CARIBIC flight paths space and time for N_2O, O_3, CH_4, H_2O, CO_2 and CO tracers at flight pressure level. The Theil-Sen correlation fits and 1:1 correlation lines are shown in *Figure 3.20*.

The EMAC MOM model resolves carbon dioxide concentrations the best of these 6 species when compared with the CARIBIC measurement data, where the fit and 1:1 correlation line are the closest together, and the Pearson's correlation coefficient r = 0.9178. Also, ozone and nitrous oxide show a good fit between the observations and the model with r = 0.9059 and r = 0.9036, respectively. For methane, the models performs well for lower MRs up to around 1,700 ppbv, but for higher MRs the model significantly underestimates. Water tracer also shows better correlation for lower MRs up to around 200 ppmv, whereas the data scattering gets broader after that point, ending with an overall correlation coefficient of r = 0.8549. As for latter tracer the model underestimates also H_2O MRs over 200 ppmv point. Carbon monoxide shows the same trend as CH_4 and H_2O species, better correlation at lower

MRs in the range of around 25 – 100 ppbv, but the model significantly underestimates the MRs after that point.

In general the 6 GHG species discussed here show substantially better comparison between the EMAC MOM model compared to carbonyl sulfide. These 6 GHG species excist much longer in the models and the atmospheric reactivity and aging is resolved to much greater extent. Sulfur kinetics still need significant improvement in the EMAC MOM model.

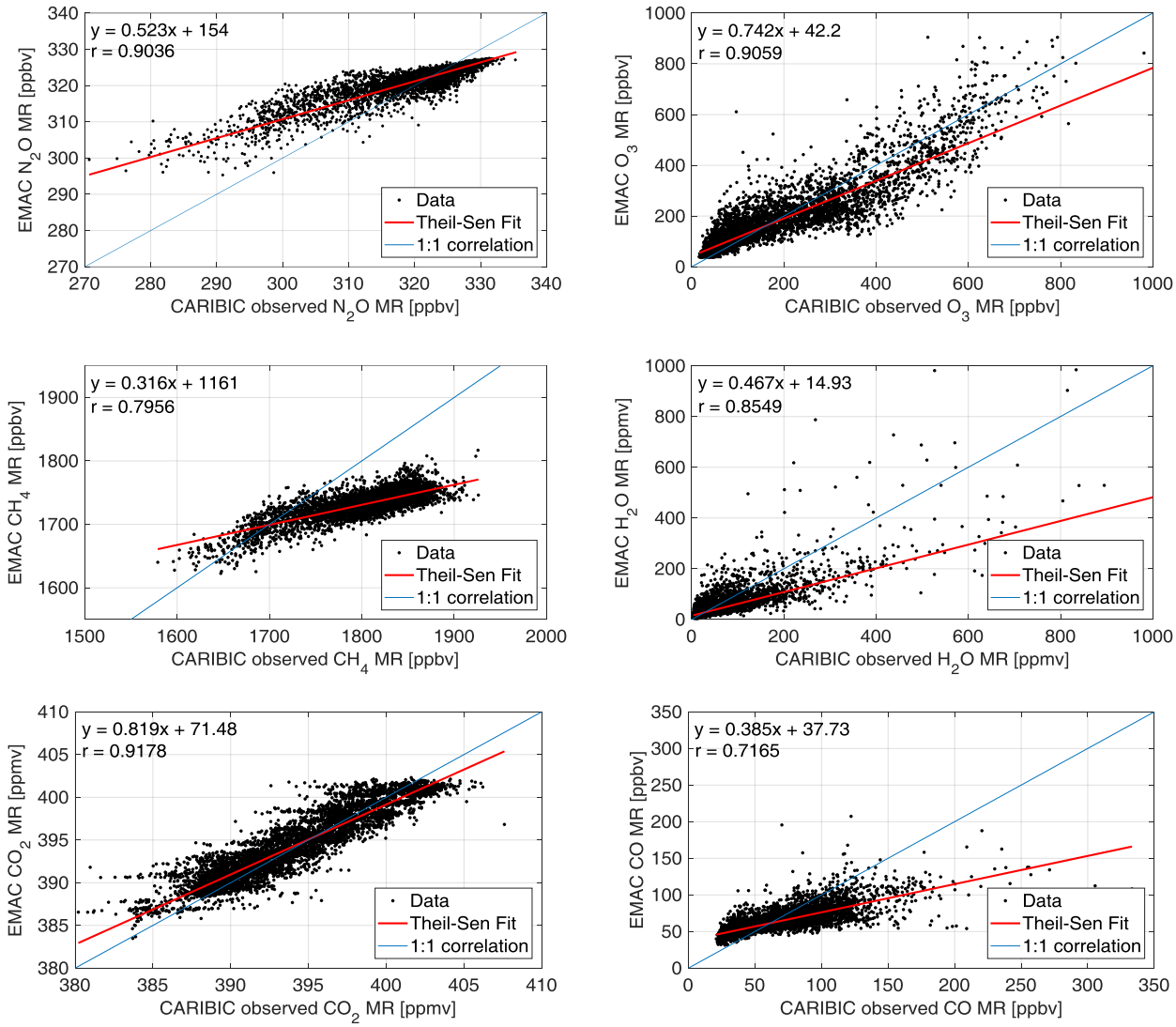

Figure 3.20 EMAC MOM model comparison at CARIBIC flight path space and time with CARIBIC observational data at flight pressure coordinate. Data from 2009 – 2016. Each individual graph shows the correlation for N_2O, O_3, CH_4, H_2O, CO_2 and CO species.

3.9.5 Age of air and OCS correlation

The age of air (AoA) at the flight UT/LMS altitude measured by the CARIBIC was determined from the SF_6 measurements in the CARIBIC whole air samples, and from the correlation to the Mauna Loa, Hawaii ground based SF_6 measurements. Sulfur hexafluoride

is extremely stable and long lived anthropogenic compound, with lifetime around 3,200 years (Ravishankara *et al.*, 1993). As SF_6 is in steady atmospheric growth (Abernethy *et al.*, 2018), this allows for the AoA determination: CARIBIC SF_6 measurement value is related back to Mauna Loa station SF_6 measurement value back in time. The time back when the same SF_6 MR was measured at ground level is determined as the AoA.

The correlation between AoA and CARIBIC OCS is seen in *Figure 3.21*. The AoA ranged from 2.14 ± 0.13 years to -1.17 ± 0.08 years where the OCS samples were collected. Negative AoA could indicate deep convective transfer of pollution from the lower troposphere to the higher levels. General trend between AoA and OCS MR shows lower MR of OCS in aged air, which is reasonable as OCS is further oxidized and removed from the atmosphere as time goes on.

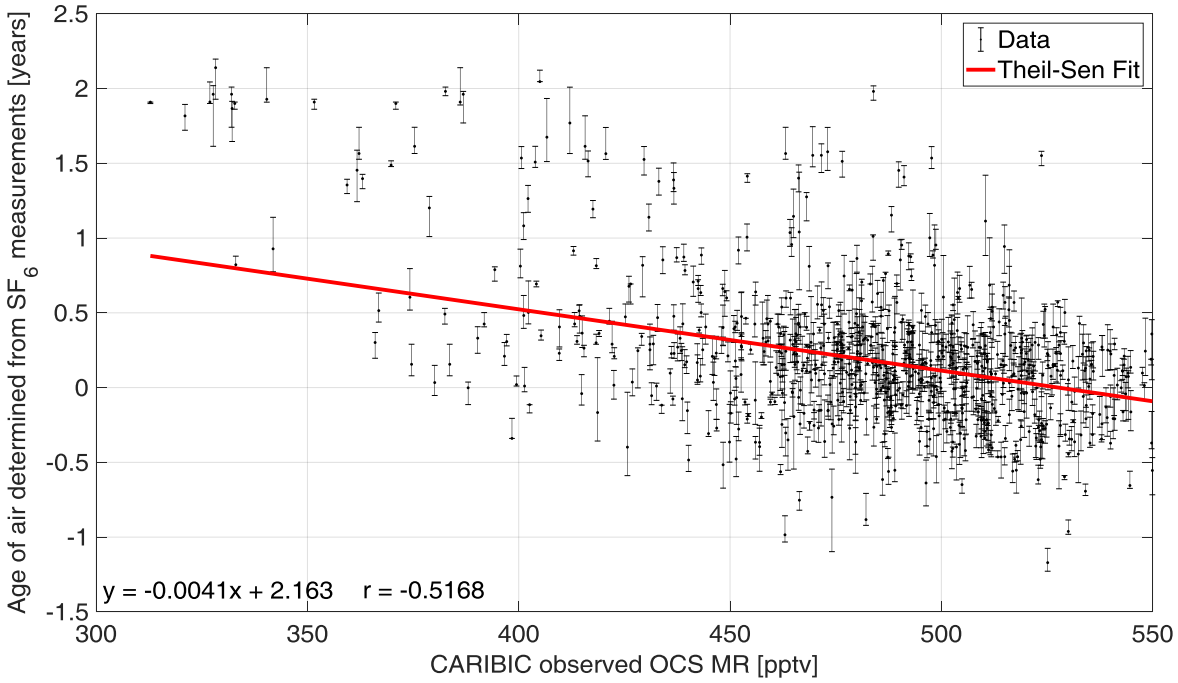

Figure 3.21 Correlation between carbonyl sulfide MR and age of air determined from SF_6 measurements. Error bars on the y-axis represent uncertainty of AoA on 1σ level, x-axis OCS MR error bars are omitted for clarity. Red line is the Theil-Sen Fit.

3.10 CARIBIC OCS summary

By August 2018 (CARIBIC flight 553), 523 whole air samples were successfully measured on the newly developed Entech-GC-AEDIII analytical system explained in detail in *Chapter 2*. The mean OCS MR measured on the CARIBIC flight routes was 414.7 pptv ± average uncertainty of 25.2 pptv (the corresponding median of 441.1 ± 20.4 pptv). The global average tropospheric (PV < 2) OCS MR of 459.2 ± 20.0 pptv was measured (median of 460.7 ± 17.4 pptv) with N = 211. With thermal tropopause filtering (H_{tp} < 0) the tropospheric OCS MR was 459.3 ± 19.9 pptv (median 460.8 ± 17.3 pptv) with 219 samples. With chemical tropopause sample filtering based on the ozone MR (H_{O3}), the average tropospheric MR (H_{O3} < 0) of OCS was 462.8 ± 23.9 pptv (median 470.1 ± 17.1 pptv), N = 55 was analyzed.

The lowermost stratosphere (with PV > 2 filter) showed average OCS MR of 386.9 ± 19.8 pptv (N = 106), which is around 7% lower in comparison to the tropospheric air. The LMS median (PV > 2) OCS MR of 396.7 ± 16.7 pptv was measured (PV > 2). Lower stratospheric air with H_{tp} > 0 was analyzed on average to have 380.2 ± 20.1 pptv of carbonyl sulfide, which is 383.2 ± 17.1 pptv on the median statistics with N = 97. With chemical tropopause sample filtering based on the ozone MR (H_{O3}), the mean stratospheric (H_{O3} > 0) OCS MR of 376.7 ± 22.3 pptv (median of 375.7 ± 17.5 pptv) was measured, with N = 82. The average tropospheric and stratospheric OCS MRs with different filters can be seen in *Figure 3.22*. All the other samples which were excluded from the tropospheric / stratospheric air analysis did not have PV, H_{tp} or H_{O3} parameter available for the associated sampling data points.

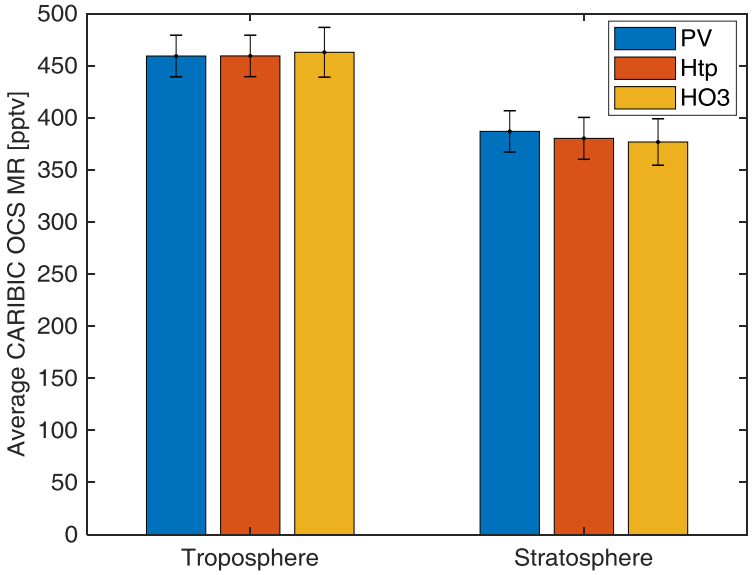

Figure 3.22 Average CARIBIC observed carbonyl sulfide MRs.

From pressure point of view all samples above 300 hPa have an average OCS MR of 464.6 ± 25.4 pptv (with an average pressure of 333.6 hPa and 8 538 m altitude), N = 28. All samples below 300 hPa (N = 505) were measured to have OCS MR of 411.9 ± 25.2 pptv (where the average pressure was 228.2 hPa and average altitude of 10 972 m). Samples below 300 hPa have around 11% lower MRs.

The analysis in this chapter suggests that OCS emissions from the ocean, including direct emissions also DMS and CS_2 oxidation into OCS, are the major source into the global sulfur budget. As vegetative uptake of carbonyl sulfide is often underestimated, the global atmospheric budget gets severely unbalanced. The unknown missing source could lie in the ocean, especially in the Southern Ocean and potentially in the Pacific Ocean. Unfortunately, these are exactly the regions which are not covered by the CARIBIC flights. Further airborne and ship based measurements in these regions would be extremely valuable to the OCS community.

4 BOREAL FOREST FIELD MEASUREMENT CAMPAIGN, HYYTIÄLÄ – IBAIRN 2016

4.1 Intro

The boreal forest (taiga) comprises 33% of the Earth's forest cover, making it the second largest biome in the world. Even in the epoch of the Anthropocene approximately ¾ of the boreal forest remains natural (Brandt *et al.*, 2013). As vegetative uptake is the single largest sink of carbonyl sulfide, with an estimated of 0.69 – 1.40 Tg yr^{-1} (Sandoval-Soto *et al.*, 2005), it is of a great interest to conduct a field campaign in the Finnish boreal forest to advance knowledge on global sulfur chemistry. The IBAIRN (Influence of Biosphere-Atmosphere Interactions on the Reactive Nitrogen budget) field measurement campaign took place in September 2016, organized by the Max Planck Institute for Chemistry. As seen in *Figure 3.16* in *Section 3.9.2*, ~ 60° N latitude (boreal forest) is expected to have the lowest OCS MRs during late summer to early autumn, thus it was especially valuable to join the field campaign to get more insights for OCS in this period. This was also a great opportunity to test the newly developed Entech-GC-AEDIII system in the field, the instrument which was described in the instrumental development section, *Chapter 2*. This was the first ever field campaign with the new 3rd generation JAS AED detector, as we were one of the first groups to receive it in July 2016 (after 1.5 yearlong R&D delay by the JAS company). As the Entech-GC-AEDIII could also measure other than just sulfur species, I was also on the search for new unknown volatile trace compounds (including species containing Br, I, Si, Hg, Se and As), and furthermore to support the other measurements with the VOC data.

4.2 Measurement site

The measurement campaign took place in September 2016 at Hyytiälä, Finland. The measurements were conducted in the boreal forest of southern Finland at the SMEAR II (Station for Measuring Forest Ecosystem-Atmosphere Relations II) located at 61°51' N, 24°17' E at 180 m above sea level (Hari and Kulmala, 2005). A map location of the

measurement site is depicted in *Figure 4.1*. SMEAR II is roughly in 50 km radius from larger cities. City of Tampere (population roughly 226,000, 430 inhabitants km^{-2}) is situated 49 km south-west from the site, city of Jyväskylä (population roughly 137,000, 120 inhabitants km^{-2}) is 88 km north-east of the station. Therefore, anthropogenic emissions at the measurement site are normally low. The cleanest air usually comes with prevailing northerly winds from the sparsely populated areas. There is a known source of monoterpenes originating from 5 km south-east from SMEAR II, where lies Korkeakoski sawmill and wood pellet factory (Williams *et al.*, 2011; Hakola *et al.*, 2012).

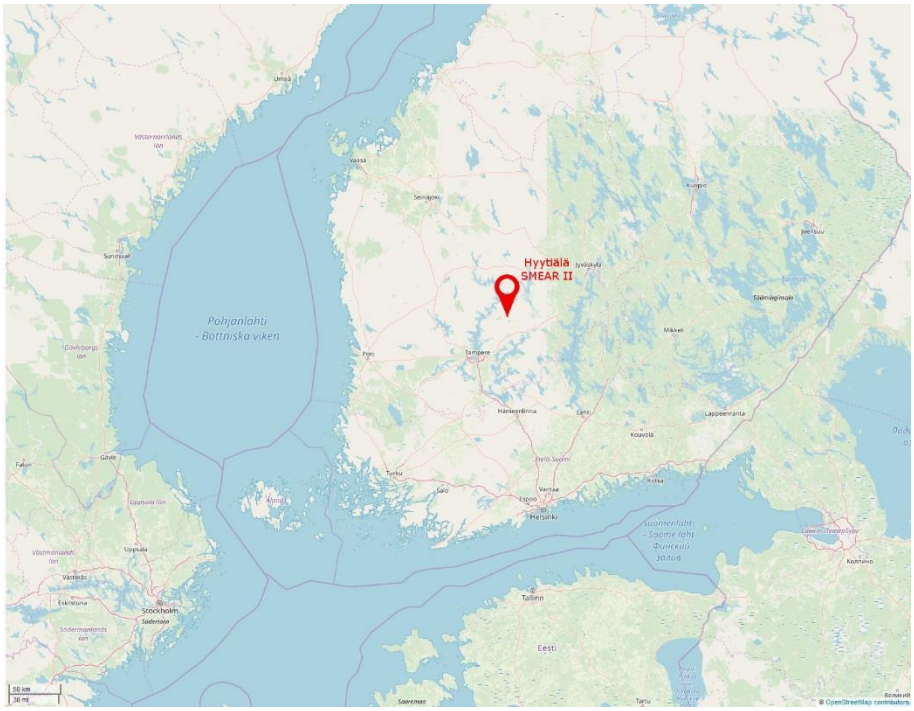

Figure 4.1 Map location of SMEAR II measurement station in Hyytiälä, Finland. Map data from © *OpenStreetMap contributors 2019*, data available under the Open Database License.

Wind speed and direction was measured near the top of the canopy at 16 m height. From *Figure 4.2*, it can be seen the prevailing winds were from the north, especially from north-west and north-east, summing up to about 60% of the time. During the campaign least wind originated from south-east sector and about third of the time from south-west. As seen on the wind chart, the wind speed were rather low throughout the campaign. The low wind conditions helped to form a stable boundary layer during nighttime.

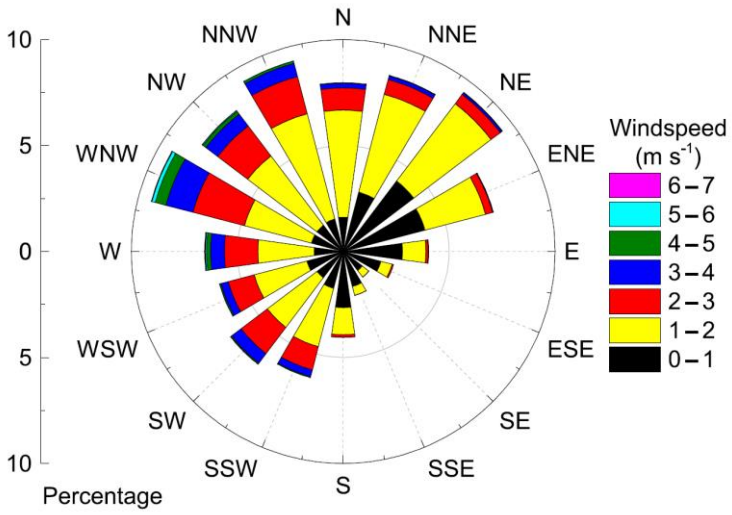

Figure 4.2 Prevailing wind speeds and directions during the September 2016 IBAIRN measurement campaign at SMEAR II measurement site. Source: Liebmann *et al.* 2018.

Throughout the campaign the general meteorological parameters like temperature, relative humidity, precipitation, wind speed and direction were recorded at various heights at the 128 m SMEAR II measurement tower. More details on those measurements can be found in (Hari and Kulmala, 2005; Hari *et al.*, 2013).

By far the predominant vegetation species around the measurement site is Scots pine (*Pinus sylvestris*), which are over 60% of the trees. Other tree species include birch (*Betula sp.*), Norway spruce (*Picea abies*) and aspen (*Populus sp.*). The average tree density is 1,370 stems per hectare (where tree diameter at breast height is over 5 cm) and the height of the canopy is around 20 m. The more common vascular species in the area include wavy hair grass (*Deschampsia flexuosa*), heather (*Calluna vulgaris*), bilberry (*Vaccinium myrtillus L.*) and lingonberry (*Vaccinium vitis-idea L.*). Red-stemmed feathermoss (*Pleurozium schreberi*) and dicranum moss (*Dricanum sp.*) are generally covering the ground (Ilvesniemi *et al.*, 2009). Picture of the vegetation in the vicinity is shown in *Figure 4.3*.

Figure 4.3 Photo of the surrounding boreal forest from the Hyytiälä aerosol tower.

At Hyytiälä, September is the time of year during which daylight hours transition from about 14 to 11.5 hours per day, and the end of summer becomes autumn. Throughout the campaign, within the canopy the ambient temperature varied from 2°C to 20°C, see Figure 4.4. The relative humidity was at its lowest at 40%, and reached 100% during most of the nights. By the end of the campaign ground frost started to occur, also deciduous trees had started to lose their leaves. Often during the night time significant temperature inversions of up to 5–7°C between heights of 8 and 128 m were observed, which restricted the air parcel mixing. Furthermore, relative humidity up to 100% was frequently measured directly after the sunset and throughout the night, as indicated in *Figure 4.8*.

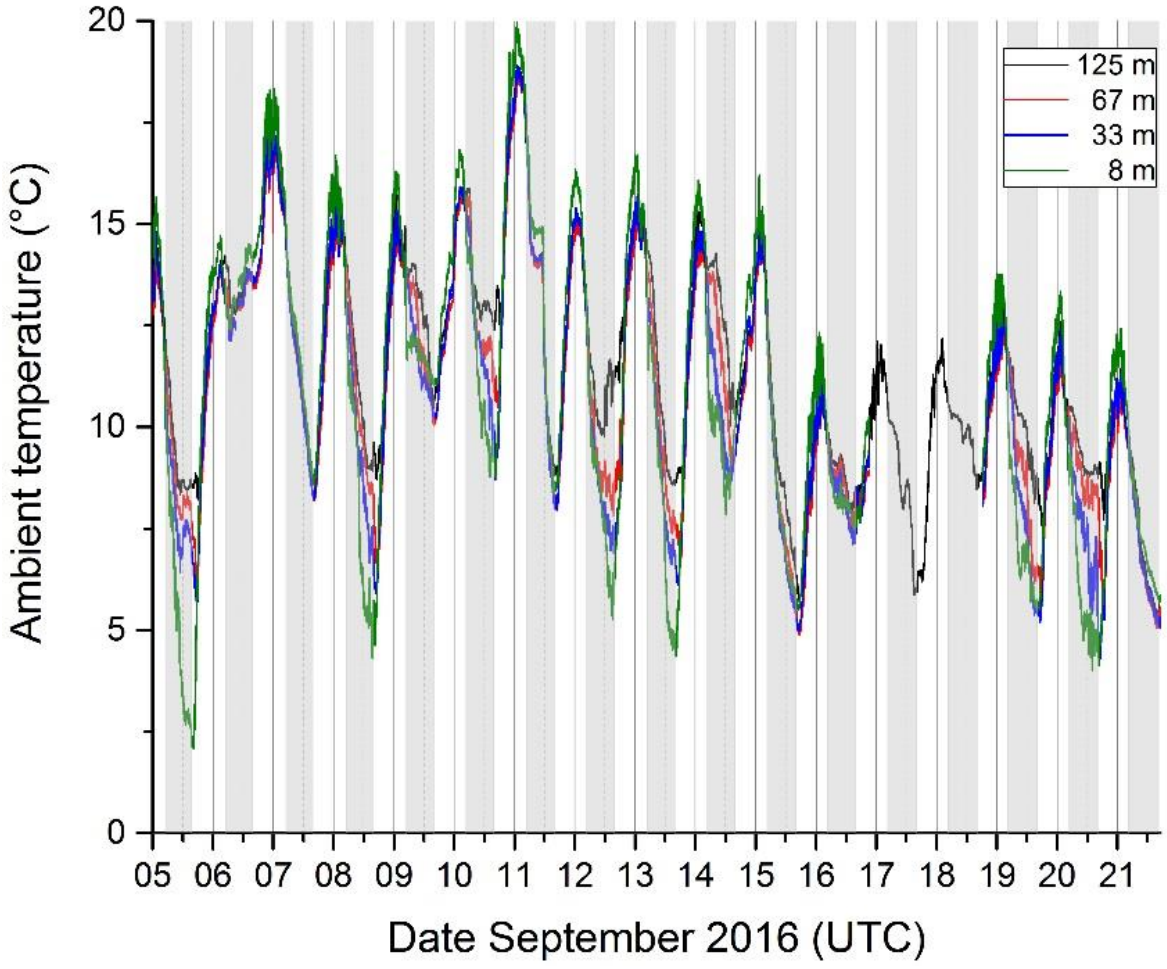

Figure 4.4 Temperatures measured at the SMEAR II tower throughout the campaign at 4 heights (8 – 125 m). Gray shaded areas represent the dark hours after the sunset.

4.3 Experimental setup

4.3.1 Entech-GC-AEDIII in a container at SMEAR II measurement site

The newly established Entech-GC-AEDIII consisted of a cryogenic pre-concentrator coupled to a gas chromatograph and further coupled to an atomic emission detector, detailed description in *Chapter 2*. The instruments were installed within an air-conditioned measurement container maintained at 25°C at the Hyytiälä SMEAR II site, as seen in *Figure 4.5*. Nevertheless, of separate and delicate packing of the spectrometer of the AEDIII for transport, the optics had gotten misaligned during the land and sea transportations of the containers. As this was the first field experience with this new instrument, the optics were needed to be realigned on the go. The precise realignment restored the sensitivity of the AEDIII which was experienced in the lab in Mainz before the campaign.

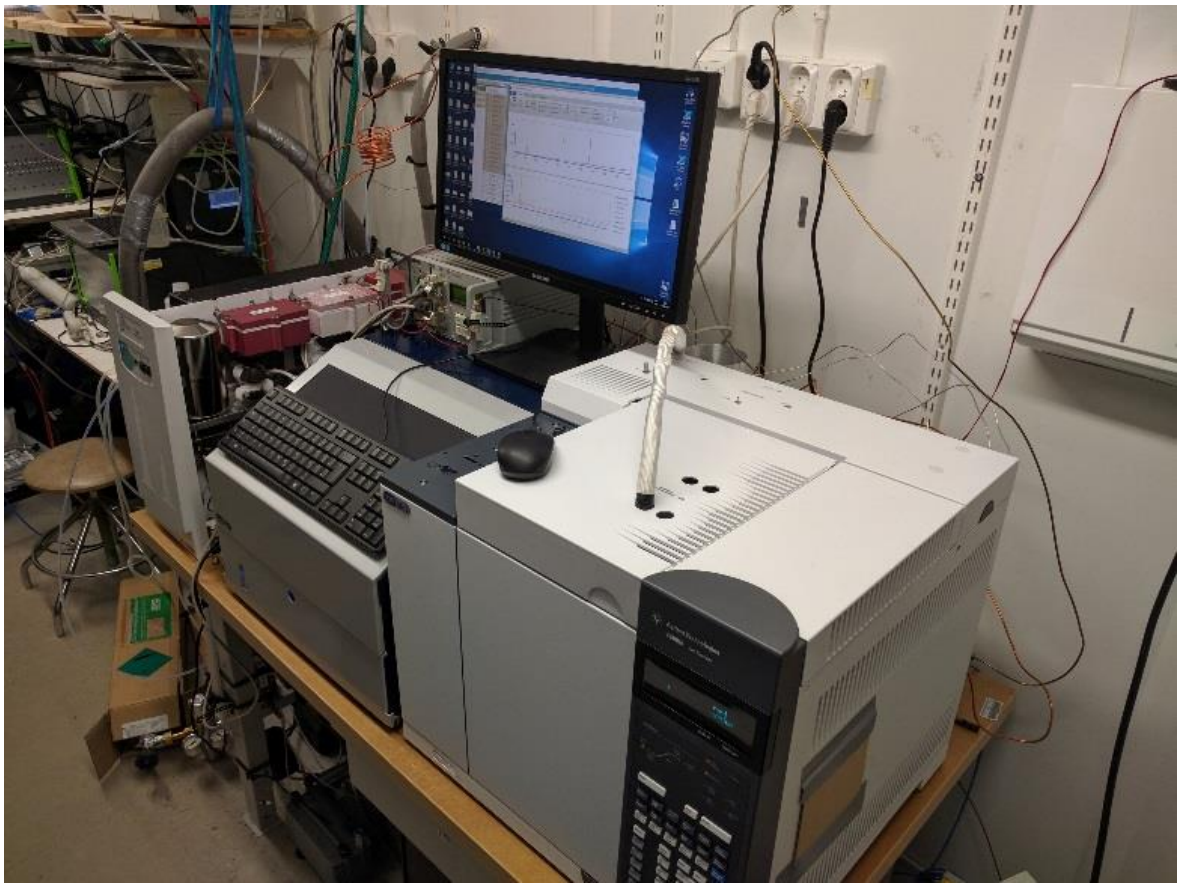

Figure 4.5 Photo of Entech-GC-AEDIII system setup in SMEAR II instrument container during IBAIRN-2016 measurement campaign.

The AEDIII system measured ambient air from the center of the common MPIC 8.5 m high-flow inlet (15 cm in diameter, flowrate of ~ 10 m^3 min^{-1}) for most part of the campaign. A 15 m long ½″ (1.27 cm in diameter) PFA tubing was used to draw air from the high-flow common inlet to the AEDIII container with a flowrate of 20 L min^{-1} (transmission time 3.3

s). The AEDIII inlet line was insulated and heated (to 10°C above ambient) to avoid sunlight interactions and condensation. The ambient air was filtered for particles at the beginning of the 15 m line with 5.0 μm PTFE (47 mm in diameter) membrane filters (Sartorius AG, Göttingen, Germany) and replaced after every 5 days. The experimental setup description of the Entech-GC-AEDIII is also published in the supplement of (Liebmann *et al.*, 2018b). The containers, aerosol measurement tower and 8.5 m common inlet are depicted in *Figure 4.6*.

Figure 4.6 Photo of the MPIC measurement containers installed in place for the IBAIRN-2016 campaign, including 8.5 m common inlet for the instruments.

4.3.2 IBAIRN sampling procedure

The newly developed gas chromatographic analytical method described in detail in *Chapter 2* was used during the campaign. The ambient air and calibration standards were sampled and analyzed with exactly the same method as the *in situ* measurements to minimize the instrumental uncertainty. The cryogenic sample trapping phase took place with flowrate of 200 mL min^{-1} from the inlet line guided from the common inlet, and 1,400 ml of gas was trapped in total for each sample. The mean sample throughput time interval was 1 h 22 min.

The approximate liquid nitrogen consumption rate was 2.5 L h^{-1}. Evidently, it was not easy to arrange liquid nitrogen in such large amounts to a forest site. With the help of the local site managers it was possible to arrange two industrial size liquid nitrogen dewars, a 670 L and a 240 L to be delivered to the measurement site. The dewars were filled several times during the campaign. Liquid nitrogen loss from the dewars was larger than initially

anticipated which together with liquid nitrogen delivery delays occasionally led to short data interruptions.

A full broad range calibration of the Entech-GC-AEDIII system was carried out *in-situ* at the beginning and end of the field campaign with an 84-component gravimetrically prepared gas-phase calibration standard with an uncertainty better than ± 5% (Apel-Riemer Environmental, Inc., USA) which was described in more detail in *Section 2.4.7* and the components can be seen in *Table 6.1* in *Appendix*. The ~ 50 ppbv reference standard was diluted on demand with zero-air (synthetic air through a heated catalyst) at 5 relevant concentration steps (50 – 1000 pptv). All the MFC flows were calibrated to standard flows according to the standard temperature and pressure (STP) conditions with a Gilibrator primary standard bubble volumetric flowmeter (Sensidyne LP, Gilian Gilibrator-2, USA). In between the ambient sample measurements also zero-air and pressurized ambient working standard collected at the SMEAR II site were measured. Zero-air was used for making sure there is no carry over or contamination by any compounds. The working standard was used to monitor the instrumental sensitivity drift and for applying corrections if necessary. The instrument was regularly checked against the 84-component Apel-Riemer primary reference standard (see *Table 6.1* in the *Appendix* for detail). The campaign average total uncertainty of the AEDIII system was calculated to be 14% based on a geometric mean calculation of calibration standard accuracy, precision from repeated calibration standard measurement and uncertainty from the dilution flow measurements.

Since monoterpenes become a major part of the NO_3 reactivity and also measured by the Entech-GC-AEDIII system, the following 5 monoterpenes α-pinene, Δ-3-carene, β-pinene, camphene and d-limonene were individually calibrated to lower the uncertainty associated with the measurement. The detection limits for the 5 monoterpene compounds were 1.0, 0.9, 0.4, 0.5 and 0.3 pptv, respectively. This setup has also been published in (Liebmann *et al.*, 2018b) in the section of technical description of the GC-AED.

4.4 Organosulfur species in a boreal forest

The MRs of OCS and CS_2 were measured throughout the IBAIRN measurement campaign. DMS MRs were below the limit of detection, thus not reported here. No other sulfur compounds were resolved with the analytical method described.

Between September 3 – 23 in 2016, campaign average OCS MR of 310 ± 61 pptv and CS_2 MR of 1.53 ± 0.86 pptv was measured by the Entech-GC-AEDIII system. The ± indicates 1σ standard deviation between all the measurement data points.

The substantially lower average OCS MR of 310 pptv in September at the Hyytiälä measurement site compared to northern hemisphere yearly average surface MR of 476 pptv (see *Table 3.5*) confirms boreal forest as a strong sink for the carbonyl sulfide budget. As discussed in *Section 3.9.2*, the EMAC model is prescribed globally with the lowest OCS MR in September around 44° - 75° N, which also coincides with the SMEAR II boreal forest measurement location. The EMAC model is prescribed with an OCS MR of 407 pptv at the surface in that specific bin, which is a significantly (31%) larger MR than observed during the campaign. This supports the substantially stronger vegetation sink suggested by *Sandoval-Soto et al*. in 2005. This could also be one of the reasons why the EMAC model strongly overestimates the lower OCS MRs in the stratosphere compared to the observations.

4.4.1 OCS diel cycle

In *Figure 4.7* the diel cycle of OCS measured at the Hyytiälä site in September 2016 is reported. On average the highest OCS MRs were measured between 9:00 and 15:00 UTC (12:00 and 18:00 local time), where the campaign median MR at that time frame was around 350 pptv. Surprisingly, the lowest MRs were measured around midnight and 5:00 UTC (3:00 and 8:00 local time), whereas stronger OCS uptake was expected to take place during daytime due to the similarity to CO_2 molecule and similar uptake pathways. For a long time it was thought canopy OCS uptake would be only active during the sunlight hours, but recently it was discovered that canopy OCS uptake can continue without sunlight, and it was found that the nighttime OCS deposition fluxes are dominated by canopy uptake in a boreal forest (Kooijmans *et al.*, 2017). They demonstrated the light independence of the OCS fixing carbonic anhydrase (CA) enzyme. The prerequisite for OCS fixing at nighttime is the incomplete closure of stomata, which allows for OCS stomatal diffusion. The stomatal opening can be independent from light and driven by the vegetation and atmospheric humidity and temperature levels. The temperature and relative humidity of the ambient air, measured from the MPIC 8.5 m common inlet where the Entech-GC-AEDIII instrument was drawing the air samples is shown in *Figure 4.8*. The temperature ranged from 1.5°C to 20°C and relative humidity from 41% to 100%, and almost every night relative humidity reached 100%. These conditions are favorable for nighttime stomatal opening, or only partial closure.

It has been confirmed that nighttime stomatal conductance exists at the Hyytiälä boreal forest (Kooijmans *et al.*, 2017).

Therefore, the low atmospheric boundary layer observed during nighttime and low wind speeds throughout the campaign led to a limited mixing of air masses. This limited mixing restricted the inmixing of higher OCS MRs from above the boundary layer and led to the lowest OCS MRs at the surface in the nighttime due to the continuation of the vegetative OCS uptake.

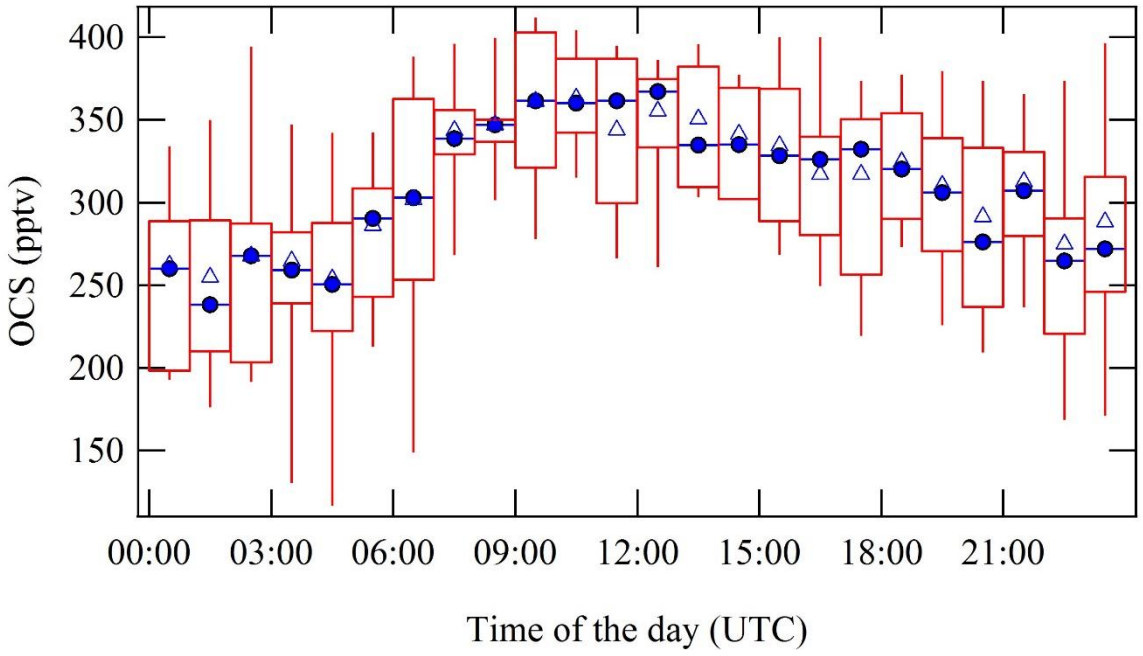

Figure 4.7 Diel cycle of carbonyl sulfide MRs based on all AEDIII measured data points throughout the IBAIRN campaign. Blue triangles show the overall hourly mean and blue circles show the hourly median values. The red rectangles with the whiskers show the data spread, where 50% of the data falls into the rectangles. The upper whiskers represent the upper 75 percentile data spread and the lower whiskers denote the lower 25 percentile data variation.

The nighttime uptake of OCS dominance by vegetation was confirmed by the radon-tracer and eddy-covariance methods, from which *Kooijmans et al*. in 2017 concluded the nighttime soil uptake contributes 34-40% of the total nighttime uptake flux. They also estimated that the nighttime uptake contributes around 17% of the whole daily OCS uptake flux.

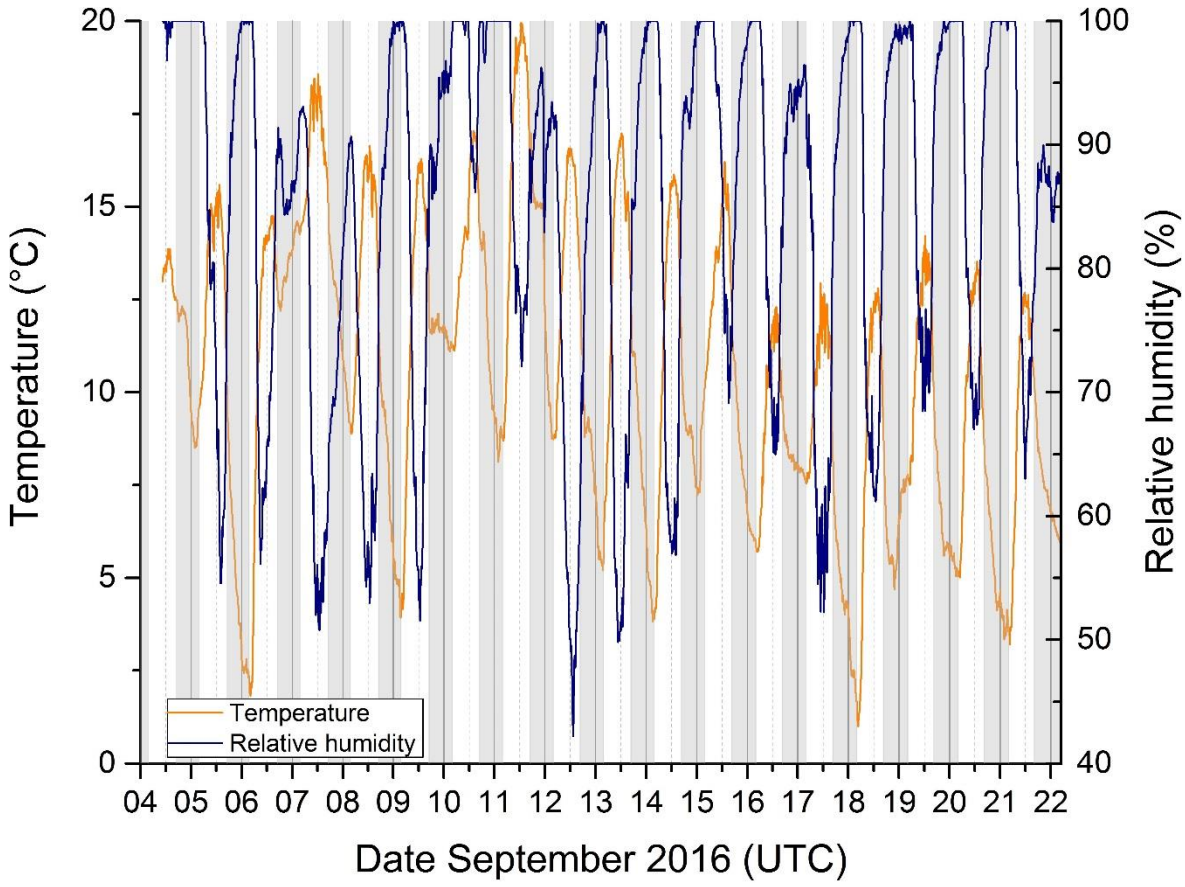

Figure 4.8 Ambient air temperature (orange) and relative humidity (blue) measured from the MPIC 8.5 m high common inlet. Gray shaded areas represents nighttime determined from light intensity measurement with a photometer.

4.4.2 CO_2 diel cycle

Carbon dioxide was measured at the SMEAR II tower located 130 m north-northwest (337.5°) from the common MPIC inlet area, where Entech-GC-AEDIII was drawing air samples. The MRs of CO_2 in dry air were measured by a Li-Cor LI-840 infrared light absorption analyzer. The campaign average hourly diel cycle of CO_2 measured from the 8.4 m SMEAR II tower inlet is shown in *Figure 4.9*.

Opposite to the OCS diel cycle, the diel cycle of CO_2 is to a large extent a mirror image of the former. Between 9:00 and 15:00 UTC (12:00 and 18:00 local time), during the sunlight maxima hours the lowest CO_2 levels (around 395 ppmv in median) were measured, when the CO_2 fixing photosynthesis is most active. The highest CO_2 levels were observed between midnight and 5:00 UTC (3:00 and 8:00 local time), with median MR around 413 ppmv (18 ppmv more compared to daytime), which is surprisingly an opposite trend to the OCS molecule discussed above.

The CO_2 and OCS vegetative uptake differences, especially the possible uptake continuation of OCS molecule at nighttime due to the CA enzyme light independence, further complicate the use of OCS as gross primary productivity tracer. As the nighttime OCS uptake was reported to be 17% of the whole day fixation in Finnish boreal forest from June to November 2015, it plays a significant role (Kooijmans *et al.*, 2017). Thus, the vegetation nighttime OCS uptake should be globally further characterized and implemented into model mechanisms and OCS budgets. This is also essential for using OCS as GPP tracer accurately.

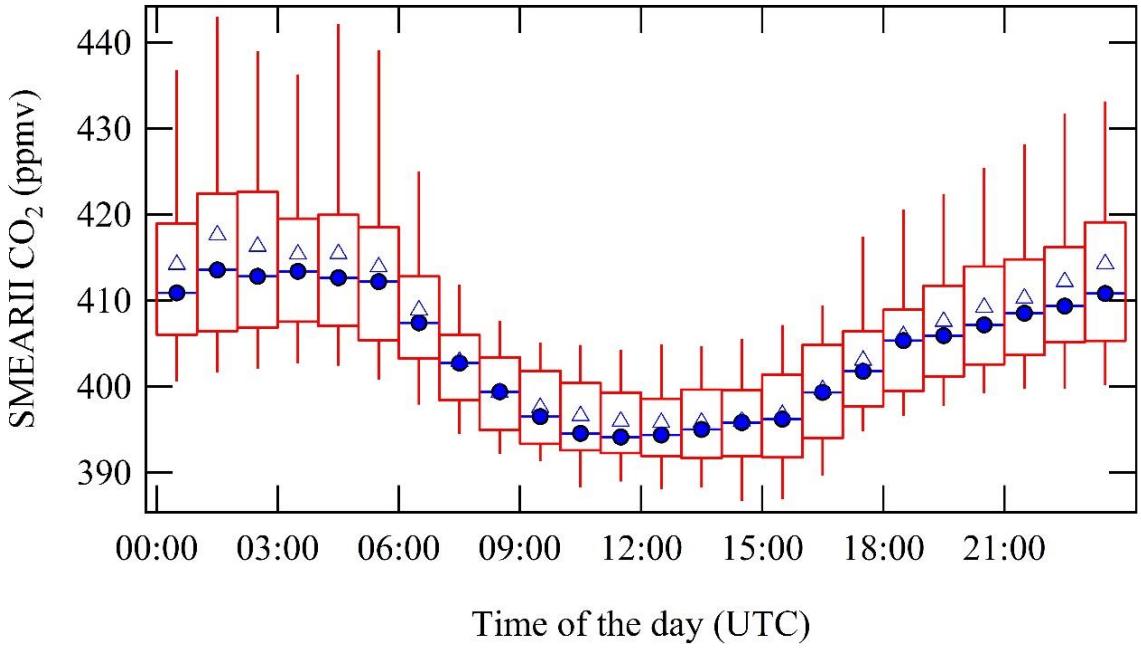

Figure 4.9 Diel cycle of CO_2 measured at the SMEAR II tower 8.4 m inlet throughout the measurement campaign in September 2016. Blue triangles show the campaign total hourly mean and blue circles show the hourly median values. The red rectangles with the whiskers represent the data spread, where 50% of the data falls into the rectangles. The upper whiskers show the upper 75 percentile data spread and the lower whiskers indicate the lower 25 percentile data variation. Data obtained from (Junninen *et al.*, 2009)**.**

4.4.3 O_3 diel cycle

The ozone MRs were higher during daylight hours and at higher heights. The highest campaign average O_3 MRs at around 30 ppbv were measured at the 125 m height at the SMEAR II tower around 15:00 UTC. The lowest average O_3 MRs were measured from the 4 m inlet at around 14 ppbv. The largest day and night O_3 MR difference were observed for the lower inlet levels. The largest difference was for the 4 m inlet being ~ 14 ppbv at night and ~ 28 ppbv (double as much) during day time. The campaign average ozone MRs are depicted in *Figure 4.10*. The vertical profiles of ozone were measured using a TEI 49C ozone analyzer at the SMEAR II tower.

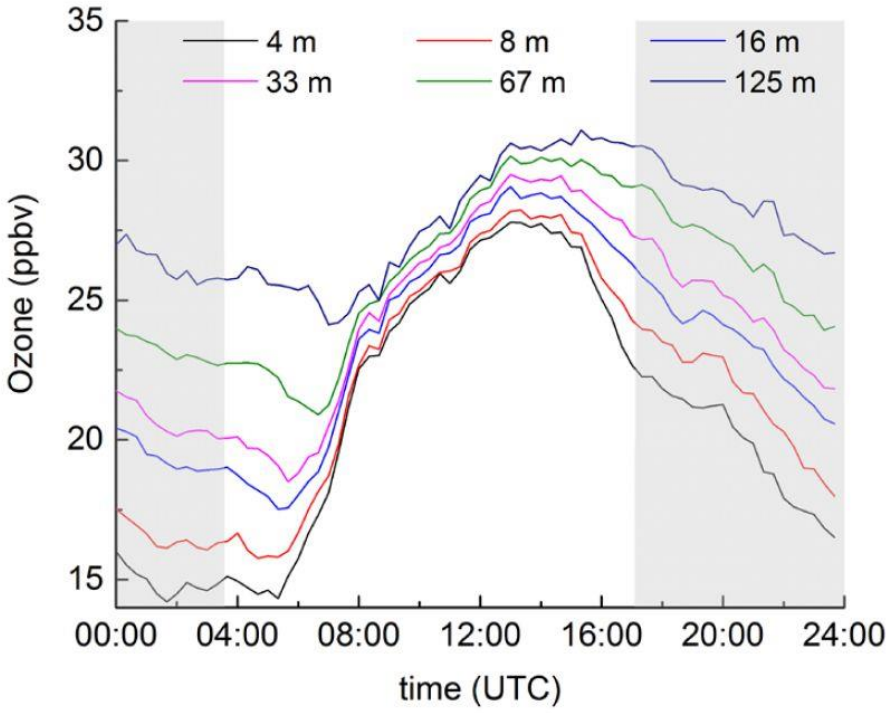

Figure 4.10 Campaign averaged diel cycle of ozone MRs at 6 different heights (4 to 125 m) measured at the SMEAR II tower. Gray rectangles represent the dark hours without direct sunlight. Figure as in Liebmann *et al*. 2018b supplement.

The largest day and night ozone differences were observed for the lowest heights, below and around the canopy. Tropospheric ozone is commonly removed by reaction with reactive trace gases (mainly with unsaturated VOCs and NO via addition to the double bond) and near the surface by vegetative stomatal uptake (Emberson *et al.*, 2000) and dry deposition, including losses to surfaces (Zhang, Brook and Vet, 2002) and soil (Stella *et al.*, 2011). Probably the strong temperature inversion measured during most of the nights throughout the campaign (see *Figure 4.4*), accompanied by saturated relative humidity (see *Figure 4.8*) and low wind speeds (see *Figure 4.2*) suggest a weak nocturnal air mixing below the boundary layer and within the canopy. In addition, the inmixing or ventilation with the lowermost boundary layer restricts the input of ozone rich dry air from higher above. This also leads to a nocturnal depletion of trace species which show a net nighttime sink flux on the ground and canopy level, as was seen and discussed for OCS (see *Section 4.4.1*), and the opposite is seen for the trace species which have a net nighttime source flux, causing increased MRs at the lower layer near the ground, for example monoterpenes (see *Section 4.5*).

A strong anti-correlation between NO_3 radical reactivity and O_3 during the campaign suggest a different loss mechanism for the two species. A strong correlation between monoterpenes and NO_3 reactivity was measured throughout the campaign discussed further in *Section 4.5*

and published in (Liebmann *et al.*, 2018a). As discussed in the paper, the O_3 loss with the levels of monoterpenes measured at the site, however, would only explain 2% of the total O_3 loss at nighttime. Thus, the large O_3 losses observed can be attributed to stomatal, surface and soil deposition or chemical sinks which remain unknown. Nocturnal stomatal conductance and ozone uptake by this pathway has been reported previously (Musselman and Minnick, 2000) and is also in agreement which was measured for OCS uptake (see *Section 4.4.1*).

Recent modelling studies using SMEAR II boreal forest measurement site observational data confirm that strong ozone depletion events are associated with a low boundary layer and saturating relative humidity (Zhou *et al.*, 2017; Chen *et al.*, 2018). Zhou *et al*. concluded in 2017 that chemical reactivity pathway plays only an insignificant role for strong O_3 sink events seen at the Hyytiälä site. They suggest the dominant ozone nocturnal sink to be deposition to wet surfaces and canopy at high (> 70%) relative humidity. The nighttime stomatal conductance also suggests a stomatal sink of O_3, which should be further investigated. Nocturnal O_3 uptake is weaker compared to daytime uptake, but still plays a significant role for the ozone budget and is important to include in modelling studies.

The ozone analysis was used to further confirm the shallow nocturnal boundary layer seen in the Finnish boreal forest during late summer / early autumn, and to provide additionally support for the carbonyl sulfide nighttime uptake trends as seen earlier.

4.4.4 CS_2 time series

From organosulfur species also the much shorter lived carbon disulfide was measured with the Entech-GC-AEDIII system. The time series of CS_2 is shown in *Figure 4.11*. Occasional data interruptions were mainly caused by pre-concentration cryogen – liquid nitrogen supply availability, due to the underestimated losses from the industrial scale tanks. In addition, newly developed software bugs and failures played a role. The two longest day long interruptions occurred on midday of September 8 and 15. The carbon disulfide MRs varied between around 0.5 to 5 pptv throughout the campaign. The campaign average CS_2 MR of 1.6 ± 0.4 pptv was measured. The highest MR of 5.3 ± 1.2 pptv was measured on September 9 around 20:00 UTC (23:00 local time). CS_2 did not show a distinct diel pattern as it does not have any known vegetative uptake pathways unlike OCS, as seen in *Figure 4.12*. The main sink of CS_2 in the atmosphere is the reaction with OH radical (Chin and Davis, 1993). Furthermore, no clear correlation between measured CS_2 MR and temperature was observed,

as visible in *Figure 4.11*. In addition, no apparent trend between CS_2 and relative humidity or was comprehended.

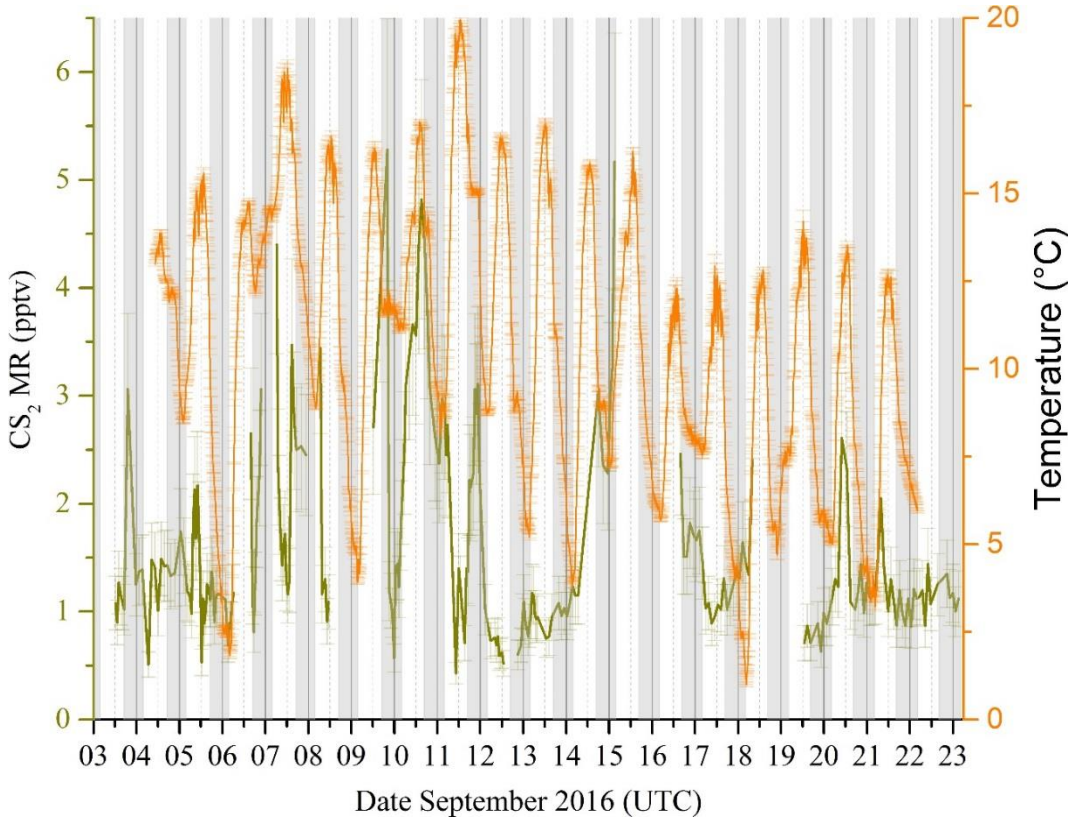

Figure 4.11 Time series of carbon disulfide measured with the Entech-GC-AEDIII system during the IBAIRN 2016 field measurement campaign, shown in olive and overlaid with temperature measurement in orange. The error bars show the 1σ uncertainty. The gray shaded area represents the nighttime.

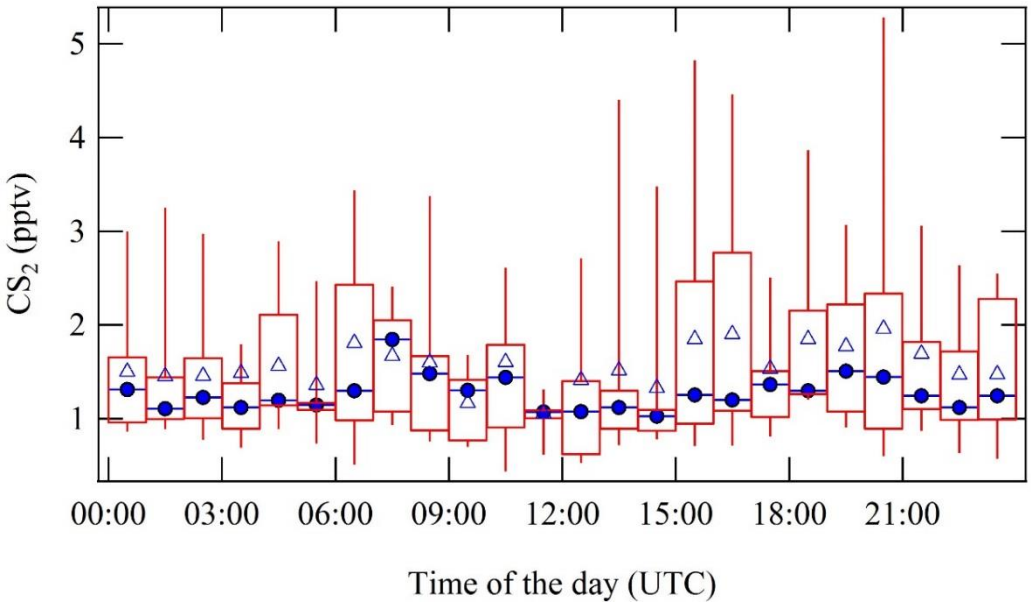

Figure 4.12 Diel cycle of carbon disulfide MRs based on all AEDIII measurements in September 2016. Blue triangles show the overall hourly mean and blue circles represent the hourly median values. The red rectangles with the whiskers indicate the data spread, where 50% of the data falls into the rectangles. The upper whiskers represent the upper 75 percentile data spread and the lower whiskers denote the lower 25 percentile data variation.

4.5 Terpenoids in boreal forest

As the Entech-GC-AEDIII was developed to also measure other VOCs than just organosulfur species, thus it served the IBAIRN 2016 campaign with auxiliary VOC data to support the main goal of this campaign, the reactive nitrogen species analysis. Vegetation and forests emit biogenic volatile organic compounds (BVOCs) in vast quantities. The reactive unsaturated hydrocarbons, terpenoids like isoprene (C_5H_8, methylbuta-1,3-diene), monoterpenes ($C_{10}H_{16}$) and sesquiterpenes ($C_{15}H_{24}$), play a substantial role on the oxidative reactions taking place in the troposphere. Often OH, O_3 and NO_3 determine the atmospheric oxidative capacity, while halogen radicals can under certain circumstances also contribute to it. Furthermore, the BVOCs significantly contribute to the secondary organic aerosol (SOA) formation.

It has been found that total OH reactivity in an Amazonian rainforest dry-season (peaking at 72 s^{-1}) is about three times higher compared to a reactivity in a megacity Beijing (peaking at 26 s^{-1}), emphasizing that BVOCs play a dominant role in global atmospheric reactivity (Williams *et al.*, 2016). During the Amazonian forest wet-season, the total OH reactivity is approximately as fast as in the megacity. In addition, during the Amazonian rainforest dry-season on average 79% unaccounted missing OH reactivity was observed, but only 5 – 15% during the wet-season (Nölscher *et al.*, 2016). Furthermore, at the same Hyytiälä site in 2010 a total missing OH reactivity of 58% was reported for normal conditions and a missing reactivity up to 89% when the forest was under an extensive heat stress (Nölscher *et al.*, 2012). The missing OH radical reactivity has been accounted to unmeasured primary biogenic emissions and to their photochemical oxidation products (Sinha *et al.*, 2010; Nölscher *et al.*, 2016).

It was determined that the NO_3 reactivity measured during the IBAIRN campaign could be explained to a great extent by the monoterpene emissions observed throughout the campaign.

4.5.1 Shallow nocturnal boundary layer

The night-time shallow boundary layer also played an important role for the monoterpene abundance. The combination of the temperature inversion, low wind speeds, air masses coming from south-east and a shallow nocturnal boundary layer could have contributed to a reduced mixing between emission-rich near the surface, including canopy air with drier and more diluted boundary layer air masses. This phenomena effectively traps the emissions into the near the surface air, and enhances the buildup of trace gases in the low layer.

4.5.2 Time series of monoterpenes

The 5 most predominant monoterpenes measured at the Hyytiälä boreal forest were: α-pinene, Δ-3-carene, β-pinene, camphene and d-limonene, plotted in *Figure 4.13*. Two longest measurement breaks (about a day long) occurred on midday of September 8 and 15, as mentioned earlier due to liquid nitrogen availability and no earlier delivery availability.

From the measured monoterpenes, α-pinene's concentration dominated throughout the campaign, with a mean MR of 176 ± 25 pptv. From the abundance Δ-3-carene, β-pinene, camphene and d-limonene followed with a campaign average MR of 98 ± 14, 48 ± 7, 34 ± 5 and 11 ± 2 pptv, respectively. The average 1σ uncertainty resembles the campaign average, geometric mean of the measurement error, calibration standard uncertainty and flow measurement uncertainties. Furthermore, myrcene, linalool and some other monoterpenes were also detected by the Entech-GC-AEDIII system, but in much less abundance.

An especially interesting case study was observed at the night of September 9 and 10, when the emissions from the Korkeakoski sawmill reached the measurement site, which significantly elevated the monoterpene levels. The NOAA HYSPLIT back-trajectory model (GDAS global, 0.5° resolution) was used for the origin of air analysis, which indicated that the air masses passed over Korkeakoski about half an hour prior to reaching the SMEAR II measurement site (Stein *et al.*, 2015). This kind of monoterpene transport from a sawmill has also been reported earlier (Eerdekens *et al.*, 2009).

The diel cycles of the 5 monoterpenes are shown in *Figure 4.15*. In general they show a similar diel cycle like CO_2 (see *Section 4.4.2*) with daytime lows and nighttime highs. The day to day variations are significantly larger for the evening and night. All the 5 monoterpenes show a very similar trend, lowest MRs from 7:00 to 15:00 UTC (10:00 to 18:00 local time) with relatively small deviations. For the remaining ⅔ of the campaign the deviations were larger, depending on the temperature, inversion layer, boundary layer depth, wind direction and speed. On several days limonene showed daily higher peaks at 9:00, 10:00 and 14:00 UTC (12:00, 13:00 and 17:00 local time), which could potentially be associated with anthropogenic emissions as was not seen in the other monoterpene species diel cycles.

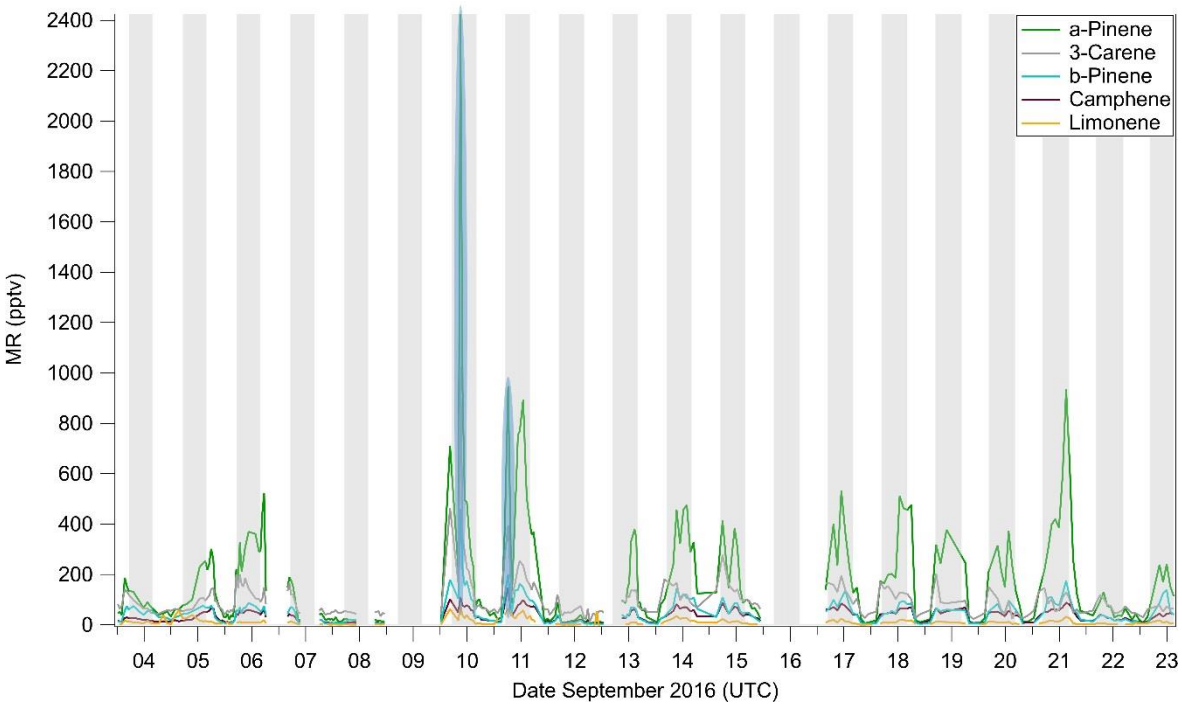

Figure 4.13 Monoterpene time series observed at the SMEAR II Finnish boreal forest measurement site in September 2016, measured with Entech-GC-AEDIII. The campaign maximum monoterpene MRs were measured during the night of September 9 and 10, when the air originated from the Korkeakoski sawmill, represented with the two translucent blue oval areas. Uncertainties are omitted from the graph for clarity, but were about 14% on average.

4.5.3 Time series of isoprene

The time series of isoprene is depicted in *Figure 4.14*. The MRs of isoprene ranged from 2 ± 0.5 to 50.5 ± 12.1 pptv, and a campaign average of 16.5 ± 4 pptv was measured. The diel cycle is included in *Figure 4.15*. The variability was significantly larger. Likewise, isoprene contributed to the NO_3 reactivity, but to much less extent compared to monoterpenes.

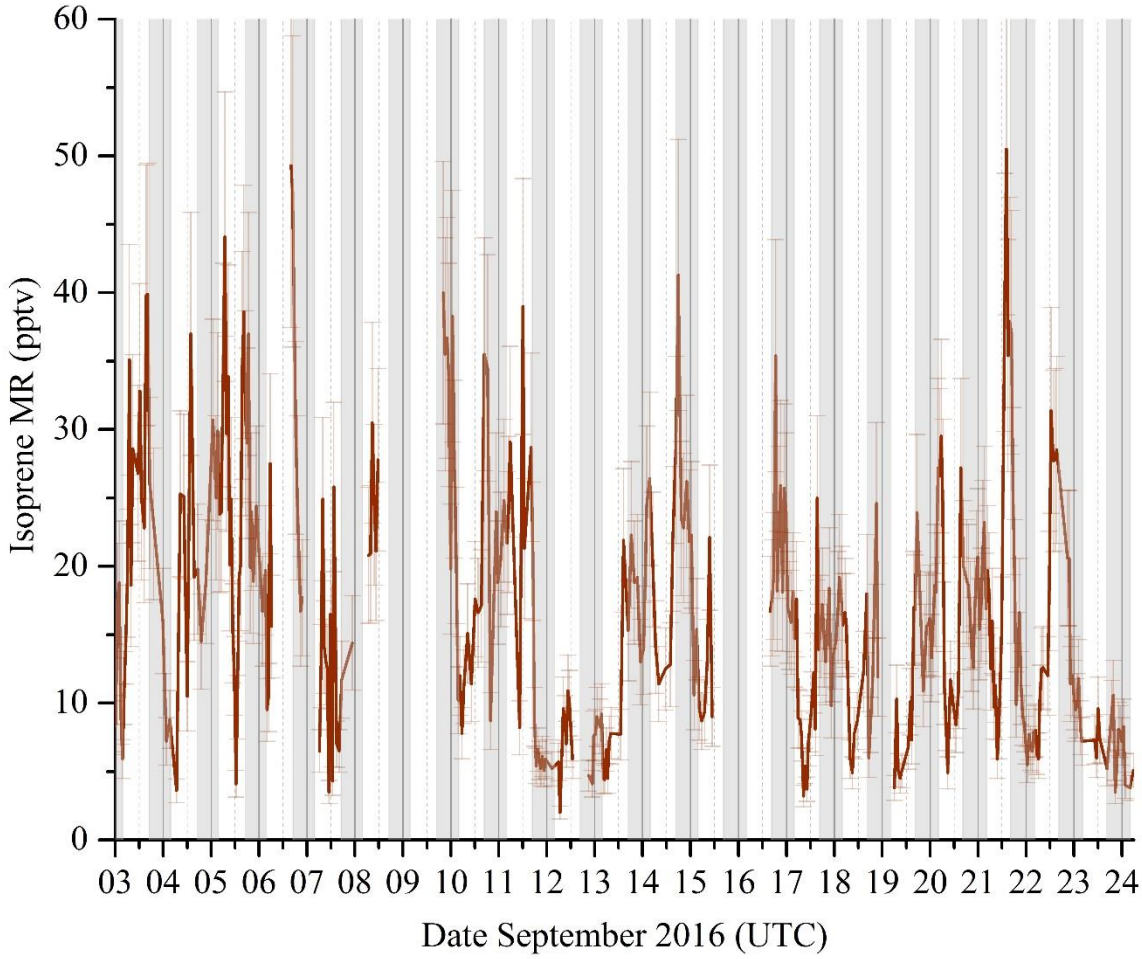

Figure 4.14 Time series of isoprene measured with the Entech-GC-AEDIII system from the 8.5 m MPIC common inlet during the IBAIRN 2016 field measurement campaign. Error bars represent the 1σ uncertainty.

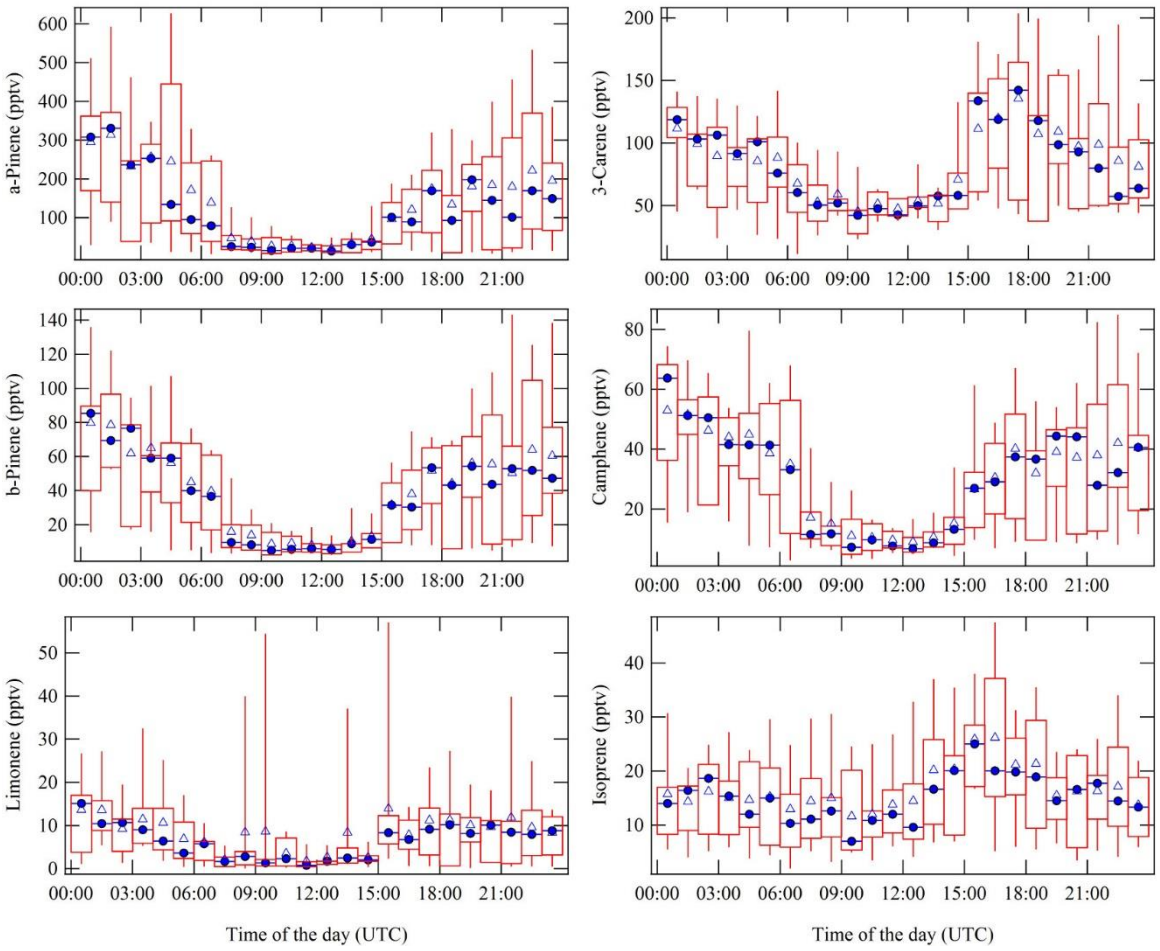

Figure 4.15 Campaign average diel cycles of α-pinene, Δ-3-carene, β-pinene, camphene, d-limonene and isoprene measured from the MPIC common inlet. For not including the sawmill monoterpene emission event, the data from September 9 until 11 6:30 UTC was excluded from the diel cycles. Blue triangles resemble the campaign overall hourly average and blue circles represent the hourly median values. The red rectangles with the whiskers show the data spread, where 50% of the data falls into the rectangles. The upper whiskers signify the upper 75 percentile data spread and the lower whiskers indicate the lower 25 percentile of the data variation. Substantially higher MRs were measured at nighttime compared to day.

4.6 NO_3 radical reactivity in a boreal forest

The nitrate radical (NO_3) is formed by a reaction between NO_2 and O_3, where O_2 is the second product. NO_3 is the main tropospheric oxidant during nighttime. Also, the main nocturnal BVOC loss is initiated by NO_3 radical. The instant photodissociation of NO_3 radical by sunlight and the reaction with NO reduces nitrate radical lifetime typically to a few seconds during daytime. (Brown and Stutz, 2012; Mogensen *et al.*, 2015; Lee Ng *et al.*, 2017) Reactivity is the inverse of the lifetime and measured per time unit, often as s^{-1} for radicals.

The IBAIRN 2016 campaign led to a publication of the "Direct measurement of NO_3 radical reactivity in a boreal forest" paper in the Atmospheric Chemistry and Physics journal in 2018, where I am the second co-author (Liebmann *et al.*, 2018a).

4.6.1 Direct NO_3 radical reactivity measurements

The direct NO_3 radical reactivity measurements at the SMEAR II Finnish boreal forest were conducted with a custom built flow-tube cavity-ring-down spectroscopy (CRDS) instrument described in (Liebmann *et al.*, 2017). At the beginning, 40 – 60 pptv of NO_3 radicals were synthetically created with the reaction between NO_2 and O_3. In turns, either zero-air (to determine the losses in the system) or ambient air was mixed in into a cylindrical flow-tube, which was kept at 21°C. After a reaction time of 10.5 s, the remaining NO_3 was measured by the CRDS instrument at 662 nm. The typical NO_3 radical LOD was 0.7 pptv and the total combined NO_3 uncertainty around 16%. A flow of 2.9 L min^{-1} was used to draw air samples into the system. (Liebmann *et al.*, 2017).

The NO_2 was analyzed by one channel of the thermal dissociation – cavity ring down spectrometer (TD-CRDS) at 405 nm with a LOD of 60 pptv (1 min average) and an uncertainty of 6%. The second channel of the TD-CRDS was measuring at 662 nm and detecting the NO_3 radicals with a LOD of 1.3 pptv (1 min average) with a 25% uncertainty (Sobanski *et al.*, 2016). The NO was analyzed using a modified chemiluminescence detector (CLD 790 SR) based on the reaction between NO and O_3 (ECO Physics, Switzerland). The LOD for NO was 5 pptv (5 s average) with the total average uncertainty of 20% (2σ level) (Li *et al.*, 2015). The O_3 was detected based on optical absorption by two independent instruments. The instruments used were a Thermo Environmental Instruments Inc. Model 49 (USA) and a 2B-Technology Model 202 (USA), both with a LOD of ~ 1 ppbv. The instruments had uncertainties of 2% and 5% (given by producer), respectively. Agreement between the two O_3 measurements was outstanding throughout the campaign with a slope of 1.000 ± 0.001, an offset of 0.21 ppbv and a R^2 correlation of 0.98. The NO_3 reactivity flow-tube CRDS instrument together with the NO_2, NO and O_3 instruments was drawing ambient air from the same MPIC high-flow 8.5 m high common inlet as the Entech-GC-AEDIII system.

The combined data from the instrumentation provided a dynamic measurement range of 0.005 – 45 s^{-1} for the NO_3 loss rate constant with an accuracy between 0.005 – 0.158 s^{-1}, depending mainly on the flow dilution accuracy, NO levels and on the stability of the NO_3

radical source (Liebmann *et al.*, 2017, 2018a). The directly observed NO_3 loss in ambient air was compared against zero-air and converted to a reactivity by numerical simulation of a simple reaction scheme, using *in situ* measured amounts of NO, NO_2 and O_3 (Liebmann *et al.*, 2017). The parameter, k_{OTG} stands for the NO_3 radical reactive loss to organic trace gases (OTG), where the contributions from NO and NO_2 have been removed (Liebmann *et al.*, 2018a). In the publication and throughout this thesis k_{OTG} and NO_3 reactivity are considered as equivalent terms.

4.6.2 Discussion of NO_3 reactivity in boreal forest

In general, surprisingly high NO_3 reactivities were measured in a Finnish boreal forest site during the late summer / early autumn period in 2016 as seen in *Figure 4.17*. The maximum reactivity measured was 0.94 s^{-1} (lifetime of 1.06 s). The highest reactivity was associated with strong temperature inversion, low boundary layer and high level of monoterpenes, as described earlier. Pronounced diel cycles of NO_3 reactivity (see *Figure 4.18*) were observed during the campaign, with campaign average daytime reactivity of 0.04 s^{-1} (lifetime of 25 s) and almost 3 times higher campaign average nocturnal reactivity of 0.11 s^{-1} (lifetime of 9.1 s). The overall campaign median maxima was seen typically at 17:00 UTC (20:00 local time) with a reactivity of 0.14 s^{-1} (lifetime of 7.1 s), and overall median minima typically between 09:00 – 12:00 UTC (12:00 – 15:00 local time) with lifetime of 29 s, i.e. reactivity 0.035 s^{-1}.

The daytime NO_3 reactivity with OTG was large enough to compete with NO_3 radical photolysis and reaction with NO. The simultaneous measurement of BVOCs (see *Section 4.5*) hinted that monoterpenes played a prevailing role on the NO_3 reactivity.

The measured NO_3 reactivity was compared and tried to be constrained by the observed BVOCs and their literature rate constants with the NO_3 radical (Ammann *et al.*, 2017) in a numerical simulation. The 5 most abundant monoterpenes and isoprene measured by the Entech-GC-AEDIII system and their rate constants with the NO_3 radical from the IUPAC summary were combined to determine the k_{AED}, loss rate coefficient time series. It was determined that α-pinene and Δ-3-carene played a dominant role for the NO_3 reactivity, followed to a smaller extent by d-limonene. D-limonene was measured with lowest concentrations of the 5 dominant monoterpenes, but due to its fast reaction with the NO_3 radical the contribution grew more important. The fractional contribution of individual monoterpene species are shown in *Figure 4.16*. The NO_3 reactivity (k_{OTG}) and k_{AED} do not agree within their combined uncertainties. The nocturnal NO_3 reactivity could be explained

by the monoterpene levels measured to around 70% and on average 40% during daytime. The missing reactivity, $k_{OTG} - k_{AED}$, could potentially rise from the point that not all organic trace gases which contribute to the NO_3 reactivity were measured for the k_{AED} determination. Especially important might be sesquiterpenes, which were not measured by the Entech-GC-AEDIII system, whereas levels of already ~ 10 pptv contribute significantly to NO_3 loss rates. (Liebmann *et al.*, 2018a) The missing NO_3 reactivity was significantly lower compared to the missing OH reactivity measured at the same SMEAR II boreal forest site during the HUMPPA-COPEC 2010 (Hyytiälä United Measurements of Photochemistry and Particles in Air – Comprehensive Organic Precursor Emission and Concentration) study in July and August 2010. It has been reported that during HUMPPA-COPEC 2010 89% of the measured OH reactivity was unaccounted from the organic trace gas measurement, during the time when the boreal forest was under a strong temperature stress (Nölscher *et al.*, 2012).

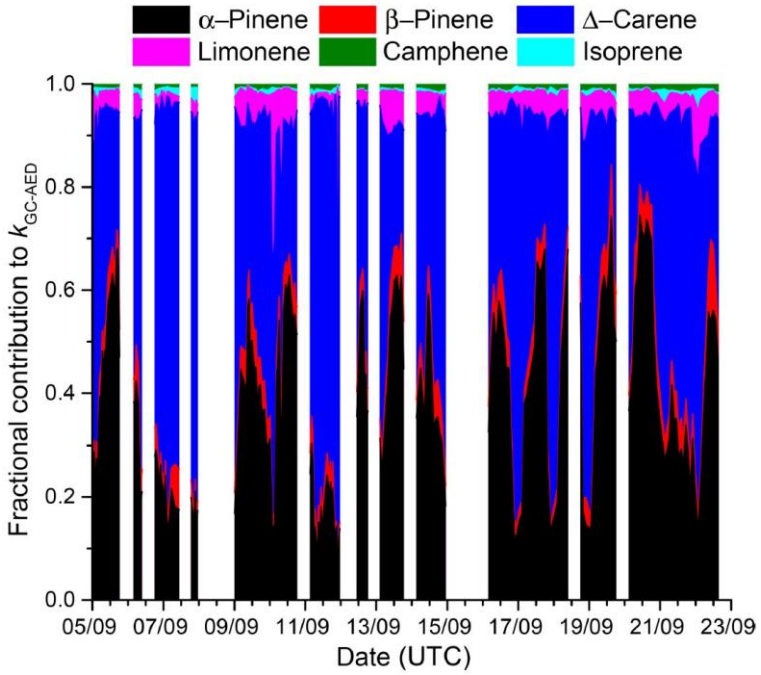

Figure 4.16 Fractional contribution of individual monoterpene species presented in different colors to the total reactivity (k_{AED}) determined by the numerical simulation. Figure as in Liebmann *et al.* 2018a.

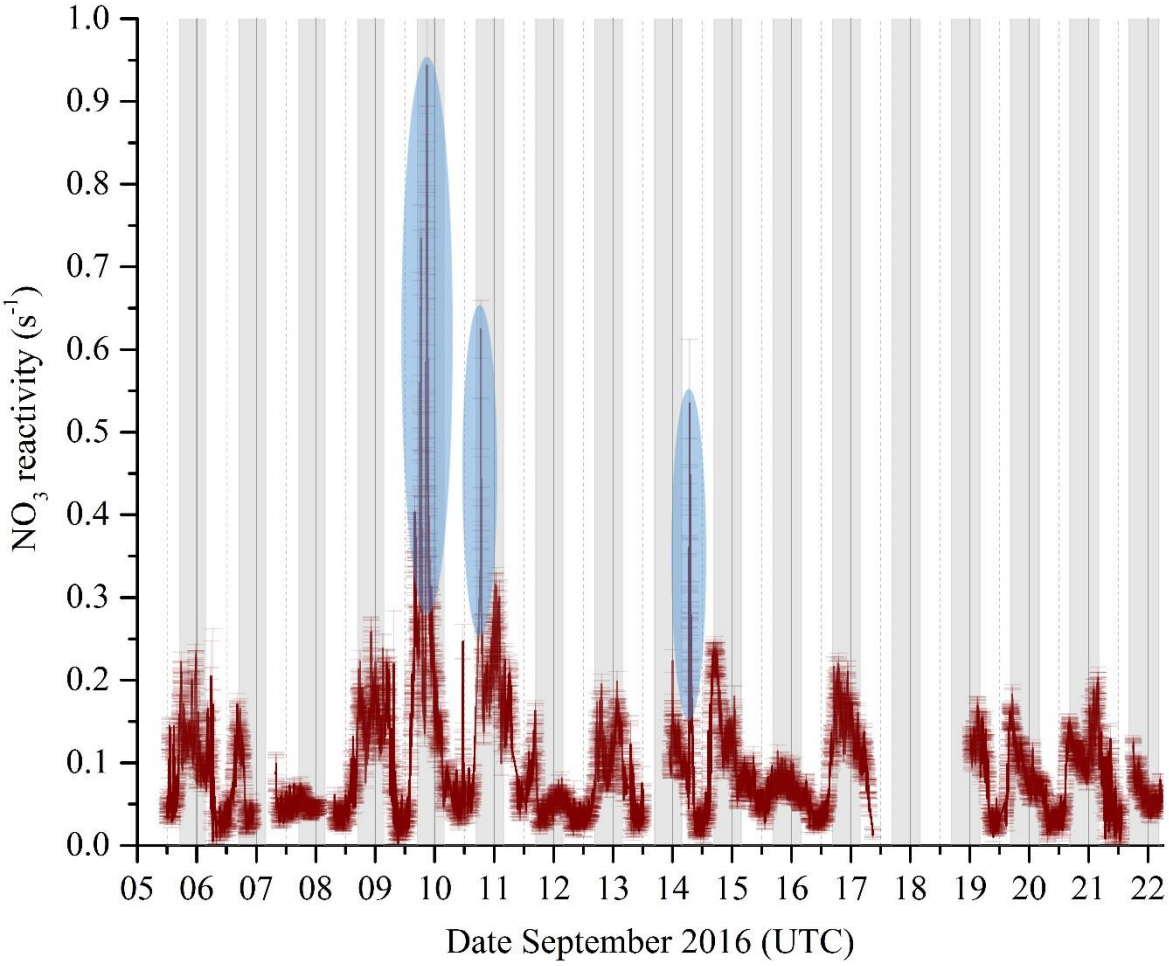

Figure 4.17 Time series of NO_3 reactivity (k_{OTG}) measured in a Finnish boreal forest. The translucent error bars represent the measurement uncertainty. The gray shaded regions show the nighttime. The 3 transparent blue ovals signify the monoterpene emission events as the air from the Korkeakoski sawmill reached the measurement site during the night of September 9 and 10, as discussed in *Section 4.5.2*.

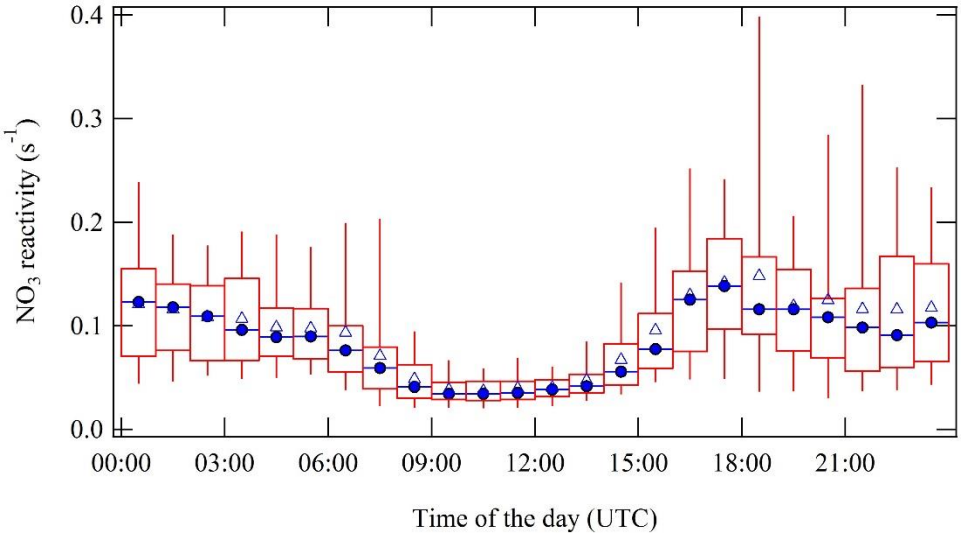

Figure 4.18 Whole IBAIRN 2016 campaign daily average diel cycle of NO_3 reactivity measured from the MPIC 8.5 m common inlet. Blue triangles show the overall hourly mean and blue circles show the hourly median values. The red rectangles with the whiskers show the data spread, where 50% of the data falls into the rectangles. The upper whiskers represent the upper 75 percentile data spread and the lower whiskers denote the lower 25 percentile data variation.

4.7 IBAIRN 2016 campaign summary

The field measurement campaign IBAIRN, which took place at the Finnish boreal forest measurement station SMEAR II, Hyytiälä in September 2016 was the first employment of the new Entech-GC-AEDIII analytical system in the field. The system proved to be able to measure various VOCs, like organosulfur species, monoterpenes, NMHCs and other species in near real-time with low detection limits. From sulfur species in the boreal forest the system was able to detect OCS and CS_2. The measured OCS data confirms the nocturnal OCS uptake by vegetation shown by Kooijmans *et al*. in 2017. Furthermore, the newly developed instrument was able to quantify speciated key monoterpenes necessary for the analysis of the NO_3 reactivity data.

The significant limitation of this instrument, as a field campaign device, is the large liquid nitrogen consumption (about 2.5 L h^{-1}) and low sample throughput resolution (on average 1 h 22 min). In addition, regular software crashes complicated the continuous measurements even further, but probably this shortcoming could be overcame with more mature software versions. The advantage, on the other hand is the element specific emission lines for easier compound identification and the ability to measure some VOCs which are not detectable with a FID instrument, e.g. carbonyl sulfide. No volatile traces compounds containing other elements than sulfur, carbon or nitrogen were measured over the Entech-GC-AEDIII detection limit, including bromine, iodine, silicon, mercury, selenium or arsenic.

The campaign was characterized by strong nocturnal temperature inversions and relative humidity up to 100% for most of the nights. The nighttime low boundary layer combined with low wind speeds reduced the mixing of near the surface layer air with the drier and less VOCs containing boundary layer and free troposphere air. This led to a nocturnal accumulation of VOCs (i.e. terpenoids) into the near the surface and canopy air layer, which have a source at the ground level or to a depletion (i.e. OCS), which has a vegetative sink at the surface by vegetation.

Throughout the campaign, an average OCS MR of 310 ± 61 pptv and CS_2 MR of 1.53 ± 0.86 pptv were measured, where the ± represents the 1σ variation throughout the recorded dataset. The northern hemisphere yearly average surface MR of OCS is 476 pptv, which is significantly larger than which was observed during the campaign. The global 3D chemistry EMAC model is prescribed with an OCS MR of 407 pptv at the surface for September in the specific bin where also Hyytiälä location falls into, which is significantly (31%) larger than the observed OCS MRs during the campaign. This justifies the substantially stronger

vegetation sink suggested by Sandoval-Soto *et al*. in 2005. Furthermore, nocturnal OCS uptake continuation in a boreal forest was measured for all the nights, confirming the nighttime stomatal conductance and the light independence of the carbonic anhydrase enzyme. It has been estimated that the vegetative nighttime OCS uptake accounts to around 17% of the daily uptake (Kooijmans *et al.*, 2017), thus plays a significant role on the OCS budget. The light independence of the CA enzyme and thereby nocturnal uptake of OCS by vegetation further complicates the use of OCS as gross primary productivity tracer. Thus, further nighttime OCS uptake measurements are required in various regions with various vegetation and over different seasons for accurate nocturnal uptake parametrization to use OCS as GPP tracer.

Furthermore, it was found out that monoterpenes were dominating the nocturnal directly measured NO_3 radical reactivity and also during the daytime monoterpenes played a substantial role on the NO_3 reactivity. It was determined that on average about 70% of the directly measured NO_3 reactivity measured by the CRDS instrument could be explained by observed monoterpene levels at nighttime and on average 40% during the daytime.

5 CONCLUSIONS

Throughout this PhD thesis work a new analytical gas phase measurement system was established based on gas chromatography, termed Entech-GC-AEDIII. The instrument is based on cryogenic gas sample pre-concentration, GC separation and on atomic emission detection. This is the first instrument for gas phase sample measurement based on an AED. A method was established for simultaneous measurements of compounds in the C3 – C14 range. The system proved to be sensitive on the pptv (pg L^{-1}) level for various VOCs and was especially sensitive for sulfur containing species. The Entech-GC-AEDIII demonstrated an equimolar and linear response on a compound specific basis and also allowed for a compound independent calibration via per atom response factors. The drawbacks of the system are high liquid nitrogen and helium consumption and particularly importantly the short lifetime of the helium plasma discharge tube.

The Entech-GC-AEDIII system was effective in measuring canisters containing whole air samples from UT/LMS region collected from on board the IAGOS-CARIBIC aircraft. The system demonstrated the ability to measure organosulfur species, NMHCs, halogenated compounds etc., some which are not detectable with a FID instrument. Furthermore, the instrument was applied on a field measurement campaign in a Finnish boreal forest in September 2016 for near real-time measurements of various VOCs including OCS, CS_2 and terpenoids like isoprene, α-pinene, Δ-3-carene, β-pinene, camphene and d-limonene.

For the work presented here, from the samples collected on board the CARIBIC aircraft with a global coverage between December 2015 till December 2018, the carbonyl sulfide molecule proved to be the most interesting species for this study. During that period 708 whole air samples from CARIBIC TRAC and HIRES samplers were successfully analyzed on the Entech-GC-AEDIII system. A mean OCS MR of 460.7 ± 27.2 pptv in the UT and an average LMS OCS MR of 383.1 ± 23.4 pptv was measured, varying significantly spatially and temporally.

From the CARIBIC OCS analysis a global average tropospheric OCS lifetime of 2.1 ± 1.3 years through the variability analysis of other measured trace gases with well-known lifetimes. A substantially longer stratospheric lifetime of 47 ± 16 years were determined by N_2O and OCS tracer-tracer correlation in the LMS. In addition, an OCS flux from the

troposphere into the stratosphere of 118 ± 39 Gg (S) yr^{-1} was estimated. A stratospheric sink of OCS was estimated as 44 – 90 Gg (S) yr^{-1} from the computed stratospheric lifetime. The 43% smaller sink compared to the flux serves as a 51 Gg (S) yr^{-1} estimate of the OCS fraction which is transported back from the stratosphere to the troposphere.

The global 3D atmospheric chemistry EMAC model was used to run the numerical calculations to determine OCS MRs and sampled at the CARIBIC flight paths. A comparison between CARIBIC observations and EMAC model simulations led to a conclusion that the EMAC model significantly overestimates OCS MRs in the upper atmosphere. This result suggests that sulfur chemistry in the model should be revised and known sinks should be added to the model, rather than only nudging ground based observations to the model surface data.

The IBAIRN 2016 boreal forest campaign was characterized by strong nocturnal temperature inversions, relative humidity up to 100%, low nighttime boundary layer and low wind speeds. This resulted a reduced mixing of near the surface and canopy layer air with the drier free tropospheric air. This caused a nocturnal buildup of species concentration which have a source at the ground or in the canopy, like was seen with monoterpenes or to a nighttime depletion for species which have a sink. Throughout the campaign, an average OCS MR of 310 pptv was measured which is significantly lower compared to the 407 pptv, which is used to describe the EMAC model at the corresponding model grid bin. Furthermore, it was observed that nighttime OCS uptake continues, which confirms the stomatal opening or only partial closure at night and the light independence of the OCS fixing carbonic anhydrase enzyme. Thus, this work confirms the recent literature studies claiming substantially stronger vegetation sinks.

In addition, it was found using the same Entech-GC-AEDIII system that monoterpenes played a dominant role on the NO_3 radical reactivity. It was analyzed that on average around 70% of the directly measured NO_3 reactivity could be explained by the Entech-GC-AEDIII measured monoterpene levels at nighttime and on average 40% during the daytime.

6 SUGGESTIONS FOR FUTURE STUDIES

Here I would recommend some topics which could further develop the knowledge and understanding of global sulfur cycle. As the carbonyl sulfide budget to a large extent still remains unbalanced, it is important to continue research into the OCS molecule.

- The kinetic conversion efficiencies of shorter lived organosulfur species (DMS, CS_2 etc.) in the atmosphere are not well established and remain with high uncertainties, originate from more than two decades ago. I would strongly recommend lab based kinetic studies of DMS and CS_2 for finding out more accurate reaction pathways and conversion efficiencies into OCS.
- The OCS vegetative sink proved to be strong as some literature have suggested, thus it is more likely that there is rather a missing or underestimated source of OCS and the sinks are not overestimated. Therefore, I would suggest more oceanic measurements in the regions where there is current lack of knowledge, especially in the Southern Ocean and Pacific Ocean. These emissions include direct OCS emissions and indirectly through DMS and CS_2 atmospheric processing.
- The 3D global chemistry model EMAC has a significantly outdated sulfur compound chemistry reaction pathway scheme. This new scheme should definitely include OCS production via DMS and CS_2 atmospheric processing pathways. Furthermore, the known sources and sinks of OCS should be added into the EMAC model rather than nudging the surface with observational OCS data.
- Last but not least, isotopic studies of OCS should be conducted, which could make the search of the potential missing source easier via enabling the separation of natural and anthropogenic OCS fraction.

A REFERENCES

Abernethy, R., Ackerman, S. A., Adler, R., Albanil Encarnación, A., Aldeco, L. S., Alfaro, E. J., Aliaga-Nestares, V., Allan, R. P., Allan, R., Alves, L. M., Amador, J. A., Anderson, J., Andreassen, L. M., Argüez, A., Armitage, C., Arndt, D. S., McVicar, T. R., *et al.* (2018) 'State of the climate in 2017', *Bulletin of the American Meteorological Society*.

Akritas, M. G., Murphy, S. A. and LaValley, M. P. (1995) 'The Theil-Sen estimator with doubly censored data and applications to astronomy', *Journal of the American Statistical Association*.

Ammann, M., Cox, R. A., Crowley, J. N., Herrmann, H., Jenkin, M. E., McNeill, V. F., Mellouki, A., Rossi, M. J., Troe, J. and Wallington, T. J. (2017) *IUPAC - Task Group on Atmospheric Chemical Kinetic Data Evaluation*. Available at: http://iupac.pole-ether.fr (Accessed: 28 March 2019).

Andreae, M. O. and Crutzen, P. J. (1997) 'Atmospheric aerosols: Biogeochemical sources and role in atmospheric chemistry', *Science*.

Appenzeller, C. and Davies, H. C. (1992) 'Structure of stratospheric intrusions into the troposphere', *Nature*.

Asaf, D., Rotenberg, E., Tatarinov, F., Dicken, U., Montzka, S. A. and Yakir, D. (2013) 'Ecosystem photosynthesis inferred from measurements of carbonyl sulphide flux', *Nature Geoscience*.

Aydin, M., Williams, M. B., Tatum, C. and Saltzman, E. S. (2008) 'Carbonyl sulfide in air extracted from a South Pole ice core: A 2000 year record', *Atmospheric Chemistry and Physics*.

Aydin, M., Fudge, T. J., Verhulst, K. R., Nicewonger, M. R., Waddington, E. D. and Saltzman, E. S. (2014) 'Carbonyl sulfide hydrolysis in antarctic ice cores and an atmospheric history for the last 8000 years', *Journal of Geophysical Research*.

Aydin, M., Campbell, J. E., Fudge, T. J., Cuffey, K. M., Nicewonger, M. R., Verhulst, K. R. and Saltzman, E. S. (2016) 'Changes in atmospheric carbonyl sulfide over the last 54,000 years inferred from measurements in Antarctic ice cores', *Journal of Geophysical Research*.

Baker, A. K., Slemr, F. and Brenninkmeijer, C. A. M. (2010) 'Analysis of non-methane hydrocarbons in air samples collected aboard the CARIBIC passenger aircraft', *Atmospheric Measurement Techniques*.

Baldwin, B., Pollack, J. B., Summers, A., Toon, O. B., Sagan, C. and Van Camp, W. (1976) 'Stratospheric aerosols and climatic change', *Nature*.

Barkley, M. P., Palmer, P. I., Boone, C. D., Bernath, P. F. and Suntharalingam, P. (2008) 'Global distributions of carbonyl sulfide in the upper troposphere and stratosphere', *Geophysical Research Letters*.

Barnes, I., Becker, K. H. and Patroescu, I. (1994) 'The tropospheric oxidation of dimethyl sulfide: A new source of carbonyl sulfide', *Geophysical Research Letters*.

Beenaker, C. I. M. (1977) 'Evaluation of a microwave-induced plasma in helium at atmospheric pressure as an element-selective detector for gas chromatography', *Spectrochimica Acta Part B: Atomic Spectroscopy*.

Bell, M. L. and Davis, D. L. (2001) 'Reassessment of the lethal London fog of 1952: Novel indicators of acute and chronic consequences of acute exposure to air pollution', *Environmental Health Perspectives*.

Berry, J., Wolf, A., Campbell, J. E., Baker, I., Blake, N., Blake, D., Denning, A. S., Kawa, S. R., Montzka, S. A., Seibt, U., Stimler, K., Yakir, D. and Zhu, Z. (2013) 'A coupled model of the global cycles of carbonyl sulfide and CO2: A possible new window on the carbon cycle', *Journal of Geophysical Research: Biogeosciences*.

Bethan, S., Vaughan, G. and Reid, S. J. (1996) 'A comparison of ozone and thermal tropopause heights and the impact of tropopause definition on quantifying the ozone content of the troposphere', *Quarterly Journal of the Royal Meteorological Society*.

Bluth, G. J. S., Doiron, S. D., Schnetzler, C. C., Krueger, A. J. and Walter, L. S. (1992) 'Global tracking of the SO2 clouds from the June, 1991 Mount Pinatubo eruptions', *Geophysical Research Letters*.

Bond, T. C., Streets, D. G., Yarber, K. F., Nelson, S. M., Woo, J. H. and Klimont, Z. (2004) 'A technology-based global inventory of black and organic carbon emissions from combustion', *Journal of Geophysical Research: Atmospheres*.

Brandt, J. P., Flannigan, M., Maynard, D. G., Thompson, I. and Volney, W. J. a (2013) 'An introduction to Canada's boreal zone: Ecosystem processes, health , sustainability, and environmental issues', *Environmental Reviews*.

Brenninkmeijer, C. A. M., Crutzen, P., Boumard, F., Dauer, T., Dix, B., Ebinghaus, R., Filippi, D., Fischer, H., Franke, H., Frieß, U., Heintzenberg, J., Helleis, F., Hermann, M., Kock, H. H., Koeppel, C., Lelieveld, J., Leuenberger, M., Martinsson, B. G., Miemczyk, S., Moret, H. P., Nguyen, H. N., Nyfeler, P., Oram, D., O'Sullivan, D., Penkett, S., Platt, U., Pupek, M., Ramonet, M., Randa, B., Reichelt, M., Rhee, T. S., Rohwer, J., Rosenfeld, K., Scharffe, D., Schlager, H., Schumann, U., Slemr, F., Sprung, D., Stock, P., Thaler, R., Valentino, F., van Velthoven, P., Waibel, A., Wandel, A., Waschitschek, K., Wiedensohler, A., Xueref-Remy, I., Zahn, A., Zech, U. and Ziereis, H. (2007) 'Civil Aircraft for the regular investigation of the atmosphere based on

an instrumented container: The new CARIBIC system', *Atmospheric Chemistry and Physics*.

Brito, J. (2011) *A Lightweight High-sensitivity Chemical Mass Spectrometer for Organic Compounds, Physics department*.

Brown, S. S. and Stutz, J. (2012) 'Nighttime radical observations and chemistry', *Chemical Society Reviews*.

Brühl, C., Lelieveld, J., Crutzen, P. J. and Tost, H. (2012) 'The role of carbonyl sulphide as a source of stratospheric sulphate aerosol and its impact on climate', *Atmospheric Chemistry and Physics*.

Buck, A. L. (1981) 'New Equations for Computing Vapor Pressure and Enhancement Factor', *Journal of Applied Meteorology*.

Budyko, M. I. (1977) 'Climatic Changes', *American Geophysical Society*.

Bundke, U., Berg, M., Houben, N., Ibrahim, A., Fiebig, M., Tettich, F., Klaus, C., Franke, H. and Petzold, A. (2015) 'The IAGOS-CORE aerosol package: Instrument design, operation and performance for continuous measurement aboard in-service aircraft', *Tellus, Series B: Chemical and Physical Meteorology*.

Bunk, R., Behrendt, T., Yi, Z., Andreae, M. O. and Kesselmeier, J. (2017) 'Exchange of carbonyl sulfide (OCS) between soils and atmosphere under various CO2 concentrations', *Journal of Geophysical Research: Biogeosciences*.

Burkholder, J. B., Sander, S. P., Abbatt, J., Barker, J. R., Huie, R. E., Kolb, C. E., Kurylo, M. J., Orkin, V. L., Wilmouth, D. M. and Wine, P. H. (2015) 'Chemical Kinetics and Photochemical Data for Use in Atmospheric Studies Evaluation Number 18', *Jet Propulsion Laboratory*.

Campbell, J. E., Carmichael, G. R., Chai, T., Mena-Carrasco, M., Tang, Y., Blake, D. R., Blake, N. J., Vay, S. A., Collatz, G. J., Baker, I., Berry, J. A., Montzka, S. A., Sweeney, C., Schnoor, J. L. and Stanier, C. O. (2008) 'Photosynthetic control of atmospheric carbonyl sulfide during the growing season', *Science*.

Campbell, J. E., Whelan, M. E., Seibt, U., Smith, S. J., Berry, J. A. and Hilton, T. W. (2015) 'Atmospheric carbonyl sulfide sources from anthropogenic activity: Implications for carbon cycle constraints', *Geophysical Research Letters*.

Cantrell, C. A. (2008) 'Technical Note: Review of methods for linear least-squares fitting of data and application to atmospheric chemistry problems', *Atmospheric Chemistry and Physics*.

Chen, X., Quéléver, L. L. J., Fung, P. L., Kesti, J., Rissanen, M. P., Bäck, J., Keronen, P., Junninen, H., Petäjä, T., Kerminen, V. M. and Kulmala, M. (2018) 'Observations of ozone depletion events in a Finnish boreal forest', *Atmospheric Chemistry and Physics*.

Chin, M. and Davis, D. D. (1993) 'Global sources and sinks of OCS and CS2 and their

distributions', *Global Biogeochemical Cycles*.

Chin, M. and Davis, D. D. (1995) 'A reanalysis of carbonyl sulfide as a source of stratospheric background sulfur aerosol', *Journal of Geophysical Research*.

Crutzen, P. J. (1976) 'The possible importance of CSO for the sulfate layer of the stratosphere', *Geophysical Research Letters*.

Crutzen, P. J. (2006a) 'Albedo Enhancement by Stratospheric Sulfur Injections: A Contribution to Resolve a Policy Dilemma?', *Climatic Change*.

Crutzen, P. J. (2006b) 'The "Anthropocene"', *Earth System Science in the Anthropocene*.

Curtius, J., Weigel, R., Vössing, H. J., Wernli, H., Werner, A., Volk, C. M., Konopka, P., Krebsbach, M., Schiller, C., Roiger, A., Schlager, H., Dreiling, V. and Borrmann, S. (2005) 'Observations of meteoric material and implications for aerosol nucleation in the winter Arctic lower stratosphere derived from in situ particle measurements', *Atmospheric Chemistry and Physics*.

Daubert, T. E. and Danner, R. P. (1989) 'Physical and thermodynamic properties of pure chemicals: data compilation', *DC: Taylor & Francis;*

Davis, D. L. (2002) *When smoke ran like water: Tales of environmental deception and the battle against pollution*. New York Basic Books.

Deshler, T. (2008) 'A review of global stratospheric aerosol: Measurements, importance, life cycle, and local stratospheric aerosol', *Atmospheric Research*.

Van Diest, H. and Kesselmeier, J. (2008) 'Soil atmosphere exchange of carbonyl sulfide (COS) regulated by diffusivity depending on water-filled pore space', *Biogeosciences*.

Ditas, J., Ma, N., Zhang, Y., Assmann, D., Neumaier, M., Riede, H., Karu, E., Williams, J., Scharffe, D., Wang, Q., Saturno, J., Schwarz, J. P., Katich, J. M., McMeeking, G. R., Zahn, A., Hermann, M., Brenninkmeijer, C. A. M., Andreae, M. O., Pöschl, U., Su, H. and Cheng, Y. (2018) 'Strong impact of wildfires on the abundance and aging of black carbon in the lowermost stratosphere', *Proceedings of the National Academy of Sciences*.

Douwes, J., Thorne, P., Pearce, N. and Heederik, D. (2003) 'Bioaerosol health effects and exposure assessment: Progress and prospects', in *Annals of Occupational Hygiene*.

Dyroff, C., Fütterer, D. and Zahn, A. (2010) 'Compact diode-laser spectrometer ISOWAT for highly sensitive airborne measurements of water-isotope ratios', *Applied Physics B: Lasers and Optics*.

Eerdekens, G., Yassaa, N., Sinha, V., Aalto, P. P., Aufmhoff, H., Arnold, F., Fiedler, V., Kulmala, M. and Williams, J. (2009) 'VOC measurements within a boreal forest during spring 2005: On the occurrence of elevated monoterpene concentrations during night time intense particle

concentration events', *Atmospheric Chemistry and Physics*.

Elkins, J., Dlugokencky, E., Hall, B., Dutton, G., Nance, D. and Mondeel, D. (2018) 'National Oceanic and Atmospheric Administration Earth System Research Laboratory (NOAA/ESRL) Combined Global Halocarbons & other Atmospheric Trace Species Group (HATS) Nitrous Oxide Data File'.

Elliott, S., Lu, E. and Rowland, F. S. (1989) 'Rates and Mechanisms for the Hydrolysis of Carbonyl Sulfide in Natural Waters', *Environmental Science and Technology*.

Emberson, L. D., Ashmore, M. R., Cambridge, H. M., Simpson, D. and Tuovinen, J. P. (2000) 'Modelling stomatal ozone flux across Europe', in *Environmental Pollution*.

European Comission (2003) 'Indoor air pollution: new EU research reveals higher risks than previously thought', *European Comission*.

Filges, A., Gerbig, C., Chen, H., Franke, H., Klaus, C. and Jordan, A. (2015) 'The IAGOS-core greenhouse gas package: A measurement system for continuous airborne observations of CO2, CH4, H2O and CO', *Tellus, Series B: Chemical and Physical Meteorology*.

von Glasow, R. (2010) 'Atmospheric chemistry in volcanic plumes', *Proceedings of the National Academy of Sciences*.

Goulette, M., Brown, S., Dinesan, H., Dubbé, W., Hübler, G., Orphal, J., Ruth, A. and Zahn, A. (2016) 'A New Cavity Ring-down Instrument for Airborne Monitoring of N2O5, NO3, NO2 and O3 in the Upper Troposphere Lower Stratosphere', in *Imaging and Applied Optics 2016*.

Graedel, T. E. (1977) 'The homogeneous chemistry of atmospheric sulfur', *Reviews of Geophysics*.

Güsten, H., Heinrich, G., Mönnich, E., Nolle, M. and Weppner, J. (2003) 'Two automated ozone analyzers for use on civil aircraft operating in the tropopause region', *Journal of Atmospheric and Oceanic Technology*.

Hakola, H., Hellén, H., Hemmilä, M., Rinne, J. and Kulmala, M. (2012) 'In situ measurements of volatile organic compounds in a boreal forest', *Atmospheric Chemistry and Physics*.

Hallquist, M., Wenger, J. C., Baltensperger, U., Rudich, Y., Simpson, D., Claeys, M., Dommen, J., Donahue, N. M., George, C., Goldstein, A. H., Hamilton, J. F., Herrmann, H., Hoffmann, T., Iinuma, Y., Jang, M., Jenkin, M. E., Jimenez, J. L., Kiendler-Scharr, A., Maenhaut, W., McFiggans, G., Mentel, T. F., Monod, A., Prévôt, A. S. H., Seinfeld, J. H., Surratt, J. D., Szmigielski, R. and Wildt, J. (2009) 'The formation, properties and impact of secondary organic aerosol: Current and emerging issues', *Atmospheric Chemistry and Physics*.

Hari, P., Nikinmaa, E., Pohja, T., Siivola, E., Bäck, J., Vesala, T. and Kulmala, M. (2013) 'Station for measuring ecosystem-atmosphere relations: SMEAR', in *Physical and Physiological Forest*

Ecology.

Hari, P. and Kulmala, M. (2005) 'Station for measuring ecosystem-atmophere relations (SMEAR II)', *Boreal Environment Research*.

Hermann, M., Weigelt, A., Assmann, D., Pfeifer, S., Müller, T., Conrath, T., Voigtländer, J., Heintzenberg, J., Wiedensohler, A., Martinsson, B. G., Deshler, T., Brenninkmeijer, C. A. M. and Zahn, A. (2016) 'An optical particle size spectrometer for aircraft-borne measurements in IAGOS-CARIBIC', *Atmospheric Measurement Techniques*.

Hermann, M. and Wiedensohler, A. (2001) 'Counting efficiency of condensation particle counters at low-pressures with illustrative data from the upper troposphere', *Journal of Aerosol Science*.

Hirsch, A. I., Michalak, A. M., Bruhwiler, L. M., Peters, W., Dlugokencky, E. J. and Tans, P. P. (2006) 'Inverse modeling estimates of the global nitrous oxide surface flux from 1998-2001', *Global Biogeochemical Cycles*.

Höpfner, M., Glatthor, N., Grabowski, U., Kellmann, S., Kiefer, M., Linden, A., Orphal, J., Stiller, G., Von Clarmann, T., Funke, B. and Boone, C. D. (2013) 'Sulfur dioxide (SO2) as observed by MIPAS/Envisat: Temporal development and spatial distribution at 15-45 km altitude', *Atmospheric Chemistry and Physics*.

Houghton, J. T., Ding, Y., Griggs, D. J., Noguer, M., van der Linden, P. J., Dai, X., Maskell, K. and Johnson, C. (2001) 'Intergovernmental Panel on Climate Change (IPCC) Climate Change 2001 report: The Scientific Basis', *Climate Change 2001: The Scientific Basis*.

Hoyle, C. R., Boy, M., Donahue, N. M., Fry, J. L., Glasius, M., Guenther, A., Hallar, A. G., Huff Hartz, K., Petters, M. D., Petäjä, T., Rosenoern, T. and Sullivan, A. P. (2011) 'A review of the anthropogenic influence on biogenic secondary organic aerosol', *Atmospheric Chemistry and Physics*.

Huang, J., Golombeck, A., Prinn, R., Weiss, R., Fraser, P., Simmonds, P., Dlugokencky, E. J., Hall, B., Elkins, J., Steele, P., Langenfelds, R., Krummel, P., Dutton, G. and Porter, L. (2008) 'Estimation of regional emissions of nitrous oxide from 1997 to 2005 using multinetwork measurements, a chemical transport model, and an inverse method', *Journal of Geophysical Research Atmospheres*.

Ilvesniemi, H., Levula, J., Ojansuu, R., Kolari, P., Kulmala, L., Pumpanen, J., Launiainen, S., Vesala, T. and Nikinmaa, E. (2009) 'Long-term measurements of the carbon balance of a boreal Scots pine dominated forest ecosystem.', *Boreal Environmental Research*.

IPCC (2014) *Climate Change 2014: Synthesis Report. Contribution of Working Groups I, II and III to the Fifth Assessment Report of the Intergovernmental Panel on Climate Change, Core Writing Team, R.K. Pachauri and L.A. Meyer*.

Jacob, D. J. (1999) *Introduction to Atmospheric Chemistry*. 1st edn. Princeton University Press.

Jobson, B. T., Parrish, D. D., Goldan, P., Kuster, W., Fehsenfeld, F. C., Blake, D. R., Blake, N. J. and Niki, H. (1998) 'Spatial and temporal variablity of nonmethane hydrocarbon mixing ratios and their relation to photochemical lifetime', *Journal of Geophysical Research Atmospheres*.

Jöckel, P., Kerkweg, A., Pozzer, A., Sander, R., Tost, H., Riede, H., Baumgaertner, A., Gromov, S. and Kern, B. (2010) 'Development cycle 2 of the Modular Earth Submodel System (MESSy2)', *Geoscientific Model Development*.

Joint Analytical Systems GmbH (2017a) *AEDIII Specifications*. Available at: https://www.jas.de/en/products/jas/aed/aed3/ (Accessed: 8 August 2018).

Joint Analytical Systems GmbH (2017b) *AEDIII User Manual*.

Jones, A. M. and Harrison, R. M. (2004) 'The effects of meteorological factors on atmospheric bioaerosol concentrations - A review', *Science of the Total Environment*.

Junge, C. E. (1974) 'Residence time and variability of tropospheric trace gases', *Tellus*.

Junge, C. E. and Manson, J. E. (1961) 'Stratospheric aerosol studies', *Journal of Geophysical Research*.

Junninen, H., Lauri, A., Keronen, P., Aalto, P., Hiltunen, V., Hari, P. and Kulmala, M. (2009) 'Smart-SMEAR: On-line data exploration and visualization tool for SMEAR stations', *Boreal Environment Research*.

Keith, D. W. (2000) 'Geoengineering and the Climate: History and Prospect', *Annual Review of Energy and the Environment*.

Kerminen, V. M., Petäjä, T., Manninen, H. E., Paasonen, P., Nieminen, T., Sipilä, M., Junninen, H., Ehn, M., Gagné, S., Laakso, L., Riipinen, I., Vehkaḿaki, H., Kurten, T., Ortega, I. K., Dal Maso, M., Brus, D., Hyv̈arinen, A., Lihavainen, H., Leppä, J., Lehtinen, K. E. J., Mirme, A., Mirme, S., Hõrrak, U., Berndt, T., Stratmann, F., Birmili, W., Wiedensohler, A., Metzger, A., Dommen, J., Baltensperger, U., Kiendler-Scharr, A., Mentel, T. F., Wildt, J., Winkler, P. M., Wagner, P. E., Petzold, A., Minikin, A., Plass-Dülmer, C., Pöschl, U., Laaksonen, A. and Kulmala, M. (2010) 'Atmospheric nucleation: Highlights of the EUCAARI project and future directions', *Atmospheric Chemistry and Physics*.

Kettle, A. J., Kuhn, U., Von Hobe, M., Kesselmeier, J. and Andreae, M. O. (2002) 'Global budget of atmospheric carbonyl sulfide: Temporal and spatial variations of the dominant sources and sinks', *Journal of Geophysical Research Atmospheres*.

Kirchhoff, G. and Bunsen, R. (1860) 'Chemical analysis by means of spectral observations', *Annalen der Physik und der Chemie (Poggendorff)*.

Kirkby, J., Curtius, J., Almeida, J., Dunne, E., Duplissy, J., Ehrhart, S., Franchin, A., Gagné, S.,

Ickes, L., Kürten, A., Kupc, A., Metzger, A., Riccobono, F., Rondo, L., Schobesberger, S., Tsagkogeorgas, G., Kulmala, M., *et al.* (2011) 'Role of sulphuric acid, ammonia and galactic cosmic rays in atmospheric aerosol nucleation', *Nature*.

Klepeis, N. E., Nelson, W. C., Ott, W. R., Robinson, J. P., Tsang, A. M., Switzer, P., Behar, J. V., Hern, S. C. and Engelmann, W. H. (2001) 'The National Human Activity Pattern Survey (NHAPS): A resource for assessing exposure to environmental pollutants', *Journal of Exposure Analysis and Environmental Epidemiology*.

Ko, M. K. W., Sze, N. D. and Weisenstein, D. K. (1991) 'Use of satellite data to constrain the model-calculated atmospheric lifetime for N2O: implications for other trace gases', *Journal of Geophysical Research*.

Kooijmans, L. M. J., Maseyk, K., Seibt, U., Sun, W., Vesala, T., Mammarella, I., Kolari, P., Aalto, J., Franchin, A., Vecchi, R., Valli, G. and Chen, H. (2017) 'Canopy uptake dominates nighttime carbonyl sulfide fluxes in a boreal forest', *Atmospheric Chemistry and Physics*.

Kooijmans, L. M. J. (2018) *Carbonyl sulfide, a way to quantify photosynthesis*. University of Groningen.

Kremser, S., Thomason, L. W., von Hobe, M., Hermann, M., Deshler, T., Timmreck, C., Toohey, M., Stenke, A., Schwarz, J. P., Weigel, R., Fueglistaler, S., Prata, F. J., Vernier, J. P., Schlager, H., Barnes, J. E., Antuña-Marrero, J. C., Fairlie, D., Palm, M., Mahieu, E., Notholt, J., Rex, M., Bingen, C., Vanhellemont, F., Bourassa, A., Plane, J. M. C., Klocke, D., Carn, S. A., Clarisse, L., Trickl, T., Neely, R., James, A. D., Rieger, L., Wilson, J. C. and Meland, B. (2016) 'Stratospheric aerosol—Observations, processes, and impact on climate', *Reviews of Geophysics*.

Krysztofiak, G., Té, Y. V., Catoire, V., Berthet, G., Toon, G. C., Jégou, F., Jeseck, P. and Robert, C. (2015) 'Carbonyl sulphide (OCS) variability with latitude in the atmosphere', *Atmosphere - Ocean*.

Kunz, A., Konopka, P., Müller, R. and Pan, L. L. (2011) 'Dynamical tropopause based on isentropic potential vorticity gradients', *Journal of Geophysical Research Atmospheres*.

Lacis, A. A. and Mishchenko, M. I. (1995) 'Climate forcing, climate sensitivity, and climate response: A radiative modeling perspective on atmospheric aerosols', *Aerosol Forcing of Climate*.

Launois, T., Belviso, S., Bopp, L., Fichot, C. G. and Peylin, P. (2015) 'A new model for the global biogeochemical cycle of carbonyl sulfide - Part 1: Assessment of direct marine emissions with an oceanic general circulation and biogeochemistry model', *Atmospheric Chemistry and Physics*.

Lee, C., Martin, R. V., Van Donkelaar, A., Lee, H., Dickerson, R. R., Hains, J. C., Krotkov, N., Richter, A., Vinnikov, K. and Schwab, J. J. (2011) 'SO2 emissions and lifetimes: Estimates from inverse modeling using in situ and global, space-based (SCIAMACHY and OMI) observations',

Journal of Geophysical Research Atmospheres.

Lee Ng, N., Brown, S. S., Archibald, A. T., Atlas, E., Cohen, R. C., Crowley, J. N., Day, D. A., Donahue, N. M., Fry, J. L., Fuchs, H., Griffin, R. J., Guzman, M. I., Herrmann, H., Hodzic, A., Iinuma, Y., Kiendler-Scharr, A., Lee, B. H., Luecken, D. J., Mao, J., McLaren, R., Mutzel, A., Osthoff, H. D., Ouyang, B., Picquet-Varrault, B., Platt, U., Pye, H. O. T., Rudich, Y., Schwantes, R. H., Shiraiwa, M., Stutz, J., Thornton, J. A., Tilgner, A., Williams, B. J. and Zaveri, R. A. (2017) 'Nitrate radicals and biogenic volatile organic compounds: Oxidation, mechanisms, and organic aerosol', in *Atmospheric Chemistry and Physics*.

Leedham Elvidge, E. C., Oram, D. E., Laube, J. C., Baker, A. K., Montzka, S. A., Humphrey, S., O'Sullivan, D. A. and Brenninkmeijer, C. A. M. (2015) 'Increasing concentrations of dichloromethane, CH2Cl2, inferred from CARIBIC air samples collected 1998-2012', *Atmospheric Chemistry and Physics*.

Lelieveld, J., Roelofs, G. J., Ganzeveld, L., Feichter, J. and Rodhe, H. (1997) 'Terrestrial sources and distribution of atmospheric sulphur', *Philosophical Transactions of the Royal Society B: Biological Sciences*.

Lelieveld, J., Evans, J. S., Fnais, M., Giannadaki, D. and Pozzer, A. (2015) 'The contribution of outdoor air pollution sources to premature mortality on a global scale', *Nature*.

Lelieveld, J., Gromov, S., Pozzer, A. and Taraborrelli, D. (2016) 'Global tropospheric hydroxyl distribution, budget and reactivity', *Atmospheric Chemistry and Physics*.

Lelieveld, J., Klingmüller, K., Pozzer, A., Pöschl, U., Fnais, M., Daiber, A. and Münzel, T. (2019) 'Cardiovascular disease burden from ambient air pollution in Europe reassessed using novel hazard ratio functions', *European Heart Journal*.

Lelieveld, J., Klingmüller, K., Pozzer, A., Burnett, R. T., Haines, A. and Ramanathan, V. (2019) 'Effects of fossil fuel and total anthropogenic emission removal on public health and climate', *Proceedings of the National Academy of Sciences*. National Academy of Sciences.

Lelieveld, J., Haines, A. and Pozzer, A. (2018) 'Age-dependent health risk from ambient air pollution: a modelling and data analysis of childhood mortality in middle-income and low-income countries', *The Lancet Planetary Health*.

Lenschow, D. H., Paluch, I. R., Bandy, A. R., Thornton, D. C., Blake, D. R. and Simpson, I. (1999) 'Use of a mixed-layer model to estimate dimethylsulfide flux and application to other trace gas fluxes', *Journal of Geophysical Research Atmospheres*.

Li, J., Reiffs, A., Parchatka, U. and Fischer, H. (2015) 'In situ measurements of atmospheric CO and its correlation with NOX and O3 at a rural mountain site', *Metrology and Measurement Systems*.

Li, M., Karu, E., Brenninkmeijer, C., Fischer, H., Lelieveld, J. and Williams, J. (2018) 'Tropospheric OH and stratospheric OH and Cl concentrations determined from CH4, CH3Cl, and SF6 measurements', *npj Climate and Atmospheric Science*.

Lide, D. R. (2016) 'CRC Handbook of Chemistry and Physics, 97th Edition, 2016-2017', *Handbook of Chemistry and Physics*.

Liebmann, J., Karu, E., Sobanski, N., Schuladen, J., Ehn, M., Schallhart, S., Quéléver, L., Hellen, H., Hakola, H., Hoffmann, T., Williams, J., Fischer, H., Lelieveld, J. and Crowley, J. N. (2018a) 'Direct measurement of NO3 radical reactivity in a boreal forest', *Atmospheric Chemistry and Physics*.

Liebmann, J., Karu, E., Sobanski, N., Schuladen, J., Ehn, M., Schallhart, S., Quéléver, L., Hellen, H., Hakola, H., Hoffmann, T., Williams, J., Fischer, H., Lelieveld, J. and Crowley, J. N. (2018b) 'Supplement of: Direct measurement of NO3 radical reactivity in a boreal forest', *Atmospheric Chemistry and Physics*.

Liebmann, J. M., Schuster, G., Schuladen, J. B., Sobanski, N., Lelieveld, J. and Crowley, J. N. (2017) 'Measurement of ambient NO3 reactivity: Design, characterization and first deployment of a new instrument', *Atmospheric Measurement Techniques*.

Lin, G., Penner, J. E., Sillman, S., Taraborrelli, D. and Lelieveld, J. (2012) 'Global modeling of SOA formation from dicarbonyls, epoxides, organic nitrates and peroxides', *Atmospheric Chemistry and Physics*.

Liu, Y., Misztal, P. K., Xiong, J., Tian, Y., Arata, C. and Nazaroff, W. W. G. A. H. (2017) 'Spatially and temporally resolved measurements of volatile organic compounds in a residence', *Healthy Buildings 2017 Europe*.

Marandino, C. A., Tegtmeier, S., Krüger, K., Zindler, C., Atlas, E. L., Moore, F. and Bange, H. W. (2013) 'Dimethylsulphide (DMS) emissions from the western Pacific Ocean: A potential marine source for stratospheric sulphur?', *Atmospheric Chemistry and Physics*.

Masson-Delmotte, V., Zhai, P., Pörtner, H.-O., Roberts, D., Skea, J., Shukla, P. R., Pirani, A., Moufouma-Okia, W., Péan, C., Pidcock, R., Connors, S., Matthews, J. B. R., Chen, Y., Zhou, X., Gomis, M. I., Lonnoy, E., Maycock, T., Tignor, M. and Waterfield, T. (2018) 'Global warming of 1.5°C An IPCC Special Report', *Report of the Intergovernmental Panel on Climate Change*.

Matthias-Maser, S., Obolkin, V., Khodzer, T. and Jaenicke, R. (2000) 'Seasonal variation of primary biological aerosol particles in the remote continental region of Lake Baikal/Siberia', *Atmospheric Environment*.

Mccormack, A. J., Tong, S. C. and Cooke, W. D. (1965) 'Sensitive Selective Gas Chromatography Detector Based on Emission Spectrometry of Organic Compounds', *Analytical Chemistry*.

Moene, A. F. and van Dam, J. C. (2014) *Transport in the Atmosphere-Vegetation-Soil Continuum*, *Transport in the Atmosphere-Vegetation-Soil Continuum*.

Mogensen, D., Gierens, R., Crowley, J. N., Keronen, P., Smolander, S., Sogachev, A., Nölscher, A. C., Zhou, L., Kulmala, M., Tang, M. J., Williams, J. and Boy, M. (2015) 'Simulations of atmospheric OH, O3 and NO3 reactivities within and above the boreal forest', *Atmospheric Chemistry and Physics*.

Montzka, S. a., Reimann, S., Engel, A., Kruger, K., O'Doherty, S., Sturges, W., Blake, D., Dorf, M., Fraser, P., Froidevaux, L., Jucks, K., Kreher, K., Kurylo, M. J., Mellouki, A., Miller, J., Nielsen, O.-J., Orkin, V. L., Prinn, R. G., Rhew, R., Santee, M. L., Stohl, A., Verdonik, D. and Al., E. (2011) 'Ozone depleting substances (ODSs) and related chemicals', in *Scientific Assessment of Ozone Depletion: 2010, Global Ozone Research and Monitoring Project-Report No. 52*.

Montzka, S. A., Aydin, M., Battle, M., Butler, J. H., Saltzman, E. S., Hall, B. D., Clarke, A. D., Mondeel, D. and Elkins, J. W. (2004) 'A 350-year atmospheric history for carbonyl sulfide inferred from Antarctic firn air and air trapped in ice', *Journal of Geophysical Research D: Atmospheres*.

Montzka, S. A., Calvert, P., Hall, B. D., Elkins, J. W., Conway, T. J., Tans, P. P. and Sweeney, C. S. (2007) 'On the global distribution, seasonality, and budget of atmospheric carbonyl sulfide (COS) and some similarities to CO2', *Journal of Geophysical Research Atmospheres*.

Montzka, S. and Elkins, J. (2018) 'Oceanic and Atmospheric Administration, Earth System Research Laboratory, Global Monitoring Division (NOAA/ESRL/GMD) Global Carbonyl Sulfide Data File from Halocarbons & other Atmospheric Trace Species Group (HATS)'.

Murphy, D. M. and Fahey, D. W. (1994) 'An estimate of the flux of stratospheric reactive nitrogen and ozone into the troposphere', *Journal of Geophysical Research*.

Musselman, R. C. and Minnick, T. J. (2000) 'Nocturnal stomatal conductance and ambient air quality standards for ozone', *Atmospheric Environment*.

National Academy of Sciences (1992) *Policy Implications of Greenhouse Warming: Mitigation, Adaptation, and the Science Base, Public Policy*.

Nguyen, H., Gudmundsson, A. and Martinsson, B. (2006) 'Design and calibration of a multi-channel aerosol sampler for tropopause region studies from the CARIBIC platform', *Aerosol Science and Technology*.

Nölscher, A. C., Williams, J., Sinha, V., Custer, T., Song, W., Johnson, A. M., Axinte, R., Bozem, H., Fischer, H., Pouvesle, N., Phillips, G., Crowley, J. N., Rantala, P., Rinne, J., Kulmala, M., Gonzales, D., Valverde-Canossa, J., Vogel, A., Hoffmann, T., Ouwersloot, H. G., Vilà-Guerau De Arellano, J. and Lelieveld, J. (2012) 'Summertime total OH reactivity measurements from

boreal forest during HUMPPA-COPEC 2010', *Atmospheric Chemistry and Physics*.

Nölscher, A. C., Yañez-Serrano, A. M., Wolff, S., De Araujo, A. C., Lavrič, J. V., Kesselmeier, J. and Williams, J. (2016) 'Unexpected seasonality in quantity and composition of Amazon rainforest air reactivity', *Nature Communications*.

O'Sullivan, D. A. (2008) *PhD Thesis: Temporal and spatial variability of halogenated compounds and other trace gases*. University of East Anglia.

OpenStreetMap© contributors (2019). Available at: https://www.openstreetmap.org/copyright (Accessed: 19 March 2019).

Oppenheimer, C., Francis, P. and Stix, J. (1998) 'Depletion rates of sulfur dioxide in tropospheric volcanic plumes', *Geophysical Research Letters*.

Plumb, R. A. and Ko, M. K. W. (1992) 'Interrelationships between mixing ratios of long-lived stratospheric constituents', *Journal of Geophysical Research*.

Prather, M. J., Hsu, J., DeLuca, N. M., Jackman, C. H., Oman, L. D., Douglass, A. R., Fleming, E. L., Strahan, S. E., Steenrod, S. D., Søvde, O. A., Isaksen, I. S. A., Froidevaux, L. and Funke, B. (2015) 'Measuring and modeling the lifetime of nitrous oxide including its variability', *Journal of Geophysical Research*.

Prather, M. J., Holmes, C. D. and Hsu, J. (2012) 'Reactive greenhouse gas scenarios: Systematic exploration of uncertainties and the role of atmospheric chemistry', *Geophysical Research Letters*.

Pringle, K. J., Tost, H., Message, S., Steil, B., Giannadaki, D., Nenes, A., Fountoukis, C., Stier, P., Vignati, E. and Lelieveld, J. (2010) 'Description and evaluation of GMXe: A new aerosol submodel for global simulations (v1)', *Geoscientific Model Development*.

Protoschill-Krebs, G., Wilhelm, C. and Kesselmeier, J. (1996) 'Consumption of carbonyl sulphide (COS) by higher plant carbonic anhydrase (CA)', *Atmospheric Environment*.

Quimby, B. D. and Sullivan, J. J. (1990) 'Evaluation of a microwave cavity, discharge tube, and gas flow system for combined gas chromatography-atomic emission detection', *Analytical Chemistry*.

Randel, W. J., Park, M., Emmons, L., Kinnison, D., Bernath, P., Walker, K. A., Boone, C. and Pumphrey, H. (2010) 'Asian monsoon transport of pollution to the stratosphere', *Science*.

Ravishankara, A. R., Solomon, S., Turnipseed, A. A. and Warren, R. F. (1993) 'Atmospheric lifetimes of long-lived halogenated species', *Science*.

Rex, M., Wohltmann, I., Ridder, T., Lehmann, R., Rosenlof, K., Wennberg, P., Weisenstein, D., Notholt, J., Krüger, K., Mohr, V. and Tegtmeier, S. (2014) 'A tropical West Pacific OH minimum and implications for stratospheric composition', *Atmospheric Chemistry and Physics*.

Risby, T. H., Talmi, Y. and Uden, P. C. (1983) 'Microwave induced electrical discharge detectors for gas chromatography'. Taylor & Francis.

Roeckner, E., Bäuml, G., Bonaventura, L., Brokopf, R., Esch, M., Giorgetta, M., Hagemann, S., Kirchner, I., Kornblueh, L., Rhodin, A., Schlese, U., Schulzweida, U., Tompkins, A., Manzini, E., Rhodin, A., Schlese, U., Schulzweida, U. and Tompkins, A. (2003) *The atmospheric general circulation model ECHAM5. Part I: Model description., MPI Report*.

Russell, R. (2011) *UCAR - The Stratosphere: overview*. Available at: https://scied.ucar.edu/shortcontent/stratosphere-overview (Accessed: 1 April 2019).

Sachs, L. (1999) *Angewandte Statistik - Anwendung statistischer Methoden*. Springer.

Sander, R., Kerkweg, R., Jöckel, P. and Lelieveld, J. (2010) 'Technical Note: The new comprehensive atmospheric chemistry module MECCA', *Atmospheric Chemistry and Physics Discussions*.

Sander, R. (2015) 'Compilation of Henry's law constants (version 4.0) for water as solvent', *Atmospheric Chemistry and Physics*.

Sander, S. P., Abbatt, J., Barker, J. R., Burkholder, J. B., Friedl, R. R., Golden, D. M., Huie, R. E., Kolb, C. E., Kurylo, M. J., Moortgat, G. K., Orkin, V. L. and Wine, P. H. (2011) 'Chemical Kinetics and Photochemical Data for Use in Atmospheric Studies Evaluation Number 17', *JPL Publication 10-6, Jet Propulsion Laboratory*.

Sandoval-Soto, L., Stanimirov, M., von Hobe, M., Schmitt, V., Valdes, J., Wild, a. and Kesselmeier, J. (2005) 'Global uptake of carbonyl sulfide (COS) by terrestrial vegetation: Estimates corrected by deposition velocities normalized to the uptake of carbon dioxide (CO_2)', *Biogeosciences Discussions*.

Saxena, P. and Hildemann, L. M. (1996) 'Water-soluble organics in atmospheric particles: A critical review of the literature and application of thermodynamics to identify candidate compounds', *Journal of Atmospheric Chemistry*.

Scharffe, D., Slemr, F., Brenninkmeijer, C. A. M. and Zahn, A. (2012) 'Carbon monoxide measurements onboard the CARIBIC passenger aircraft using UV resonance fluorescence', *Atmospheric Measurement Techniques*.

Schuck, T. J., Brenninkmeijer, C. A. M., Slemr, F., Xueref-Remy, I. and Zahn, A. (2009) 'Greenhouse gas analysis of air samples collected onboard the CARIBIC passenger aircraft', *Atmospheric Measurement Techniques*.

Seinfeld, J. H. and Pandis, S. N. (2016) *ATMOSPHERIC CHEMISTRY AND PHYSICS From Air Pollution to Climate Change, Third Edition, 3rd edition. Wiley*.

Sheng, J. X., Weisenstein, D. K., Luo, B. P., Rozanov, E., Stenke, A., Anet, J., Bingemer, H. and

Peter, T. (2015) ‘Global atmospheric sulfur budget under volcanically quiescent conditions: Aerosol-chemistry-climate model predictions and validation’, *Journal of Geophysical Research*.

Sinha, V., Williams, J., Lelieveld, J., Ruuskanen, T. M., Kajos, M. K., Patokoski, J., Hellen, H., Hakola, H., Mogensen, D., Boy, M., Rinne, J. and Kulmala, M. (2010) ‘OH reactivity measurements within a boreal forest: Evidence for unknown reactive emissions’, *Environmental Science and Technology*.

Smith, S. J., Van Aardenne, J., Klimont, Z., Andres, R. J., Volke, A. and Delgado Arias, S. (2011) ‘Anthropogenic sulfur dioxide emissions: 1850-2005’, *Atmospheric Chemistry and Physics*.

Sobanski, N., Schuladen, J., Schuster, G., Lelieveld, J. and Crowley, J. N. (2016) ‘A five-channel cavity ring-down spectrometer for the detection of NO2, NO3, N2O5, total peroxy nitrates and total alkyl nitrates’, *Atmospheric Measurement Techniques*.

Solomon, S., Portmann, R. W., Garcia, R. R., Thomason, L. W., Poole, L. R. and McCormick, M. P. (1996) ‘The role of aerosol variations in anthropogenic ozone depletion at northern midlatitudes’, *Journal of Geophysical Research Atmospheres*.

Spracklen, D. V., Jimenez, J. L., Carslaw, K. S., Worsnop, D. R., Evans, M. J., Mann, G. W., Zhang, Q., Canagaratna, M. R., Allan, J., Coe, H., McFiggans, G., Rap, A. and Forster, P. (2011) ‘Aerosol mass spectrometer constraint on the global secondary organic aerosol budget’, *Atmospheric Chemistry and Physics*.

Stein, A. F., Draxler, R. R., Rolph, G. D., Stunder, B. J. B., Cohen, M. D. and Ngan, F. (2015) ‘Noaa’s hysplit atmospheric transport and dispersion modeling system’, *Bulletin of the American Meteorological Society*.

Stella, P., Loubet, B., Lamaud, E., Laville, P. and Cellier, P. (2011) ‘Ozone deposition onto bare soil: A new parameterisation’, *Agricultural and Forest Meteorology*.

Stimler, K., Montzka, S. A., Berry, J. A., Rudich, Y. and Yakir, D. (2010) ‘Relationships between carbonyl sulfide (COS) and CO2 during leaf gas exchange’, *New Phytologist*.

Stocker, T. F., Qin, D., Plattner, G. K., Tignor, M. M. B., Allen, S. K., Boschung, J., Nauels, A., Xia, Y., Bex, V. and Midgley, P. M. (2013) *IPCC, 2013: Climate Change 2013: The Physical Science Basis: Working Group I Contribution to the Fifth Assessment Report of the Intergovernmental Panel on Climate Change, Cambridge University Press, Cambridge, United Kingdom and New York, NY, USA*.

Stratmann, G., Ziereis, H., Stock, P., Brenninkmeijer, C. A. M., Zahn, A., Rauthe-Schöch, A., Velthoven, P. V., Schlager, H. and Volz-Thomas, A. (2016) ‘NO and NOy in the upper troposphere: Nine years of CARIBIC measurements onboard a passenger aircraft’, *Atmospheric Environment*.

Sturges, W. T., Penkett, S. A., Barnola, J. M., Chappellaz, J., Atlas, E. and Stroud, V. (2001) 'A long-term record of carbonyl sulfide (COS) in two hemispheres from firn air measurements', *Geophysical Research Letters*.

Sun, J. and Ariya, P. A. (2006) 'Atmospheric organic and bio-aerosols as cloud condensation nuclei (CCN): A review', *Atmospheric Environment*.

Suntharalingam, P., Kettle, A. J., Montzka, S. M. and Jacob, D. J. (2008) 'Global 3-D model analysis of the seasonal cycle of atmospheric carbonyl sulfide: Implications for terrestrial vegetation uptake', *Geophysical Research Letters*.

Syakila, A. and Kroeze, C. (2011) 'The global nitrous oxide budget revisited', *Greenhouse Gas Measurement and Management*.

Thomason, L. and Peter, T. (2006) *Assessment of stratospheric aerosol properties (ASAP), SPARC Reports*.

Trenberth, K. E. and Smith, L. (2005) 'The mass of the atmosphere: A constraint on global analyses', *Journal of Climate*.

Turco, R. P., Whitten, R. C., Toon, O. B., Pollack, J. B. and Hamill, P. (1980) 'OCS, stratospheric aerosols and climate', *Nature*.

Ulshöfer, V. S. and Andreae, M. O. (1997) 'Carbonyl sulfide (COS) in the surface ocean and the atmospheric COS budget', *Aquatic Geochemistry*.

Umezawa, T., Baker, A. K., Oram, D., Sauvage, C., O'Sullivan, D., Rauthe-Schöch, A., Montzka, S. A., Zahn, A. and Brenninkmeijer, C. A. M. (2014) 'Methyl chloride in the upper troposphere observed by the CARIBIC passenger aircraft observatory: Large-scale distributions and Asian summer monsoon outflow', *Journal of Geophysical Research*.

Vehkamäki, H., Kulmala, M., Napari, I., Lehtinen, K. E. J., Timmreck, C., Noppel, M. and Laaksonen, A. (2002) 'An improved parameterization for sulfuric acid-water nucleation rates for tropospheric and stratospheric conditions', *Journal of Geophysical Research Atmospheres*.

van Velthoven, P. F. J. (2018) *Meteorological analysis of CARIBIC, Koninklijk Nederlands Meteorologisch Instituut (KNMI)*. Available at: https://projects.knmi.nl/campaign_support/CARIBIC/ (Accessed: 4 September 2018).

De Vos, J. M., Joppa, L. N., Gittleman, J. L., Stephens, P. R. and Pimm, S. L. (2015) 'Estimating the normal background rate of species extinction', *Conservation Biology*.

Voulgarakis, A., Naik, V., Lamarque, J. F., Shindell, D. T., Young, P. J., Prather, M. J., Wild, O., Field, R. D., Bergmann, D., Cameron-Smith, P., Cionni, I., Collins, W. J., Dalsøren, S. B., Doherty, R. M., Eyring, V., Faluvegi, G., Folberth, G. A., Horowitz, L. W., Josse, B., MacKenzie, I. A., Nagashima, T., Plummer, D. A., Righi, M., Rumbold, S. T., Stevenson, D. S., Strode, S. A.,

Sudo, K., Szopa, S. and Zeng, G. (2013) 'Analysis of present day and future OH and methane lifetime in the ACCMIP simulations', *Atmospheric Chemistry and Physics*.

Wallace, L. A. (1987) 'The Total Exposure Assessment Methodology (TEAM) Study', *U.S. Environmental Protection Agency, Office of Research and Development*.

Walter, D., Heue, K. P., Rauthe-Schch, A., Brenninkmeijer, C. A. M., Lamsal, L. N., Krotkov, N. A. and Platt, U. (2012) 'Flux calculation using CARIBIC DOAS aircraft measurements: SO2 emission of Norilsk', *Journal of Geophysical Research Atmospheres*.

Watts, S. F. (2000) 'The mass budgets of carbonyl sulfide, dimethyl sulfide, carbon disulfide and hydrogen sulfide', *Atmospheric Environment*.

Weschler, C. J. (2009) 'Changes in indoor pollutants since the 1950s', *Atmospheric Environment*.

Wexler, A. (1976) 'Vapor pressure formulation for water in range 0 to 100 C. A revision', *Journal of Research of the National Bureau of Standards Section A: Physics and Chemistry*.

Whelan, M. E., Lennartz, S. T., Gimeno, T. E., Wehr, R., Wohlfahrt, G., Wang, Y., Kooijmans, L. M. J., Hilton, T. W., Belviso, S., Peylin, P., Commane, R., Sun, W., Chen, H., Kuai, L., Mammarella, I., Maseyk, K., Berkelhammer, M., Li, K. F., Yakir, D., Zumkehr, A., Katayama, Y., Oge, J., Spielmann, F. M., Kitz, F., Rastogi, B., Kesselmeier, J., Marshall, J., Erkkila, K. M., Wingate, L., Meredith, L. K., He, W., Bunk, R., Launois, T., Vesala, T., Schmidt, J. A., Fichot, C. G., Seibt, U., Saleska, S., Saltzman, E. S., Montzka, S. A., Berry, J. A. and Elliott Campbell, J. (2018) 'Reviews and syntheses: Carbonyl sulfide as a multi-scale tracer for carbon and water cycles', *Biogeosciences*.

WHO (2018) *World Health Organization: 9 out of 10 people worldwide breathe polluted air, but more countries are taking action*. Available at: https://www.who.int/news-room/detail/02-05-2018-9-out-of-10-people-worldwide-breathe-polluted-air-but-more-countries-are-taking-action (Accessed: 4 April 2019).

WHO (2019) *World Health Organization: Ten threats to global health in 2019*. Available at: https://www.who.int/emergencies/ten-threats-to-global-health-in-2019 (Accessed: 4 April 2019).

Wigley, T. M. L. (2006) 'A combined mitigation/geoengineering approach to climate stabilization', *Science*.

Williams, D. R. (2017) *NASA: Earth Fact Sheet, NASA Goddard Space Flight Center*. Available at: https://nssdc.gsfc.nasa.gov/planetary/factsheet/earthfact.html (Accessed: 3 April 2019).

Williams, J., Gros, V., Bonsang, B. and Kazan, V. (2001) 'HO cycle in 1997 and 1998 over the southern Indian Ocean derived from CO, radon, and hydrocarbon measurements made at Amsterdam Island', *Journal of Geophysical Research Atmospheres*.

Williams, J., Crowley, J., Fischer, H., Harder, H., Martinez, M., Petäjä, T., Rinne, J., Bäck, J.,

Boy, M., Dal Maso, M., Hakala, J., Kajos, M., Keronen, P., Rantala, P., Aalto, J., Aaltonen, H., Lelieveld, J., *et al.* (2011) 'The summertime Boreal forest field measurement intensive (HUMPPA-COPEC-2010): An overview of meteorological and chemical influences', *Atmospheric Chemistry and Physics*.

Williams, J., Keßel, S. U., Nölscher, A. C., Yang, Y., Lee, Y., Yáñez-Serrano, A. M., Wolff, S., Kesselmeier, J., Klüpfel, T., Lelieveld, J. and Shao, M. (2016) 'Opposite OH reactivity and ozone cycles in the Amazon rainforest and megacity Beijing: Subversion of biospheric oxidant control by anthropogenic emissions', *Atmospheric Environment*.

Woolfenden, E. (2010a) 'Sorbent-based sampling methods for volatile and semi-volatile organic compounds in air. Part 1: Sorbent-based air monitoring options', *Journal of Chromatography A*.

Woolfenden, E. (2010b) 'Sorbent-based sampling methods for volatile and semi-volatile organic compounds in air. Part 2. Sorbent selection and other aspects of optimizing air monitoring methods', *Journal of Chromatography A*.

Worldometers (2019) *World Population Clock: Current World Population*. Available at: http://www.worldometers.info/world-population/ (Accessed: 4 April 2019).

YouGov (2018) *The Indoor Generation Report*.

Yu, X., Wang, Z., Zhang, M., Kuhn, U., Xie, Z., Cheng, Y., Pöschl, U. and Su, H. (2016) 'Ambient measurement of fluorescent aerosol particles with a WIBS in the Yangtze River Delta of China: Potential impacts of combustion-related aerosol particles', *Atmospheric Chemistry and Physics*.

Zahn, A., Christner, E., van Velthoven, P. F. J., Rauthe-Schöch, A. and Brenninkmeijer, C. A. M. (2014) 'Processes controlling water vapor in the upper troposphere/lowermost stratosphere: An analysis of 8years of monthly measurements by the IAGOS-CARIBIC observatory', *Journal of Geophysical Research*.

Zahn, A. and Brenninkmeijer, C. A. M. (2003) 'New directions: A chemical tropopause defined', *Atmospheric Environment*.

Zahn, A., Brenninkmeijer, C. A. M. and van Velthoven, P. F. J. (2004) 'Passenger aircraft project CARIBIC 1997-2002, Part I: the extratropical chemical tropopause', *Atmospheric Chemistry and Physics Discussions*.

Zell, H. (2013) *NASA: Earth's Upper Atmosphere*. Available at: https://www.nasa.gov/mission_pages/sunearth/science/mos-upper-atmosphere.html (Accessed: 1 April 2019).

Zhang, L., Brook, J. R. and Vet, R. (2002) 'On ozone dry deposition - With emphasis on non-stomatal uptake and wet canopies', *Atmospheric Environment*.

Zhou, P., Ganzeveld, L., Rannik, U., Zhou, L., Gierens, R., Taipale, D., Mammarella, I. and Boy, M. (2017) ‘Simulating ozone dry deposition at a boreal forest with a multi-layer canopy deposition model’, *Atmospheric Chemistry and Physics*.

Будыко(Budyko), M. I. (1974) ‘Измения Климата (Climate Changes)’, *Gidrometeoizdat*.

B APPENDICES

LIST OF APPENDICES

APEL-RIEMER-2015 84 MULTI-COMPONENT GAS CALIBRATION STANDARD

Table 6.1 Retention times of Apel-Riemer Environmental, Inc. 84 multi-component gas phase calibration mix in UHP nitrogen balance. Stated uncertainty better than ± 5% for all components. MR certificate analysis date: June 9, 2015.

IBAIRN-2016	**CARIBIC-2018**			
RT 35°C (min)	**RT 30°C (min)**	**Compound**	**CAS #**	**Concentration (ppb)**
3.43	3.46	Propene	115-07-1	51.8
3.47	3.50	Carbonyl sulfide	463-58-1	51.2
3.51	3.55	Dichlorodifluoromethane (R-12)	75-71-8	49.6
3.56	3.61	Chlorodifluoromethane (HCFC-22)	75-45-6	50.8
3.82	3.91	1,2-Dichlorotetrafluoroethane (R-114)	76-14-2	55.5
3.97	4.06	Chloromethane	74-87-3	52.5
4.17	4.31	Isobutene	115-11-7	51.3
4.25	4.39	Vinyl Chloride	75-01-4	52.3
4.34	4.50	1,3-Butadiene	106-99-0	51.7
4.57	4.77	Acetaldehyde	75-07-0	58.2
4.91	5.20	Methanol	67-56-1	51.7
5.10	5.38	Bromomethane	74-83-9	55
5.38	5.72	Chloroethane	75-00-3	54.8
6.00	6.50	Trichlorofluoromethane (F-11)	75-69-4	51.8
6.20	6.77	Pentane	109-66-0	61.8
6.63		Ethanol	64-17-5	45.3
6.80	7.61	Isoprene	78-79-5	52.4
7.15	8.24	Acrolein	107-02-8	46.1
		Propanal	123-38-6	43.2
7.31	8.38	1,1-Dichloroethene	75-35-4	75.4
		1,1,2-Trichloro-1,2,2-Trifluoroethane (CFC-113)	76-13-1	70.6

7.52		Acetone	67-64-1	43.2
7.67	8.85	Methyl Iodide	74-88-4	69.4
7.80	9.00	Carbon Disulfide	75-15-0	47
7.90	9.44	2-Propanol	67-63-0	50.7
8.24	9.95	Acetonitrile	75-05-8	50
8.55		Dichloromethane	75-09-2	52.2
8.60	10.22	Cyclopentane	287-92-3	52.8
	11.14	Acrylonitrile	107-13-1	64.3
9.14	11.03	trans-1,2-Dichloroethene	156-60-5	62.3
		Methyl Tertiary Butyl Ether (MTBE)	1634-04-4	61
9.68	11.82	Hexane	110-54-3	52.1
10.03	12.25	Methacrolein	78-85-3	48.9
10.13	12.36	1,1-Dichloroethane	75-34-3	57.8
10.21	12.58	Vinyl Acetate	108-05-4	56.4
10.40	12.93	1-Propanol	71-23-8	51.4
11.02	13.57	Butanal	123-72-8	59.6
11.07	13.66	Methyl Vinyl Ketone	78-94-4	74.4
11.42	14.05	cis-1,2-Dichloroethene	156-59-2	52.3
	14.10	Methyl Ethyl Ketone	78-93-3	51.1
12.08	14.90	Chloroform	67-66-3	51.9
12.43	15.32	1,1,1-Trichloroethane	71-55-6	52.4
12.50		Cyclohexane	110-82-7	53.4
12.77	15.65	Tetrachloromethane	56-23-5	51.4
13.20	16.18	Benzene	71-43-2	48.1
13.33	16.36	1,2-Dichloroethane	107-06-2	58.5
14.48	17.83	Trichloroethylene	79-01-6	54.8
14.62		1-Butanol	71-36-3	40.5
14.76	18.04	Isopropyl nitrate	1712-64-7	44.7
15.00	18.31	Hydroxyacetone	116-09-6	53.1
		2-Pentanone	107-87-9	50.2

15.13	18.40	1,2-Dichloropropane	78-87-5	50.5
15.23	18.56	Pentanal	110-62-3	59.9
15.29	18.64	3-Pentanone	96-22-0	52.5
15.37	18.69	1,4-Dioxane	123-91-1	50.7
15.70	19.07	Bromodichloromethane	75-27-4	49.2
16.35	19.81	Propyl nitrate	627-13-4	47.4
16.69	20.14	cis-1,3-Dichloropropene	10061-01-5	49.6
16.97	20.47	4-Methyl-2-Pentanone	108-10-1	51.7
17.36	20.85	Toluene	108-88-3	51.6
17.73	21.33	trans-1,3-Dichloropropene	10061-02-6	51.3
17.93	21.49	1,1,2-Trichloroethane	79-00-5	52.9
18.31	21.90	Isobutyl nitrate	543-29-3	45
18.53	22.14	3-Hexanone	598-38-8	50.9
18.57		Tetrachloroethylene	127-18-4	55.5
18.81	22.44	2-Hexanone	591-78-6	52
19.05	22.68	Hexanal	66-25-1	55.8
19.45	23.06	1,2-Dibromoethane	106-93-4	50.2
20.55	24.21	Chlorobenzene	108-90-7	53.3
20.75	24.42	Ethyl Benzene	100-41-4	50.8
21.03	24.71	m-Xylene	108-38-3	50.8
		p-Xylene	106-42-3	51.5
21.96	25.66	o-Xylene	95-47-6	50.6
21.99	25.70	Styrene	100-42-5	52.5
22.44	26.16	Bromoform	75-25-2	52.4
23.58	27.34	1,1,2,2-Tetrachloroethane	79-34-5	50.7
24.22	27.96	1,3,5-Trimethylbenzene	108-67-8	51.2
25.12	28.88	1,2,4-Trimethylbenzene	95-63-6	50.7
25.85	29.61	(m-)1,3-Dichlorobenzene	541-73-1	52.9
26.07	29.84	(p-)1,4-Dichlorobenzene	106-46-7	55.6
26.15	29.91	1,2,3-Trimethylbenzene	526-73-8	46.2

26.38	30.15	Benzyl Chloride	100-44-7	61.7
26.99	30.75	(o-)1,2-Dichlorobenzene	95-50-1	61.8
31.06		1,2,4-Trichlorobenzene	120-82-1	52.7

NATIONAL PHYSICAL LABORATORY (NPL) 30 COMPONENT NMHC PRIMARY CALIBRATION STANDARD (NPL-2017)

Table 6.2 Retention times of NPL-2017 30 ozone precursor NMHC gas phase primary calibration reference material in UHP nitrogen balance. Stated uncertainties are based on 2σ, providing a coverage probability of ~ 95%. Calibration date 7 May – 21 June 2017.

IBAIRN 2016	**AQABA 2017**	**CARIBIC 2018**		NPL-2017 (Bottle: D51 7546)	
RT 35°C (min)	**RT -20°C (min)**	**RT 30°C (min)**	**Sample**	**Mixing ratio (pmol/mol)**	**Uncertainty (pmol/mol)**
			Ethene	3930	80
			Ethyne	4140	210
3.33	3.57	3.15	Ethane	4010	80
3.43	4.74	3.46	Propene	3930	80
			Propane	3950	80
3.85	7.01	3.93	Isobutane	4030	110
4.18	8.63	4.31	1-Butene	3980	80
4.22	8.76	4.36	n-Butane	3990	80
4.34	9.28	4.50	1,3-Butadiene	4040	80
4.43	9.65	4.60	trans-2-Butene	4000	80
4.67	10.47	4.88	cis-2-Butene	3990	80
5.53	12.71	5.90	Isopentane	3940	80
6.06	13.85	6.58	1-Pentene	4040	80
6.20	14.11	6.76	n-Pentane	3960	80
6.56	14.79	7.28	trans-2-Pentene	3980	80
6.80	15.09	7.61	Isoprene	4140	90
8.47	17.47	10.11	2-Methylpentane	4150	80
9.68	18.92	11.81	n-Hexane	4150	80
13.20	22.55	16.17	Benzene	4140	80
13.30	22.67	16.33	2,2,4-Trimethylpentane	3900	80
13.72	23.10	16.84	n-Heptane	4160	80

17.36	26.64	20.84	Toluene	4020	110
17.54	26.83	21.08	n-Octane	3910	80
20.75	29.96	24.41	Ethylbenzene	4350	110
21.03	30.23	24.70	m-Xylene p-Xylene	8460	220
21.96	31.15	25.64	o-Xylene	4160	110
24.22	33.38	27.95	1,3,5-Trimethylbenzene	3940	100
25.12	34.28	28.86	1,4,4-Trimethylbenzene	4060	110
26.15	35.30	29.90	1,2,3-Trimethylbenzene	3890	100

APEL-RIEMER-2015 GAS STANDARD CALIBRATION CURVES

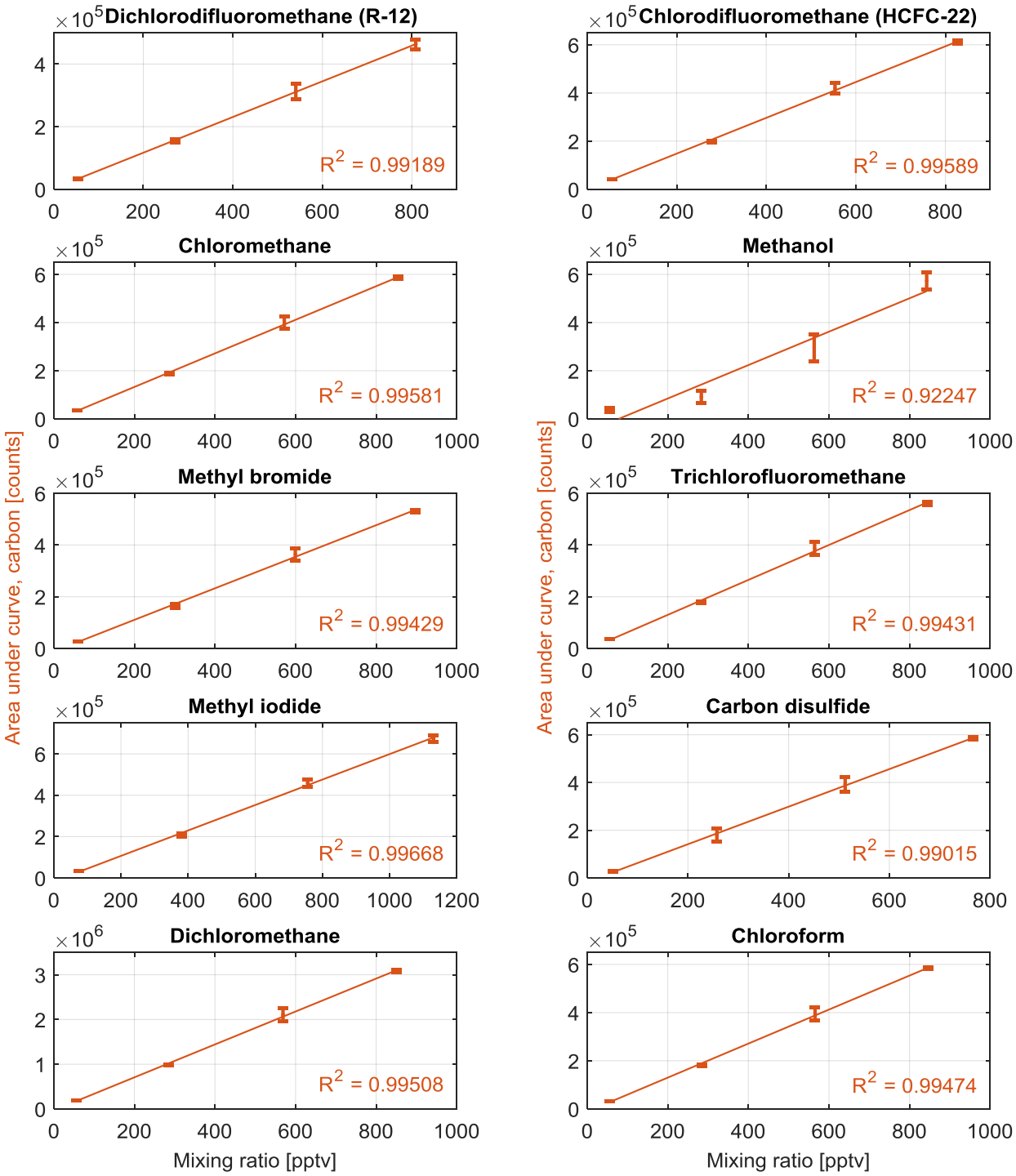

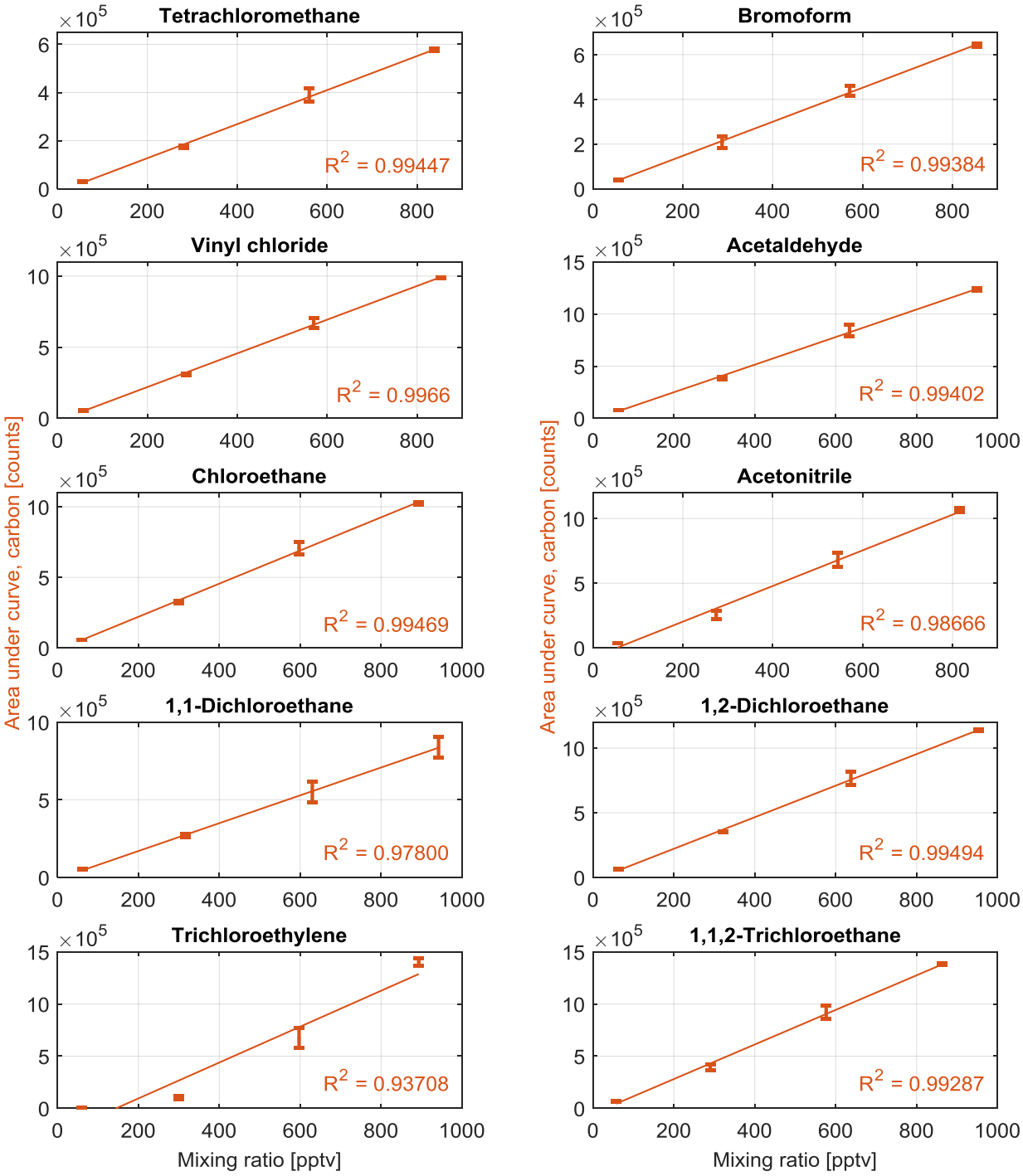
Tetrachloromethane
R2 = 0.99447
Bromoform
R2 = 0.99384
Vinyl chloride
R2 = 0.9966
Acetaldehyde
R2 = 0.99402
Chloroethane
R2 = 0.99469
Acetonitrile
R2 = 0.98666
1,1-Dichloroethane
R2 = 0.97800
1,2-Dichloroethane
R2 = 0.99494
Trichloroethylene
R2 = 0.93708
1,1,2-Trichloroethane
R2 = 0.99287
Area under curve, carbon [counts]
Mixing ratio [pptv]

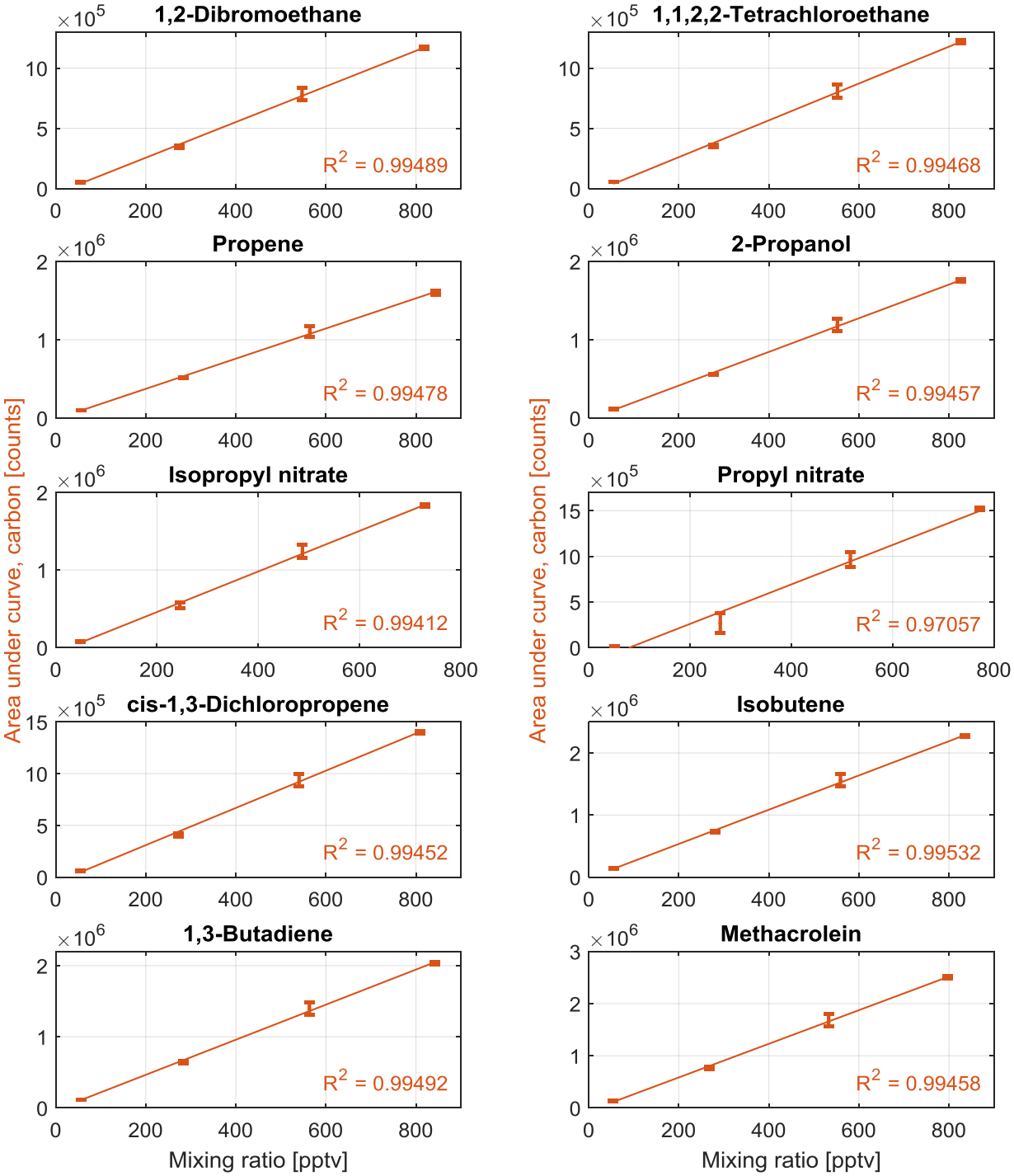
1,2-Dibromoethane
R2 = 0.99489
1,1,2,2-Tetrachloroethane
R2 = 0.99468
Propene
R2 = 0.99478
2-Propanol
R2 = 0.99457
Isopropyl nitrate
R2 = 0.99412
Propyl nitrate
R2 = 0.97057
cis-1,3-Dichloropropene
R2 = 0.99452
Isobutene
R2 = 0.99532
1,3-Butadiene
R2 = 0.99492
Methacrolein
R2 = 0.99458
Area under curve, carbon [counts]
Mixing ratio [pptv]

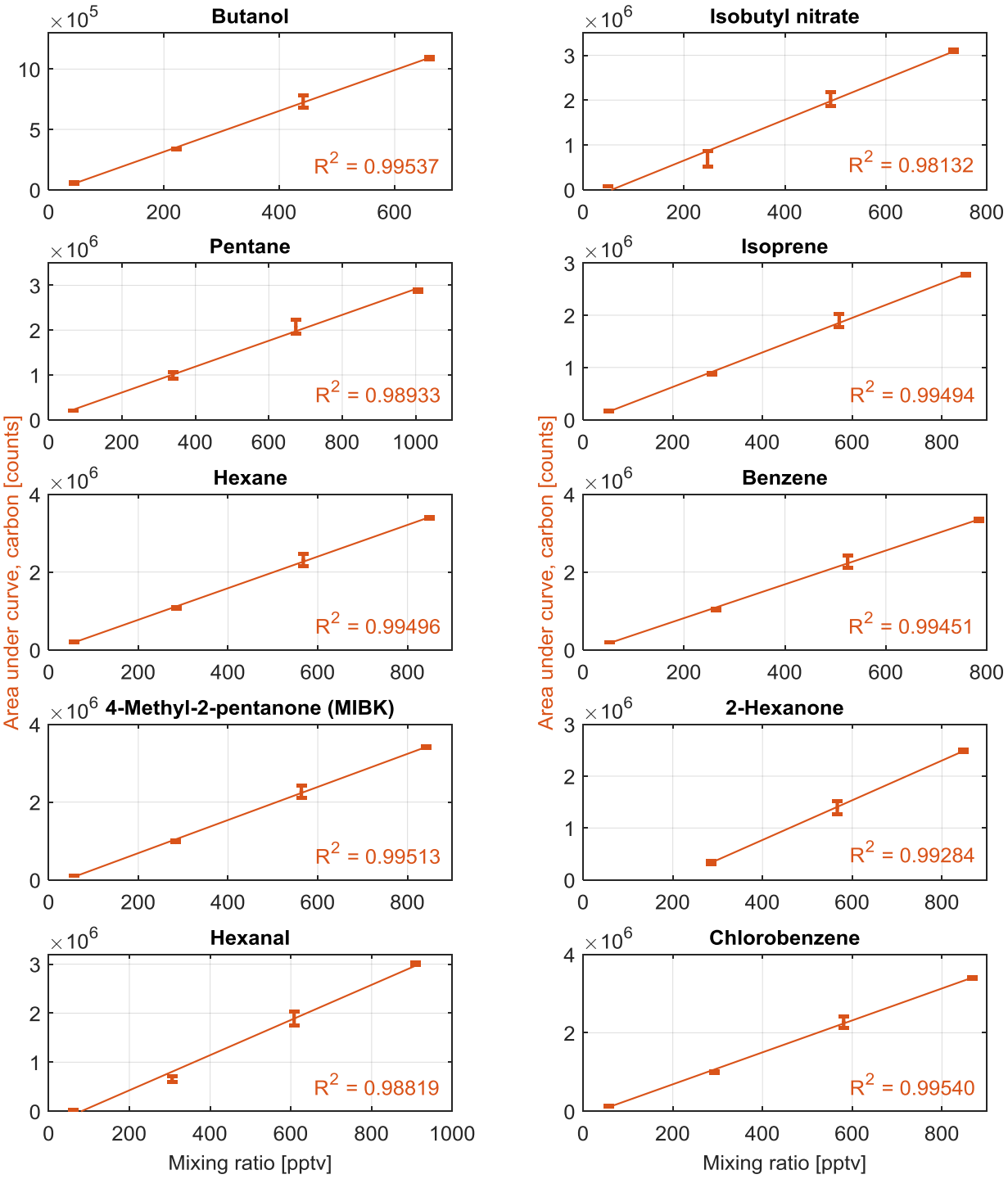
Butanol
R² = 0.99537
Isobutyl nitrate
R² = 0.98132
Pentane
R² = 0.98933
Isoprene
R² = 0.99494
Hexane
R² = 0.99496
Benzene
R² = 0.99451
4-Methyl-2-pentanone (MIBK)
R² = 0.99513
2-Hexanone
R² = 0.99284
Hexanal
R² = 0.98819
Chlorobenzene
R² = 0.99540
Area under curve, carbon [counts]
Mixing ratio [pptv]

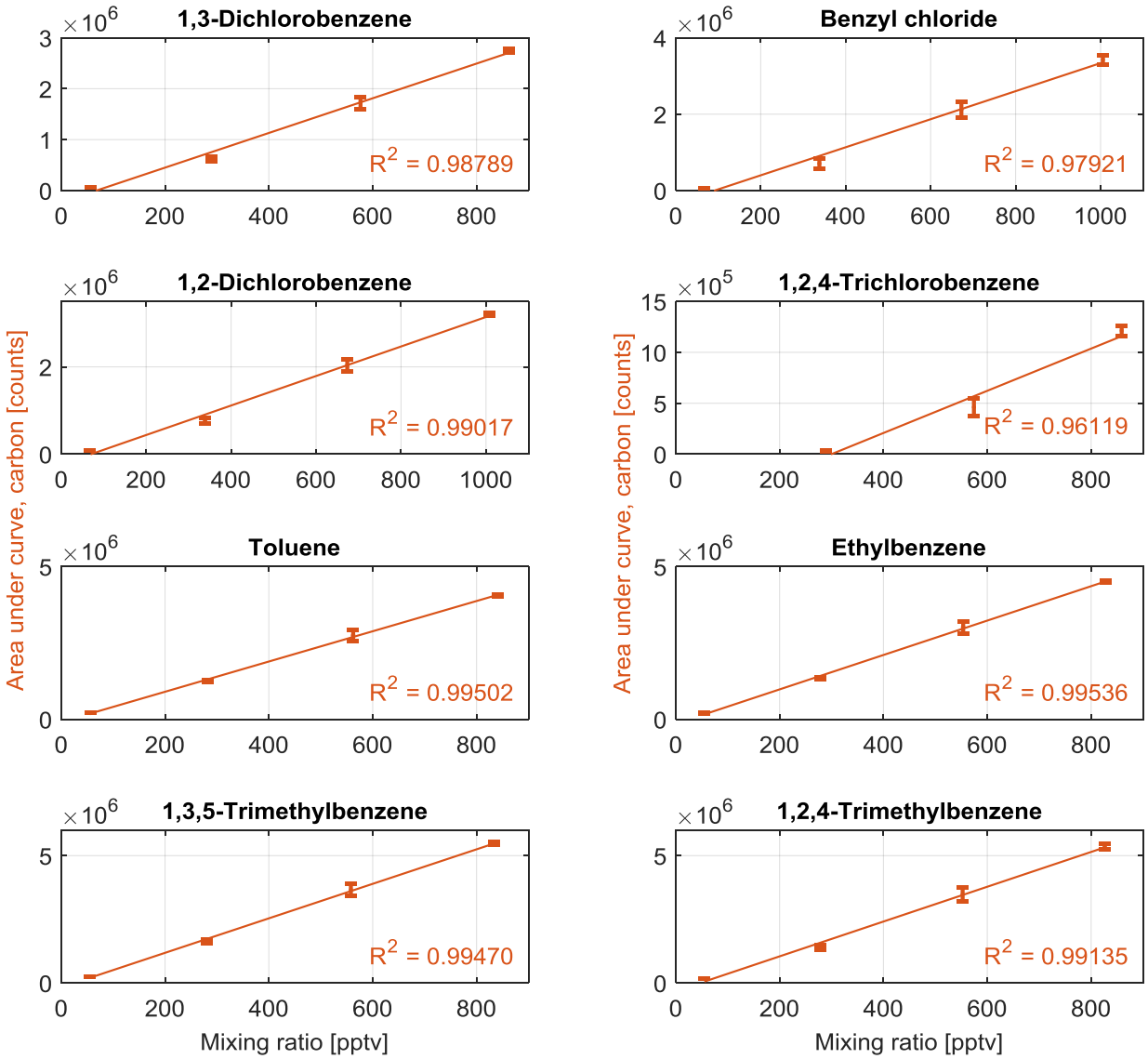

Figure 6.1 Entech-GC-AEDIII system calibration curves of Apel-Riemer-2015 gas standard. 1 – 15 mL min^{-1} standard gas was diluted with 1 L min^{-1} zero-air prior to 1.4 L sample pre-concentration.

NPL-2017 PRIMARY NMHC REFERENCE GAS STANDARD CALIBRATION CURVES

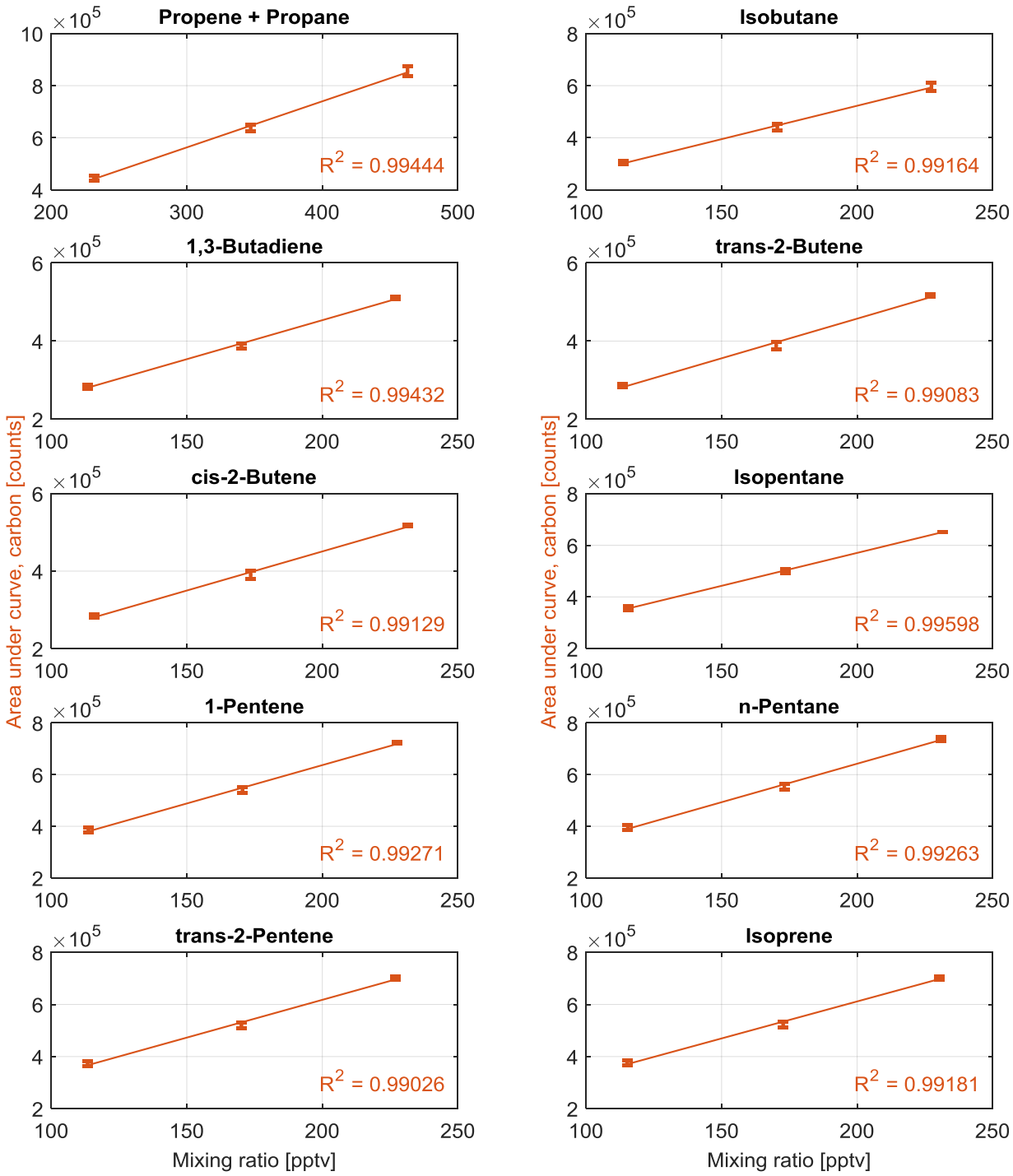

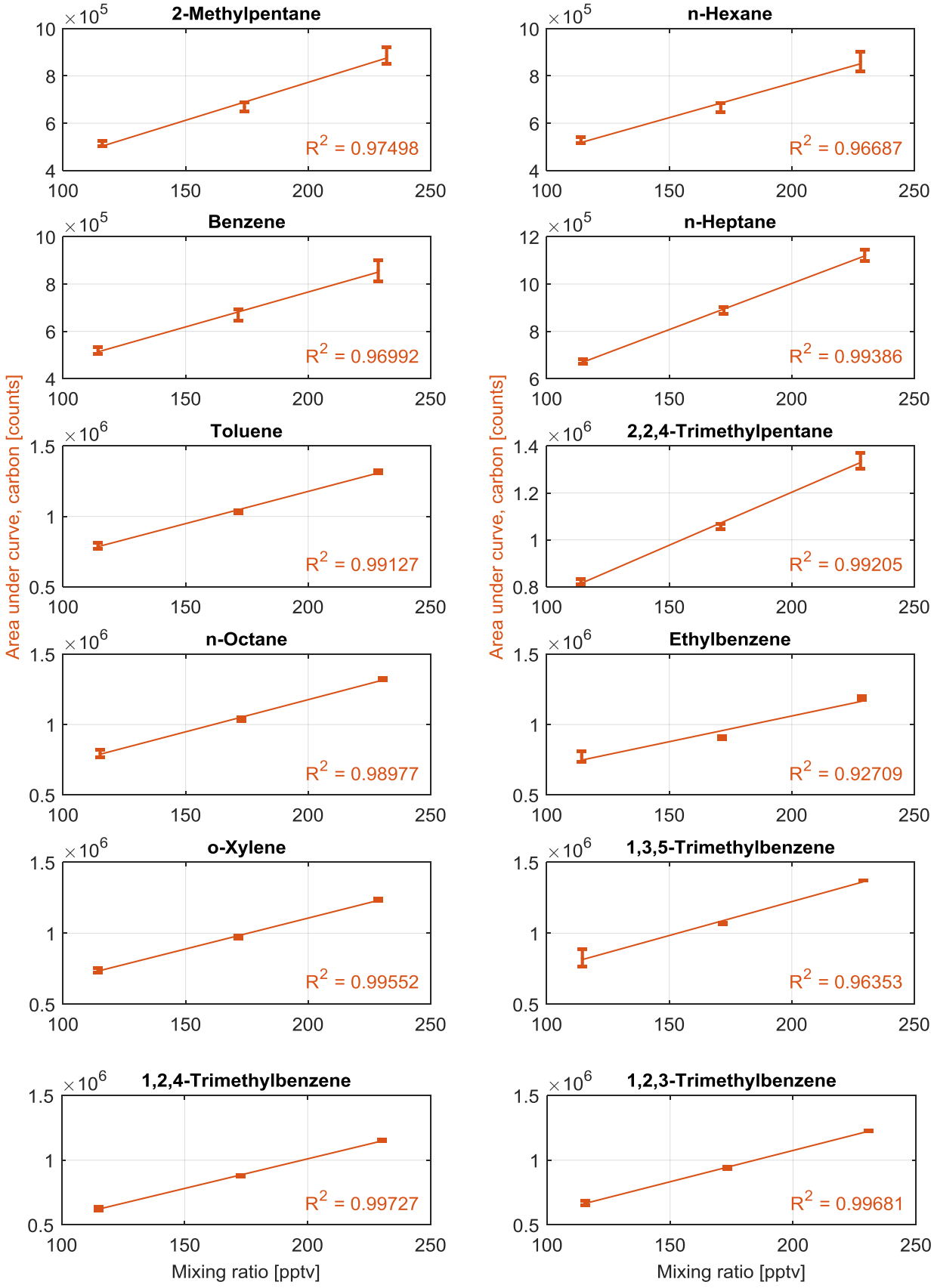

Figure 6.2 Entech-GC-AEDIII system calibration curves of NPL-2017 primary NMHC gas standard. 40 – 80 mL standard gas was pre-concentration.

CARIBIC GLOBAL OCS MEASUREMENT DATA

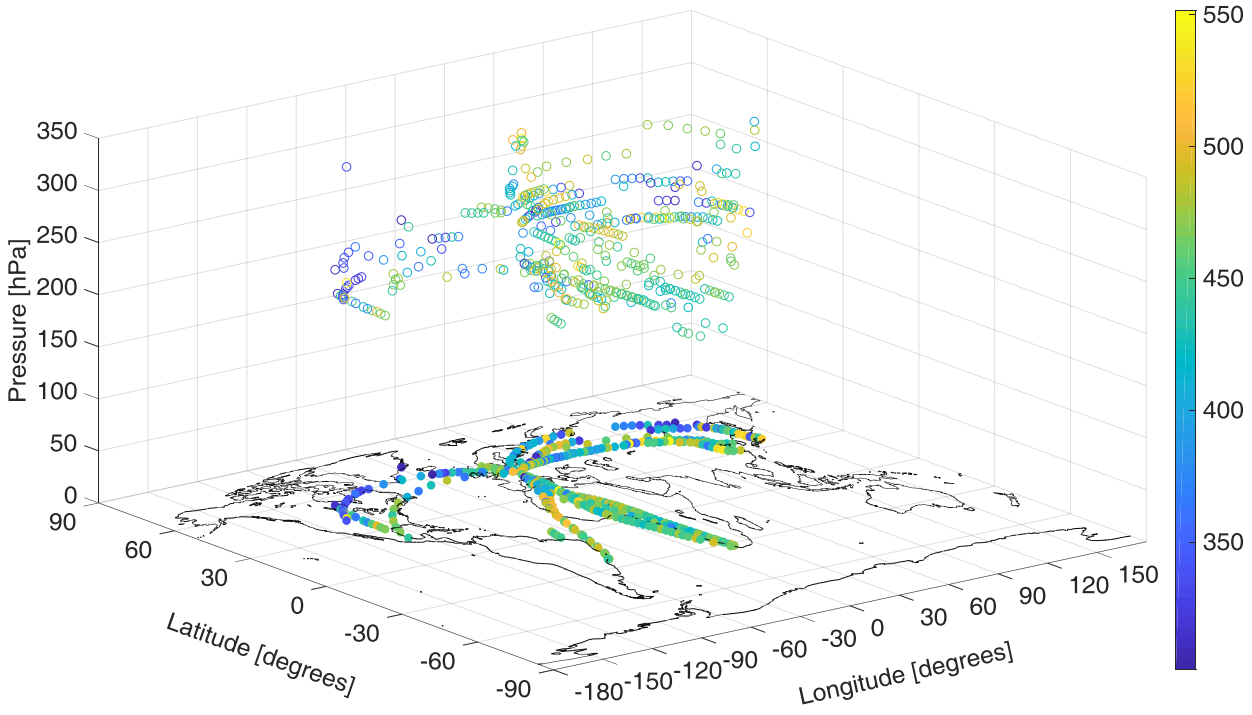

Figure 6.3 3D representation of global CARIBIC MPIC Entech-GC-AEDIII OCS measurement data. Z-axis denotes the flight pressure where the sample was collected [hPa]. Color coded circles represent OCS MRs [pptv].

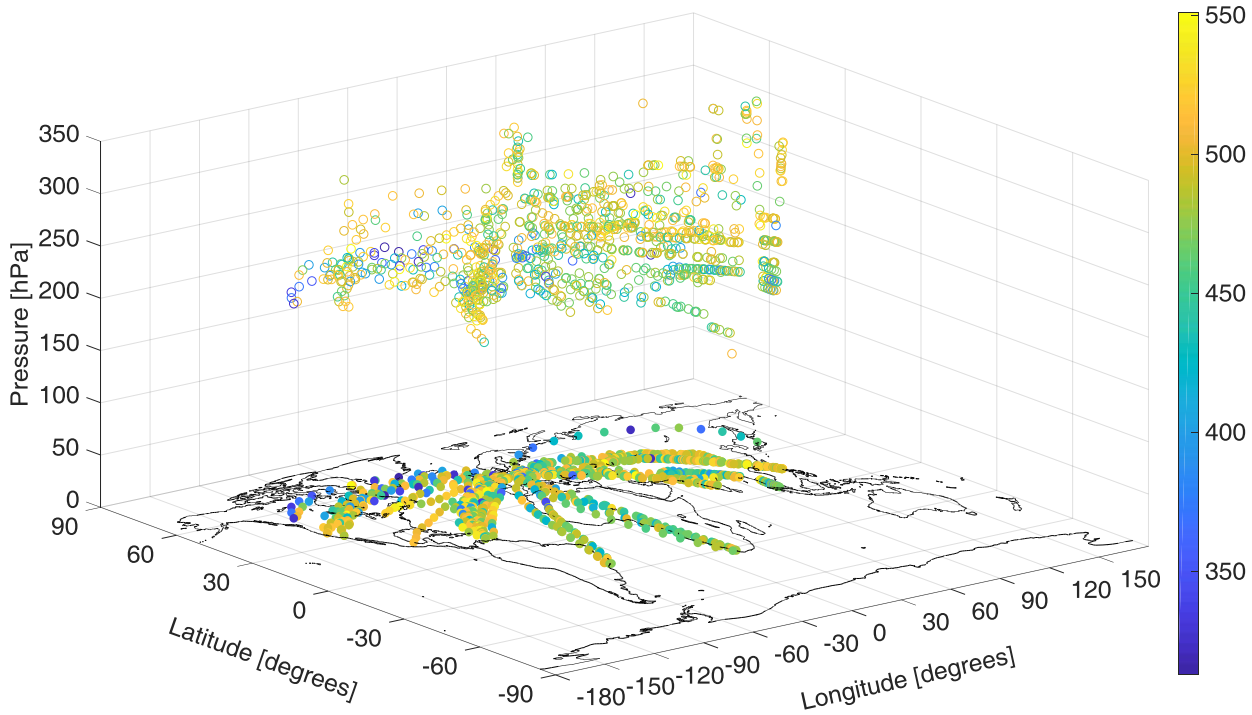

Figure 6.4 3D graph of color coded OCS MRs [pptv] collected with TRAC samplers on board CARIBIC aircraft and analyzed by UEA. Z-axis represents pressure [hPa]

SUPPORTING FIGURES FOR THE EMAC MODEL SECTION

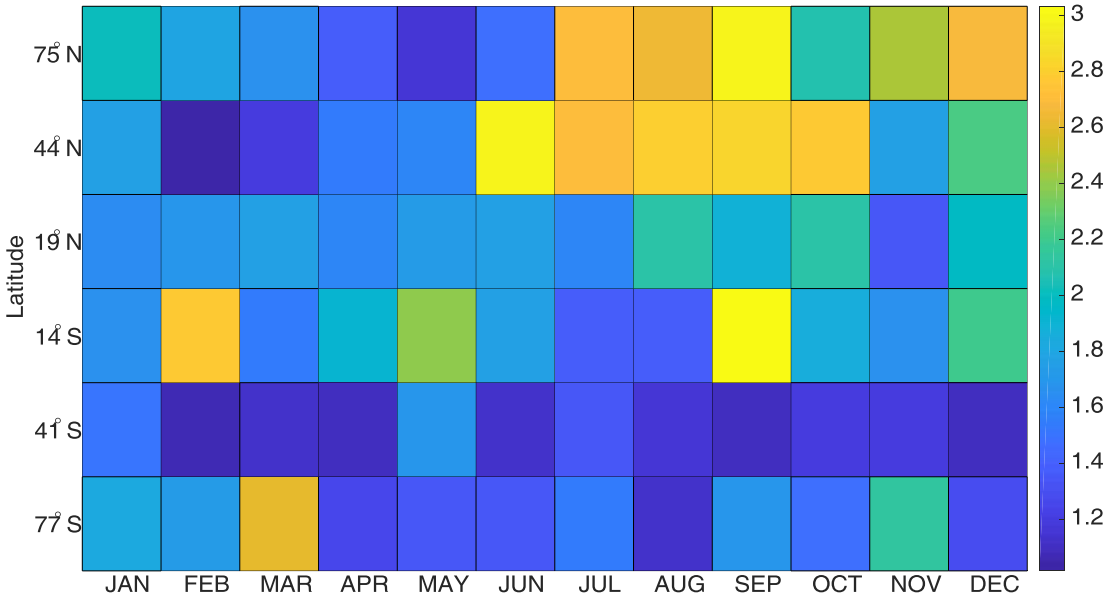

Figure 6.5 The corresponding RSD plot of global zonal monthly average of ground level observed OCS MRs (presented in *Figure 3.16*), showing the dispersion of each grid cell OCS MR in percentage [%] from year 2000 – 2016.

C LIST OF FIGURES

D LIST OF TABLES

E LIST OF EQUATIONS

F ACKNOWLEDGEMENTS

Not included in the electronic version.

G CURRICULUM VITAE

Not included in the electronic version.

H PUBLICATIONS

E.Karu, M.Li, L.Ernle, C.Brenninkmeijer, J.Lelieveld, J. Williams. A new system for gas phase trace gas analysis based on cryogenic pre-concentration, gas chromatographic separation and atomic emission detection (CryoTrap-GC-AED). Case study on carbonyl sulfide collected onboard the Lufthansa IAGOS-CARIBIC passenger aircraft. (*in preparation*)

J.Liebmann, N.Sobanski, J.Schuladen, **E.Karu**, H.Hellén, H.Hakola, Q. Zha, M.Ehn, M.Riva, J.Williams, H.Fischer, J.Lelieveld, J.N.Crowley. Alkyl nitrates in the boreal forest: Formation via the NO_3, OH and O_3 induced oxidation of BVOCs and ambient lifetimes. *Atmospheric Chemistry and Physics* (*ACP public discussion until 19 July 2019*)

E.Karu, D.Gentner. Sodium thiosulfate coating method for preparing selective ozone scrubbers. *European Patent Application* (2018)

J.Ditas, N.Ma, Y.Zhang, D.Assmann, M.Neumaier, H.Riede, **E.Karu**, J.Williams, D.Scharffe, Q.Wang, J.Saturno, J.P.Schwarz, J.M. Katich, G.R. McMeeking, A.Zahn, M.Hermann, C.A.M. Brenninkmeijer, M.O. Andreae, U.Pöschl, H.Su, Y.Cheng. Strong impact of wildfires on the abundance and aging of black carbon in the lowermost stratosphere. *Proceedings of the National Academy of Sciences of the United States of America* 115(50):E11595–E11603 (2018)

M.Li, **E.Karu**, C.Brenninkmeijer, H.Fischer, J.Lelieveld, J. Williams. Tropospheric OH and stratospheric OH and Cl concentrations determined from CH_4, CH_3Cl, and SF_6 measurements. *Nature: Climate and Atmospheric Science* 1(29) (2018)

J.Liebmann, **E.Karu**, N.Sobanski, J.Schuladen, M.Ehn, S.Schallhart, L.Quéléver, H.Hellen, H.Hakola, T.Hoffmann, J.Williams, H.Fischer, J.Lelieveld, J.N. Crowley. Direct measurement of NO_3 radical reactivity in a boreal forest. *Atmospheric Chemistry and Physics* 18(5):3799-3815 (2018)

M.Brüggemann, **E.Karu**, T.Hoffmann. Critical assessment of ionization patterns and applications of ambient desorption/ionization mass spectrometry using FAPA–MS. *Journal of Mass Spectrometry* 51(2):141-149 (2016)

M.Brüggemann, **E.Karu**, T.Stelzer, T.Hoffmann. Real-Time Analysis of Ambient Organic Aerosols Using Aerosol Flowing Atmospheric-Pressure Afterglow Mass Spectrometry (AeroFAPA-MS). *Environmental Science & Technology* 49(9):5571–5578 (2015)